UNIVERSITY OF CALIFORNIA,
IRVINE

Calibration Decision System of MEMS Gyroscope for Bio-Inertial Application

DISSERTATION

submitted in partial satisfaction of the requirements
for the degree of

DOCTOR OF PHILOSOPHY

in Biomedical Engineering

by

Sina Askari

Dissertation Committee:
Professor Andrei M. Shkel, Chair
Professor Hamid R. Djalilian
Professor Zoran Nenadic

2019

DEDICATION

To my father who taught me it's okay to guide your life by the stars
as long as you carry the sextant.

TABLE OF CONTENTS

LIST OF FIGURES

LIST OF TABLES

LIST OF SYMBOLS

Main characterization keywords

Symbol	Description
B_{offset}	Bias–Deterministic nonzero sensor output when given input rotation is zero
B_i	Bias instability–The instability of the B_{offset} as a random walk
B_s	Bias stability–The variation in B_{offset} from run-to-run as a random constant
C_f	Feedback capacitor
e_n	Equivalent voltage noise density
f	Center frequency of X-mode, Y-mode or average of the two (Hz)
i_n	Current noise density
k	Angular gain factor
Q-factor	Measurement of overall damping of X-mode or Y-mode
R_f	Feedback resistor
Z_i	Input impedance
c_x, c_y, s_x, s_y	Pendulum variables
E, Q, S, R, L	Invariant quantities in whole-angle mode of operation
(x, y, z)	Primary axes of motion of gyroscope or accelerometer
ω	Center frequency of X-mode, Y-mode or average of the two (rad/s)
θ	Angle of pattern (precession) of the corresponding elliptical orbit
ϕ_0	Initial phase of the corresponding elliptical orbit
Ω	Rate of angular rotation
Δf	Measurement of gyroscope anisoelasticity error, $\Delta f = \lvert f_x - f_y \rvert$
$\Delta(1/\tau)$	Measurement of gyroscope anisodamping error, $\Delta(1/\tau) = \lvert 1/\tau_x - 1/\tau_y \rvert$

LIST OF ABBREVIATIONS

Abbrv.	Shortened form of
ADEV	Allan Deviation
AG	Angular Gain
AGC	Amplitude Gain Control
ARW	Angle Random Walk
CVG	Coriolis Vibratory Gyroscope
DSP	Digital Signal Processing
DUT	Device Under Test
EAM	Electromechanical Amplitude Modulation
EMG	Electromyography or electrical activity produced by muscles
FRB	Force-to-ReBalance
IMU	Inertial Measurement Unit
LCC	Leadless Chip Carrier
PCB	Printed Circuit Board
PID	Proportional, Integral, Differential
PLL	Phase-Locked Loop
QCL	Quadrature Control Loop
QMG	Quad Mass Gyroscope
RCL	Rate Control Loop
RIG	Rate Integrating Gyroscope
RRW	Rate Random Walk
SF	Scale-Factor
SONAR	SOund Navigation And Ranging sensors
TED	Thermoelastic Damping
UITS	Universal Inertial Test System
MCE	Multichannel Cuff Electrode
MCU	Micro Controller Unit
MEMS	MicroElectroMechanical Systems
MTN	Mechanical-Thermal Noise
WA	Whole-Angle
WA-CL	Whole-Angle Closed-Loop
WA-OL	Whole-Angle Open-Loop
ZRO	Zero Rate Output
ZUPT	Zero velocity UPdaTe

ACKNOWLEDGMENTS

First, I would like to extend my appreciation to my doctoral program adviser Prof. Andrei M. Shkel to serve as my dissertation chair. I am truly indebted and thankful to his support, encouragement and vast knowledge of the field. I would like to thank my dissertation and qualifying exam committee members: Prof. Hamid R. Djalilian, Prof. Zoran Nenadic, Prof. Harrison Lin, Prof. William C. Tang, and Prof. Lorenzo Valdevit for their time, guidance and suggestions.

I am extremely grateful to my colleagues and friends at UCI MicroSystems Laboratory, who helped me in many ways for their assistance: Dr. Mohammad H. Asadian, Dr. Radwan M. Noor, Chi-Shih Jao, Yusheng Wang, Yu-Wei Lin and Kasra Kakavand for their support to drive my research activity and providing insightful discussions, Dr. Doruk Senkal, Dr. Brenton Simon and Dr. Sergei Zotov who helped me by providing generous amounts of advice which this dissertation is a continuation of their work in the past. And also thanks to my close friends who supported me throughout the way Dr. Kai Ding and Venu Gundeti.

I also would like to thank Prof. Harrison Lin's team, Dr. Alessandro Pressacco and Dr. Ronald Sahyouni for their collaboration opportunity in the development of an electrical current stimulation platform used for animal study.

Above all, I would like to thank the funding resources: Defense Advanced Research Projects Agency (DARPA) and U.S. Navy under Contract No. N66001-12-C-4035 (PASCAL-UCI/NGC), Contract No. N66001-16-1-4021 (PRIGM-AIMS), U.S. Department of Commerce, National Institute of Standards and Technology (NIST) under Contract No. 70NANB17H192.

Finally, I would like to express my gratitude to my parents, my sister, and my brother for their encouragement, support, and great patience at all times.

CURRICULUM VITAE

Sina Askari

EDUCATION

Doctor of Philosophy in Biomedical Engineering **2019**
University of California Irvine *Irvine, California, USA*

Master of Science in Electrical Engineering **2014**
University of California Irvine *Irvine, California, USA*

Master of Science in Biomedical Engineering **2012**
University of Southern California *Los Angeles, California, USA*

Bachelor of Science in Electrical Engineering **2010**
California State University Los Angeles *(3^{rd}-4^{th} year)* *Los Angeles, California*

University of Tehran *(1^{st}-2^{nd} year)* *Tehran, Iran*

EXPERIENCE

Graduate Research Assistant **2013–2019**
University of California, Irvine *Irvine, California, USA*

Graduate Research Assistant **2010–2012**
University of Southern California *Los Angeles, California, USA*

Sensor R&D Algorithm Engineer **20010–2012**
Medtronic, Minimed Inc. *Northridge, California, USA*

Undergraduate Student Researcher **2009–2010**
California State University Los Angeles *Los Angeles, California, USA*

REFEREED JOURNAL PUBLICATIONS

S. Askari, M. H. Asadian, and A. M. Shkel. Quad mass gyroscope instrumented to operate in the angular rate mode. *IEEE Sensors J.*, Under review.

S. Askari, M. H. Asadian, and A. M. Shkel. Whole-angle gyroscopes: A case study of MEMS quadruple mass design. *IEEE Sensors J.*, In preparation.

M. H. Asadian, S. Askari, and A. M. Shkel. An ultrahigh vacuum packaging process demonstrating over 2 million Q-factor in MEMS vibratory gyroscopes. *IEEE Sensors Letters*, 1(6):1–4, 2017.

D. Senkal, M. J. Ahamed, M. H. A. Ardakani, S. Askari, and A. M. Shkel. Demonstration of 1 million Q-factor on microglassblown wineglass resonators with out-of-plane electrostatic transduction. *IEEE/ASME J. Microelectromech. Syst.*, 24(1):29–37, 2015.

S. Askari, T. Chao, and R. D. de Leon. The effect of timing electrical stimulation to robotic-assisted stepping on neuromuscular activity and associated kinematics. *J. Rehabil. Res. Dev.*, 50(6):875, 2013.

T. Chao, S. Askari, R. De Leon, and D. Won. A system to integrate electrical stimulation with robotically controlled treadmill training to rehabilitate stepping after spinal cord injury. *IEEE Trans. Neural Syst. Rehabil.*, 20(5):730–737, 2012.

P. Agrawal, J. B. Welsh, B. Kannard, S. Askari, Q. Yang, and F. R. Kaufman. Usage and effectiveness of the low glucose suspend feature of the Medtronic Paradigm Veo insulin pump. *J. Diabetes Sci. and Technol.*, 5(5):1137–1141, 2011.

PREFEREED CONFERENCE PUBLICATIONS

S. Askari, M. H. Asadian, and A. M. Shkel. Performance of a high Q-factor QMG in open-loop and closed-loop instrumentations. In *IEEE/ION Position Location and Navigation Symposium*, Portland, OR, USA, Apr. 20–23, 2020 Accepted.

S. Askari, C.-S. Jao, Y. Wang, and A. M. Shkel. Learning-based calibration decision system for bio-inertial motion application. In *IEEE Sensors Conf.*, Montréal, Canada, Oct. 27–30 2019.

S. Askari, M. H. Asadian, and A. M. Shkel. Retrospective correction of angular gain by virtual carouseling in MEMS gyroscopes. In *IEEE Int. Symp. Inertial Sensors and Systems*, Naples, FL, USA, Apr. 1–5 2019.

S. Askari, C.-S. Jao, Y. Wang, and A. M. Shkel. A laboratory testbed for self-contained navigation. In *IEEE Int. Symp. Inertial Sensors and Systems*, Naples, FL, USA, Apr. 1–5, 2019.

Y. Wang, S. Askari, C.-S. Jao, and A. M. Shkel. Directional ranging for enhanced performance of aided pedestrian inertial navigation. In *IEEE Int. Symp. Inertial Sensors and Systems*, Naples, FL, USA, Apr. 1–5, 2019.

D. Vatanparvar, M. H. Asadian, S. Askari, and A. M. Shkel. Characterization of scale factor nonlinearities in coriolis vibratory gyroscopes. In *IEEE Int. Symp. Inertial Sensors and Systems*, Naples, FL, USA, Apr. 1–5 2019.

M. H. Asadian, S. Askari, Y. Wang, and A. M. Shkel. Characterization of energy dissipation mechanisms in dual foucault pendulum gyroscopes. In *IEEE Int. Symp. Inertial Sensors and Systems*, Naples, FL, USA, Apr. 1–5, 2019.

Y. Wang, S. Askari, and A. M. Shkel. Study on mounting position of IMU for better accuracy of ZUPT-aided pedestrian inertial navigation. In *IEEE Int. Symp. Inertial Sensors and Systems*, Naples, FL, USA, Apr. 1–5, 2019.

M. H. Asadian, S. Askari, I. B. Flader, Y. Chen, D. D. Gerrard, D. D. Shin, H.-K. Kwon, T. W. Kenny, and A. M. Shkel. High quality factor mode ordered dual foucault pendulum gyroscope. In *IEEE Sensors Conf.*, New Delhi, India, Oct. 28–31, 2018.

S. Askari, A. Presacco, R. Sahyouni, H. Djalilian, A. Shkel, and H. Lin. Closed loop microfabricated facial reanimation device coupling EMG-driven facial nerve stimulation with a chronically implanted multichannel cuff electrode. In *IEEE Int. Eng. Med. Biol. Soc. (EMBC)*, Honolulu, HI, USA, July 17–21 2018.

S. Askari, M. H. Asadian, and A. M. Shkel. High quality factor MEMS gyroscope with whole angle mode of operation. In *IEEE Int. Symp. Inertial Sensors and Systems*, Lake Como, Italy, Mar. 26–29, 2018.

S. Askari, M. H. Asadian, and A. Shkel. Performance requirements of MEMS based vestibular prosthesis. In *Biomed. Eng. Soc.*, Phoenix, AZ, USA, Oct. 11–14 2017.

M. H. Asadian, Yusheng Wang, S. Askari, and A. Shkel. Controlled capacitive gaps for electrostatic actuation and tuning of 3D fused quartz micro wineglass resonator gyroscope. In *IEEE Int. Symp. Inertial Sensors and Systems*, Honolulu, HI, USA, Jan. 5–9 2017.

S. Askari, M. H. Asadian, K. Kakavand, and A. M. Shkel. Near-navigation grade quad mass gyroscope with Q-factor limited by thermo-elastic damping. In *Solid-State Sensors, Actuators, and Microsystems Workshop*, Hilton Head Island, SC, USA, June 5–9, 2016.

S. Askari, M. H. Asadian, K. Kakavand, and A. M. Shkel. Vacuum sealed and getter activated MEMS quad mass gyroscope demonstrating better than 1.2 million quality factor. In *IEEE Int. Symp. Inertial Sensors and Systems*, Laguna Beach, CA, USA, Feb. 23–25, 2016.

A. Efimovskaya, D. Senkal, S. Askari, and A. M. Shkel. Origami-like folded MEMS for realization of TIMU: Fabrication technology and initial demonstration. In *IEEE Int. Symp. Inertial Sensors and Systems*, Hapuna Beach, HI, USA, March 23–26 2015.

D. Senkal, M. J. Ahamed, M. H. Asadian, S. Askari, and A. M. Shkel. Out-of-plane electrode architecture for fused silica micro-glassblown 3-D wineglass resonators. In *IEEE Sensors Conf.*, Valencia, Spain, Nov. 2–5 2014.

D. Senkal, M. J. Ahamed, S. Askari, and A. M. Shkel. MEMS micro-glassblowing paradigm for wafer-level fabrication of fused silica wineglass gyroscopes. In *Int. Conf. Solid-State Sensors and Actuators (TRANSDUCERS)*, Brescia, Italy, Sept. 7–10 2014.

D. Senkal, M. J. Ahamed, S. Askari, and A. M. Shkel. 1 million Q-factor demonstrated on micro-glassblown fused silica wineglass resonators with out-of-plane electrostatic transduction. In *Solid-State Sensors, Actuators, and Microsystems Workshop*, Hilton Head Island, SC, USA, June 8–12, 2014.

D. Senkal, S. Askari, M. J. Ahamed, E. J. Ng, V. Hong, Y. Yang, C. H. Ahn, T. W. Kenny, and A. M. Shkel. 100k Q-factor toroidal ring gyroscope implemented in wafer-level epitaxial silicon encapsulation process. In *IEEE Int. Conf. Micro Electro Mechanical Systems*, San Francisco, CA, USA, Jan. 26–30, 2014.

S. Askari, P. Kamgar, T. Chao, E. Diaz, R. D. de Leon, and D. S. Won. Modulation of ankle EMG in spinally contused rats through application of neuromuscular electrical stimulation timed to robotic treadmill training. In *IEEE Int. Eng. Med. Biol. Soc. (EMBC)*, San Diego, CA, USA, Aug. 28–Sept. 1 2012.

S. Askari, T. Chao, L. Conn, E. Partida, T. Lazzaretto, P. A. See, C. Chow, R. D. de Leon, and D. S. Won. Effect of functional electrical stimulation (FES) combined with robotically assisted treadmill training on the emg profile. In *IEEE Int. Eng. Med. Biol. Soc. (EMBC)*, Boston, MA, USA, Aug. 30–Sept. 3 2011.

S. Askari, M. Zhang, and D. S. Won. An EMG-based system for continuous monitoring of clinical efficacy of parkinson's disease treatments. In *IEEE Int. Eng. Med. Biol. Soc. (EMBC)*, Buenos Aires, Argentina, Aug. 31–Sept. 4 2010.

S. Askari and D. Won. Implementation of an EMG-based measure of rigidity in a PD symptom quantification. In *Biomed. Eng. Soc.*, Austin, TX, USA, Oct. 6–9 2010.

ABSTRACT OF THE DISSERTATION

Calibration Decision System of MEMS Gyroscope for Bio-Inertial Application

By

Sina Askari

Doctor of Philosophy in Biomedical Engineering

University of California, Irvine, 2019

Professor Andrei M. Shkel, Chair

This Ph.D. dissertation presents a development of calibration methods of microelectromechanical (MEMS) gyroscopes for a vestibular prosthesis. The vestibular prosthesis senses head orientation and provides electrical stimulation to the ampullary nerves. The prosthesis utilizes a micro sensing element, which is susceptible to environmental changes resulting in drift. Consequently, encoding the input rotation to stimulate pulses using a MEMS sensing architecture would mislead the nervous system and inadvertently cause additional damage to other sensing organs. Not mitigating the issues of short-term and long-term drift would take away all benefits of the prosthesis.

The focus of this dissertation is toward algorithm design and hardware development for the identification of sources of errors in bias and scale-factor of a MEMS gyroscope and to introduce sensor calibration methods for providing accurate electrical stimulation. A Silicon micromachined Quad Mass Gyroscope (QMG) was used, as a test structure device, and was utilized to identify sensor-level calibration algorithms needed for the prosthesis. For this realization, a standalone electronics platform for MEMS gyroscope characterization was designed and developed to identify the needed control algorithms to satisfy the required bandwidth and linearity of the prosthesis. As a calibration technique for the prosthesis system, a flexible solution platform for integration and data processing from multiple foot-

mounted inertial sensors was designed and developed for the purpose of providing an aiding solution to calibrate the prosthesis sensitivity and drift. The developed calibration methods demonstrated the potential to identify sources of errors and compensate for the drift, a functionality that would not be possible by simply utilizing off-the-shelf MEMS gyroscopes for the vestibular prosthesis.

Chapter 1

Introduction

This dissertation delves deeper into the identification of sources of error of microelectromechanical systems (MEMS) gyroscope sensor used for a vestibular prosthesis. The sensitivity of device parameters and the challenges involved in integration as a system to restore head movements are reported. This chapter is organized as follow: first, the contribution of the drift in the prosthesis, second, a summary of the neural dynamic responses involved in the system, followed by a literature review on the existing developed vestibular prostheses and its performance. Finally, the objectives of the research are defined and an outline of the dissertation is provided.

1.1 Motivation

Low-cost sensors offer new opportunities in biomedical research and clinical studies, whose applications keep growing. This small size sensing technology shows promise in a wide range of applications from robotics to prostheses. For example, electrohydraulic haptic transmission system for minimally invasive robotics [1], or incorporating pressure sensors

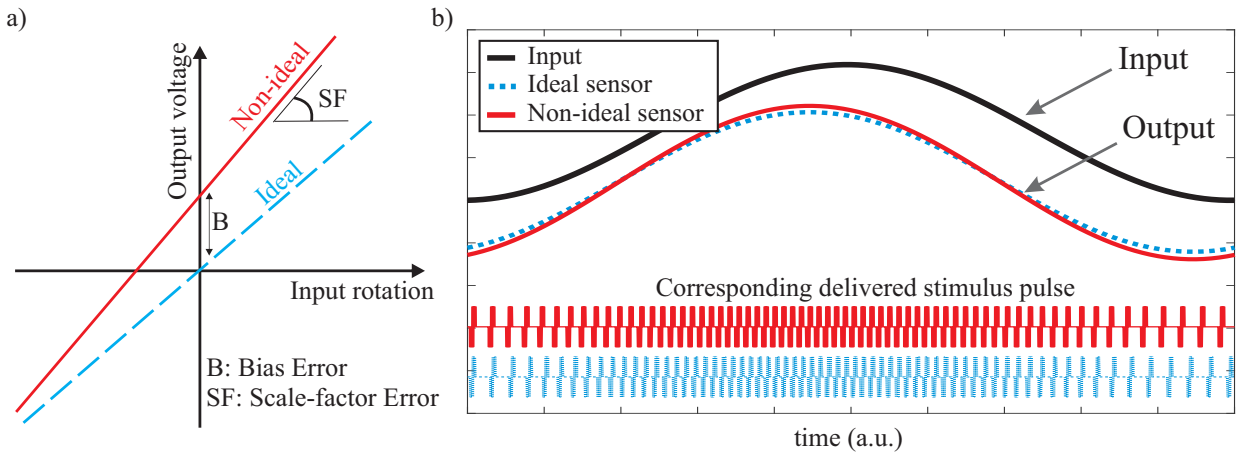

Figure 1.1: Illustration of bias and scale-factor drift on biphasic electrical stimulation pulses delivered to the vestibular nerve. a) gyroscope's measured response vs. ideal case, b) biphasic current pulses delayed due to sensor's B and SF drift.

for implantable with autonomous drug delivery [2]. However, due to the high drift of their sensing elements, these sensors require calibration and control, and simply using them may not be applicable for the biomedical prosthesis.

Hearing, vision, proprioception, and balance are supported by the vestibular system. Dysfunction of the vestibular organs results in losing balance, consequently dizziness, gaze and image instability. While MEMS-based vestibular prosthesis (VP) would restore the balance function of patients with instability problems, the analysis of sensor performances including short-term (in-run) and long-term drifts due in-operation Bias (B) and Scale-Factor (SF) errors of the sensor [3], underlying this rehabilitation is lacking.

The transfer function involved in the vestibular organ in chinchillas has been modeled with a sigmoid curve by [4], relating head rotation to the neural firing rate. In a VP, the rotational movement is captured by a gyroscope sensor and corresponding electrical stimulus is being provided [5, 6]. Typically a MEMS gyroscope suffers from bias and scale-factor drift. Fig. 1.1-a illustrates this drift concept graphically for a non-ideal sensor. For a low-cost MEMS gyroscope which categorized under rate grade class the bias ranges from 10 to 1,000 °/hr and scale-factor percent changes is <1 % [7]. Fig. 1.1-b shows the responses of the system for

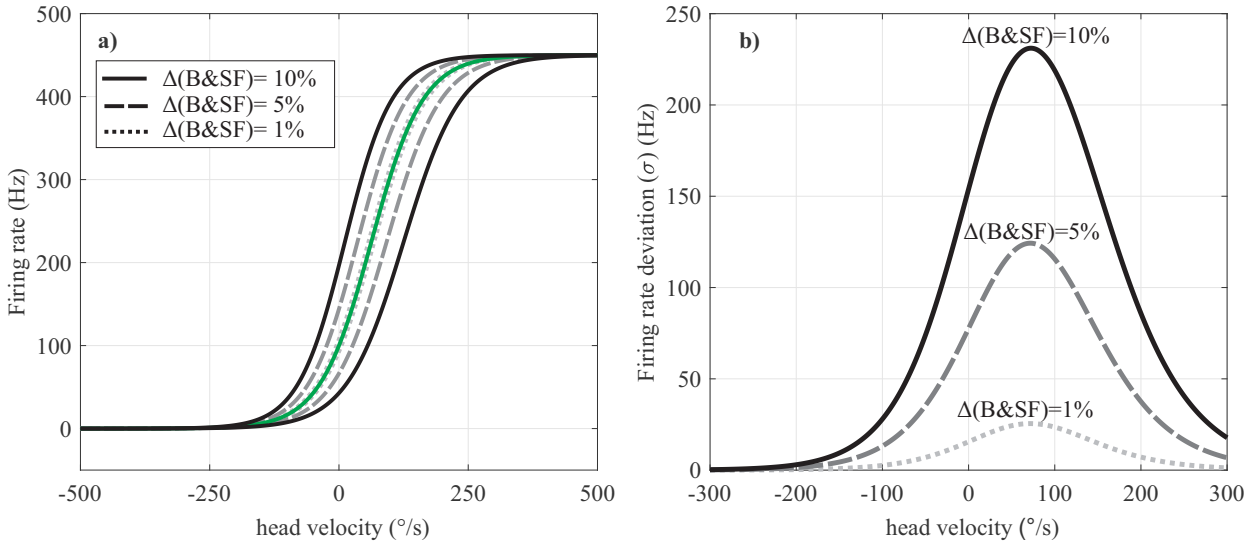

Figure 1.2: Simulation result of bias and scale-factor error on firing rate due to different drift conditions of 1, 5 and 10 %. The drift is shown as: a) the transfer function characteristic, and b) variation of firing rate error vs. head velocity.

both ideal and non-ideal sensors, using model by [8]. Fig. 1.2 illustrates the corresponding numerical drift into the delivered pluses for changes of 1, 5 and 10 % and also the total error compared to an ideal case, using model [4]. For example, under no input rotation, the baseline activity of the electrical stimulation deviates to 75 Hz under 5 % changes in both bias and scale-factor, and similarly deviates to a maximum of 125 Hz electrical stimulation drift under input rotation.

Vestibular losses significantly increase the detection threshold from 0.5 °/s to 5.8 °/s [9]. As a result of short-term and long-term drifts for the prosthetic device, a normal human sensitivity could fall into the vestibular dysfunction category. Fig. 1.3 demonstrated these thresholds, in the Allan variance plot for different classes of gyroscopes. Allan variance plot provides information on what accuracy is expected if the output is averaged for a given averaging time, τ. Thus as a design point of view, the time to reach the detectable threshold is important for the prosthesis to be considered.

Therefore the design requirement for a vestibular prosthesis can be realized using a MEMS

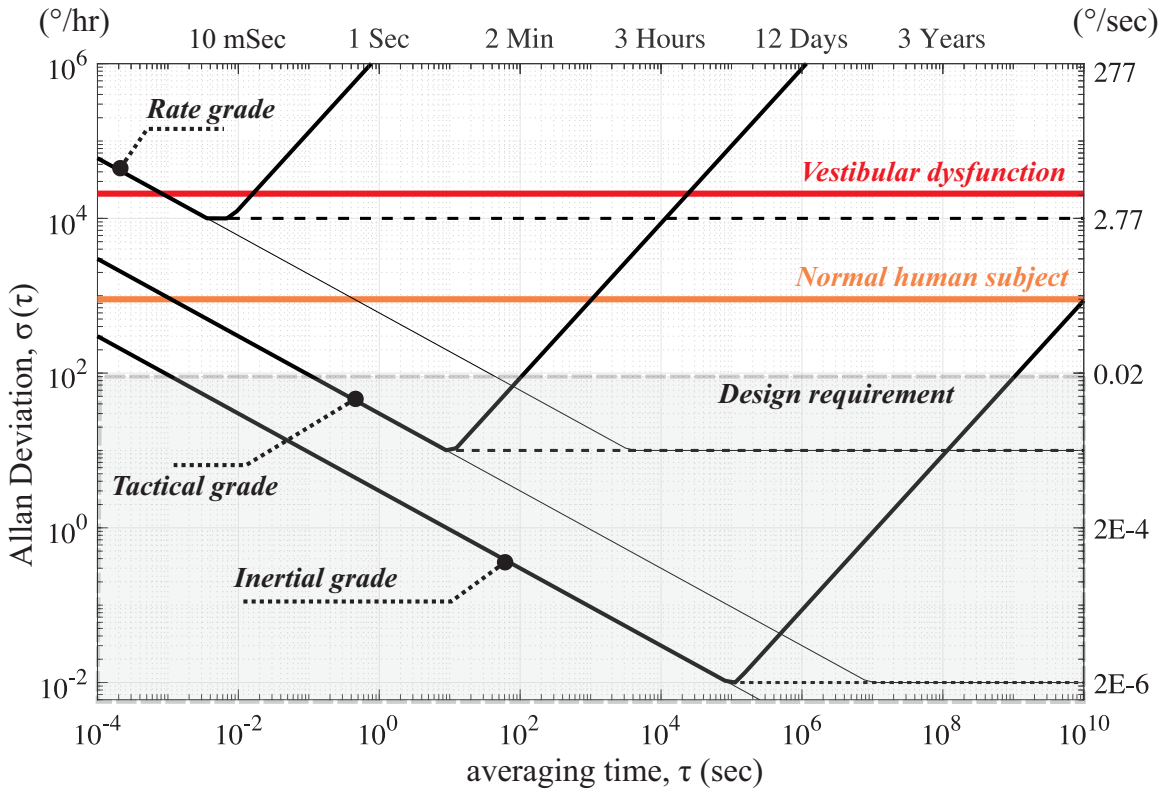

Figure 1.3: Allan variance estimations of gyroscope grades and its error propagation over time due to Mechanical-Thermal Noise. Illustrating the trade-off in minimum detectable for each grade compared to the minimum detectable of human subjects.

gyroscope. To allow room for error and to mimic normal human sensitivity for the prosthesis, a gyroscope sensor with sensitivity of below 0.02 °/s with capability of continuous sensor calibration throughout the operation are required for the device.

1.2 Background

Merging electronic technology with advances in biology results in an immense impact each year and every day of our lives. As soon as the transistors became available, biomedical engineers and clinical professionals saw the opportunity to develop a low power implantable unit. From this multidisciplinary approach, bioengineered devices have been developed, which, today we have taken almost for granted. For example, heart pacemakers that supply cardiac

signal including circuitry and control, spinal cord stimulators for management of chronic pain relief, cochlear implants for activation of the auditory nerve, deep brain stimulators for treating Parkinson's disease, and phrenic nerve stimulations for assisted breathing [10–14].

According to a report by the Vestibular Disorders Association and Johns Hopkins Medicine, in the United States, 69 million Americans have experienced balance problems, and more than 48 million have reported some degree of hearing loss [15, 16]. Recent observational studies have suggested vestibular dysfunction as a recognized complication of diabetes [17]. A separate study in 2001 projected that in the United States 18 million people will have diabetes by 2050 [18], therefore vestibular-related complications is expected to increase. As this trend worsening, this will lead to dramatic increases which would be inevitable anyway in the number of Americans with vestibular loss which will lead to greater need for prosthesis.

Inside the human inner ear, there are three individual orthogonal semicircular canals (SCC) - anterior, posterior and horizontal - and two otolith organs, located in - utricule and saccula - which together as a system intervene in the dynamic equilibrium of the body's balance. Fig. 1.4 illustrates the vestibular branch organ, where it senses the changes in a fluid called endolymph by head rotation or tilt relative to the neck. This information, combines with sensory receptors from the visual organ and hearing changes from the auditory system, are process together as the vestibular system. The system provides information to the brain on the position of the head and the body in space, thus allowing the person to carry out the proper alignment. A dysfunctional vestibular organ can cause balance problems as well as headaches.

Activation of the vestibular system induced by angular rotation or linear force causes eye movement by countering movement of the head which is called the Vestibulo-Ocular Reflex (VOR). The VOR gain is a reference point to assess the efficacy of vestibular rehabilitation. The activation of the vestibular system translates to firing rate pulses. For example, in a squirrel monkey, the activation profile for SCC and otolith were extracted under different

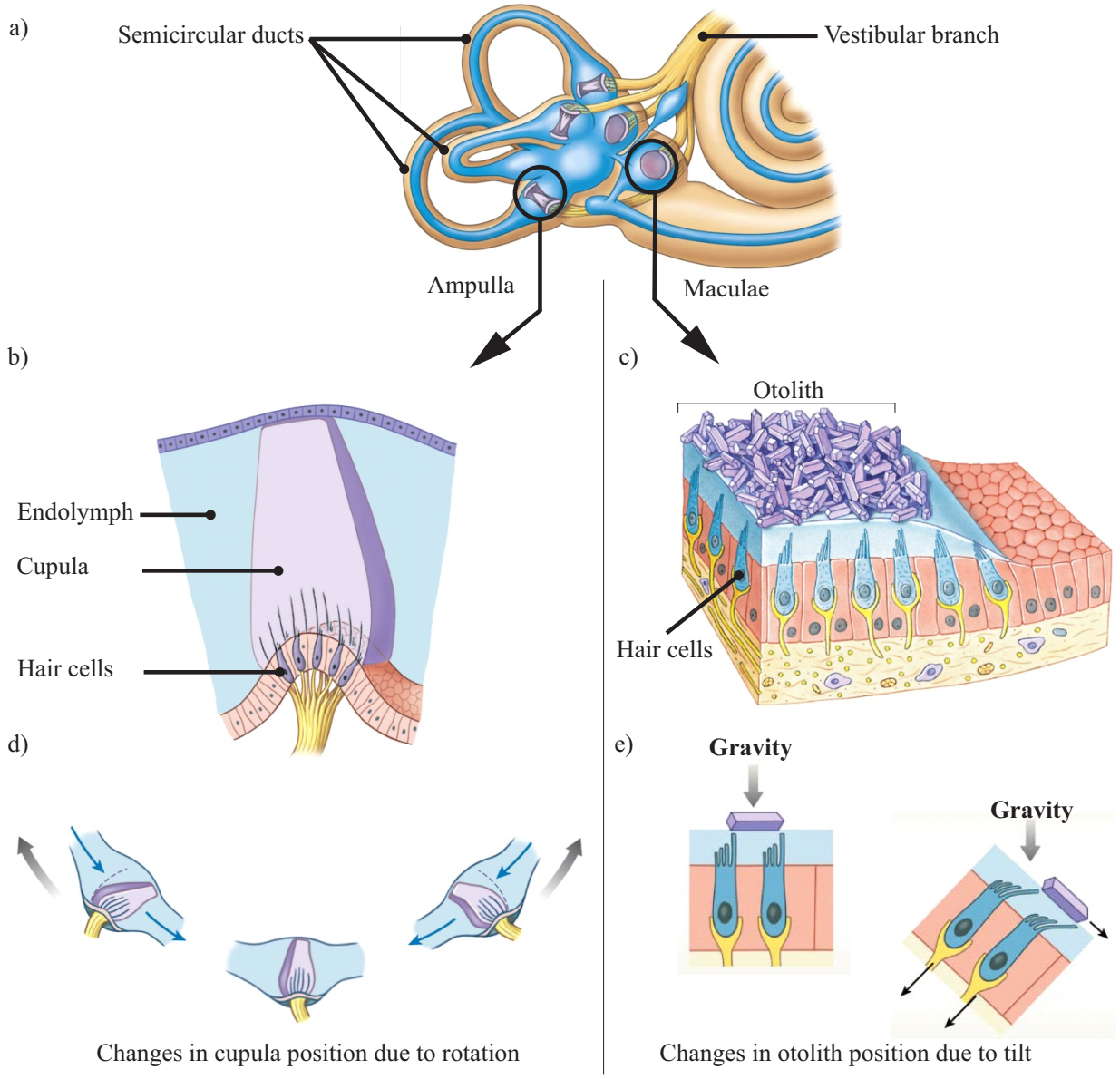

Figure 1.4: Breakdown illustration of the membranous labyrinth elements includes vestibular organs and the cochlea. a) vestibular branch contains three SCC and two otolith organs, b) the ampulla area contains the cupula wall and hair cells where stress is being sensed, c) the otolith in resting position bundle with the hair cells, d) endolymph movement in the membranous labyrinth of the inner ear resulted deformation of the cupula, e) demonstration of otoconial membrane deformation as a result of acceleration force. Individual photos courtesy of Pearson Education, Inc., [19].

experimental conditions, Fig. 1.5. Similar experiments were performed for a human to derive the characteristics. Increases in vestibular perceptual thresholds were shown in patients with vestibular functional loss compared to healthy subjects, [9]. Fig. 1.6 shows these differences

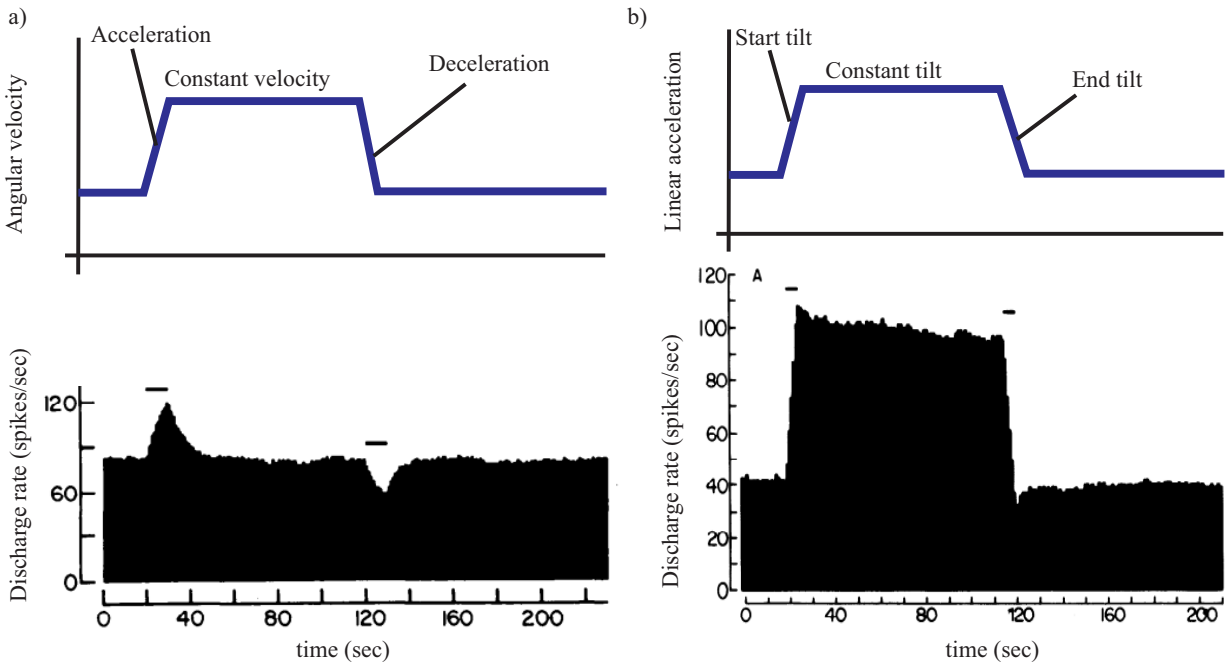

Figure 1.5: Responses elicited in the squirrel monkey from, a) semicircular canals, b) otolith organs. Top row) Profile given as physical stimulus to the head, bottom row) stimulus response recorded. Discharge rate photos adapted from [8, 20].

graphically under the different axes of rotation.

On the other hand, normal subjects can distinguish the direction of rotation in the yaw direction as low as $0.5\,^{\circ}/s$ [21], see Fig. 1.7-a, similarly minimum of $5.8\,^{\circ}/s$ for vestibular dysfunction patients [9]. The minimum linear acceleration threshold detected by a human is $0.005\,g$ [22], see Fig. 1.7-b.

The algorithm involved in the vestibular organ has been modeled and categorized in three different levels from top to bottom in a hierarchy: 1) the dynamic involved in the semicircular canal or otolith mass, 2) hair cells, and 3) synaptic transmission neural activity. These models have been validated in several literature reports. Table 1.1 summarizes the behavior of the vestibular input-output algorithm introduced and the transfer function modeled for the organ. In this dissertation, we used the model introduced by [4] as a reference to answer the research questions of the work.

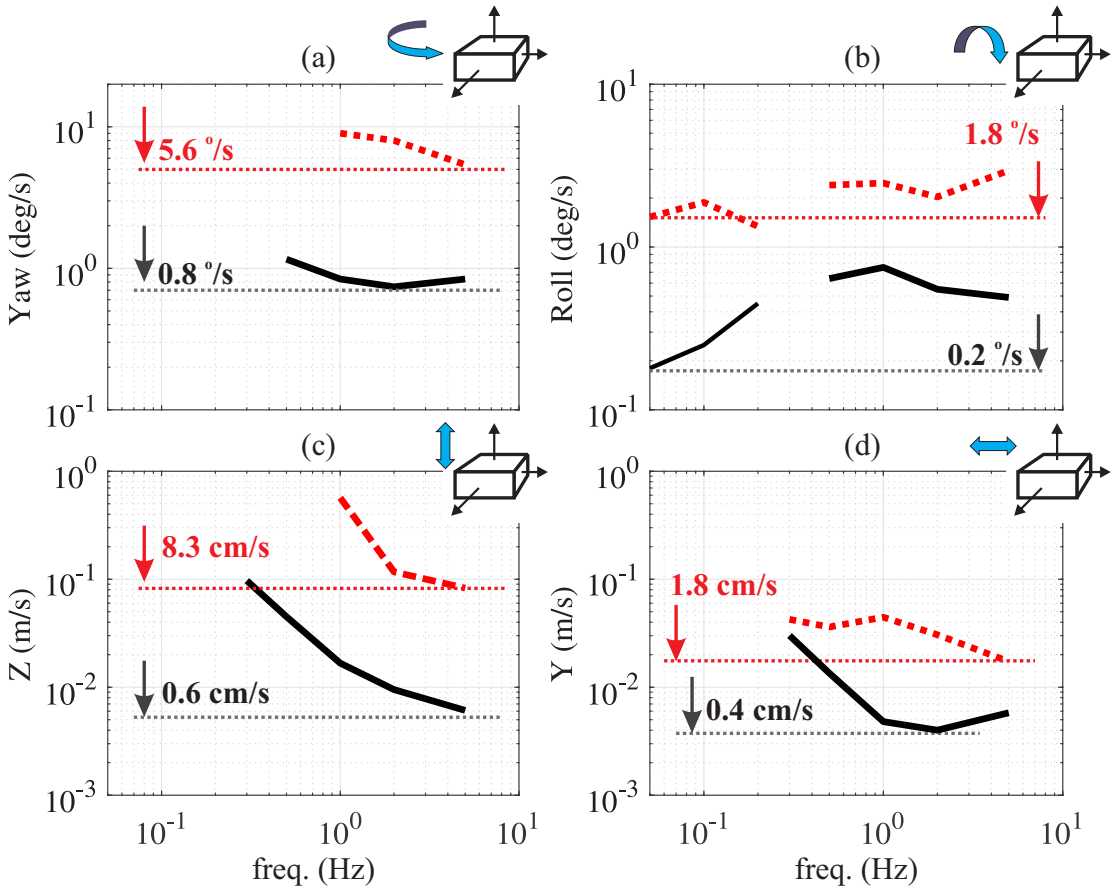

Figure 1.6: Minimum detectable for patients experiencing total bilateral vestibular loss (dash line) alongside healthy subjects (bold line), a) yaw rotation, b) roll-tilt, c) z-translation, and d) y-translation. Measurement data points extracted from [9].

As the research field advances, the range of integration of multiple sensors for biomedical applications becomes more developed. MEMS are microstructure devices that contain tiny miniaturized mechanical parts. MEMS gyroscope and accelerometer sensors provide information on linear and rotational forces. An example of a non-invasive system application using these sensors is to track and monitor the occurrence of impact on athlete for concussion management [28]. Patients with balance disorder can also benefit from mainly sensors with orientation and acceleration information. These patients have different yaw and tilt rotation thresholds and also experience decrees in the angular velocity of their walking as compared to healthy patients [29, 30]. The vestibular prosthesis can be implanted in patients with a balance disorder [31]. Electrodes with fine wires on the stimulation site provide safe

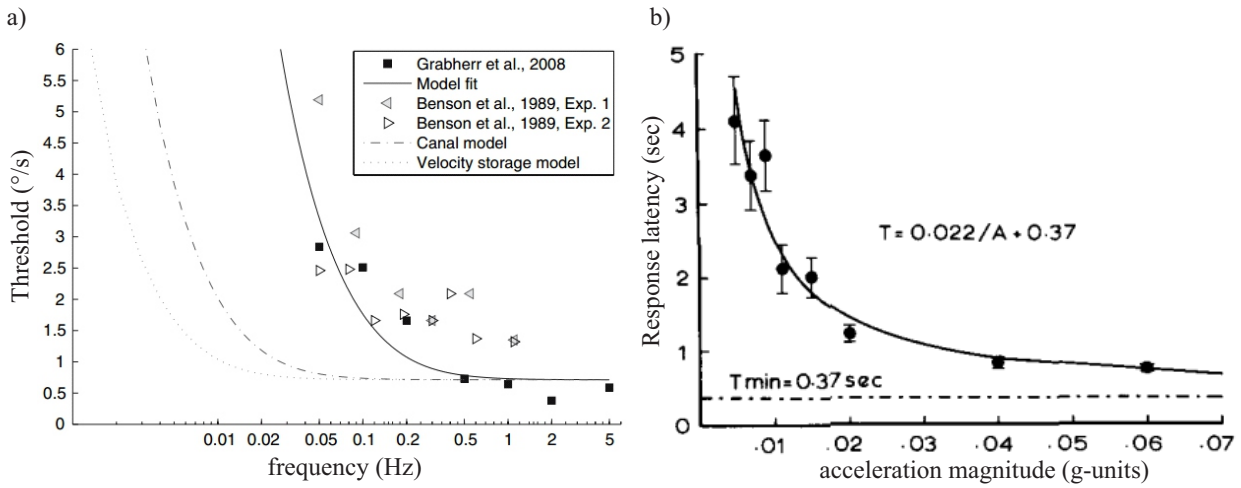

Figure 1.7: Minimum threshold detected by a human when the body undergoes a physical input a) angular rotation, or b) acceleration force. Photos adapted from [21, 22].

delivery of electrical charges to tissue.

An angular position or velocity-based auditory by prosthetic feedback benefits patients with vestibular loss [32]. Sway and tilt are captured by the velocity transducer attached to the subject. Loudspeakers provide biofeedback noises surrounding the subject to help identify the direction. Another treatment for the vestibular disorder is the use of radio-frequency linked to the implantable electrode for prosthetic electrical stimulation, thus opening a wide opportunity to explore embedded wearable devices for R&D on vestibular prosthesis [33]. A conceptual system to help a person with vestibular dysfunction by using a single-axis gyroscope with the integration of discrete electronics was proposed and demonstrated experimentally at UCI MicroSystems laboratory by [34]; however, the requirement on sensor sensitively for this prosthesis device as a system is still unknown. A vestibular prosthesis prototype that comprises gyroscope devices has shown performance constraints, and the importance of resolution level has been acknowledged [35, 36], also the use of tactical grade gyroscope devices has been suggested [37].

Besides the minimum sensitively and the need for long-term calibration for the vestibular prosthesis, two important design considerations are: the latency and the dynamic range

Table 1.1: The dynamic involved in the vestibular organ modeled by different algorithms

Vestibular system	Ref.	Mathematical model	
Coord. trans.		3-Semi Circular Canal (SCC) (3-axis gyroscope)	2-Otoliths (Utricle/Saccule) (3-axis accelerometer)
Neural Dynamic (ND): Differential equations	[8, 20]	$\Theta\frac{\mathrm{d}^2\xi}{\mathrm{d}t^2} + \Pi\frac{\mathrm{d}\xi}{\mathrm{d}t} + \Delta\xi(t) = \Theta\alpha(t)$ $H(s) = \frac{\tau_a s}{(1+\tau_a s)}\frac{(1+\tau_L s)}{(1+\tau_1 s)(1+\tau_2 s)}$	$H_{oto}(s) = \frac{1}{(1+\tau_M s)}\frac{(1+k_A\tau_{A,oto}s)}{(1+\tau_{A,oto}s)}$
	[23]	$\frac{\phi}{\Omega}(s) = \frac{\alpha T_1 T_2 s}{(T_1 s+1)(T_2 s+1)}$	N/A
	[24]	N/A	$C\frac{\mathrm{d}V}{\mathrm{d}t} = I_{syn} - I_{Na} - I_K - I_L$ $\tau(V)\frac{\mathrm{d}n}{\mathrm{d}t} = (n_\infty(V) - n)\cdot a^{\frac{T-T_0}{10}}$
Freq. mod. (FM): Look up table	[4]	$f = 0.5 \times f_{max} \times (1 + tanh(A + C(\frac{ADC(\Omega)}{2048} - 1)))$ $A = tanh^{-1}(2 \times f_{baseline}/f_{max} - 1), C = [1 - 10]$	
	[25]	$f = f_{middle} + f_{range}\left[tanh(\frac{\omega}{S_{shape}})\right] = 150 + 100\left[tanh(\frac{\omega}{250})\right]$	
	[26]	$f = \frac{f_{max}-f_{min}}{2\lvert Limit_c\rvert}Reading_c + \frac{f_{max}+f_{min}}{2}$	
Amp. mod. (AM)	[27]	$I_1 = gain_{x1}\omega_x + gain_{y1}\omega_y + gain_{z1}\omega_z + baseline\ amplitude$	

bandwidth of the sensor. The latency of the VOR in humans is being shown to be short and ranges between 10 to 60 ms [38]. Measurement shows that the vestibular system's firing rate response to a wide input range from ∼0.2 to 450 °/s [39]. Therefore, achieving these requirements simply with low-cost MEMS gyroscopes is not possible. When substituting this organ with a prosthesis for those with a balance disorder, a high-performance MEMS gyroscope device with calibration and compensation loops is necessary to achieve these requirements. This dissertation investigates the integration and implementation of these calibration loops.

1.3 Literature Review

The following is an overview of the field in the development of vestibular prostheses toward implementation in humans and nonhuman primates, including 1) vestibular rehabilitation, 2) development of the prosthesis, and 3) performance and resolution.

1.3.1 Vestibular Rehabilitation

In the vestibular prosthesis system, microelectrodes were placed close to ampullary branches to artificially restore the vestibular ocular reflex. Devices with multichannel independent vestibular electrode arrays have been developed for clinical studies [4]. The development of a three-dimensional multi-channel vestibular prosthesis has been investigated in chinchillas and rhesus monkeys [40, 41]. Currently, the focus of multi-channel vestibular prosthesis is to identify the challenges in human trials [42]. This same configuration has been used in humans [31], resulting in a three-fold increase in VOR at for input rotation of 0.5 Hz and above. The following is an overview of the few approaches on vestibular rehabilitation which have been reported so far:

Gong et al., 2000 [5] demonstrated a prototype on measuring the angular velocity of an animal's head using a piezoelectric gyroscope with a single-channel prosthesis. The dynamics of semicircular canals were replicated and applied at various currents according to a table created by an ad-hoc function. This preliminary design was tested on guinea pigs, and the results were gathered by measuring the VOR. In the experiment, the prosthesis was being used while the animal was stationary; therefore, the results may contain a mixture of the signal received from the device and the signal received from the vestibular system. The results showed only mild VOR gain improvement which could be due to a variety of reasons, including lack of time given for the animal to adapt,

the need for higher values for stimulation current, varying pulse duration, placement of the electrodes, and the contradiction of signals present in the specimen's head.

Fitzpatrick et al., 2004 [43] reported the use of a galvanic current stimulation as a simple way to modulate artificially the firing rate of vestibular afferent signals. Evidence shows evoked sway responses as a result of this vestibular stimulation; however, it is still unknown how this stimulation provides input to the whole system.

Danilov et al., 2007 [44] reported the first human pilot study using the BrainPort vestibular balance device by electrotactile stimulation of the tongue through sensing the patient's head movement using an accelerometer. As the head and body move in different directions, the patient gets trained to have a proper posture by keeping the stimulation in the center of the tongue. Due to the non-surgical aspect of this technology, the same device was used for the purpose of helping those with visual impairment by providing a stimulation pattern of the object recorded by an external camera sent to the tongue [45].

Vuillerme et al., 2008 [46] have shown the effectiveness of improving postural performance through electro-tactile stimulation of a patient's tongue in both the healthy and those with balance disorders.

Lawson et al., 2012 [47] documented the use of tactile situation awareness for pilots during flight as an alternative feedback for balance information by providing body sway cues through the vest to the torso.

Berg et al., 2012 [48] reported the first human experiment on an implanted vestibular prosthesis, which did not sense head rotation but was designed to override vestibular signals.

Pelizzone et al., 2014 [49] reported for the first time a successful human subject experiment using a device which senses head rotation. They were able to demonstrate that

the artificial restoration of the VOR is possible via amplitude modulation of pulses delivered as electrical stimulation of the vestibular nerve branches using a 3-axis gyroscope to estimate head rotation in a horizontal plane. The results agree with the fundamentals of balance restoration and envision a path towards clinical studies.

Guinand et al., 2016 [50] reported the first near real world walking task using a motion-modulated stimulation with vestibular implant on patients with bilateral vestibular loss. The experiment showed a close-to-normal response in visual acuity abilities in the test subject when the prototype was enabled. These preliminary findings in the field suggested a need for more fundamental studies in the development of vestibular mechanisms for prosthesis devices. More recently, the group also reported the use of a video head impulse test to assess the VOR responses in patients by modulating electrical stimulation strength [51].

Thompson et al., 2018 [52] reported a balance platform system to investigate the postural responses of a rhesus monkey using vestibular prosthesis. This diagnostic system enabled them to assess the effectiveness of implanted prosthesis on posture. The animals were trained to stand still on a balance platform with dynamic tilts in the roll axis. While the animal was standing on the platform, conditions such as quiet stances and head-turns to illuminating target, were evaluated by observing reaction forces, head, and trunk sway.

Jiang et al., 2018 [53] demonstrated the use of frequency modulated pulsed infrared radiation (IR) to directly stimulate the individual SCC in animal model. This opens up the research possibility to investigate on optical neural stimulation in inner ear.

1.3.2 Vestibular Prosthesis System Development

There is an abundance of considerations for developing a vestibular prosthesis, from electrical circuits and signal processing units to the safe delivery of current pulses to the tissue. The following is an overview of the development of this bioengineered device in the recent past:

Shkel et al., 2006 [34] first reported the development of a unilateral vestibular prosthesis using a custom 1-axis microelectromechanical system gyroscope and a circuit to deliver electrical current pulses proportional to head angular acceleration using dynamics described by [54].

Constandinou et al., 2009 [55] described the design and implantation of a vestibular algorithm into hardware ASIC and its feasibility for implantable clinical study. The design considerations are speed, size, and power efficiency.

Nguyen et al., 2014 [27] reported the use of a customized system with commercial signal processing platforms (FPGA, and host PC, LabVIEW software) to interface with a modified cochlear implant to stimulate semicircular canals.

Andreou et al., 2014 [56] used a microfluidic gyroscope based on a fluidic mass that deflects as a sensing element similar to the biological semicircular canal. The detection scheme for this device requires an external current source to measure the change in resistance corresponding to the angular rate of rotation.

Töreyin et al., 2016 [57] reported the development of a small-footprint low-power ASIC signal processor unit for a vestibular prosthesis. The unit interfaces with inertial sensors that use coordinate system transformation to deal with misalignment between natural and implanted sensors. The paper hypothesized that patient-dependent parameters are critical features in the improvement of their stimulation efficacy. The main control

parameters were a baseline neural firing rate when the head is stationary, firing rate range, asymmetry ratio, and gain.

Hageman et al., 2016 [58] developed a custom neural interface ASIC to provide biphasic current pulses for stimulation. They reported using off-the-shelf components and a commercially available microcontroller for signal processing. The functionality of this system is application-specific for the stimulation of three semicircular canals; devices are known as multichannel vestibular prostheses (MVPs).

1.3.3 Algorithm and Sensory Performance

The vestibular prosthesis has shown improvement in animal studies; however, the importance of resolution level has only minimally been acknowledged [35, 36]. Any adjustment in VOR over time would eventually be corrected by neural plasticity in the human brain. These adjustments would cause rapid, severe nausea or even vomiting [59]. Errors resulting from gyroscope drift, signal processing, and misalignment could cause a drift in pulse delivery, which would require correction and/or adjustment [60]. Therefore, calibration and correction are necessary.

DiGiovanna et al., 2012 [61] suggested that providing an initial condition that is close to the natural semicircular canal is required to decrease learning time for brain neural plasticity and may increase mapping accuracy. The study used an extra sensor mounted on the patient's head and five cameras for calibration. A rotational matrix for calibration was extracted by comparing angular velocity measurements in the head with a bite-bar sensor and a prosthetic sensor. In their findings, the alignment error was superior to any surgical alignment. A caveat for this experiment is that the method required an additional sensor and had to account for multiple independent measurement noises.

Sadovnichii et al., 2013 [24] delved into a corrector of output signals from the gravitoinertial mechanoreceptor of a vestibular apparatus. The study focused on minimizing instrument errors in the output signals of the micro accelerometer by using the Hodgin-Huxley model to correct personal orientation in space.

Soto-Eguibar et al., 2014 [62] suggested a prosthesis unit that uses a neuromimetic model of the vestibular function by detecting angular and linear movement using MEMS sensors, translating head rotation information into electric pulses or continuous galvanic current stimulation. This model replicated the mathematical model of the natural vestibular system using differential equations.

Jiang et al., 2015 [63] reported that independent parallel stimulation in vivo to the three semicircular canals with minimal mixed crosstalk was achieved using three ASICs. The error in vestibular prosthesis misalignment arose from stimulation current spread from one canal to the others. Therefore, the group developed parallel stimulation management by power isolation to the three stimulators for each canal. Memory-based stimulation control was achieved by independently managing parallel stimulation. The prototype established versatile stimulation management and neural recording for feedback, which opening up a more promising approach for algorithm development.

Boutros et al., 2016 [64] experimented on rhesus macaques and studied the resolution needed on stimulator circuitry for a head velocity-to-pulse rate map by comparing smooth and stair-step approximation of pulse-frequency modulated transfer functions. The approximation map discretized the input-output map and posed more of a problem at high pulse rates compared to low rates in which they closely followed each other. This finding showed that temporal discretization errors resulted in no significant difference in VOR gain.

1.4 Research Objective

MEMS gyroscope sensor drift comes from numerous sources of errors, which makes identifying it visually a particular challenge. This drift in MEMS gyroscopes is known as bias and scale-factor error. The use of a MEMS gyroscope in an implantable vestibular prosthesis sets a challenging limit to the performance of the device which varies by environmental conditions and method of characterizations. These challenges range from fabrication imperfection of the device, resulting in an asymmetric structure, to the selection of control algorithms for operating the device. Therefore, careful design, control, circuitry, and calibration solutions need to be taken into consideration to address the requirements for the prosthesis.

This dissertation aims to identify and address these limitations for the prosthesis. Fig. 1.8 illustrates the hierarchy of calibration levels for a MEMS IMU sensor. As shown, the calibrations fall into the following main categories: a) device structure b) electronics actuation and front-end detection, c) control algorithm for gyroscope mode of operation, d) state estimation on the output IMU for positioning and navigation, and e) application-specific calibration. Therefore, if a MEMS gyroscope is being used for the prosthesis, for each category control algorithms are needed to be implemented to produced error-free firing rate output. In this dissertation, we aim to discuss and explore the characterization and the calibration methods on the device, the electronics, the control algorithms, and the application by selecting a sensing structure and compensating the frequency mismatch of the structure, identifying the needed hardware architecture, characterizing the control loops and using aiding functionality.

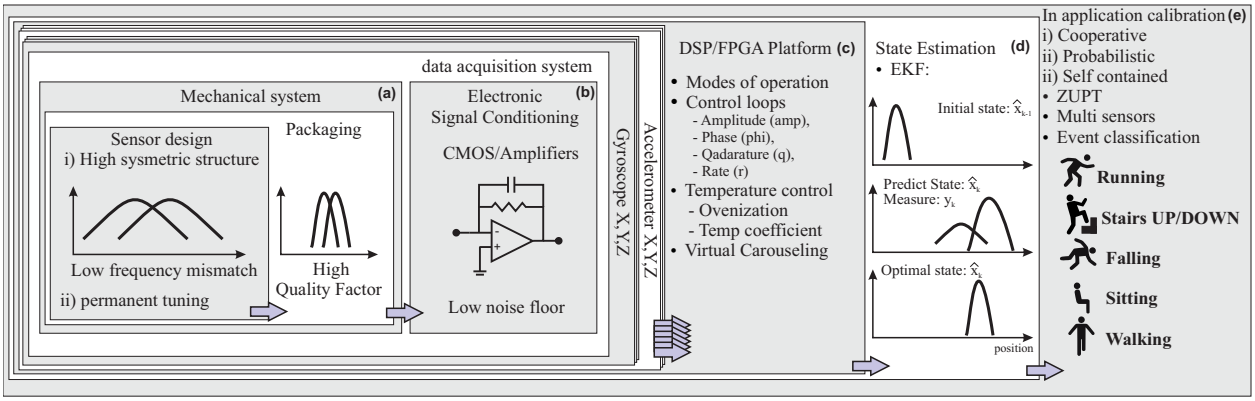

Figure 1.8: Hierarchy of calibration levels for a MEMS IMU sensor. Calibration on a) device level, b) electronics signal conditioning, c) control loops algorithm, d) state estimation, and e) event detection.

1.5 Dissertation Outline

In Chapter 2, we discuss the bottom-up building blocks needed for the characterization and implementation of algorithms on a MEMS gyroscope used for the prosthesis. A fabricated MEMS gyroscope sensor with a high Q-factor was selected as a test structure to study the sources of errors in device-, algorithm- and system-levels. The development process of electronics characterization platforms and interfaces needed for implementation of the control algorithm for both a fabricated sensor or a commercially available MEMS IMU were discussed. The operation of the device structure, the characterization on quality factor extraction, the stability of the quality factor over time, the selection decision and modeling in support of the engineering design and noise characterization of the system are being provided. In Chapter 3, the selected MEMS gyroscope sensor was instrumented in rate mode of operation to characterize the in-run drift. A method was developed for frequency tuning. The performance analysis on control loop accuracy, scale factor linearity, bandwidth, and noise analysis were reported. The results were compared and analyzed to lower the Q-factor of the same design. In Chapter 4, the same high Q-factor device was instrumented in angle mode of operation. The principle of operation and implantation of the algorithm

in hardware were discussed. Error identifications of the sensor were enabled through the developed virtual carouseling algorithm. In chapter 5, an aiding calibration algorithm was developed on the fusion of multiple sensors for correction of drift sensed by head-mounted IMU for vestibular prosthesis. In Chapter 6, a prototype with one channel electrical current stimulation integrated with the cuff electrode was developed as a system and used to validate the electrical stimulation delivered to an animal model. Finally, Chapter 7, concludes the dissertation with a summary of contribution and outlook.

Chapter 2

Motion Sensing Building Blocks

MEMS gyroscope sensors have been employed successfully in many motion-sensing applications [7], including roll-over detection for safe driving in the automotive industry [65, 66], rotation rate measurement for high-end gaming in consumer electronics [67], human motion tracking in Virtual Reality (VR) and Augmented Reality (AR) applications [68], drilling guidance in oil or gas exploration [69], north finding [70], space applications [71], and navigation applications [72]. In this chapter to study the in-run and long-term drifts of a MEMS gyroscope for a biomedical vestibular prosthesis, we describe the developed building blocks architecture considered for this investigation.

2.1 Introduction

This section summarizes the effort on the development of necessary parts to characterize and implement algorithms on a MEMS gyroscope sensor. We classified the bottom-up design architecture into four categories, a) a gyroscope device sensing elements to provide the needed prosthesis sensitivity, b) the mode of gyroscope operation and the algorithm for characterization, c) a universal standalone platform to identify the sources of errors by characterization of the fabricated sensor, and d) a platform for fusion of multiple commercially available IMUs for aiding calibration on the prosthesis. We present a discussion on the design of the test structure, as well as the electrostatic scheme for actuation and detection of the orthogonal modal frequencies and the initial frequency response characterization. The identification of the energy dissipation mechanisms in the test structure are investigated. We provide the selection of the discrete components, the implemented circuits, and the selected evaluation boards in support of the engineering design decision on the final system. We report electronic modeling and simulation involved in these steps and noise characterization of the developed platforms.

2.2 Quadruple Mass Gyroscope

A Quadruple Mass Gyroscope (QMG) comprises four coupled identical oscillators, providing an X-Y symmetry of the resonant structure [73]. The coupled oscillators have four degenerate resonance modes: (1) anti-phase, (2) in-phase, (3) double anti-phase, and (4) double in-phase, Fig. 2.1. The in-phase and double anti-phase modes are not independent and are coupled by the Coriolis force, thus they are not utilized for gyro operation in the QMG design. The anti-phase and double in-phase modes are independent and sensitive to the Coriolis coupling and can be used for gyro operation. However, the double in-phase mode is sensitive to external linear accelerations and should be avoided as the operational mode. The anti-phase motion of masses during the operation assures minimization of the total reaction forces and moments at the anchors, resulting in reduction of energy losses through the substrate, and therefore the preferential mode for gyro operation [74].

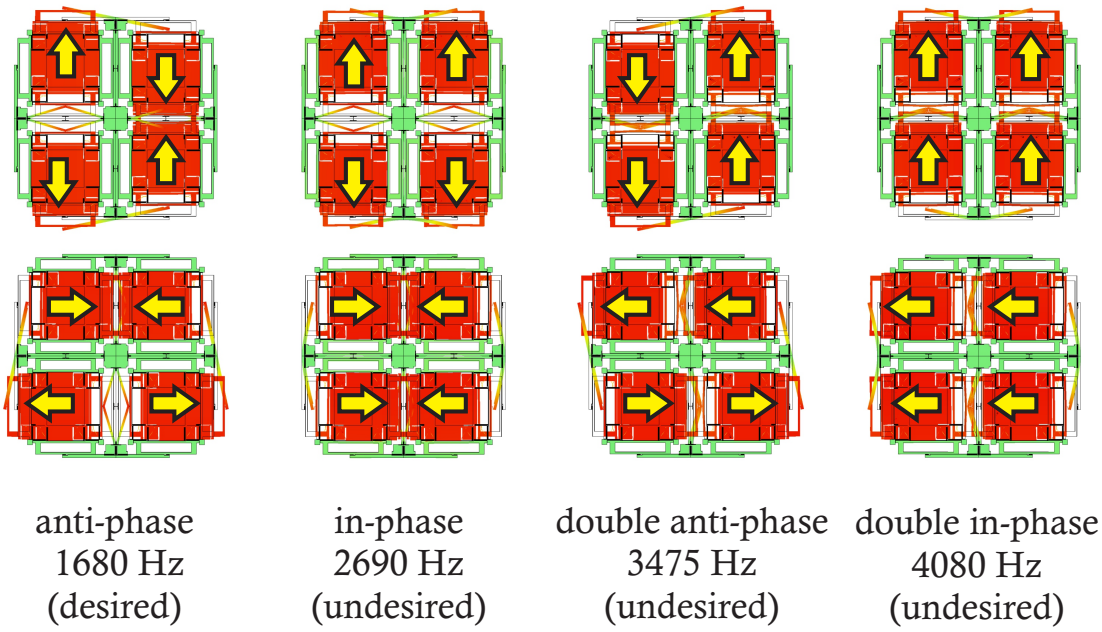

Figure 2.1: Eigen-frequency simulations of a Quad Mass Gyroscope (QMG), showing the four degenerate modes of vibration and the frequency of each resonance mode. The vibrational modes are ordered to place the desired anti-phase mode at the lowest frequency [75].

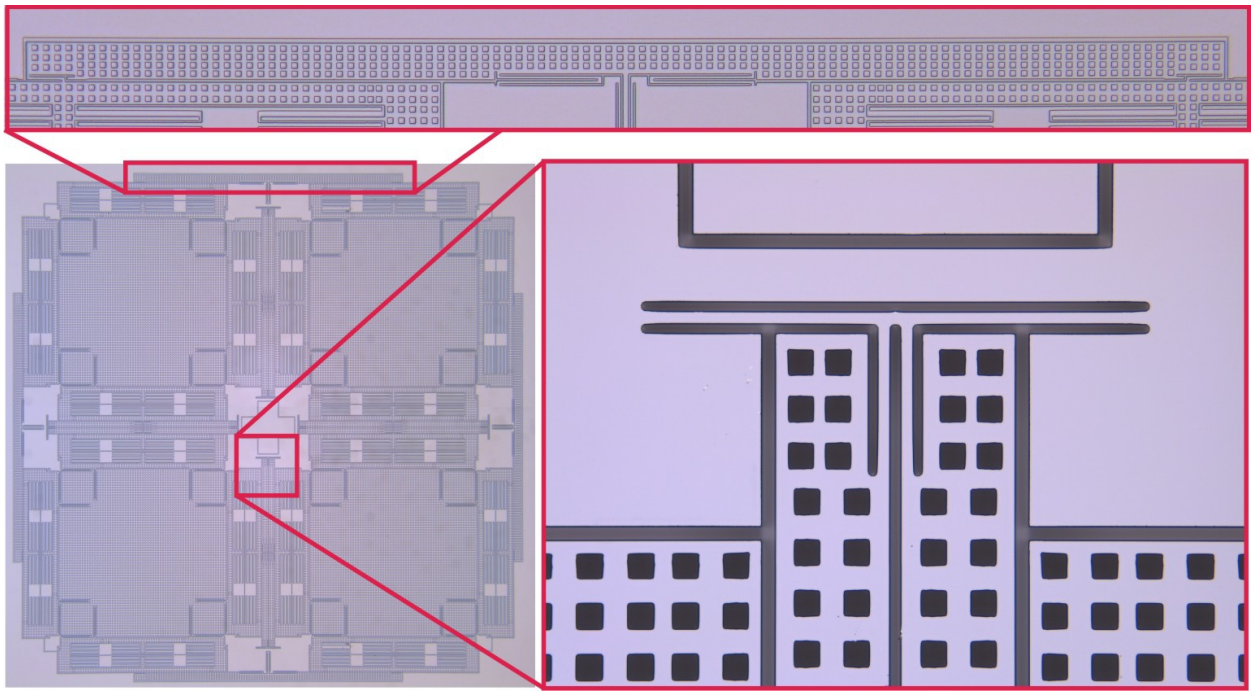

Figure 2.2: Four external lever mechanisms and four pairs of internal secondary beam resonators, responsible for ordering the eight vibrational modes of a QMG and for placing the desired anti-phase mode at the lowest frequency [76].

QMGs have one operational mode and three parasitic vibrational modes, which are sensitive to external linear and angular accelerations. In order to suppress sensitivity to environmental shock and vibrations and improve mechanical stability of the sensor's structure, the order and frequency of vibrational modes were designed using suspension elements for mode-ordering, [77]. Four outer lever synchronization mechanisms and four pairs of inner secondary beam-coupling elements were incorporated in the suspension design to couple the proof-masses (see Fig. 2.2). Advantages of these features of the design included widening of the frequency separation between desired anti-phase modes and parasitic in-phase modes, while shifting the in-phase modes to higher frequencies for common mode rejection of linear accelerations, decreasing the mode conversion losses and decreasing the drift induced by external vibrations. While the anti-phase operation was intended to reduce the energy dissipation and improve the Q-factor along each orthogonal axis, the symmetric structure of the device provided a damping and stiffness symmetry, which was shown to improve the overall performance of

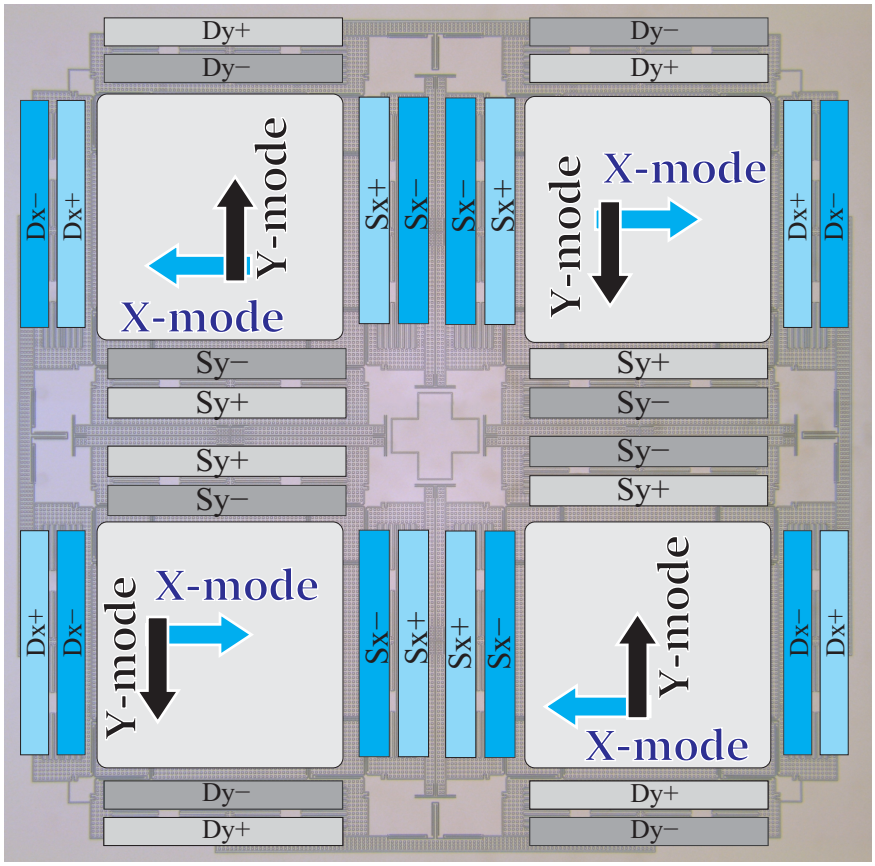

Figure 2.3: Layout of the QMG structure with symmetric features: identical proof-masses and identical drive and sense electrode structures overlaid with external forcers and internal pickoff electrodes, which were used to drive and sense each mode separately.

the gyro operating in both the rate and the rate-integrating modes [78].

In this thesis, QMGs were fabricated using a Silicon-on-Insulator (SOI) process with a 100 µm device layer, 5 µm buried oxide layer, and a 500 µm handle wafer. Using the process described, for example in [79], the moving masses were released by etching the buried oxide in a vapor HF etcher. In this design, the mass of each tine was 2×10^{-6} kg, the width of suspension beams was 8 µm, and the minimum trench width was 10 µm. The total footprint of the device was 8.6 mm×8.6 mm. The devices were diced and individual sensors were attached to ceramic Leadless Chip Carrier (LCC) packages using eutectic bonding [80].

The sensors consisted of 16 pairs of differential parallel-plate electrode arrays with 8 µm

capacitive gaps for excitation and detection of the drive and sense modes. Every four pairs of differential electrodes cover one proof-mass. In four-mass symmetric configuration, drive differential electrodes are located on the outer side of the structure, and sense differential electrodes are located on the inner side of the structure. Altogether, the parallel-plates formed 2.4 pF rest capacitance between the proof-mass and the differential electrodes for each X- and Y-modes. The differential drive signals were applied to all four masses symmetrically. For example, along the X-axis for the bottom two masses, the in-phase drive signal (+) was applied to the outer most electrodes and the out-of-phase drive signal (−) was applied to the inner electrodes; this configuration is reversed for the top two masses. The differential sense signals from all masses were lumped to one pickoff signal of the detection circuit. Fig. 2.3 shows the arrangement of electrodes for excitation and detection of the anti-phase mode of motion. The differential pairs of electrodes were labeled ("+" and "−"), for both the drive (Dx and Dy) and the sense (Sx and Sy) electrodes. These electrodes were wirebonded, such that they summed under the same subset (e.g., the Dx+ signal arrives in the LCC package to 4 different pads and distributes to 4 electrodes).

2.3 Modes of Operation

A MEMS Coriolis Vibratory Gyroscope (CVG) can be configured to operate in the rate mode, to measure the angular rate of rotation, or in the whole-angle mode, to measure the absolute angle of rotation [81]. MEMS gyroscopes are mainly instrumented to measure the angular rate of rotation [82–89]. And in principle, the angle of rotation can be estimated by integrating the gyroscope rate output. This mode of operation suffers from the accumulation of error due to the integration of noise over time [81, 90]. In the Whole-Angle (WA) mode of operation, direct measurement of angle, CVGs are used as a mechanical integrator of the angular rotation rate to directly measure the angle of a rotation. In this section the overview of both mode of operations for angular rate and whole-angle are given. The instrumentation and characterization of these mode of operations are presented in Chapter 3 and 4, and the hardware implementation is presented in Appendix F, G, D and E.

2.3.1 Rate Measuring Mode

MEMS CVGs are based on transfer of energy between primary and secondary modes of the gyroscope due to the Coriolis force coupling, in response to an input rotation [91]. Fig. 2.4 illustrates schematically the oscillation deflection in the rotating coordinate frame. The output sensed along the Y-axis is proportional to the input angular rate. Therefore this mode of operation is called “rate mode” or “rate operation”.

Several control loops are used in angular rate operation. The main ones are: The Phase-Locked Loop (PLL) to sustain the oscillation at resonance of the device resonant frequency, the Amplitude Gain Control (AGC) to stabilize the amplitude of sensed oscillation, the Quadrature and the Rate control loops (QCL and RCL) to null the output parameters sensed on the output of the gyroscope, and its called either “open-loop rate mode” or “closed-loop

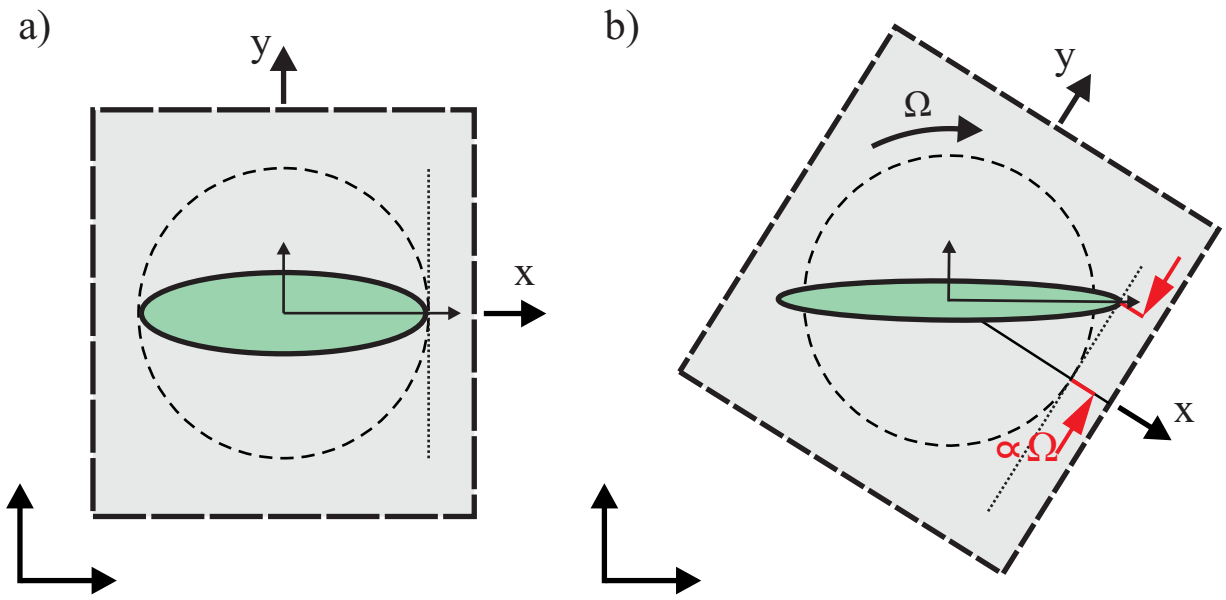

Figure 2.4: Theoretical response of a CVG to a rate of angular rotation Ω, in the gyroscope rotating frame: a) no rotation, b) applied a constant rotation.

rate mode", depending on which loops are enabled, further description is provided in Chapter 3.

2.3.2 Angle Measuring Mode

In the WA mode, the vibrational energy freely transfers between the two degenerate orthogonal modes due to the Coriolis acceleration, resulting in precession of the vibration pattern, which tracks the input rotation experienced by the device. A 2-DOF lumped mass-spring model of a gyroscope resembles a 2-dimensional coupled oscillator. The equations of motion in the gyroscope frame, along the normal mode axes, are:

$$\begin{aligned} \ddot{x} - k(2\Omega\dot{y} + \dot{\Omega}y) - (\omega^2 - \Omega^2)x &= f_x \,, \\ \ddot{y} - k(2\Omega\dot{x} + \dot{\Omega}x) - (\omega^2 - \Omega^2)y &= f_y \,, \end{aligned} \tag{2.1}$$

where Ω is the rate of angular rotation, ω is the resonance frequency of CVG, k is the angular gain factor, f_x and f_y are the forces per unit mass along the X-axis and the Y-axis, respectively. The general solution of Eq. (2.1), assuming a constant angular rate and neglecting the centrifugal terms in the X-Y plane of the gyroscope, describes an elliptical trajectory, and the modal displacements can be written in terms of the orbital parameters [92]:

$$\begin{aligned} x &= a\ cos\theta\ cos(\omega t + \phi_0) - q\ sin\theta\ sin(\omega t + \phi_0)\,, \\ y &= a\ sin\theta\ cos(\omega t + \phi_0) + q\ cos\theta\ sin(\omega t + \phi_0)\,, \end{aligned} \tag{2.2}$$

where a, q, θ, and ϕ_0 are a semi-major axis, a semi-minor axis, an inclination angle of the pattern, and an initial phase of the corresponding elliptical orbit, respectively. The orbital parameters are illustrated later in Chapter 4 Fig. 4.2.

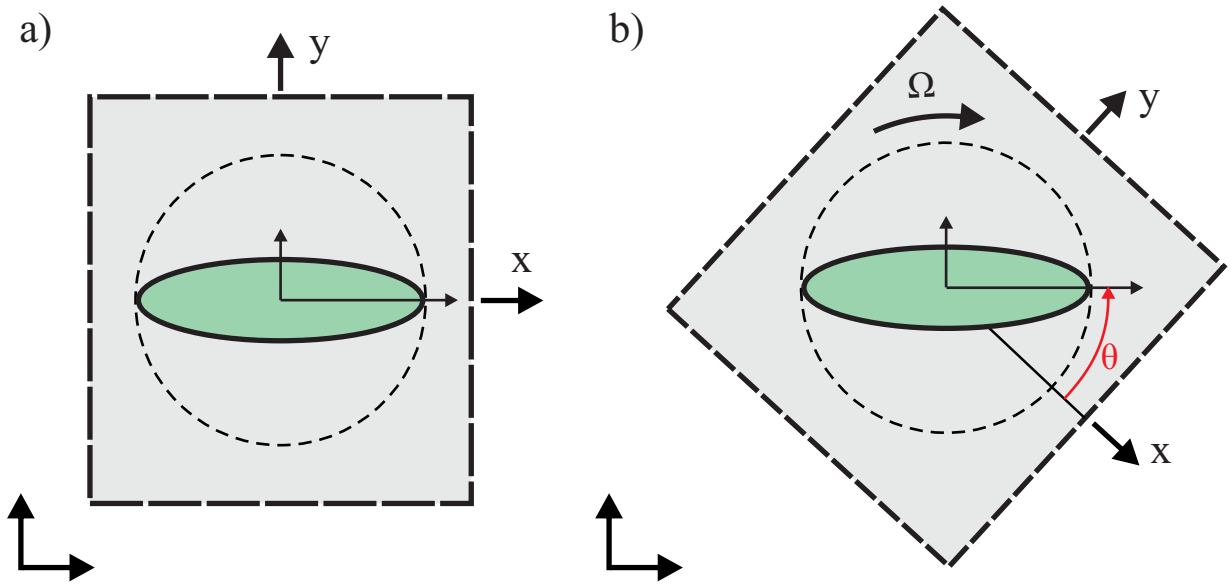

Figure 2.5: Precession of the pattern angle in the gyroscope rotating frame gives direct angle measurement of the input inertial rotation ($k = 1$, $\theta_0 = 0$): a) no rotation, b) applied rotation.

In an ideal gyroscope, the vibration pattern freely presses in response to the input rotation.

The rate of precession of the pattern angle, $\dot{\theta}$, is proportional to the angular rate of the input rotation, Ω. Thus, the instantaneous inclination of the vibration pattern is directly proportional to the angle of rotation, Eq. (2.3). The proportionality constant k is called the angular gain factor, and is defined by the geometry of the gyroscope. Fig. 2.5 illustrates schematically the precession of the vibration pattern in the defined rotating coordinate frame. A complete solution to the governing equations for an ideal and non-ideal gyroscope in the elliptical coordinates can be found, for example, in [93].

$$\begin{aligned} \dot{\theta} &= -k\Omega \\ \theta &= \theta_0 - k\int_{t_0}^{t} \Omega(\tau)d\tau \end{aligned} \tag{2.3}$$

2.4 A Universal Standalone MEMS Gyroscope Platform

To provide a flexible characterization solution on fabricated MEMS gyroscope devices, a custom universal control platform was developed. The universal control consists of five separate stages: 1) a Digital Signal Processing (DSP) board, 2) a microcontroller, 3) a buffer card containing both analog and digital signals, 4) an evaluation in-phase and in-quadrature (IQ) demodulation board, and 5) a device adapter with first stage differential amplification scheme. The developed standalone platform enables investigation of the algorithm on a custom fabricated device for the prosthesis and the development is being described in this section.

2.4.1 Electronic Instrumentation

Controller: An evaluation audio processor DSP board (EVAL-ADAU1442) was selected for the implementation of control algorithms; it produces a wide range of DC bias and AC voltages to the packaged device. An audio codec (AD1938) with 4-channel ADC, 8-channel DAC, 24-bit resolution at a sampling rate of 192 kHz was programmed. Independent variable gain controls were implemented to adjust and match the level of signals between stages.

Transimpedance amplifier: A MEMS gyroscope with differential pickoff electrodes requires a differential detection configuration. Fig. 2.6 shows a simple representation of a typical front-end circuit used for this system. A carrier frequency of 100 kHz was applied to the structure to remove the parasitic capacitance caused by input-output capacitance on the structure. The transimpedance amplifier converts the motional current ($<$20 µA) to a voltage via feedback resistor connected to the inverting input of the amplifier. The power

Table 2.1: Design requirement for standalone platform

Input current (I)		Output voltage (V)		Circuit Bandwidth	Power supply	
I_{min}	I_{max}	V_{min}	V_{max}	frequency	V_{ee}	V_{cc}
0 A	20 µA	0	2.2 V	105 kHz	0	+12 V

budget allocated for the system is 0.5 A at 12 V using a single supply source. Table 2.1 summarizes the requirements imposed on the front-end circuit design.

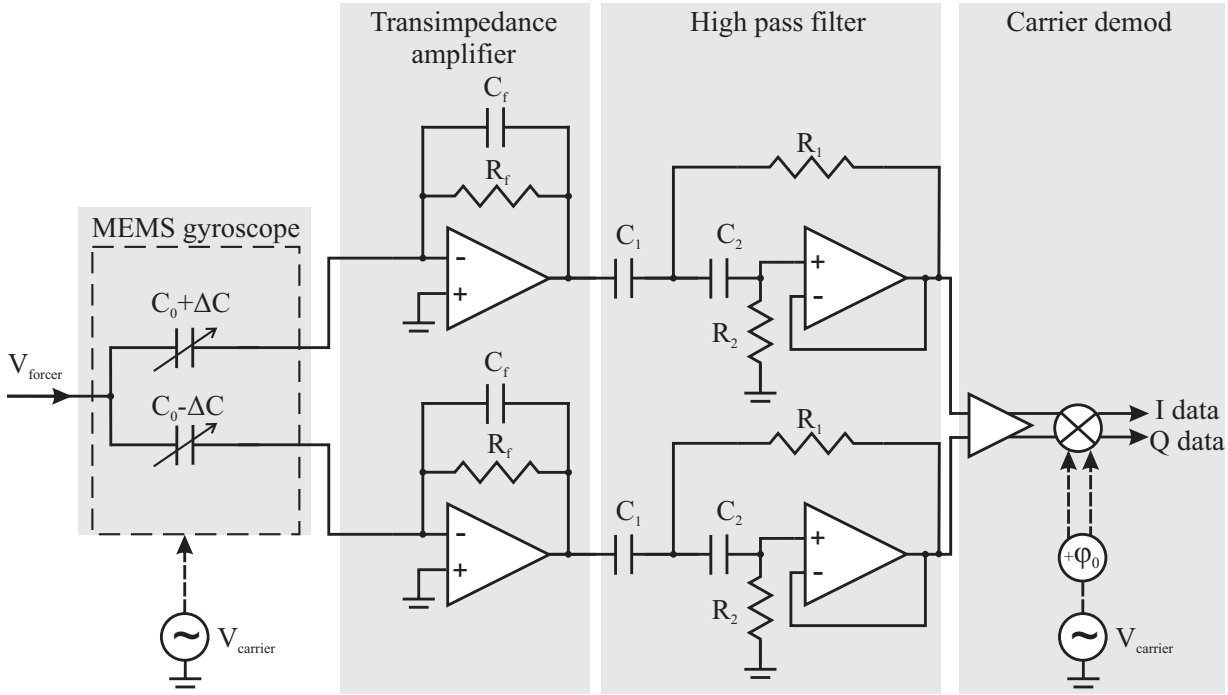

Figure 2.6: The design of a front-end circuit for a MEMS gyroscope. It includes, a) a MEMS gyroscope, b) transimpedance amplifiers, c) high-pass filters, d) IQ carrier demodulation.

For the readout detection circuit, a fully differential input/output amplifier (THS4131) was configured as a transimpedance amplifier. The advantage of this circuit is to reject common-mode voltage at the differential output. The universal platform was designed using a built-in "daughter board" approach for the first stage amplification, making it flexible for variety of MEMS packaging and wire bonding configurations; as a result, multiple top-stage electronics were developed for different designs, such as resonator, accelerometer, gyroscope, and IMU, Appendix C details the development. The result on performance is presented later in Chapter 3 and Chapter 4 using a single-ended amplifier (AD8034) configured differentially

Table 2.2: The parameters of the front-end circuit interface with MEMS gyroscope

Parameter	Description	Value
V_{cc}	Single power supply	5 to 24 V
I_q	Quiescent current	3.3 mA
$UGBW$	Unity gain bandwidth	80 MHz
C_i	Input capacitance	7 pF
C_f	Feedback capacitor	1 pF
f_0	Open-loop cut-off frequency	2×10^3
A_0	Open-loop gain	92 dB
e_n	Equivalent voltage noise density	$11\,\text{nV}/\sqrt{\text{Hz}}$
i_n	Current noise density	$0.7\,\text{fA}/\sqrt{\text{Hz}}$

(Fig 2.6) from the top-stage amplification presented in [94]. Next, we will describe the optimization process on the selection of the feedback resistor R_f. The input capacitance of the device interfaced with the circuit was measured experimentally by an existing MEMS characterization platform [95]. Table 2.2 summarizes the parameters used for analysis.

FastFET op-amp (high-speed JFET) technology provides high input impedance characteristics for transimpedance amplifier operation and thus senses small current changes at the input, making it suitable for MEMS application. For transimpedance configuration, the frequency transfer function of an inverting open-loop voltage amplifier is given by Eq. (2.4):

$$\frac{v_o}{v_i} = -A(s) = -A_0 \frac{2\pi f_0}{s + 2\pi f_0}, \tag{2.4}$$

where A_0 is the open-loop DC gain and f_0 is the open-loop cutoff frequency of the amplifier. For the system the normalized closed-loop transfer function to the feedback resistor is given by Eq. (2.5):

$$\frac{v_o}{i_i R_f} = -A \frac{1}{sC_i R_f + (1 + A)(1 + sC_f R_f)}. \tag{2.5}$$

To determine the optimal component value for resistor R_f the system amplitude and phase

responses were analyzed. Fig. 2.7 shows the response of the system from Eq. (2.5) and Eq. (2.4) for different combination of gains R_1, R_2, and R_3 equal to 40 kΩ, 450 kΩ, and 1 MΩ respectively. In the graph, the derivative of the phase over frequency known as envelope delay $\tau = \frac{d\phi(s)}{ds}$ is provided for different gains. Further details on the mathematical derivation and analysis for this circuit for photodiode application can be found in [96]. We used the analysis to study the component selection of the readout circuit for integration with MEMS gyroscope devices and validated the noise against the experimental measurement. The selection criteria are based on electronics cut-off frequency and achieving the highest closed-loop gain while the responses for the phase and the envelope delay lie within the flat portion around the frequency of operation. Here the operating frequency for the gyroscope in both drive axis and sense axis is set at the carrier frequency 100 kHz plus the local oscillation of the device ranges 1 kHz to 5 kHz. The higher value for the resistor resulted in a higher closed-loop gain and lower the cut-off frequency. The envelop delay shows that for the higher value of R_f the system will respond slowly and for a smaller value of R_f the system will have overshoot and ringing. In MEMS gyroscope readout system the delay introduced in the circuit stage is compensated by a closed-loop PLL phase shift component, to be described later in Chapter 3.

Another important characteristic of transimpedance configuration is the input impedance of the circuit which is what the MEMS gyroscope device sees; therefore due to the high input impedance the small motional current from the device is being detected. The expression for input impedance in a closed-loop circuit is given by Eq. (2.6):

$$Z_i = \frac{v_i}{i_i} = \frac{R_f}{sC_iR_f + (1+A)(1+sC_fR_f)}. \tag{2.6}$$

Replacing the A with its full expression Eq. (2.4) and reordering the total impedance can be represented in three terms: frequency-independent Z_1, band-pass term Z_2, and low-pass

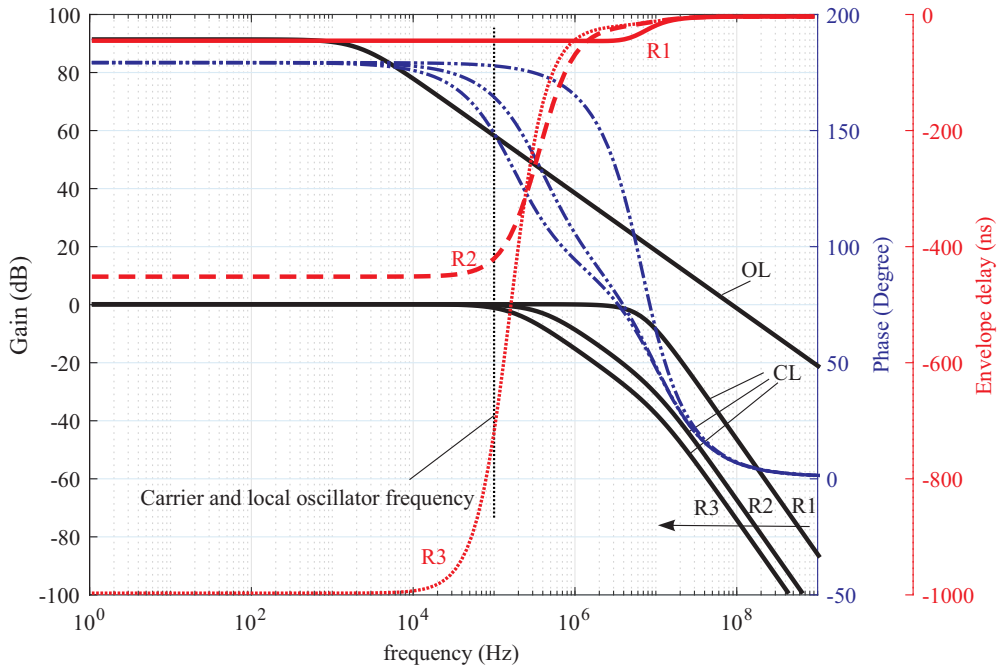

Figure 2.7: AC circuit analysis of different feedback resistor R_f on front-end detection electronics. The open-loop (OP) response is independent from R_f; however, closed-loop ("-" black), phase ("-.-" blue), and envelop delay ("." red) vary across parameters.

term Z_3, [96]. The simulated input impedance as a function of feedback resistor R_f is shown in Fig. 2.8. Increasing the feedback resistor results in higher impedance at a lower frequency, and shifts the center frequencies of both low-pass and band-pass filters characteristics of the response. At the frequency of operation, the impedance value is important as it will influence the noise gain and ultimately the total noise contribution, described next.

The minimum noise floor of a gyroscope device is limited by mechanical Brownian noise and electronics noise floor described in [97], as follow:

$$\Omega_{z(min)} = \sqrt{\Omega^2_{z(electronic)} + \Omega^2_{z(Brownian)}} \tag{2.7}$$

The Brownian noise of the device will be discussed in Chapter 3, and the electronic noise will be evaluated here using the selected components. A transimpedance amplifier can be broken down into three noise sources v_n, v_{nR}, and i_n as shown in Fig. 2.9.

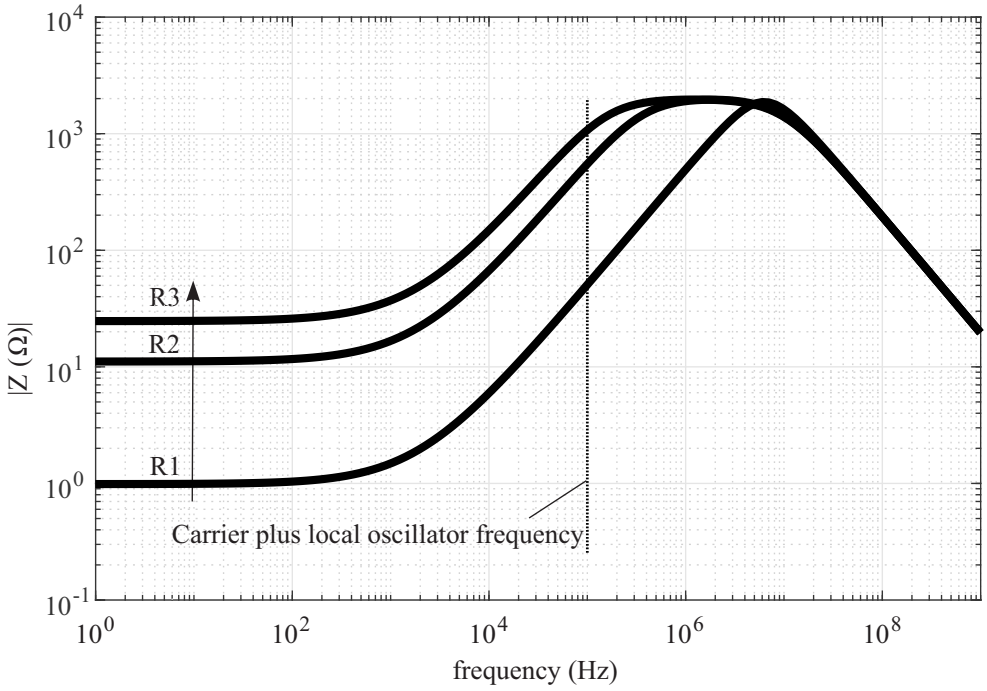

Figure 2.8: Input impedance over frequency of the transimpedance amplifier considering different feedback gains seen by the MEMS gyroscope device.

All noise sources at the input of the amplifier can be represented by a single voltage source v_{ne}, given by Eq. (2.8):

$$v_{ne} = \sqrt{v_n^2 + (i_n R_f)^2 + v_{nR}^2}, \tag{2.8}$$

where v_n is the input voltage noise source, v_{nR} is the resistor thermal noise, and i_n is the input current noise source. The resistor's thermal noise is:

$$e_{nR} = v_{nR} = \sqrt{4k_B T R_r}, \tag{2.9}$$

where k_B is the Boltzmann constant and T is the temperature. The noise gain is the ratio of v_o over v_{ne} from Eq. (2.8) yields

$$\frac{v_o}{v_{ne}} = \frac{1 + s(C_i + C_f)R_f}{1 + sC_f R_f + \frac{s+\omega_0}{A_0\omega_0}[1 + s(C_i + C_f)R_f]}. \tag{2.10}$$

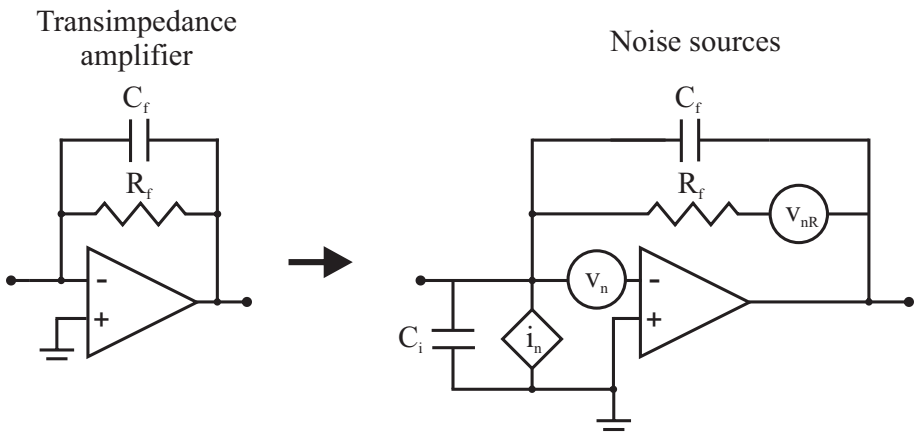

Figure 2.9: Transimpedance amplifier and its noise sources: input voltage noise (V_n), resistor thermal noise v_{nR}, and input current noise (i_n).

If the carrier modulation scheme is being utilized, the noise gain expression should not be ignored as a source of error, since it contributes to the total final noise at high frequency. Similar to impedance characterization, the noise gain of a transimpedance amplifier can be expressed into two terms: the low-pass component and the band-pass component, [96]. Fig. 2.10 demonstrates the noise gain of the transimpedance amplifier used in this integration. Increasing the R_f value resulted in higher noise gain and shifting the center frequency to the lower frequency.

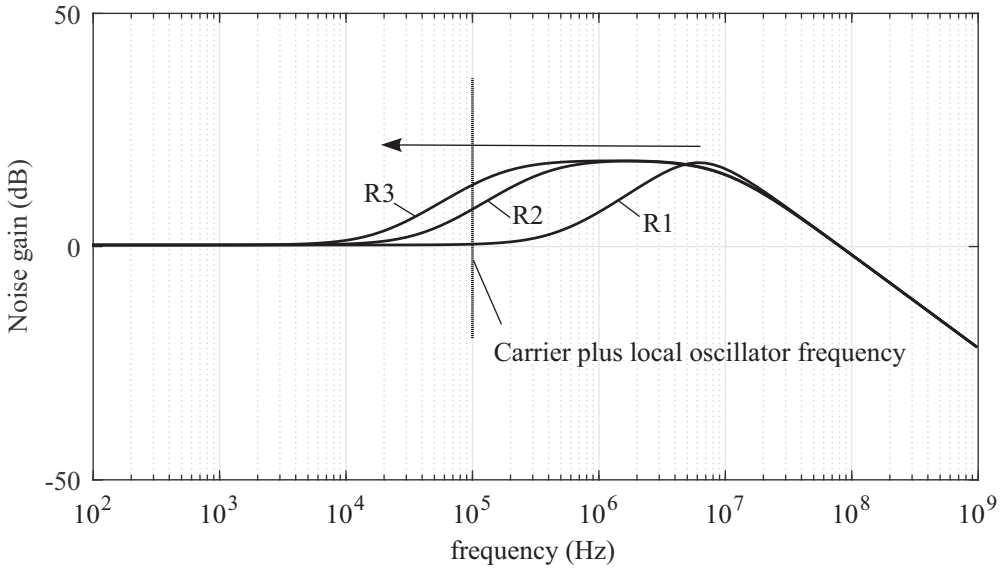

Figure 2.10: Simulated noise gain of the transimpedance amplifier using different feedback resistors.

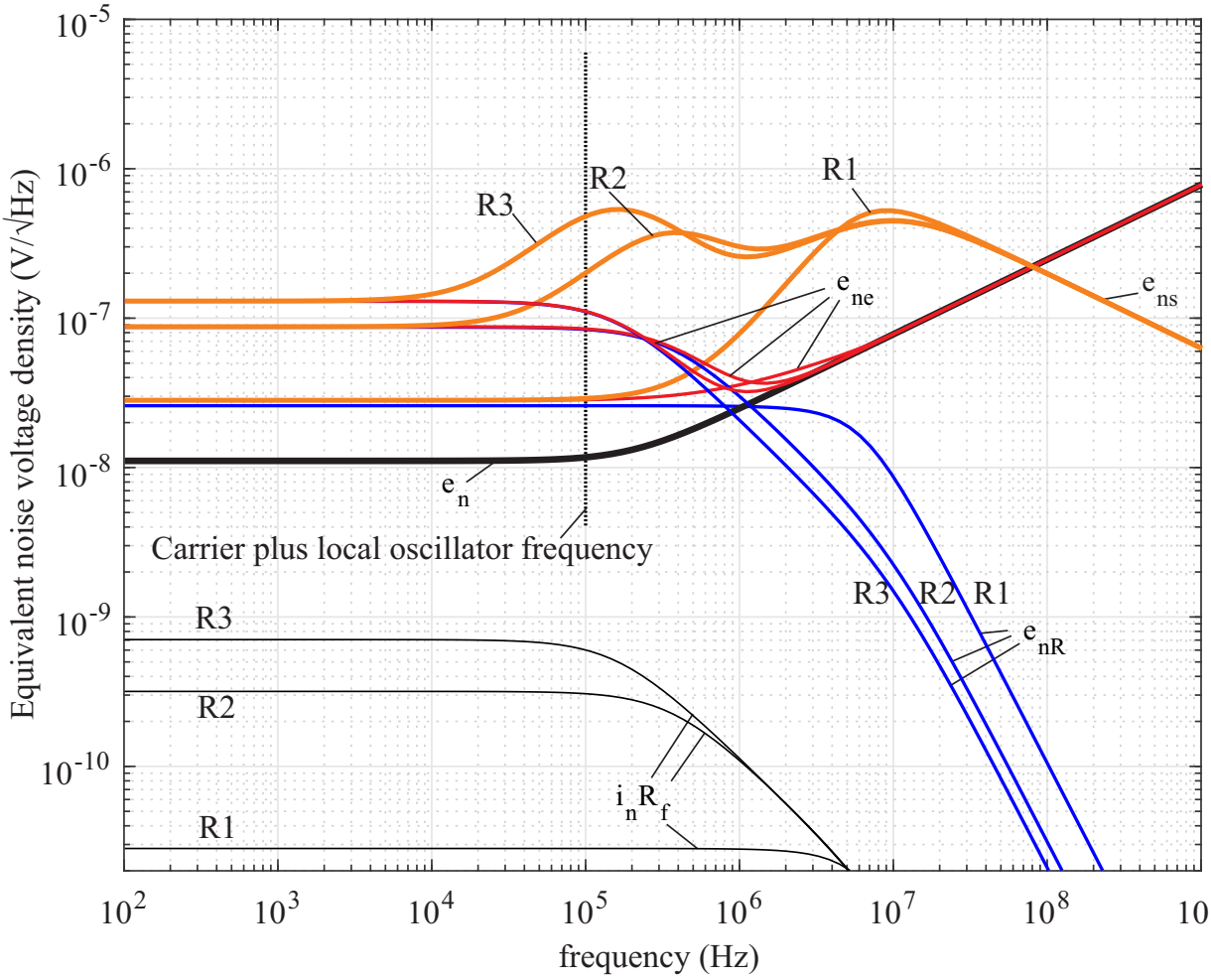

Figure 2.11: Breakdown of noise contributors in the transimpedance front-end for different feedback resistors: input current noise source (i_{nR}), equivalent resistor's thermal noise (e_{nR}), voltage noise density (e_{ne}), and the total noise source including noise gain (e_{ns}).

Fig. 2.11 shows the equivalent voltage noise density e_{ne} of the circuit in the frequency domain using Eq. (2.8) for different feedback resistors. The equivalent voltage noise multiplies by the noise gain from Eq. (2.10), resulting in total noise as follows:

$$e_{ns} = G_n \cdot e_{ne}, \tag{2.11}$$

where e_{ns} is the total equivalent noise density of the transimpedance circuit implemented in the platform. The Angle Random Walk (ARW) of the circuit can be calculated by dividing the total equivalent voltage noise density of the amplifier at the operation frequency by the

measured scale-factor (sensitivity) of the system [98], as follows:

$$ARW_{circuit} = \frac{e_{ns}}{SF} \times 60 \ \ (deg/\sqrt{hr}), \tag{2.12}$$

where the unit for SF is (V/(°/sec)), and the unit for e_{ns} is $(V/\sqrt{Hz})$. The selected feedback resistors R_1, R_2, and R_3 resulted in total equivalent voltage noise of 3×10^{-8}, 2×10^{-7} and $5 \times 10^{-7}\,\mathrm{V}/\sqrt{\mathrm{Hz}}$, respectively. For R_3, the final design candidate, this translates to an ARW of $0.01\,^{\circ}/\sqrt{\mathrm{hr}}$ for the circuit, which matches well with the experimental angular rate characterization in Chapter 3. This suggestes that the characterization to be reported later is limited by the electronics noise sources of the readout circuit. In order to suppress the electronic noise floor, an amplifier with lower input current noise and lower voltage density or a mechanical structure with higher scale-factor sensitivity is desired.

Buffer amplifiers and filters: After the first stage of current to voltage amplification, active high-pass filters were implemented to remove any unwanted low frequency signals generated by the other sources from the system. A Sallen-Key high-pass filter configuration as shown in Fig. 2.6 was chosen with transfer function defined by Eq. (2.13):

$$\frac{v_0}{v_i} = \frac{s^2}{s^2 + s(\frac{1}{R_2C_1} + \frac{1}{R_2C_2}) + \frac{1}{R_1C_1R_2C_2}}, \tag{2.13}$$

where C1 and C2 are both to be equal to 10 nF, and R1 and R2 to be equal to 1 kΩ and 2 kΩ, respectively, which will resulted in a cut-off frequency of ∼11 kHz for the developed system.

Carrier demodulation: A carrier signal was used to modulate the motional current in frequency domain; this will result in a higher signal to noise ratio and suppress further the parasitic capacitance on the device from the packaging and unwanted electronic noise, [99]. Lock-in amplifiers such as AMTEK7270 or HF2LI by Zurich Instruments are typical platforms being used for this purpose. The same functionality can be instrumented using a

single on-chip In-phase and Quadrature (IQ) demodulator (AD8333). The evaluation board of this unit was integrated in the platform as a separate stage. The demodulation operates from DC to 200 MHz carrier to extract a DC signal up to 50 MHz with a phase accuracy of $\pm 0.1^{\circ}$ and 159 dB/Hz dynamic range. The board operates on two independent input channels suitable for a MEMS gyroscope with X- and Y-axes and provides four output signals in two in in-phase and quadrature pairs. A 4x carrier signal frequency is required to be fed into the demodulation process, which is provided by a multiplier analog circuit (see Appendix C).

Post-modulation filters: Following by the demodulation, multiple feedback low-pass filters with cut-off frequency of $\sim$7 kHz were implemented.

Differential forcer: To drive differential parallel plate electrodes of the device deferentially, two Instrumentation Amplifiers (IA) (AD8429) were configured into a single ended drive input. The inverting of one IA and the non-inverting input of another IA are grouped, and the other inputs are grounded. The schematics of these circuits and the chosen components are reported in Appendix C.

Digital components: An Arduino Due ARM Cortex-M3 microcontroller was used to interface between the evaluation DSP board and the onboard function generator (AD9833) capable of generating a sinusoidal signal up to 25 MHz. Two function generator units were placed on the board using a shared high precision Temperature Compensated Crystal Oscillator (TCXO) and programmed to generate carrier signals at two distinguishable frequencies with ratios of 1x and 4x. The 1x carrier frequency applied directly to the proof-mass of the device, and the 4x carrier frequency was used to demodulate the gyroscope outputs using the IQ demodulation technique.

Power consumption: The overall power consumption of the standalone platform during operation varied between 2 W to 6 W, depending on the number of stages/algorithms being utilized. Fig. 2.12 shows the breakdown of the system with individual estimated power

for each stage compared with conventional methods for gyroscope characterization. In the conventional approach, laboratory instruments such as a lock-in amplifier and off-the-shelf carrier demodulation tools interface with the developed simple buffer electronics, differential detection and differential drive without controller, [100] (see Appendix C-PCB-C.1.2). Such development was relatively small for placing all electronics including interconnect cables inside the vacuum chamber for characterization. As shown in the chart the entire platform can be realized by using ASIC circuit and ARM7 controller together, with the estimated power budget of 310 mW, at the cost of losing its flexibility.

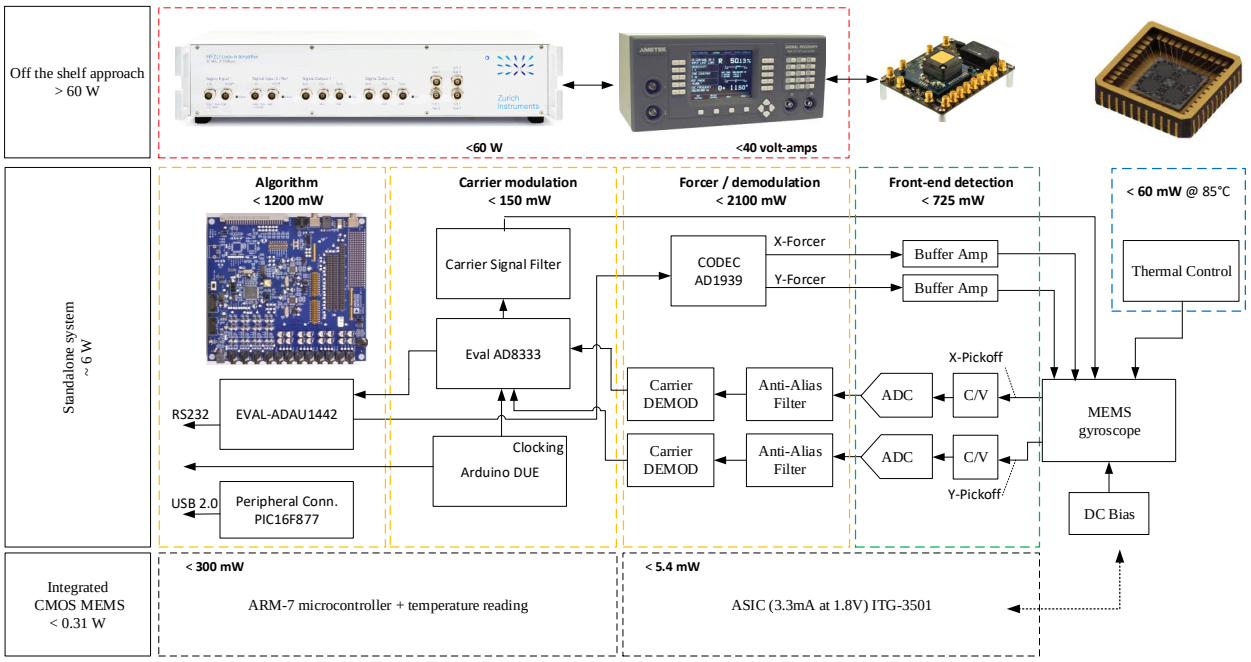

Figure 2.12: Estimated power consumption for method of characterization. Top row: conventional method using laboratory instruments, middle row: the developed standalone platform, bottom row: MEMS-ASIC solution.

2.4.2 Integrated System

Fig. 2.13 shows the final assembly of the multi-stage approach as a standalone platform with the placement of the LCC packaged device in the daughter board. The main board distributes and shares the necessary power to all active components. The developed platform

is capable of communicating with the Universal Inertial Test System (UITS) [101], where this communication was controlled by the microcontroller. The detailed schematic and the implemented layout of the described platform in this section is provided in Appendix C-PCB-C.1.4.

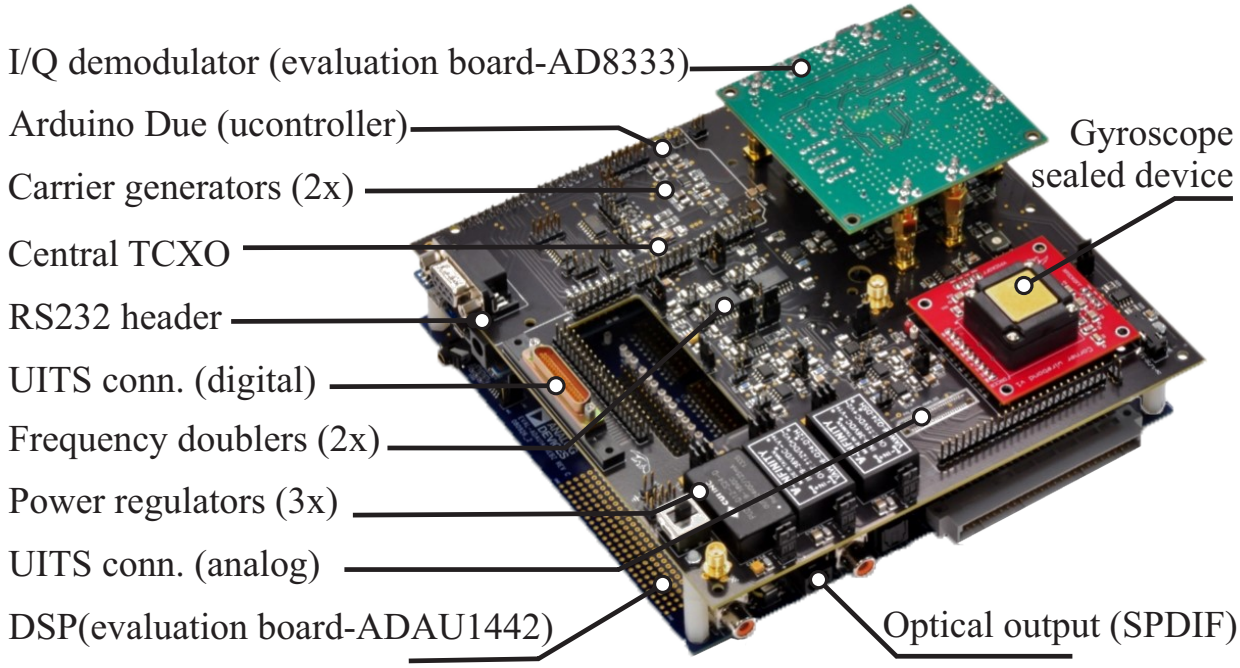

Figure 2.13: The developed standalone characterization for MEMS gyroscope. The main parts from top to bottom are, a) a packaged MEMS gyroscope (LCC packaged), b) a custom device adapter with first stage current amplification, c) an IQ carrier demodulation board, d) an analog signal conditioning board with power distribution system, and e) a DSP controller; these parts are colored gold, red, green, black, and blue respectively.

2.5 A Laboratory Testbed for Sensor Fusion

This section presented a customizable laboratory testbed for the sensor fusion of multiple Inertial Measurement Units (IMU) and SOund Navigation And Ranging sensors (SONAR), for development of aiding calibration algorithm. We described the architecture and communication interfaces for the simultaneous collection of data from two IMUs and two SONARs, however, parallel acquisition from a larger variety of sensors is also feasible. Representative human gait patterns are experimentally acquired to demonstrate the functionality of the testbed. The features extracted from gait analysis will be used later in Chapter 5 for calibration on vestibular prosthesis system.

2.5.1 Background

The use of low-cost inertial sensors for pedestrian positioning has been a subject of research over the last decade, [102], and, more recently, the research has expanded to include sensor fusion of large arrays for chip-scale personal navigation systems, particularly for scenarios when/where GPS signals are unusable. In such cases, the pedestrian trajectory is obtained through the integration of angular velocity and double integration of acceleration during the gait motion. This information is provided by the IMU which consists of multi-axis accelerometer and gyroscope sensors. Along with the integration of this information, algorithms based on so-called Zero velocity UPdaTe (ZUPT) have been used during stationary periods to correct accumulated errors of the positioning system. Other sensors, such as SONARs, have also been used for detecting the time epochs for which the updates can be applied. Among other sensors, magnetometer and barometer sensors are commonly used for pedestrian navigation, e.g., [103]. As more innovative sensors become available and are considered for utilization, the further challenges raise mainly in terms of system architecture. The key challenges of self-

contained navigation based on sensor fusion include: 1) integration of multiple sensors with different communication protocols and interfaces, 2) simultaneous use of different formats of the information stream, and 3) logging of data for algorithm development.

Many architectures have been proposed to fuse multiple sensors for pedestrian navigation, for example, the use of a custom PCB with MCU including real-time display [104], and the use of FPGA with embedded computer electronics [105]. Although the existing methods are suitable for pedestrian navigation, they are not sufficiently flexible for exploring a multitude of sensor modalities, as this typically triggers a major modification to custom electronics, firmware, and software. With such variety of available COTS sensors today and a dynamic development of new sensors, a flexible testbed for pedestrian navigation would be beneficial. Such a platform is envisioned to streamline laboratory research, while minimizing complexity of hardware integration.

2.5.2 System Architecture

For this study, a core platform by National Instruments was selected, which includes CompactRIO (cRIO-9039) with programmable FPGA Xilinx Kintex-7 and a real-time processor 1.91 GHz Intel quad-core CPU with 2GB DDR3 RAM. The platform provides easy integration with different sensors by selecting an appropriate chassis. In our case, we used the NI-9870 C Series module for UART serial interfaces and the NI-9401 and NI-9402 bidirectional digital I/O modules to achieve SPI and I2C communications, respectively. Fig. 2.14 illustrates a prototype for in-field experiments. A LiFePO4 rechargeable battery of 25.6 V with a capacity of 10 Ah was selected (CU-JAS217 Batteryspace), which was sufficient for 6 hours of in-field measurements. The system also contains a PCB for signal and power distribution, Fig. 2.14. Evaluation PCBs on power regulators were considered for power distribution. The power is fed by two Texas Instruments “AN-1443 LM3100” units for each

IMU, and by one Texas Instruments "TPS7A1601EVM-046" unit for all SONARs. The programming was done in the LabVIEW Virtual Instrument (VI) environment, for both FPGA and CPU.

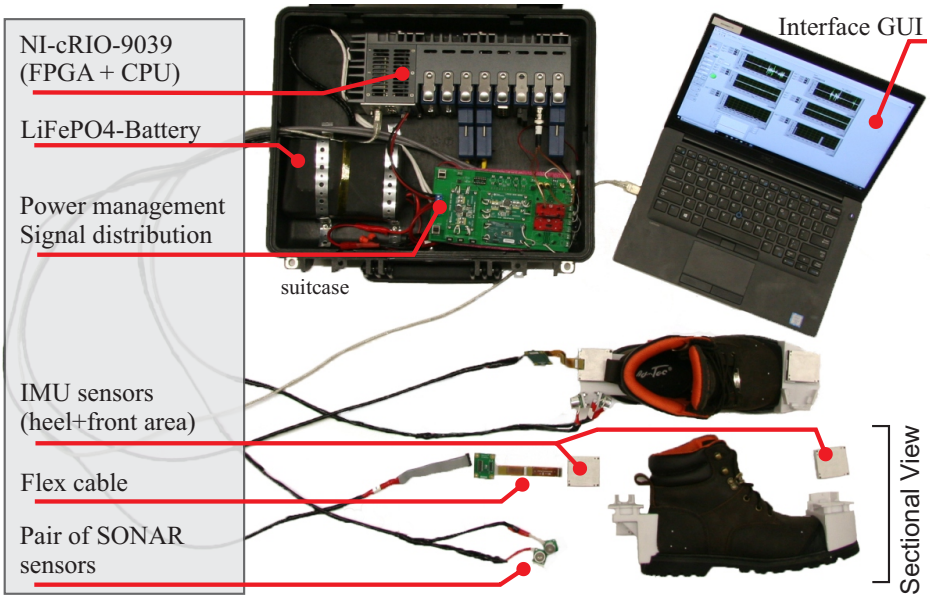

Figure 2.14: A photograph of the proposed testbed: The suitcase contains cRIO controller, battery, PCB power flow, IMU and SONAR sensors, boot-mounted sensor fixtures, and a laptop for GUI, monitoring and data storage.

The algorithm for data acquisition was implemented on the FPGA-VI part of NI CompactRIO, while the algorithm for navigation was implemented on the real-time processor using VI. The FPGA part of the platform defined sensor-specific communication protocols, requested and acknowledged data, maintained time synchronization among attached sensors, and transmitted data to the real-time processor. The processor scaled the raw data to real values, applied the navigation algorithm, and down-sampled and sent the data through the network stream channel to the host processor-VI for visualization and data logging for subsequent post-processing. The detail of the system implementation is provided in Appendix A.

2.5.3 Hardware Architecture

Two tactical grade, six degrees of freedom MEMS IMUs (Analog Devices ADIS16485) and two SONARs (Devantech SRF08) were selected to demonstrate functionality of this platform. Fig. 2.15 shows the implemented software architecture. For a higher data rate, the SPI communication scheme was used for multiple IMUs in parallel and I2C communication was used for SONAR sensors. For the commercial IMU, the noise characterization using Allan variance analysis between 32-bit and 16-bit did not show any significant differences in extracted noise parameters. Also, the Allan variance analysis did not show any significant differences between low data rate acquisition 10 Hz and high data rate acquisition 450 Hz, however the corresponding first starting point in the analysis shifts to the left as the data rate increases.

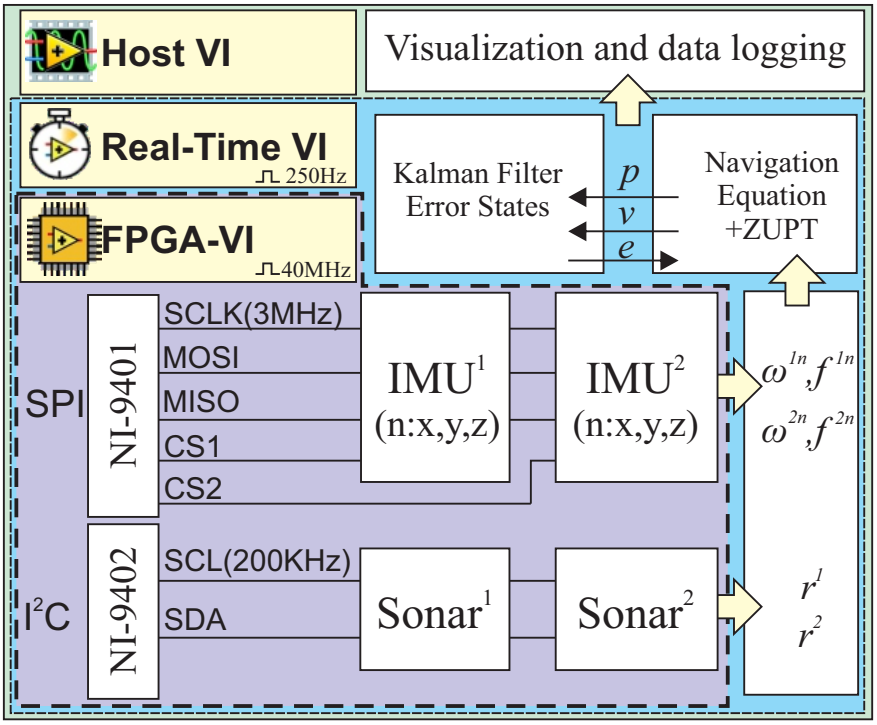

Figure 2.15: The software architecture implemented on NI-cRIO9039 for multiple inertial and SONAR sensors solution. The hierarchy of VIs demonstrates the dataflow from the low-level communication protocol to the high level. IMUs and SONARs are served at 3 MHz and 200 kHz relative to the FPGA onboard clock rate of 40 MHz.

Therefore, the fused data was transferred to the workstation for processing with 16-bit resolution for IMUs and 3-4cm resolution for SONARs. For the architecture considered in this study, the sampling limit due to VI's data-flow execution time was at 100 Hz and 20 Hz, when utilizing simultaneously two IMUs and two SONARs, respectively. The sampling number increased to 200 Hz and 25 Hz when utilizing only a single IMU and a single SONAR.

2.6 Experimental Results

The QMG used as a test structure is expected to provide the sensitivity needed for vestibular prosthesis. The standalone platform was used for this characterization and the flexible hardware was used to acquire data from commercially available IMUs. The frequency symmetry and damping of the fabricated device are investigated in this section as well as the noise analysis on the flexible hardware.

2.6.1 Frequency Response

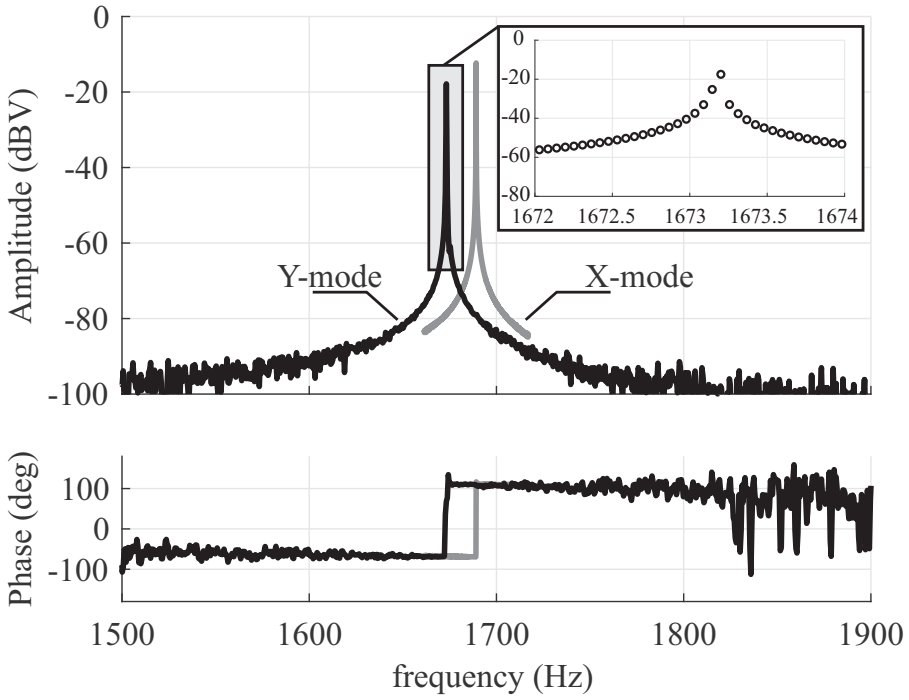

Figure 2.16: Experimental measurement of the anti-phase drive (X-mode) and the sense (Y-mode) frequency responses. Illustrating the increase in amplitude spectral density near the resonance frequency of the modes.

The initial frequency response characterizations were carried out using a custom analog signal conditioning printed circuit board, utilizing a charge amplifier (AD8034 Op Amps)

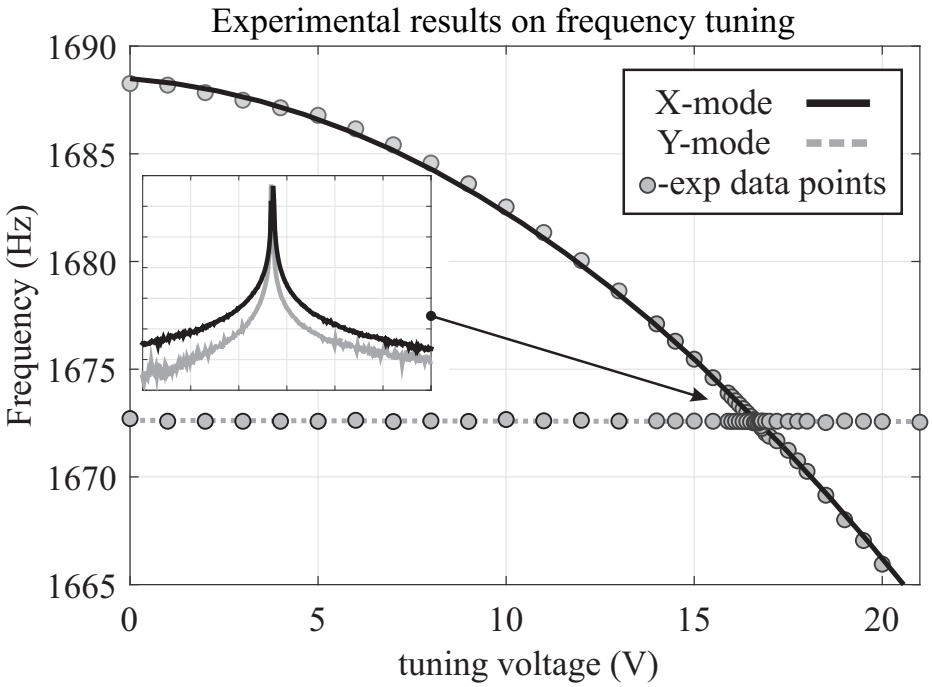

Figure 2.17: Experimentally obtained frequency response of the QMG showing the frequency separation changes between the orthogonal axes by applying DC bias to the X-mode pick-off electrodes. Illustrating the X-mode resonance frequency decreases with increase tuning voltage while Y-mode resonance frequency keeps unchanged.

with a feedback resistor (1-MΩ Vishay resistor), for capacitive detection. An HF2LI lock-in amplifier from Zurich Instruments was used for the experiments. An Electromechanical Amplitude Modulation (EAM) scheme was utilized to remove parasitic feedthrough from the forcer to pickoff electrodes [106]. A 100 kHz carrier signal was applied to the proof-masses and balanced by DC biases on all drive electrodes (equal DC voltages were applied to all differential drive pair electrodes, Dx and Dy). An AC drive signal generated by the network analyzer was applied to the drive electrodes, a differential pair Dx for the X-axis or a differential pair Dy for the Y-axis. The amplitude of the pickoff signal was estimated after demodulation at the carrier frequency and the drive frequency. The phase of the delayed carrier was initially set to 0, while the amplitude of the pickoff signal was monitored. A slightly delayed carrier was used for demodulation, allowing for an optimal phase setting of the EAM. The frequency response along the X-axis and Y-axis are plotted in Fig. 2.16, demonstrating an anti-phase resonant frequency at 1,673 Hz and an as-fabricated frequency

mismatch of 15 Hz. The frequency mismatch was electrostatically tuned down to 60 mHz (36 ppm) using 16.58 Volts DC bias applied to the sense electrodes along the X-axis, with the resolution of 3.5 digits of the power supply, Fig. 2.17.

2.6.2 Q-factor Measurement

Using the same setup as described in 2.6.1, the Q-factor was estimated by measuring the ringdown time. The ringdown time, τ, is defined as the time that it takes for the settled drive amplitude to drop down to 1/e of the initial drive amplitude under free vibration [107], and is measured in seconds. This parameter is used to extract the Q-factor, $Q = \pi f \tau$, where f is the resonant frequency measured in Hertz.

In MEMS resonators and CVGs, the Q-factor is the parameter of interest and is a measure of the overall damping from all possible loss mechanisms in a system. The primary energy dissipation mechanisms in MEMS resonant structures are viscous damping, Thermoelastic Damping (TED), anchor loss, surface-related losses, and electrical damping [108]. The overall Q-factor is the reciprocal sum of Q-factors from different loss mechanisms and is limited by

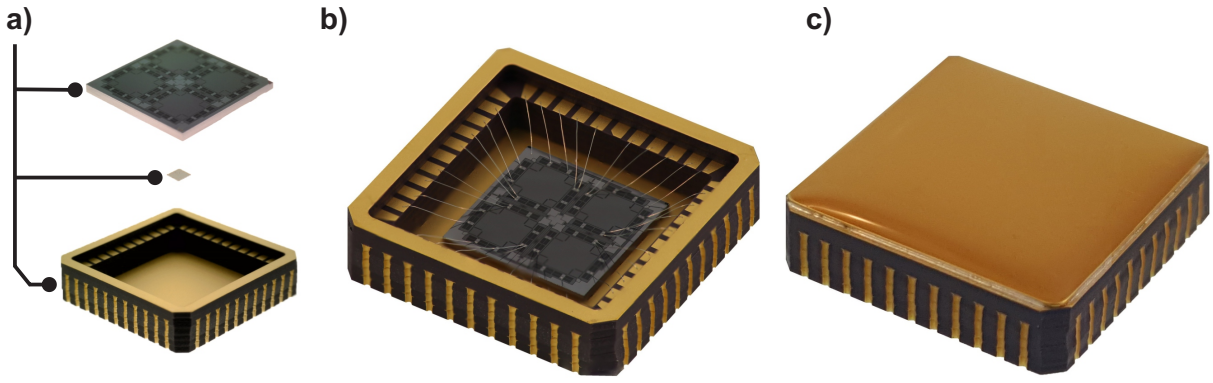

Figure 2.18: Exploded view of vacuum sealed with an activated getter material in the LCC package for SOI MEMS Quad Mass Gyroscope (QMG). a) including 8.6 mm footprint die, die attachment solder preform, LCC package, b) die attached and wire bonded, c) vacuum sealed used as test structure.

the dominant loss mechanism in the system:

$$Q_{Total}^{-1} = Q_{Viscous}^{-1} + Q_{TED}^{-1} + Q_{Anchor}^{-1} + Q_{Others}^{-1}. \tag{2.14}$$

In order to suppress the effect of viscous damping, the DUTs were sealed using an Ultra-High Vacuum (UHV) sealing process [80]. For vacuum sealing of sensors, LCC packages were pre-baked at 400 °C in a vacuum furnace for 7 hrs in high vacuum (<10 µTorr) prior to the die attachment. A vacuum compatible eutectic alloy composed of 80 % gold and 20 % tin (AuSn 80/20) was used for the die attachment. QMG sensors were sealed in vacuum at <0.1 mTorr using the SST 3150 sealing furnace. Fig. 2.18 shows the exploded view of the vacuum sealed LCC package. The Q-factors above 1 million were repeatedly achieved on QMGs using the developed sealing process. Details of the vacuum sealing process were reported in [80]. The long-term vacuum stability was characterized for over 1 year for DUT3 and demonstrated that the Q-factor does not degrade over time, and even exhibits a continues improvement, Fig. 2.19. The long-term ultra-high vacuum condition was enabled by surface desorption prior to sealing, pumping of residual gases by passive getters, and defect-free solder reflow in the sealing area.

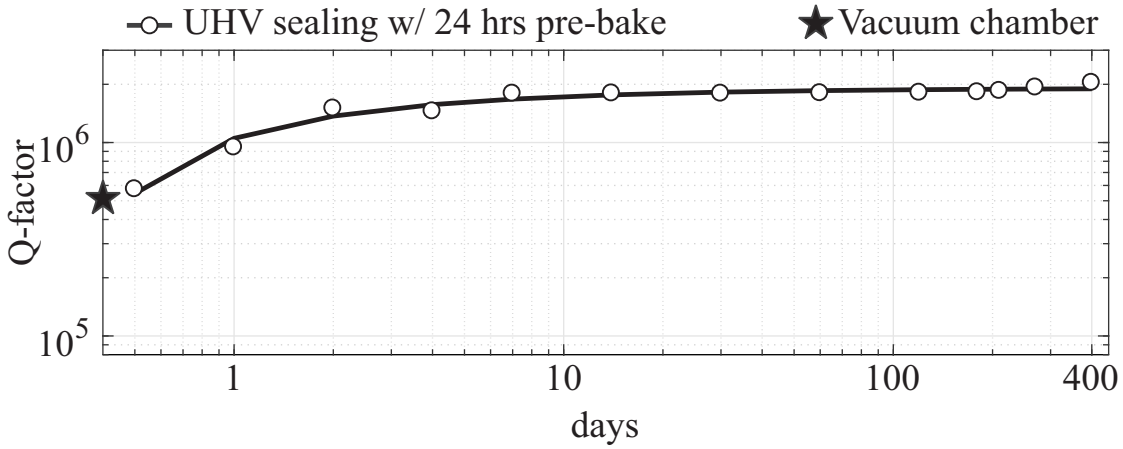

Figure 2.19: The Q-factor measurements over a long period of time revealed vacuum stability inside a sealed cavity after vacuum sealing (DUT3). The improvement of the Q-factor is related to the pumping of residual gas molecules by the activated getter [80].

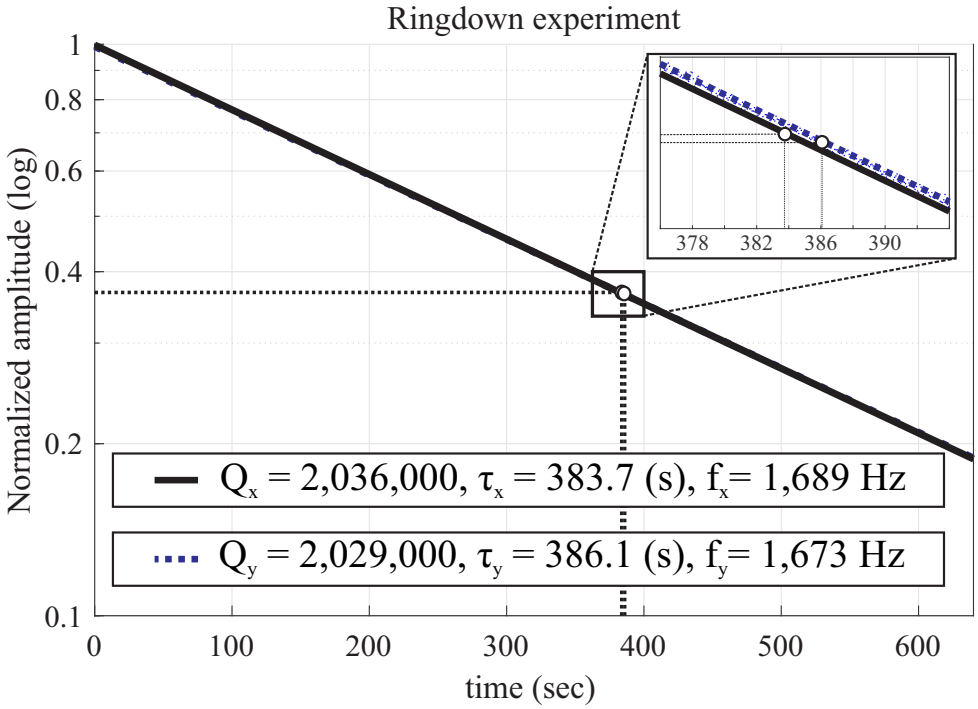

Figure 2.20: Ringdown time measurements revealed the Q-factor as high as 2 million, on both X-axis and Y-axis, after UHV sealing.

For the DUT3 in this example, the X-mode Q-factor was measured at Q_x =2,036,000, which corresponds to τ_x =383.7 (s) at f_x =1,689 Hz, and along the Y-mode it was measured at Q_y =2,029,000, which corresponds to τ_y =386.1 (s) at f_y =1,673 Hz, Fig. 2.20. The inverse of time decay mismatch between both modes $\Delta(1/\tau) = (1/\tau_x - 1/\tau_y)$ was estimated to be 1.1×10^{-4} Hz. The Q-factors after vacuum sealing approached the Q_{TED} limit of the structure, which was modeled using finite element simulation to be at 3.5 million [109].

2.6.3 Sensor Fusion

With this platform, a human gait cycle was experimentally extracted with sensors attached to the heel area of the shoe. Details of the foot motion data collected throughout the walking phase are shown in Fig. 2.21. The reported signals are: 1) magnitude of the acceleration vectors where the maximum indicates an initial contact of heel with ground, 2) pitch-axis rotation of the IMU, and 3) inter-foot distance where the information is only valid when the SONAR pairs are facing each other (TX and RX). It is important to emphasize that the SONAR information was used to identify stationary periods of the walking phase. The integration of SONAR sensors using directional ranging resulted in lower navigation errors; the detailed analysis and algorithms are reported in [110].

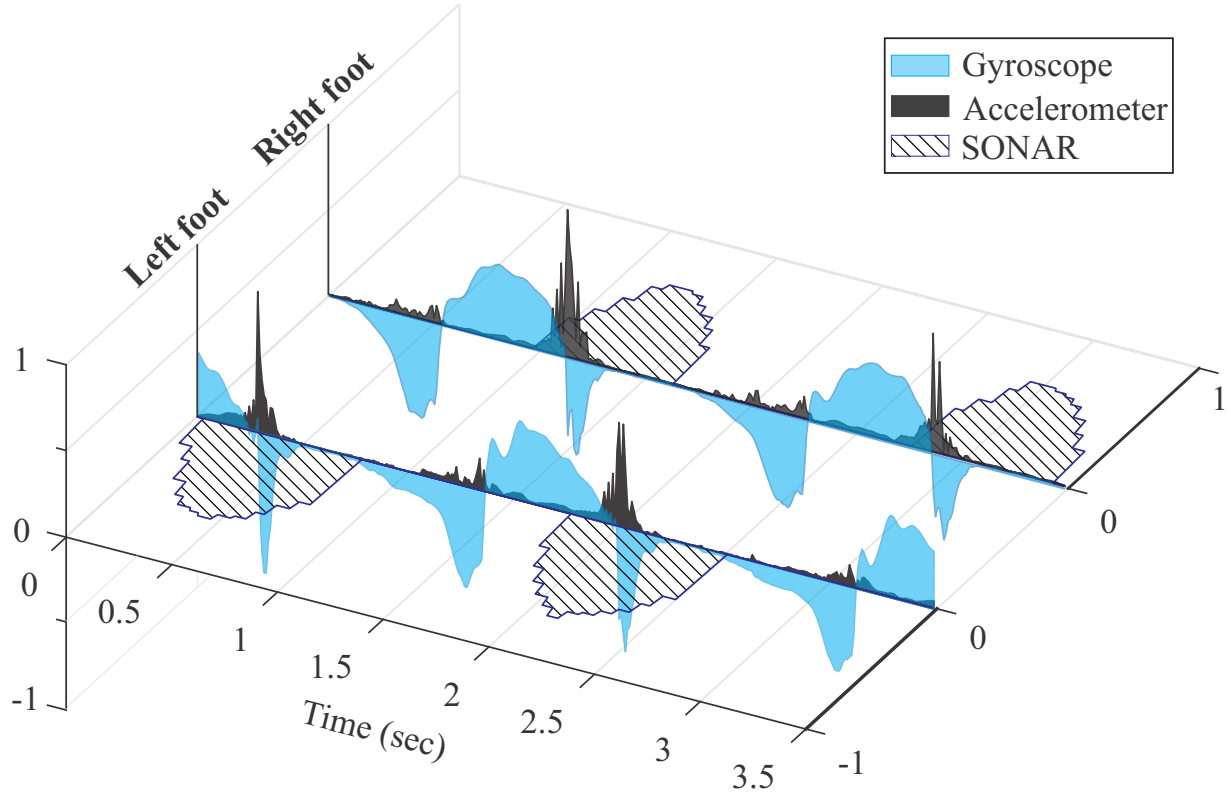

Figure 2.21: Recorded data by the platform during a normal walking from both the left- and the right-foot mounted sensors. The units are pm8 g, pm450 °/s and pm100 cm for acceleration, angular velocity, and displacement reading, respectively. The 3.5 s corresponded to two full steps.

We report noise characteristics of IMUs integrated in the system, with ADEV illustrated in Fig. 2.22. The difference between the datasheet and experimental noise values is attributed to the noise contribution from the PCB, cables and interconnects used for implementation of the system.

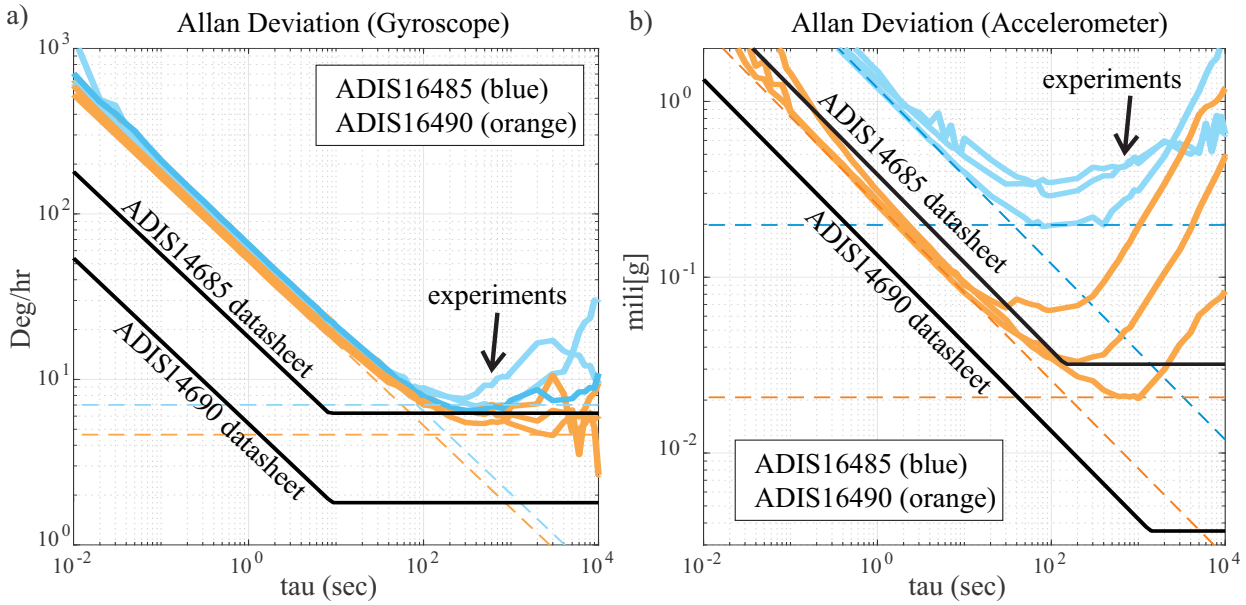

Figure 2.22: The noise characteristics of the system from 12 -hrs data were estimated and compared to the sensor performance reported in datasheets, (a) gyroscope, and (b) accelerometer. The recording was done while IMUs were mounted on the shoe fixtures at laboratory room temperature.

2.7 Conclusion

We described the features of the selected MEMS structure studied for a vestibular prosthesis. We identified the parts needed for characterization of this custom fabricated MEMS gyroscope device. We presented the development procedure of the universal standalone platform. The platform was designed to implement algorithms for device-level characterization. We discussed the considered architecture and provided intuition on the importance of the selection of components and its noise contribution to the system. We demonstrated experimentally the extraction of frequency symmetry and damping mismatch of the fabricated device using the standalone platform. We developed a flexible solution platform for integration and processing data from multiple foot-mounted inertial and foot-to-foot ranging sensors that can be adapted for investigation of human gait analysis. The flexible platform was designed to investigate on calibration algorithm for a vestibular prosthesis. The FPGA part of the platform was programmed to read/write command from/to the sensors, and the CPU part of the platform was used to utilize algorithm, while the computer-VI was used for visualization and control of filter gains. We extracted gait dynamic using all sensors and illustrated the noise performance and sampling limitation of the developed flexible platform.

Chapter 3

Bias and In-Run Drift Analysis

This chapter presents the methods and characterizations for identification of drifts for the prosthesis using a high-quality factor MEMS gyroscope. We report on trade-offs between full-scale, linearity, and noise characteristics of QMGs with different Q-factors. Allan Deviation (ADEV) and Power Spectral Density (PSD) analysis methods were used to evaluate the performance results. The devices in this study were instrumented for the rate mode of operation, with the Open-Loop (OL) and Force-to-Rebalance (FRB) configurations of the sense mode. For each method of instrumentation, we presented constraints on selection of control parameters with respect to the Q-factor of the devices. For the high Q-factor device of over 2 million, and uncompensated frequency asymmetry of 60 mHz, we demonstrated bias instability of $0.096\,^{\circ}$/hr and Angle Random Walk (ARW) of $0.0107\,^{\circ}/\sqrt{\text{hr}}$ in the OL mode of detection and bias instability of $0.065\,^{\circ}$/hr and ARW of $0.0058\,^{\circ}/\sqrt{\text{hr}}$ in the FRB mode of detection. We concluded that in a realistic MEMS gyroscope with imperfections (nearly matched, but non-zero frequency asymmetry), a higher Q-factor would increase the frequency stability of the drive axis resulting in improved noise performance, but has implementation challenges on digital control loops involved.

3.1 Introduction

A gyroscope operating in angular rate measurement due to input rotation, energy transfers between primary and secondary modes of the gyroscope [91]. Fig. 3.1 shows this exchange of energy between the drive and sense modes, when a device is experiencing a rotation. The drive axis is under continuous oscillation along the drive axis using a feedback loop for amplitude stabilization and the Coriolis acceleration induced motion is sensed along the sense axis. In the rate mode of operation, the resolution floor of the gyroscope is described by bias instability and Angle Random Walk (ARW), where ARW is a figure of merit to quantify the angle wander resulting from the integration of noise in the rate signal over time [111]. According to the Mechanical-Thermal Noise (MTN) model, a noise-equivalent rate in an open-loop gyroscope, which defines a lower bound of the performance, the Quality-factor (Q-factor) of the sense mode, frequency mismatch between the drive and the sense modes, and the drive mode amplitude are the parameters influencing the performance of the angular rate gyroscopes, [112]:

$$\Omega_{rw} \approx \sqrt{\frac{k_B T \omega_y}{A^2 M \omega_x^2 Q_y} \left[1 + \left(\frac{Q_y(\omega_y^2 - \omega_x^2)}{\omega_y \omega_x}\right)^2\right]^{-1}}, \tag{3.1}$$

where Ω_{rw} is the noise equivalent rotation rate, k_B is the Boltzmann's constant, M is the effective mass, T is the operating temperature measured in Kelvins, A is drive axis amplitude, ω_x and ω_y are the drive and sense resonant frequencies measured in rad/s, and Q_y is the sense-mode Q-factor. Equation (3.1) indicates, for example, the smaller the frequency mismatch $(\omega_x - \omega_y)$ and the higher the Q-factor, the lower the characteristic noise of a CVG. As shown earlier, Chapter 2 Fig. 2.4, illustrates schematically the oscillation deflection in the rotating coordinate frame. The output sensed along the Y-axis is proportional to the input angular rate, where MTN in Eq. (3.1) defines the minimum detectable signal. Thus, mode-matching [113] and the Q-factor maximization [114] are the key strategies to augment the measurement

sensitivity and reduce the mechanical thermal noise at any operational frequency.

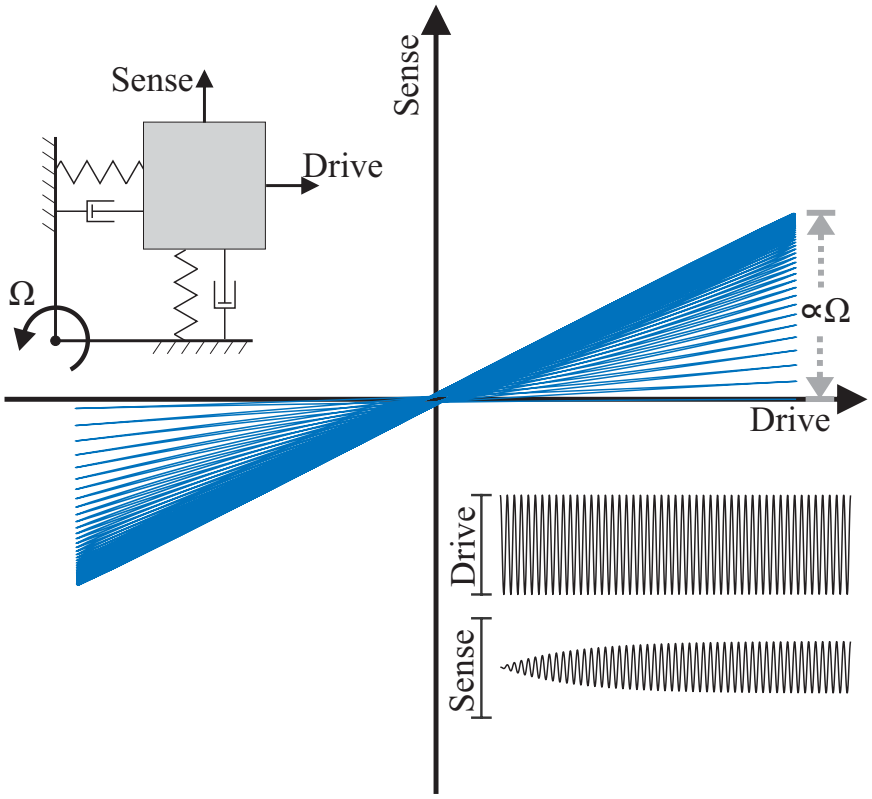

Figure 3.1: Response of a CVG operating in the angular rate mode. The response is due to rotation along the Z-axis, orthogonal to the page. Overlay plot of drive and sense axes oscillations illustrates a harmonic motion along the drive axis and changes along the sense axis, which are proportional to the applied angular rate.

Dissipation mechanisms in MEMS resonators and CVGs have been studied and several structural designs have been implemented to achieve low noise characteristics. A dual mass gyroscope architecture, with decoupled tines reported by [115] and with synchronization lever mechanism by [114], demonstrated the Q-factor of 125,000. Analogously to the dual mass, a device with four masses and coupling frames has been introduced by [116] and the Quadruple Mass Gyroscope (QMG) with anti-phase lever mechanisms by [78], demonstrating the Q-factor of 450,000. In this implementation, the neighboring frames were in a coupled arrangement and moved in anti-phase relative to each other. A QMG with as-fabricated frequency mismatch of 0.2 Hz and the Q-factor of 1,170,000 was demonstrated with 0.88 °/hr in-run bias instability and ARW of 0.06 °/$\sqrt{\text{hr}}$, operating in the Force-to-Rebalance (FRB)

mode [117]. A two-mass Dual Foucault Pendulum (DFP) architecture by [118], was designed to provide a minimal realization of a mode-matched dynamically balanced lumped mass gyroscope. The DFP was believed to provide advantages of the QMG architecture while reducing complexity of the design. An epitaxially-encapsulated Dual Foucault Pendulum (DFP) operating at 15 kHz with the Q-factor of 1,150,000 demonstrated an in-run bias instability of 1.9 °/hr and an ARW of 0.075 °/$\sqrt{\text{hr}}$ in the open-loop rate mode of operation [119]. Q-factors of over 9,290,000 were demonstrated, introducing a methodology for making the anchor losses observable by nulling the thermoelastic damping under specific cryogenic temperatures [120]. Other successful implementations of MEMS gyroscopes, are Disk Resonator Gyroscope (DRG) and Bulk Acoustic Wave (BAW) disk gyroscope. These architectures are based on flexural vibrational modes. A silicon DRG with an active temperature compensation has been reported with the Q-factor on the order of 80,000 operating at 14 kHz with in-run bias instability of 0.012 °/hr and ARW of 0.002 °/$\sqrt{\text{hr}}$ [121]. An epitaxially-encapsulated polysilicon DRG operating at 264 kHz with the Q-factor of 50,000 demonstrated an in-run bias instability of 3.26 °/hr and ARW of 0.36 °/$\sqrt{\text{hr}}$, [122]. A BAW disk gyroscope was demonstrated in [123], with the Q-factor of up to 1,380,000 at 2.745 MHz center frequency, in an actively controlled vacuum chamber. In an ideal case, the modal symmetry and balanced motion of the sensing element in QMG, DRG, DFP, and BAW disk resonators are considered to cancel out the reaction forces and moments acting at the anchor locations, thus mitigating the dissipation of energy through the substrate. In case of the DFP, for example, the anchor loss was demonstrated to be 9 times lower than the Thermoelastic Damping (TED) limit of the Q-factor [120].

The QMG device described herein has evolved considerably from the first introduction of the device in [78], in terms of its structure and control architecture, demonstrating an excellent modal symmetry and exceptional Q-factor. Features of the design discussed here are categorized into three design iterations: (QMG-I) with mass symmetry and an external lever mechanism [78, 124], (QMG-II) with mode-ordering, as well as an internal and exter-

nal levering, comb-finger drive electrodes and parallel-plate sense electrodes [125, 126], and, (QMG-III) with a complete symmetry of the design, including internal and external levering, with differential parallel-plate drive and sense electrodes [77, 127], and vacuum sealing with getters. Table 3.1 summarizes the key parameters of these iterations and the corresponding publications. From the latest design iteration, QMG-III, we will evaluate different Devices Under Test (DUT), summarized in Table 3.2 to illustrate the effect of different parameters of the device to their performances.

Table 3.1: QMG devices performance progression

Iteration	freq. [Hz]	Q-factor	Δf [Hz]	ARW [$^\circ/\sqrt{hr}$]	Ref.
QMG-I	2177	1.17M	0.2	0.06	[117]
QMG-II	3047	980	0.15	0.02-0.05	[128]
QMG-III	2085	1.1M	0.2	0.04	[129]

In this work, we discuss the noise performance and the effect of vacuum sealing on QMGs with three different Q-factors, ranging from as low as 1,000 (DUT1) to as high as 2,000,000 (DUT3), Table 3.2. DUT3 with the highest Q-factor will be used to demonstrate capabilities of the QMG design and MEMS technology. The reported devices are instrumented to operate in the rate mode.

The material of this chapter is organized as follows. In section 3.2, we report a procedure of electrostatic tuning of the frequency split, as well as analyze and discuss strategies for implementation of control algorithms and selection of control parameters for sensors with different Q-factors. The limitations of a high-Q mode-matched MEMS CVG in terms of the scale-factor nonlinearity and measurement bandwidth in the open-loop rate and force-to-rebalance rate modes are experimentally analyzed in Section 3.3. In section 3.4, a discussion on noise performance analysis of DUTs in the open-loop rate mode is presented and compared to the FRB rate mode of operation. The same section discusses two methods for deriving ARW and

bias instability from the Allan Deviation (ADEV) and the Power Spectral Density (PSD) analysis. Both methods identify and model random errors of the gyroscope output, where ADEV is extracted from the time-domain data and PSD is extracted from the frequency-domain data. And finally, stability of the drive resonance frequency is characterized and correlated to noise performance of the device.

3.2 Performance Analysis

In this section, the statistical analysis of the Zero Rate Output (ZRO) of three QMG sensors with different Q-factors and different levels of symmetry, but similar operational frequencies, are discussed. The purpose of this analysis is to provide insight into factors contributing to lower noise performance by identifying device-specific error parameters, and subsequently analyze the effect on control algorithms, and relate to complexity of control algorithm implementations. The variation in the Q-factors of DUTs is attributed to the different vacuum sealing conditions. Table 3.2 summarizes parameters of the selected sensors. The residual frequency mismatch after electrostatic tuning, control accuracy, frequency stability, and the induced noise on the ZRO output are discussed next.

Table 3.2: Characteristics of the three sensors used for the noise performance analysis

Device ID	Q-factor*	Drive frequency [Hz]	Δf [Hz] (as-fabricated)
DUT1	1,050	2040	4
DUT2	25,750	2100	25
DUT3	2,036,000	1673	15

*The difference is due to different packaging conditions.

3.2.1 Frequency Split (Δf) Extraction

Fabrication imperfections in QMGs are the primary causes of frequency mismatch between the drive and sense modes. The lowest possible noise floor is achieved when the frequency mismatch is small [130]. To correct for residual imperfections, an electrostatic frequency tuning was used, which is discussed in section 2.6.1. The frequency split/mismatch (Δf) was estimated at each discrete DC voltage level from the resonant frequency along the X-axis and the Y-axis. The extraction of Δf for high Q-factor sensors under the tuned condition (typically $<$1 Hz) is challenging. The temperature dependency of frequency sweep characterization was also investigated. As an example, for a typical room temperature fluctuation of 2 °C during the frequency sweep characterization, the resonant frequencies would shift 80 mHz. To illustrate this, we characterized experimentally the Temperature Coefficient of Frequency (TCF) of the sensor. Fig. 3.2 demonstrates the measured TCF of the sensor in a thermally-controlled environment with an average TCF value of -24ppm/°C. In the nearly-matched frequencies, the Δf was extracted by FFT spectrum analyzer of oscillations along the drive axis. Fig. 3.3 shows an extracted Δf using the procedure, confirming the ability to reach an optimal tuning voltage value at 16.15 V, achieving Δf<1 Hz. The inset plot illustrates examples of PSD with three DC voltage levels (A, B, C) at 15.80, 16.15 and 17.35 V, with an estimated Δf of 200, 60 and 1,900 mHz, respectively. The described method enables a real-time observation of the Δf for high Q-factor devices, while actively adjusting the applied DC tuning voltage.

3.2.2 CVG Control Algorithm

The CVG control algorithm was implemented based on the IEEE Std 1431 [131]. The digital control of the characterization was carried out using the HF2LI lock-in amplifier. Four primary control loops were implemented for the rate mode characterization, including Phase-

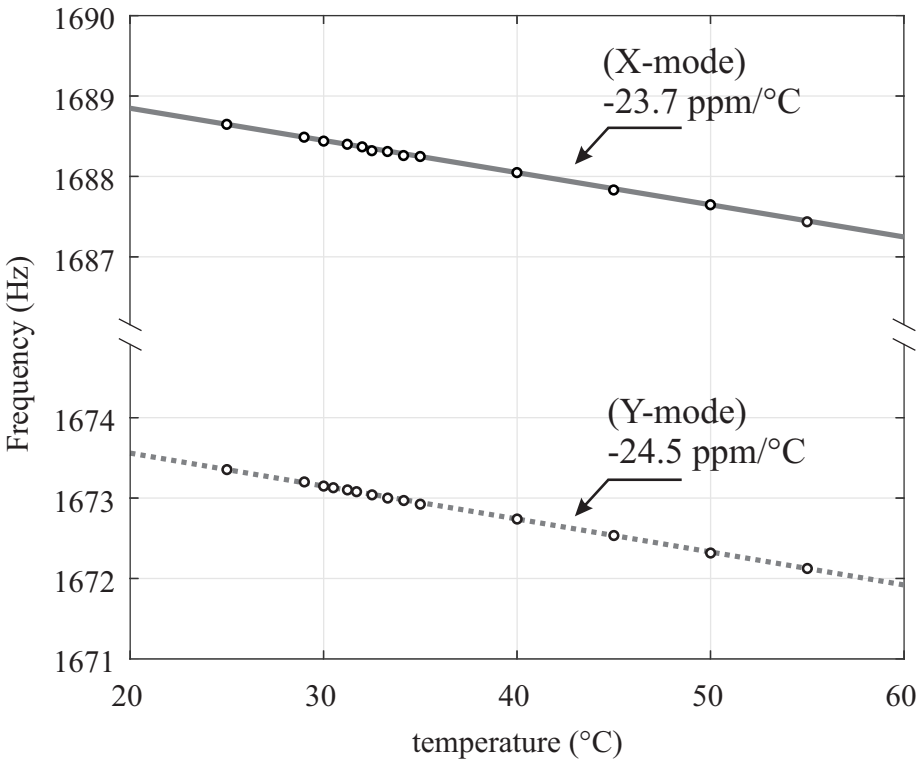

Figure 3.2: Experimental measurement of the TCF along X-axis and Y-axis of the sensor with as-fabricated Δf of 15 Hz. The measurement was performed in a thermally-controlled environment, with temperature ranging from 25 to 55 °C, and temperature fluctuations within 0.04 °C at each measurement point.

Locked Loop (PLL), Amplitude Gain Control (AGC), Quadrature Control Loop (QCL), and Rate Control Loop (RCL), Fig. 3.4. Each loop comprises: (1) a demodulator for demodulating a received signal from the device, either along X-axis or Y-axis, into in-phase (*cos*) or in-quadrature (*sin*) signals, (2) a Low-Pass Filter (LPF) for passing only low-frequency component, (3) a PID controller with a set point for controlling the DC component of the demodulation, and (4) a modulator for modulating the controlled signal to a higher frequency defined by the local reference oscillator signal. The PLL loop has two extra components, which are Phase Detector (PD) and Voltage-Controlled Oscillator (VCO). Using these control loops, a gyro can be configured to operate in the open-loop rate mode under the following conditions: a) PLL only, b) PLL and AGC, c) PLL, AGC, and QCL, or d) closed-loop rate mode where all four loops (PLL, AGC, QCL, and RCL) are established, also

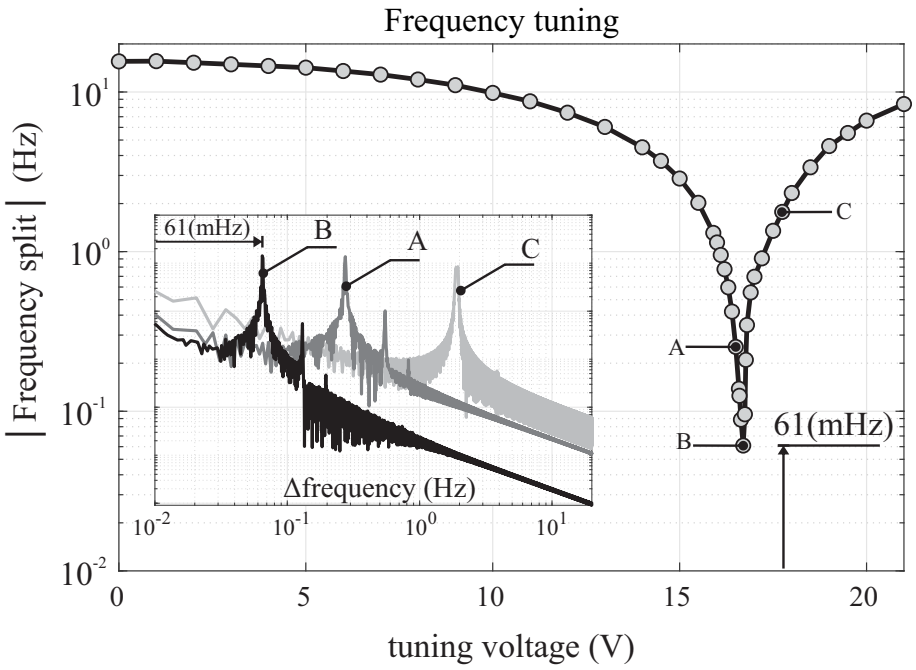

Figure 3.3: Experimental estimation of $|\Delta f|$ by monitoring the peak in the power spectrum of the nearly-matched region for a high Q-factor device. Inset figure shows the PSD of the drive signal at the corresponding reference points.

known as closed-loop FRB rate mode.

The PLL generates a reference frequency by tracking the resonant frequency of the drive mode, which is done by a VCO with negative feedback to a phase detector. The phase detector compares the phase of the received signal with respect to the local oscillator and generates an error signal; the PLL is called "locked" when the error signal is zero. The AGC loop maximizes the in-phase component of the drive signal to a pre-defined set point value, and the QCL loop nulls the in-quadrature component of the sense signal. The RCL loop is used to estimate the input rate from the in-phase component of the sense signal in the open-loop configuration, or from the voltage applied to null the rate signal in the FRB rate mode.

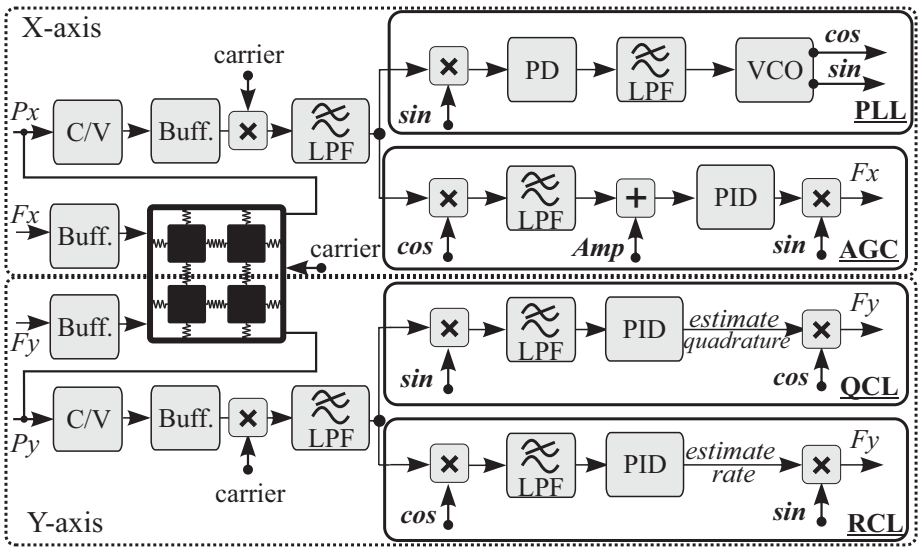

Figure 3.4: Control structure for operating devices in the rate mode. AGC and PLL were activated along the drive axis of the device (X-mode). QCL and RCL were activated along the sense axis of the device (Y-mode).

3.2.3 Control Accuracy

In this section, we highlight challenges in stabilization of the control loops for devices with different levels of symmetry and the quality factor, and derive the corresponding hardware requirements. A PID controller is needed to track and stabilize the amplitude in the drive direction, phase of the drive oscillation frequency, amplitude of the quadrature and rate parameters in the sense direction from demodulated components of the drive and sense signals (also known as slowly-varying parameters). The general PID equation can be represented by:

$$u = K_P e + K_I \int e + K_D \dot{e}\,, \tag{3.2}$$

where u is the control signal, e is the control error, and the controller parameters are K_P (proportional), K_I (integral) and K_D (derivative) gains of the linear control architecture. In this work, only the PI controller was used for feedback to stabilize parameters (amplitude,

phase, quadrature, and rate feedback). Each controller has a set point, bandwidth, and a sampling rate. Experimental results revealed that the PI parameters for a low Q-factor device (high loop bandwidth) would fail to control the high Q-factor devices (low loop bandwidth), and vice versa. Applying PI parameters, which were selected for a high Q-factor device to a low Q-factor device would result in a slower response, which is unfavorable for fast frequency tracking. Consequently, the loop bandwidth has to be set based on the device parameters. These parameters for the three selected devices (DUT1–DUT3) were set as follows: the −3 dB cutoff frequency of the loop filter in the PLL was selected to be around 100 Hz, centered at the resonant frequency of the drive axis. A phase shift occurred between the driving mass forcer signal (denoted by Fx in the diagram shown in Fig. 3.4) and the phase detector in the PLL loop (marked as PID block in the diagram shown in Fig. 3.4). The signal path includes a preamplifier buffer circuit, the device, a charge amplifier, a front-end buffer circuit, a carrier demodulation circuit, and a LPF. The phase setpoint of the PLL aligns this phase shift of the feedback signal with the forcer signal. The transfer function of a resonator PLL system dynamics is [132]:

$$\Phi(s) = \frac{1}{(t_c s + 1)}, \tag{3.3}$$

where Φ is the resonator's phase and $t_c = 2Q/(2\pi f)$ is the exponential time constant. The output propagates to a low-pass filter, where the controller adjusts the phase Φ. The PI parameters of the PLL unit are responsible for the fast lock of the resonance frequency to the reference local oscillator. The high Q-factor resonators require a narrower bandwidth ($BW = 1/t_c$), on the order of Q inverse, due to the transfer function characteristics of the system, whereas in low Q-factor resonators the bandwidth is much higher, again on the order of Q inverse.

For the DUTs in this study, the setpoints for the rate and quadrature loops were selected to be 0 Vrms and for the drive amplitude were selected to be 0.42 Vrms, to utilize the full-

scale resolution from the amplifier output to the Analog-to-Digital Converter (ADC) with an input range of ± 1.2 Volts.

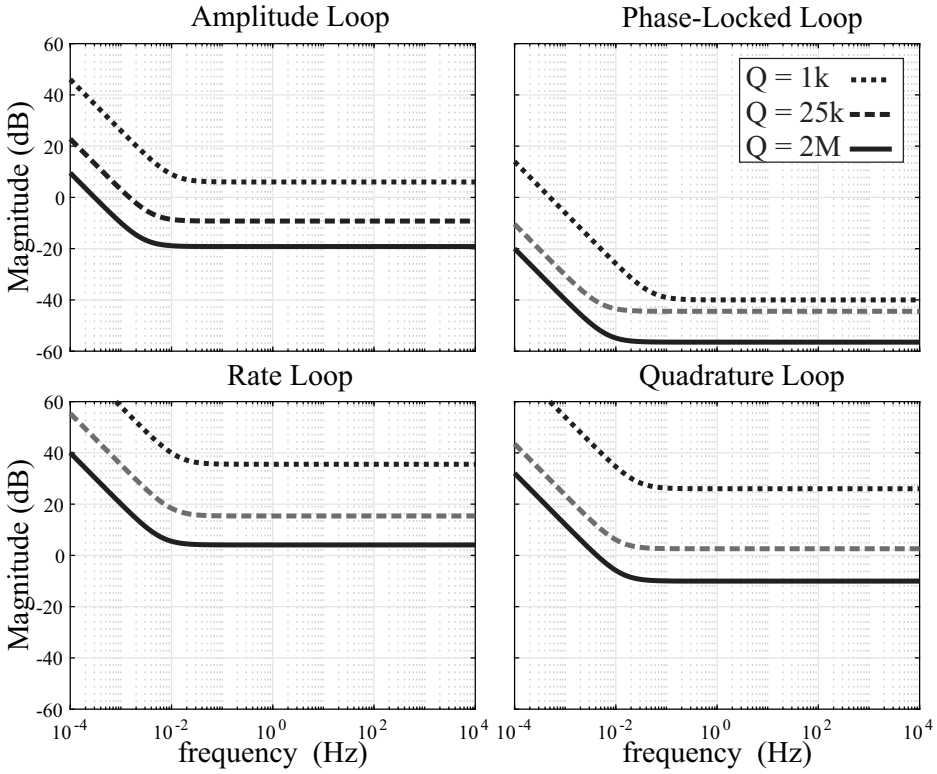

Figure 3.5: Implemented configurations of PI parameters on the amplitude (AGC), phase (PLL), quadrature (QCL) and rate (RCL) loops for QMG devices with Q-factors ranging from 1,000 to 2,000,000. PI parameters were scaled proportionally to the Q-factor of the device.

To achieve the target bandwidth and stable loop conditions, different sets of PI parameters (units for K_P are [V/Vrms] or [Hz/deg], and for K_I are [V/Vrms/s] or [Hz/deg/s]) were selected and verified experimentally for devices with different Q-factors. For a Coriolis vibratory gyroscope in a self-oscillation mode (or using an external signal generator from PLL), the Routh-Hurwitz criterion to satisfy the stability is [133]:

$$\begin{aligned} K_P &> \frac{m_x 2\pi f_x}{G_p G_f Q_x}, \\ \omega_c K_P &> K_I, \end{aligned} \tag{3.4}$$

where G_p and G_f are the gain buffer after pickoff and generated forcer signals, and ω_c is the cutoff frequency parameter of the LPF of the loop. The G_p parameter was fixed across the three DUTs, but G_f was adjusted accordingly and was selected to be lower when the Q-factor was higher. Thus, K_P is inversely proportional to the Q-factor and the G_f. Given the above parameters and initial settings for each loop, K_P and K_I were implemented and results are shown in Fig. 3.5. The figure illustrates the sensitivity constraints on the magnitude of the four primary CVG control loops vs. frequency. In the closed-loop configuration, the integrator's coefficient K_I stabilizes the proportional controller and zeros the steady-state error. As expected, the crossover integrator frequency (closed-loop bandwidth) component decreased as the device's resonance Q-factor increased. Overall, the PI parameters of the control loop need to be adjusted based on the Q-factor of the device, affecting the speed of the control loops. The sampling rate of the input signals to the four primary CVG control loops (PLL, AGC, QCL, and RCL) were set to be at 130 kHz (between 5–10x of the device's resonance frequency). The sampling rate of the PI digital controller runs one order of magnitude faster than the crossover frequency, ensuring that any changes in the signal can be controlled.

3.2.4 Open-Loop Operation in Rate Mode

In the open-loop CVG rate mode operation, the drive mode was excited to a fixed amplitude A_0, with the use of AGC, and at the frequency f_x, and with the use of PLL. Due to the Coriolis coupling, the input rate causes the excitation of the sense mode channel, and the sense mode amplitude is proportional to the input rate.

The scale-factor was extracted by applying a reference rotation using a rate table, with incremental step inputs of 0.25 °/s in the clockwise and counter-clockwise directions. The open-loop scale-factor of 2.2 mV/(°/s) was obtained for the high Q-factor device. Fig. 3.6

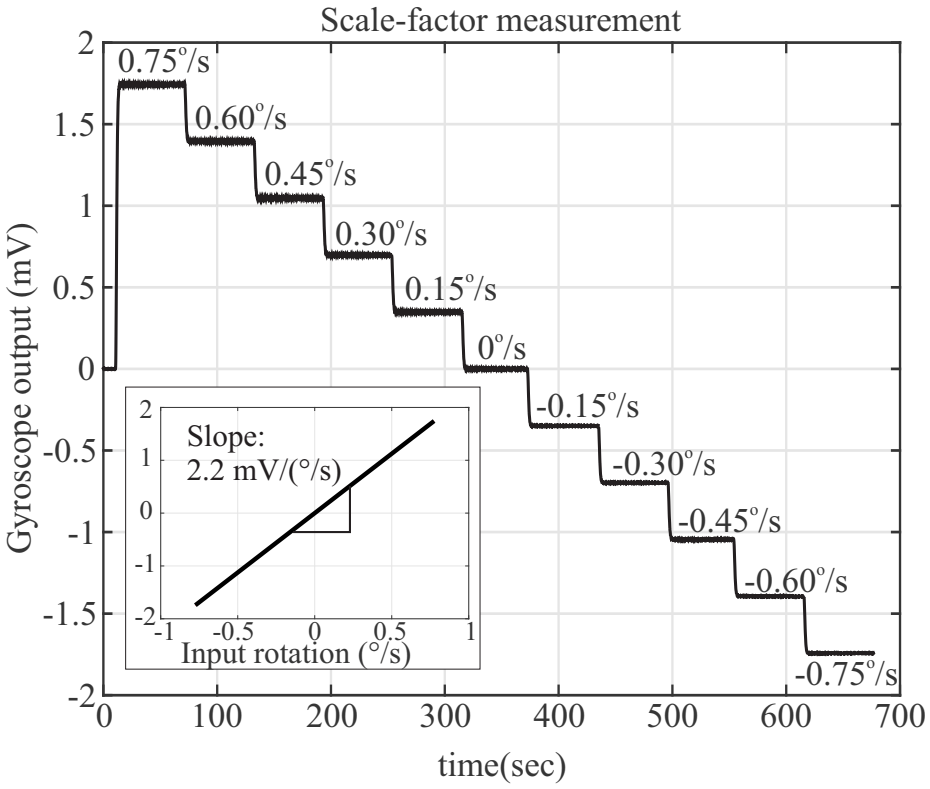

Figure 3.6: Rate characterization response to clockwise and counter-clockwise rotations with different step-input amplitudes of 0, ±0.15, ±0.30, ±0.45, ±0.60 and ±0.75 °/s, revealing an open-loop scale-factor of 2.2 mV/(°/s).

illustrates the device response over time for a small input rotation range, where the inset plot shows linearity of the input-output of the same dataset.

3.2.5 Force-to-Rebalance Operation in Rate Mode

Similar to the open-loop, in the closed-loop CVG the drive mode was excited to a fixed amplitude A_0, with the use of AGC, and at the frequency f_x, with the use of PLL. An additional force was applied along the sense mode to null the response. This force is required to null the sense mode amplitude and is proportional to the input rate, thus the architecture is called Force-to-Rebalance (FRB) or closed-loop instrumentation of CVG operating in the rate mode.

The scale-factor extraction is similar to the described open-loop architecture, and, similarly, the zero rate data could be used for noise analysis. Due to inconsistencies in the sampling time interval during data recording of the Digital-to-Analog Converter (DAC) components of the hardware setup, the noise performance of the gyroscope's output rate in the FRB mode was estimated from the input to the RCL loop (open-loop rate estimate) ADC component multiplied by inverse of the loop gain, rather than the output of DAC component (Fy signal, shown in Fig. 3.4). However for the scale-factor, the output was estimated from DAC component from maximum and minimum fluctuation response, even though with sampling time inconsistency. The FRB rate voltage output was then converted to an equivalent rotation rate in °/s.

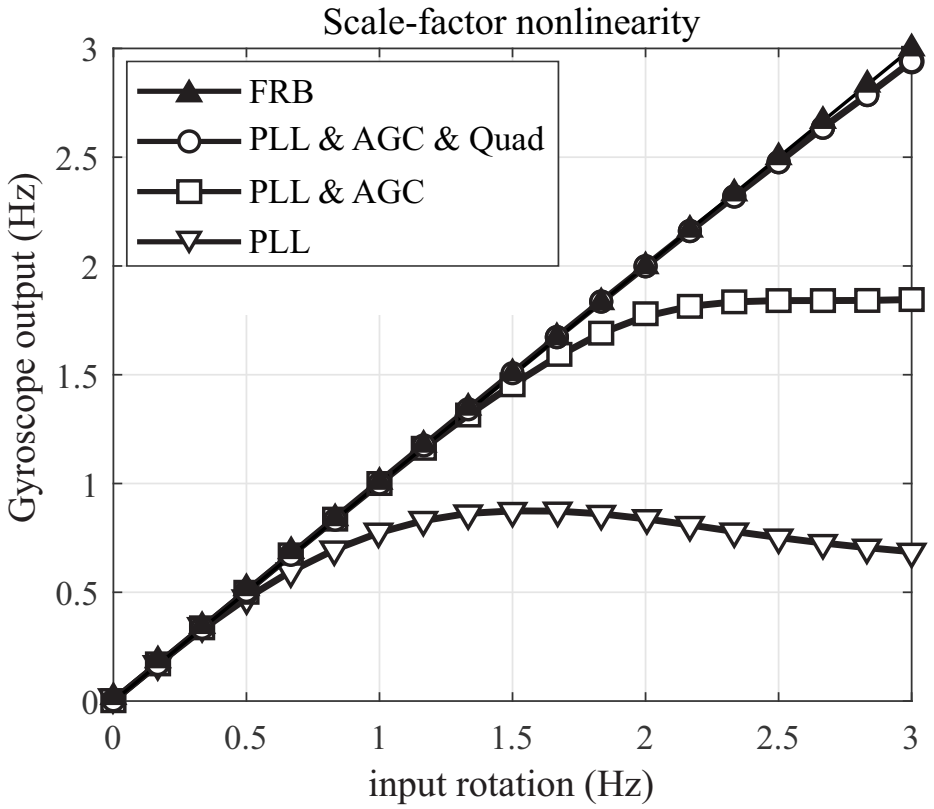

Figure 3.7: Experimental measurements of the scale-factor nonlinearity in DUT1, operating in the mode-matched condition with different configurations of control loops.

3.3 Scale-Factor Nonlinearity and Bandwidth

The advantage of the high-Q MEMS CVG operating in the mode-matched condition is a high sensitivity to the input rotation and its ability to measure low angular rates. However, the linearity of the scale-factor [134] and the measurement bandwidth [135] are limited when the sensor is operating in the open-loop rate mode. The scale-factor linearity and the bandwidth limit of the sensors operating in the open-loop and closed-loop modes were characterized experimentally.

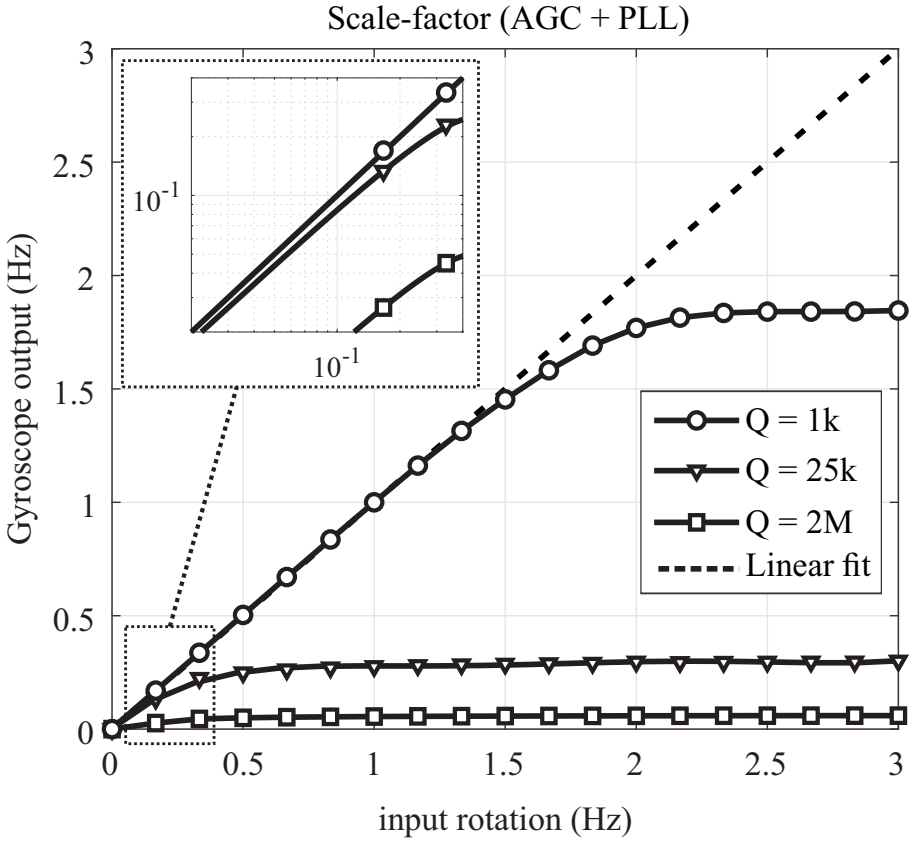

Figure 3.8: Experimental measurement of the scale-factor nonlinearity in sensors with different Q-factors and mode-matched condition, operating in the open-loop rate mode (PLL and AGC loops are enabled).

For linearity analysis, an input rotation in the range of angular rates from 0 °/s to 1,080 °/s with an increment of 60 °/s was applied using an Ideal Aerosmith 1571 rate table. The

linearity of the input-normalized output under different loop configurations were compared experimentally only for the DUT1 operating in the mode-matched condition, Fig. 3.7. DUT1 with low Q-factor was selected for flexibility of adjusting parameters and repeating the experiment at several input angular rotations. The results demonstrated that the linear range of operation is limited in the open-loop operational mode, that is when only the drive axis control loop PLL was established. The linear range increases when both PLL and AGC were activated. An extended scale-factor linearity was observed when devices operated in the closed-loop sense configuration (FRB). Based on these results, the FRB fully compensates for nonlinearity in the output response for the input rotation range from 0 to 3 Hz. It is expected to see a similar trend for DUT2 and DUT3 by activating individual control loops, however with a smaller linear region due to quality factor of these samples.

Next, we repeated measurements in the open-loop configuration, when control loops (PLL and AGC) were activated across all three DUTs. Fig. 3.8 demonstrates the scale-factor nonlinearity in the open-loop rate mode for devices with different Q-factors, operating in the mode-matched (or nearly-matched) condition. As expected, the linear input-output range of operation becomes narrower as the Q-factor increases, confirming the sensitivity of resonator's bandwidth in the open-loop operational mode relative to its drive frequency over Q-factor, f_x/Q.

In a mode-matched device, the bandwidth is determined by the Q-factor of the device, whereas for a mode mismatched device the BW is dominated by the Δf [136]. Generally, a higher bandwidth can be achieved by increasing the damping coefficient (lowering the Q-factor) or operating in the mode-mismatched condition (increasing the frequency mismatch Δf). We support this observation by a diagram shown in Fig. 3.9. In the diagram, the parameters for the drive amplitude (A) and the mass (m) are grouped as $G1 = -2mA\Omega$, and the circuit and buffer gains are grouped as $G2$. The notations $F_y(i)$ and $F_y(q)$ represent the in-phase and in-quadrature forces applied along the sense axis of the device. The input

drive voltage $F(t)$ along the sense axis in the open-loop case is

$$F(t) = -2mA\Omega sin(w_x t) + F_q cos(w_x t), \tag{3.5}$$

and in the closed-loop (FRB) case is

$$F(t) = -2mA\Omega sin(w_x t) + F_q cos(w_x t) + F_y(q) + F_y(i). \tag{3.6}$$

The Laplace transform of each of the shown components are as follows:

$$\begin{aligned} Sense(s) &= \frac{1/M}{s^2 + (w_y/Q)s + w_y^2}, \\ LPF(s) &= \frac{w_c}{s + w_c}, \\ PI(s) &= K_P(1 + \frac{K_I}{K_P}s), \\ OL(s) &= Sense(s)LPF(s)F(s), \\ FRB(s) &= (OL(s)PI(s))/(1 + OL(s)PI(s)). \end{aligned} \tag{3.7}$$

To filter out the excitation amplitude of the sense mode resonance, the selection of the LPF cutoff frequency w_c is typically 3 times lower than the Δf. The selection of the PI controller gains K_P and K_I are also device dependent and were discussed in section 3.2.3. The frequency analysis of the open-loop $OL(s)$ and the closed-loop $FRB(s)$ of the gyroscope model with respect to the input rotation $\Omega(s)$ was performed in the Matlab environment, and shown in Fig. 3.10. The analysis was repeated on all three DUTs with different Q-factors. For DUT1 and DUT2 with low and medium Q-factors, the open-loop BW analysis shows a strong dependency to the frequency split, but for the DUT3 with a high Q-factor of $2M$ and Δf of 60 mHz, the -3 dB was dominated by the Q-factor of the device and estimated to be 0.5 mHz, which is two orders of magnitude lower than the frequency split. The BW limit observed in the open-loop operation can be compensated if the device was operated in the

FRB mode. Simulation of parameters of the three DUTs shows that a higher BW is possible when FRB is selected as a preferable mode of operation. This conclusion was also verified experimentally and shown in the graph of Fig. 3.10. However, this should be understood that the FRB amplitude range is limited to the DAC forcer amplitude resolution.

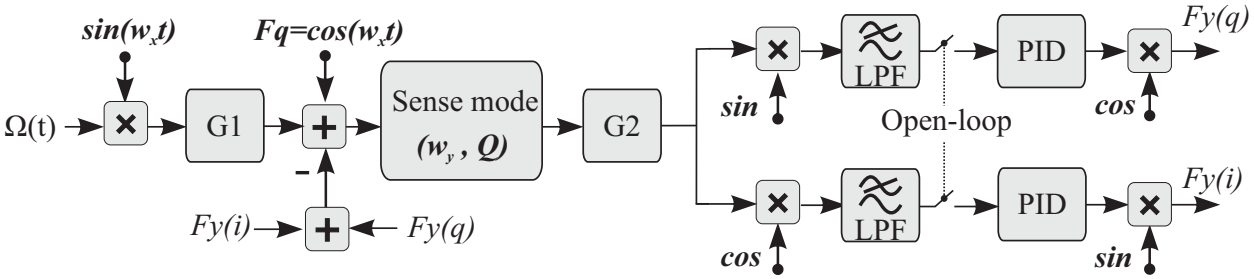

Figure 3.9: Simplified block diagram of the open-loop and closed-loop rate QMG MEMS gyroscope.

The BW of the QMG sensors were experimentally derived. Sinusoidal stimulus commands with varied frequencies, from 0.01 Hz to 5 Hz, were applied to the rate table. The experiment was repeated for the three sensors in the open-loop and the FRB rate mode mechanizations, Fig. 3.10. From the rate output measurement of each mode, the −3 dB range resolution was extracted to be at 100, 227 and 790 mHz, which is in a close agreement with the tuned Δf of the QMG devices under electrostatic tuning conditions of 450, 250 and 60 mHz, respectively. Operating the device in the FRB configuration resulted in a higher bandwidth, independent from the frequency split of the device. This was confirmed on DUT1 and DUT2. However, for the high Q-factor sensor (DUT3), and for the input angular rate of rotation around 1 Hz, the FRB utilized the full amplitude range available of the hardware along the sense axis of the device. Therefore, there was no enough force authority to fully null the input rate above this limit, and the forcer signal along the sense axis (Fy) was saturated, resulting in a faulty loop operation. This constraint resulted in −3 dB loss at 1 Hz, Fig. 3.10.

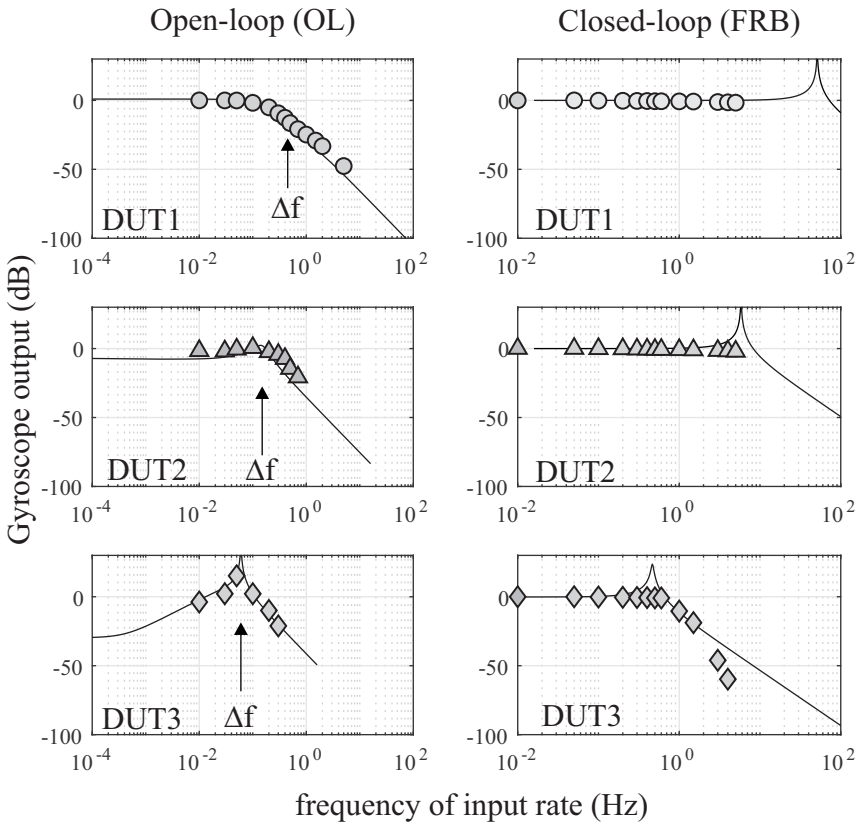

Figure 3.10: Simulation of the gyroscope bandwidth overlaid with experimental measurement points, operating in the open-loop (first column) and closed-loop (second column). Three devices with different Q-factors were used and each row represents one device.

3.4 Noise Analysis

The breakdown of all noise processes in the ZRO output of a gyroscope can be described by:

$$\sigma_T^2(\tau) = \sigma_{ARW}^2(\tau) + \sigma_B^2(\tau) + \sigma_{QN}^2(\tau) + \sigma_{RRW}^2(\tau) + \dots, \tag{3.8}$$

where ARW, B, QN and RRW represent the Angle Random Walk, Bias Instability, Quantization Noise, and Rate Random Walk, respectively, and the corresponding Allan variance σ^2 at any given τ averaging time. To extract these noise parameters individually, two statistical methods were used and compared, one in the time domain and another in the frequency domain. We analyzed the amplitude fluctuations and signal power over frequency of the rate output. Furthermore, the frequency stability was also analyzed to identify the noise sources. These methods are discussed next.

3.4.1 Allan Deviation (ADEV)

To characterize the short-term stability of the gyroscope, a two-sample deviation was measured over different time intervals. When the device was operated in the rate mode, the higher the Q-factor of the sense mode and the lower the frequency split between the drive- and the sense-modes, the lower ARW and a higher signal-to-noise ratio of the gyro response. In a still condition (no input rotation was applied), data was recorded for 16 hrs with the sampling rate of 10 Hz in the form of in-phase and in-quadrature data samples. The recording length was enough to provide an estimated ARW with 0.2 % error from the ADEV plot, bias, and RRW. The data collection for the ZRO experiment was conducted in a lab environment without any thermal compensation. Frequency mismatch of <450 mHz was achieved under electrostatic tuning for the three DUTs, summarized in Table 3.3. The initial gyroscope

bias (offset) across all DUTs were also extracted. In the open-loop mechanization, only PLL and AGC were activated. The bias instability of 0.09 °/hr and the ARW of 0.015 °/$\sqrt{\text{hr}}$ were measured for the high Q-factor device (DUT3), Fig. 3.11-line(c). As expected, the scale-factor of the sensor improved as the Q-factor increased. For the high-Q device, the noise characterization of the FRB mode of detection showed an improvement in the bias by a ratio of 0.69 and an improvement in the ARW by a ratio of 0.54. Compared to the open-loop result, in the FRB configuration it is likely the effect of frequency imperfection in the ZRO condition was eliminated [137], or despite the initial frequency mismatch condition of 60 mHz, in the FRB configuration an over-run operation might unintentionally tuned the frequency mismatch slightly as a result of the forcer being applied along the sense axis. All together, this likely led to a lower ARW. Therefore, the need for continuous tracking of frequency mismatch was identified as crucial in the open-loop and closed-loop operations.

3.4.2 Power Spectral Density (PSD)

To verify the accuracy of statistical modeling derived from the time averaging Allan Variance method, the same data was processed using the logarithmic frequency averaging, also known as Power Spectral Density (PSD). The numerical processing procedure of the rate PSD can be found in [138]. This analysis essentially provides a single-sided PSD profile by averaging adjacent frequency bins. In the PSD plot, the bias instability is associated with 1/f noise and occurs at a slope of -1. The angle random walk is characterized by white noise of the rate output. It is where the flat part of the characteristic occurs, that is a frequency interdependent part of the plot (slope 0). Fig. 3.12 shows the log-log plot of the PSD analysis of the QMG datasets, labeled as before. The fitted dashed lines represent the slope of -1 and 0. The PSD reproduced the estimated noise parameters of ARW, summarized in Table 3.3.

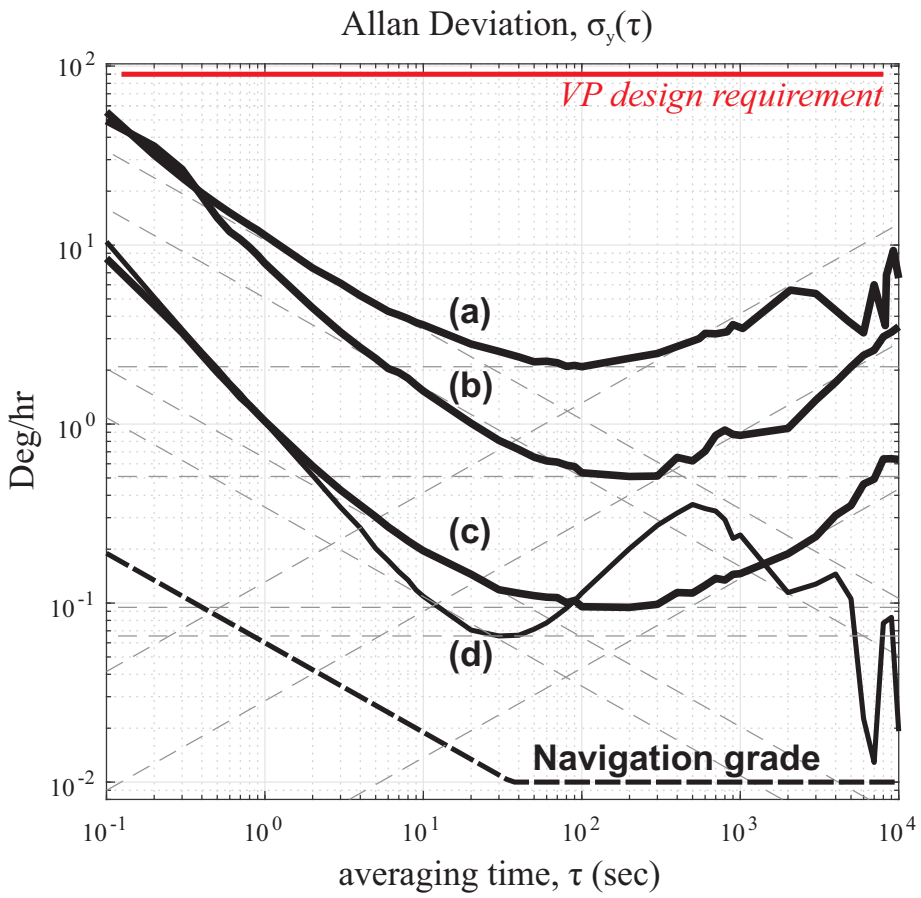

Figure 3.11: Noise performance of QMG with different Q-factor conditions with curve fit lines estimating ARW (slope −1/2), bias instability (slope 0) and RRW (slope +1/2) for QMG in the open-loop operation for a) Q=1k, b) Q=25k, c) Q=2M, and d) in the closed-loop (FRB) operation mode, Q=2M.

In the PSD analysis, the ARW component white noise is typically dominated and can be estimated well with a fit line (slope 0), whereas in the ADEV analysis the bias is dominated and estimated well with a line fitting (slope 0). In PSD, the estimation accuracy was reduced in the plot for low-frequency bins. In contrast, in ADEV, the uncertainty increased for long averaging time intervals.

Fig. 3.12 shows this analysis and for a high Q-factor device it revealed the ARW of $0.008\,^\circ/\sqrt{\text{hr}}$ and the bias of $0.0459\,^\circ/\text{hr}$. However, using the time domain integration on the same dataset, the bias instability was estimated to be $0.0946\,^\circ/\text{hr}$, the ARW to be $0.0107\,^\circ/\sqrt{\text{hr}}$, and the RRW to be $0.0043\,^\circ/\text{hr}/\sqrt{\text{hr}}$.

Both described methods are offline and require post-processing of the stored data. To demonstrate the effectiveness of both methods, the high Q-factor data was segmented into durations of 0−10min, 0−20min, 0−30min, etc, all the way to 0−16hrs, and then the ADEV and the PSD analysis were repeated. Both methods showed that the confidence of the estimated stability parameters improved as more data points were fed to the analysis. The high Q-factor data shows that the optimal size for bias estimation would reach 10 % of its final value in 10 hrs for the ADEV method (Table 3.3), and from the PSD method in 7 hrs. Similarly, for the ARW estimation, 10 % of its final value was reached in 3.5 hrs using the ADEV method, and in 5 hrs using the PSD method.

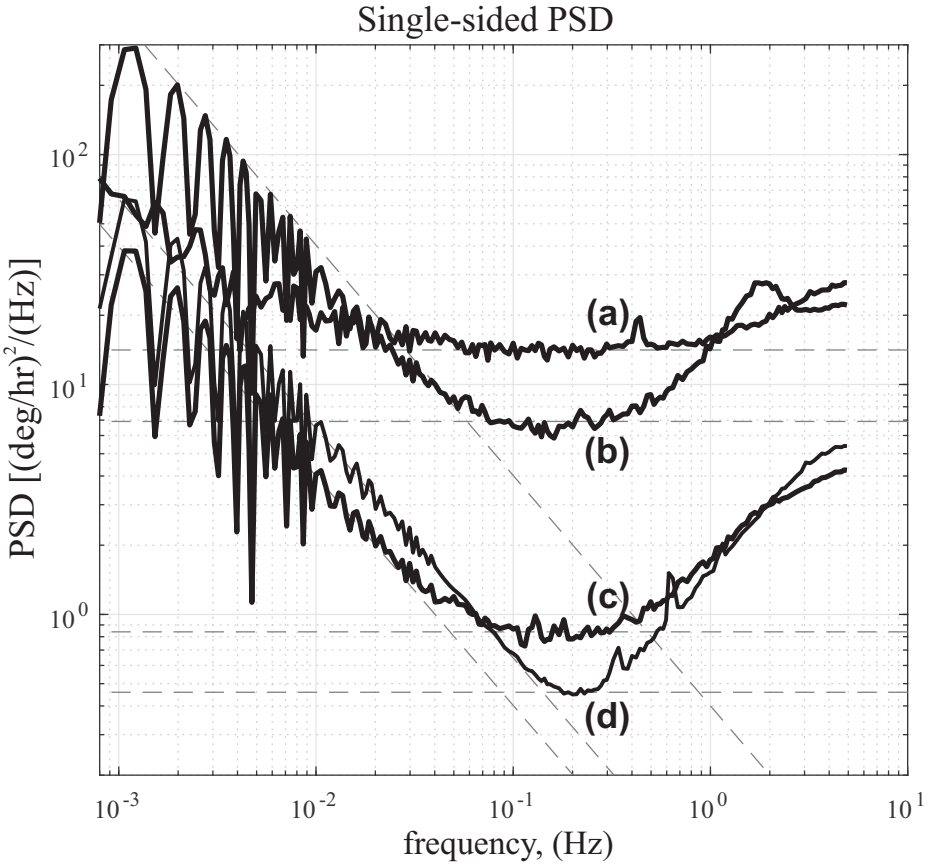

Figure 3.12: Rate PSD of static QMG data with curve fit lines estimating ARW (slope 0) and bias (slope −1). Lines (a-d) represent the same dataset and labelled in the time-domain analysis of Fig. 3.11. Data sample rate is 10 Hz.

Table 3.3: QMG summary of performance

	line	(a)	(b)	(c)	(d)
Device parameters	ID	DUT1	DUT2	DUT3	DUT3
	mode	OL	OL	OL	FRB
	Q	1k	25k	2M	2M
	Δf (tune) [Hz]	450m	250m	60m	60m
	SF $[V/(^\circ/s)]$	85.7µ	790µ	2.2m	2.6m
	offset $[^\circ/hr]$	3.0542	1.0873	1.9497	-
ARW $[^\circ/\sqrt{hr}]$	ADEV	0.1770	0.0843	0.0107	0.0058
	PSD	0.1177	0.0576	0.0080	0.0038
Bias $[^\circ/hr]$	ADEV	2.0907	0.5096	0.0946	0.0655
	PSD	-	0.3938	0.0459	0.0647
RRW $[^\circ/hr/\sqrt{hr}]$	ADEV	0.1256	0.0300	0.0043	0.0043

Abbreviations: Q-factor (Q), Frequency split (Δf), Scale-factor (SF)

Angle Random Walk (ARW), Rate Random Walk (RRW)

3.4.3 Frequency Stability

The stability of the drive mode oscillation at the resonance is a critical parameter as it directly related to the scale factor of the device. Frequency and phase are related to each other by 2π, meaning that any instantaneous frequency changes (δf) in the drive mode are wrapped by 2π to maintain the phase changes ($\delta\Phi$). For an oscillator, the instability can be approximated by $\delta f/f \approx -\delta\Phi/2Q$, where δf is a fluctuation in the drive oscillator frequency and $\delta\Phi$ represents changes in the phase [139]. Stability of the oscillator frequency

is proportional to the Q-factor. The variation in oscillations along the drive axis was analyzed experimentally. The fluctuation in frequency or phase resulted in a phase error in the drive mode of oscillation, therefore a high Q-factor is desirable to minimize this error.

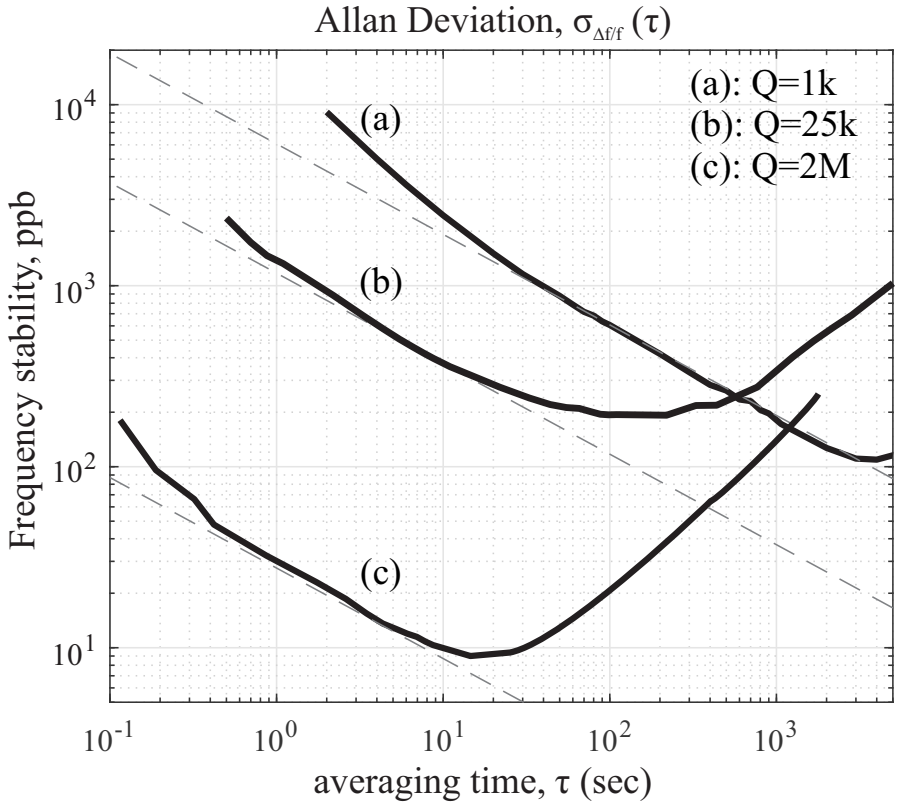

Figure 3.13: Characterization of the drive mode resonance frequency instabilities for three different Q-factors. The frequency white noise improved as the Q-factor increased.

In a simplified analysis, the CVG can be viewed as a two-dimensional oscillator, where in the rate mode of operation, the output of the device is estimated from demodulation of the sense axis with respect to the frequency of the drive mode, as defined by the PLL. In the PLL, the phase is locked to the resonance center frequency in order to provide a reference frequency signal. Therefore, variations within this frequency or phase can directly translate to the phase error. As a result of the phase error, the quadrature signal leaks into the rate signal and induces a drift in the ZRO of the sensor. The Allan deviation analysis on frequency stability ($\delta f/f$) provides an estimate of the frequency noise processes. For inertial sensors, the frequency error is typically dominated by the white noise frequency [140]. The average

integration of the white noise over time contributes to the RRW of the ZRO output (slope +1/2).

Fig. 3.13 shows the frequency stability analysis of the QMG devices with different Q-factors under the same room temperature environment, where the rate table operates in an enclosed thermal chamber. The frequency white noise was estimated to be 27.5, 1352.6 and $6072.5\,\mathrm{ppb}/\sqrt{\mathrm{Hz}}$, which is in a strong agreement with the experimentally obtained RRW in Table 3.3. As expected, higher frequency stability was observed for devices with high Q-factors. Thus, supporting the prediction that maximizing the Q-factor helps to reduce environmentally induced noises in RRW (long-term drift), including temperature and other long-term variations in the drive oscillator.

3.5 Conclusion

We presented the performance analysis of CVG devices designed to operate in the rate mode, which exceeds what is required for vestibular prosthesis ($1.6\,^\circ/\sqrt{\text{hr}}$ ARW, Chapter 1-Fig. 1.3). This chapter discussed the corresponding control challenges involved. A highly symmetric device demonstrating the Q-factor of above 2 million was compared to 1,000 and 25,000 Q-factor devices of the same design. The frequency split of all devices were electrostatically controlled to different levels. We demonstrated a possibility of achieving with MEMS devices $0.09\,^\circ$/hr bias instability and a $0.01\,^\circ/\sqrt{\text{hr}}$ ARW in the rate mode of operation in lab conditions (temperature fluctuations from 23.4 °C to 25.6 °C), with no thermal compensations on the device level.

We described the structure of the CVG control algorithm and highlighted the hardware requirements for implementation. The criteria to achieve the stable control loop conditions were examined on CVGs with different Q-factors. The dependence of the scale-factor nonlinearity on control loops was investigated in different combinations (PLL only, PLL+AGC, PLL+AGC+QCL, and FRB), which resulted in a linear full-scale dynamic range in the FRB mode. The tradeoff between bandwidth and sensitivity was shown experimentally on a CVG with different Q-factors operating in the open-loop rate mode. We verified and demonstrated that the frequency mismatch defines the operational bandwidth of the CVG in the open-loop mode, where the highest sensitivity is demonstrated for a lower Δf of mode mismatches. When the device was operated in the FRB mode, we observed deviations from linearity in the bandwidth analysis for devices with different Q-factors. We demonstrated that a higher Q-factor resulted in higher frequency stability, thus in lower rate random walk. These outcomes were predicted by our analytic analysis and supported experimentally.

We showed that a higher Q-factor and a lower frequency split can lead to the noise performance improvement by >100 fold in ARW, bias, and RRW. We derived the noise char-

acteristic parameters, using both time domain and frequency domain analyses. Performing analyses on the same dataset showed that the ADEV method leads to representation of data with significantly lower noise characteristics compared to the PSD method, and should be considered as a lower bound on the noise performance. Regardless of the Q-factor, uncertainty in the noise parameters were lower on the flat portion (slopes 0, Fig. 3.11 and Fig. 3.12), that corresponded to bias instability in ADEV and ARW in PSD.

We demonstrated that it is possible to design MEMS devices operating in rate mode of operation, by using different control modalities to satisfy requirements of the vestibular prosthesis; however the issues of drift influences and calibration remain and these will be discussed in the next chapter.

Chapter 4

Long-Term Drift and Calibration Method

In previous chapter, we discussed the sensitivity analysis on a MEMS gyroscope in rate mode of operation to be used for vestibular prosthesis, here we look for possible calibration methods. Implementation of a vibratory gyroscope in the Whole-Angle (WA) mode of operation for measurement of the absolute angle of rotation is presented. This approach enables identification of sensor parameters where it will be used for long-term calibration. The mechanical structure utilized is a micro-machined QMG with the Q-factor higher than 2 million. The WA mechanization is implemented to measure the angle of input rotation from induced by inertial forces precession of the vibration pattern about its axis of symmetry.

The intrinsic high damping symmetry of the device ($\Delta(1/\tau)$=0.1 mHz) enables the investigation of the isolated effect of anisoelasticity on the angle drift. The dependencies of control loop parameters and structural asymmetries to the precession angle variation were studied and subsequently utilized in the development of the calibration algorithms. The Virtual Carouseling (VC) algorithm was implemented on a QMG device to demonstrate the in-situ

calibration capabilities of the mechanization. The variations in frequency mismatch associated with the temperature drift were made observable through VC and compensated in the angular gain estimation. We concluded that an uncompensated frequency mismatch resulted in larger quadrature errors at lower input rates and also in errors of the angular gain estimation.

4.1 Introduction

Utilizing a mechanical integrator of absolute rotation could allow eliminating the numerical integration error of the dead reckoning computation [81]. This is possible if Coriolis Vibratory Gyroscopes (CVGs) are configured as direct angle measurement devices, estimating directly the orientation of an object. This mechanization is known as Whole-Angle mode (WA) of operation and the angle of rotation is measured with respect to an inertial coordinate frame. These measurements are based on detection of the traveling wave due to the Coriolis coupling. This mode of operation has theoretically an unlimited dynamic range and bandwidth of the mechanical response. The WA mechanization has been recently demonstrated in MEMS CVGs, for example, Disc Resonator Gyroscope (DRG) and Toroidal Ring Gyroscopes (TRG), [141, 142]. Also, the phenomenon was demonstrated in lumped mass-spring type devices, such as QMG [93] and Dual Foucault Pendulum (DFP) [143]. In the lumped mass-spring design, two identical and orthogonal resonators were mechanically coupled to exchange vibrational energy in response to an input rotation due to the Coriolis force. The vibration pattern orientation was calculated from the amplitude and phase of each resonator to estimate the precession angle; where the orientation of the axis of the precessing pattern provides a direct measure of the rotation angle with respect to the inertial coordinate frame [144].

Fig. 4.1 illustrates conceptually free oscillation of the mass on an isotropic suspension in

the rotating coordinate frame, illustrating an ideal CVG with zero damping. Due to the Coriolis acceleration, the energy is alternating between primary and secondary modes of the gyroscope, then, as shown in the plot the X-Y view of the oscillation captures directly the input angle of rotation along the Z-axis.

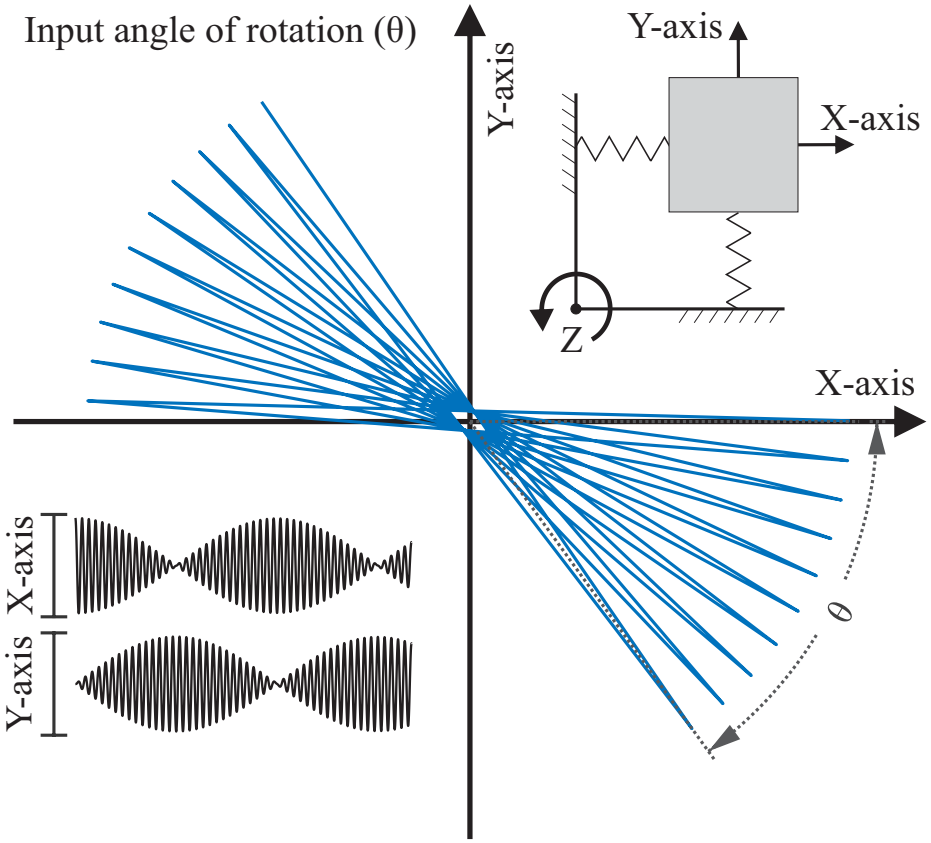

Figure 4.1: Response of a CVG operating in the whole-angle mode. Overlay plot of oscillations along the X- and Y-axes reveals changes in both amplitudes and is directly proportional to the angle of applied rotation along the Z-axis.

We demonstrated the whole-angle operation on a silicon MEMS gyroscope with the Q-factor higher than 2 million, both based on free vibrations and closed-loop energy control [145]. The decay time constant of 300 s allowed for a prolonged free precession of the vibration pattern without any feedback control loop, thus eliminating any interference between the gyroscope output and control signals and allowing to focus on the effect of fabrication imperfections. In free vibrations, the gyro angle output was collected for much longer than the time constant of 300 s (4–5 times) under free vibration, on the order of 6minutes. We also operated the

device for 10,000 s using the closed-loop energy control, but this duration is only limited by relevancy of information for any specific application. In the case of closed-loop controlled device, the control signals were applied to the excitation electrodes of the two orthogonal modes to maintain the amplitude and quadrature errors.

The angular gain is a coefficient translating the precession pattern of the sensing element to the angle of measured rotation of the object, and therefore is a key parameter in characterization of performance of WA gyros [146]. The geometric angular gain of the standing wave was shown to be extremely stable [147]. In an ideal gyroscope operating in the WA mode, with damping and stiffness isotropy, the angular gain of the precession is a function of the geometry of resonant masses. Fabrication imperfections break the symmetry of the gyro, thus making it susceptible to environmental disturbances, like temperature fluctuations, and stresses of the package. For example, a residual of the frequency mismatch was observed to be sensitive to temperature fluctuations [148]. A Force-to-Rebalance (FRB) closed-loop is often implemented to modulate a virtual rate rotation by carouseling the orientation of the drive axis using the X-Y electrodes of the gyro to observe imperfections, such as frequency, damping, and gain mismatches [126, 128, 143, 149–151].

In this work, the error identification and WA modes of operation were switched for estimation and correction of the angular gain, with interruption of the gyroscope operation. However, the redundant gyro systems can accommodate for continues operations and sequential calibration. In our study, the extracted Δf value was used in a feed-forward manner to correct for the angular gain drift. The variation in the angular gain was related to the residual frequency mismatch and anisodamping of the device. We presented the temperature dependency of the effective angular gain and proposed a correction approach based on frequency mismatch, all of the cases when the gyroscope was operating in the Whole-Angle (WA) mode.

In Chapter 2 section 2.3.2, we presented a discussion on operating principles and governing

equations of the whole-angle configuration, as well as a demonstration of the precession of rotation as predicted by the theory. The orbital parameters derived earlier in Chapter 2 Eq. (2.2) are illustrated in Fig. 4.2. In section 4.4, we present an implementation of the whole-angle operation in the open-loop and closed-loop modes. Section 4.5 discusses the implementation of virtual carouseling and how it was used for identification of error parameters. Section 4.6 presents the numerical dependency of the angular output as a function of input rotation. All theoretical results discussed in this work were verified experimentally.

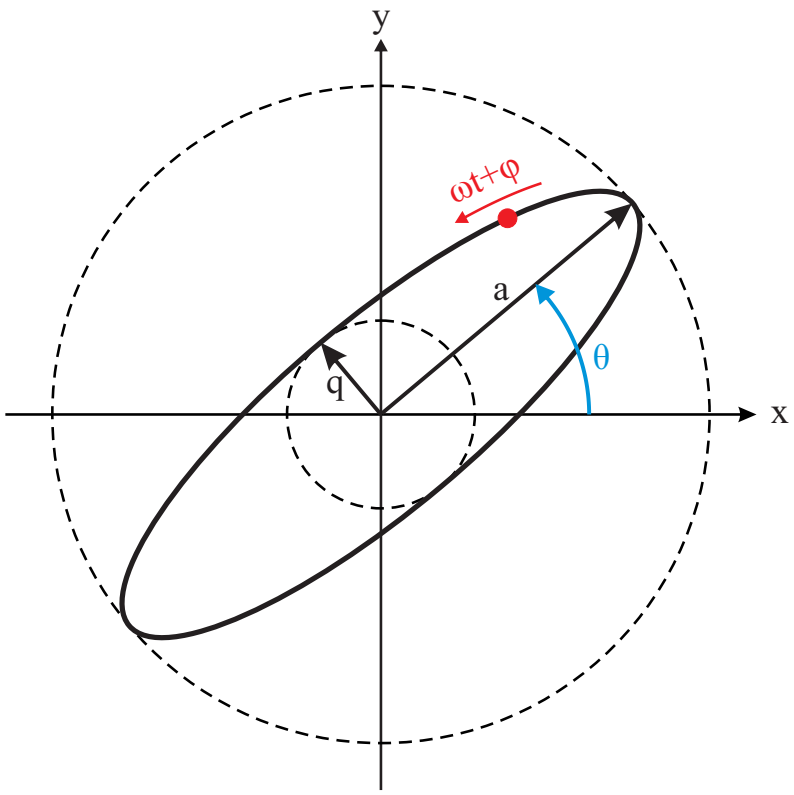

Figure 4.2: Orbital parameters of the proof-mass trajectory in XY-plane of a gyroscope. θ indicates the instantaneous orientation of the vibration pattern which librates with respect to to the input rotation. The point (ωt+ϕ) is at instantaneous frequency and instantaneous phase of the oscillation.

4.2 Precession of Vibration Pattern in Whole-Angle MEMS Gyro

The phenomena of precession of the vibration pattern was illustrated on a high-Q Quadruple Mass Gyroscope (QMG) sensor operating in the WA mode in free vibrations. The device was with as-fabricated frequency mismatch of 15 Hz, with a capability of electrostatic frequency tuning, was used to demonstrate the precession of vibration. In this experimental demonstration of principle, the sensor was mounted on a rate table and was driven into its resonance along the X-axis at a fixed amplitude. After the resonance condition was established along the drive axis, the forcer signal was turned off and an input rotation was applied using the rate table. The long energy decay time of the sensor enabled the WA operation while the device was in free vibration for more than 300 s, without applying forcer signals to maintain the oscillation. The pickoff signals in the XY-plane formed an ellipsoidal shape [152], based on the model discussed earlier. Trajectories of the vibration pattern in the XY-plane oscillation were recorded in real-time from applying a rotation to the sensing element, by physical rotation provided by the rate table. Fig. 4.3 is a plotted view of the QMG inertial frame for two different cases of initial tuning frequency mismatches, Δf of around 0.12 Hz(case(a)) and 0.06 Hz(case(b)). This experiment illustrates the principle of operation in the whole-angle mode and highlights several critical considerations in this mode of operation. For example, asymmetry causes a larger ellipticity of the trajectory, attributed to quadrature errors in gyroscopes. From that data, the area of the quadrature ellipsoid suggested that the quadrature was significantly smaller after frequency tuning from 0.12 Hz to 0.06 Hz, for example theoretically discussed in [153].

The pendulum variables, including energy (E), quadrature (Q), phase (L), and angle of precession (θ), were estimated by demodulating the pickoff signals at the phase of the oscillation with notations according to the model in [154]. The demodulation process for sensing the

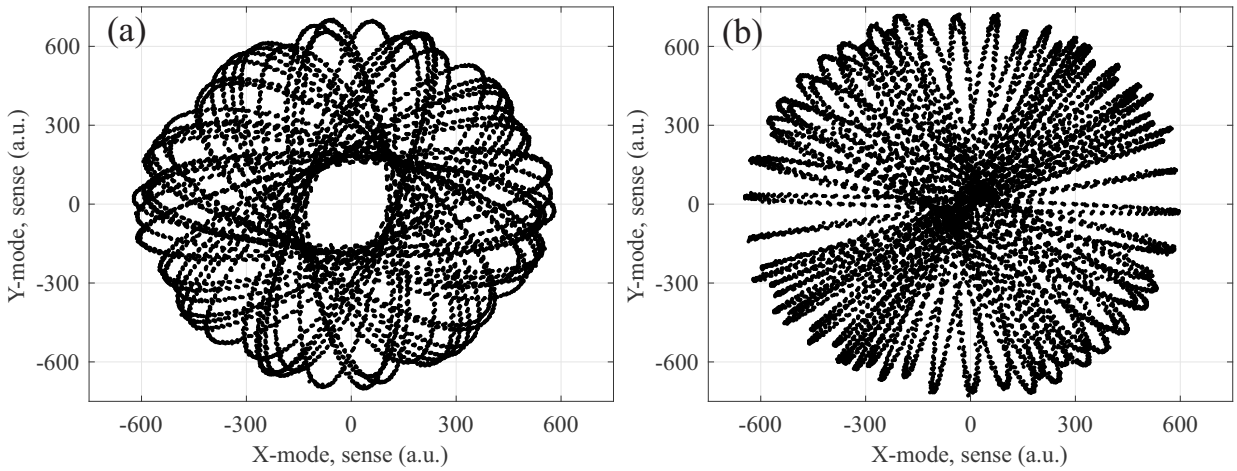

Figure 4.3: Trajectories of proof-mass oscillation in the XY-plane demonstrating the precession phenomena. The vibration pattern freely precesses, exchanging the energy between orthogonal modes due to the Coriolis coupling. Precession of the pattern angle at 100 °/s rotation with the frequency mismatch of (a) 120 mHz and (b) 60 mHz, showing the effect of non-idealities on precession and ellipticity.

response requires a reference signal, phase-locked to the phase of the elliptical orbit. The slow varying components c_x, c_y, s_x, s_y are the demodulated components of x and y pickoff signals, in-phase and in-quadrature with the reference pendulum phase (see Fig. 4.4), and they can be represented by:

$$\begin{aligned} c_x &= +a\ cos\theta,\ s_x = -q\ sin\theta \\ c_y &= +a\ sin\theta,\ s_y = +q\ cos\theta \end{aligned} \tag{4.1}$$

The projected components of the vibration pattern orientation are calculated from the amplitude and phase of each resonator [93, 143]. The components of demodulated pickoff signals make the pendulum variables observable. The amplitude of semi-major axis of elliptical orbit, a, the amplitude of semi-minor axis of elliptical orbit, q, the phase of PLL, ϕ, and the instantaneous angle of precession, $\theta(t)$, were estimated using the invariant quantities, E, Q, S, R, and L:

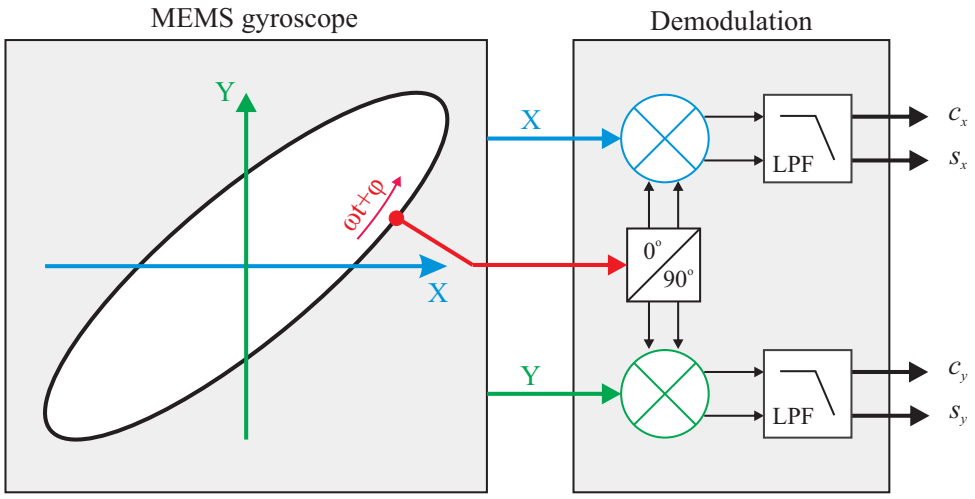

Figure 4.4: Demodulation process of pickoff signals at the reference phase of the pendulum oscillation to extract c_x, c_y, s_x, and s_y.

$$
\begin{aligned}
E &= {c_x}^2 + {s_x}^2 + {s_y}^2 + {c_y}^2 = a^2 + q^2\,, \\
Q &= 2 \times (c_x s_y - c_y s_x) = 2aq\,, \\
S &= 2 \times (c_x c_y + s_x s_y) = (a^2 - q^2)\ cos(2\theta)\,, \\
R &= {c_x}^2 + {s_x}^2 - {c_y}^2 - {s_y}^2 = (a^2 - q^2)\ sin(2\theta)\,, \\
L &= L_c + i(L_s) = (a^2 - q^2)e^{2i\delta\phi}\,, \\
L_c &= {c_x}^2 - {s_x}^2 + {c_y}^2 - {s_y}^2\,, \\
L_s &= 2 \times (c_x s_x - c_y s_y).
\end{aligned}
\tag{4.2}
$$

The amplitude of the invariant quantities that are observed, maintained, or nulled by the PID controller, depending on the configuration. The invariant quantity, L, was calculated in real-time and used to track the phase of oscillation for the demodulation process. The instantaneous value of the precession angle was calculated from S and R:

$$\theta(t) = \frac{1}{2} \arctan \frac{S}{R} \tag{4.3}$$

4.3 Noise Integration of Angular Rate Output

In most Coriolis Vibratory Gyroscope (CVG) systems, the orientation angles are obtained by integrating the angular rate, thus suffering from the error accumulation due to electronic or numerical integration of the signals along with the noise [90]. This error is represented by the Angle Random Walk (ARW) characteristic of the gyroscope. To further support the discussion of the ARW performance of the QMG device, a visual representation of integration errors over time is shown in Fig. 4.5. The noise performance of the device was characterized with ARW and bias instability equal to $0.01\,^\circ/\sqrt{\text{hr}}$ at 1 s and $0.01\,^\circ/\text{hr}$ at 100 s averaging time, respectively. Thirty randomly selected datasets, each recorded separately and 200 s long, were analyzed and the rate output signals were integrated. For the demonstration purpose, as shown in the plot, the numerical integration of the angular velocity is non-zero over time, which resulted in an error in the angular position. The variance of the short-term horizontal error drift is represented by ARW, a statistical distribution parameter extracted from Allan Deviation of the angular rate.

4.4 Whole-Angle Implementation

The WA mechanism can track directly the angle in both Open-Loop (WA-OL) and Closed-Loop (WA-CL) configurations. Typically, a device with a high Q-factor is chosen for the WA operation for better performance. So far, except for mHRG type devices [150, 155], WA-CL has been implemented on MEMS CVGs with short amplitude decay time constant, [152].

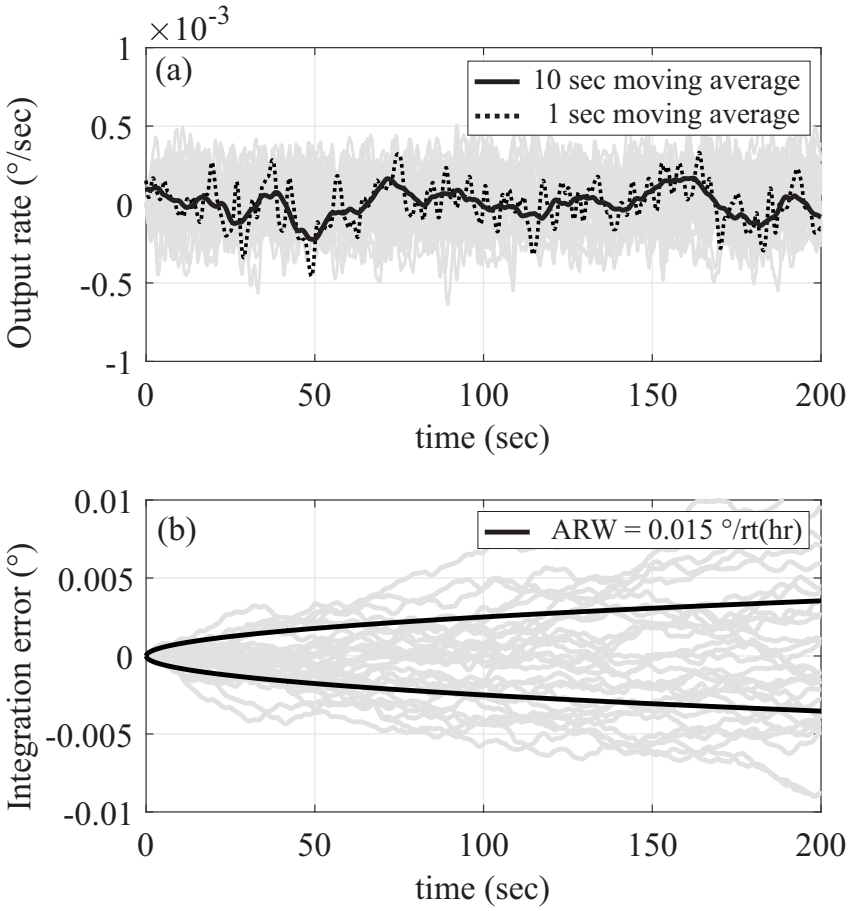

Figure 4.5: Representation of time-varying gyroscope rate output. a) randomly selected dataset with the removal of the initial offset (gray color), two solid black lines represent examples of 1 and 10 s moving average on one dataset, b) The corresponding integrated angle using rate dataset to calculate the angle, resulted in unwanted integration errors, the solid black lines represents the ±ARW coefficient of the sensor.

Table 4.1 summarizes the work done in this field, indicating design of devices and their key parameters with the Q-factor arranged in ascending order. All devices were implemented in the whole-angle mode of operation. The units for the reported $\Delta(1/\tau)$ and $\Delta(f)$ are in Hz, and "N/A" stands for those where the values were not reported. Note, that in all cases the Δf in Table 4.1 is the reported number after devices were electrostatically tuned.

An ultra high-Q vacuum sealed Quad Mass Gyroscope (QMG), with high damping symmetry ($\Delta(1/\tau)$ <0.0001 Hz) and energy decay time constant higher than 300 s, was used to demonstrate the WA mode of operation in this work. In the following, we discuss the

Table 4.1: WA implementation on CVG architectures

Device	Q-factor	$\Delta(1/\tau)$	$\Delta(f)$	WA-Algo	ref
Ring	N/A	N/A	0.03	CL	[156]
QMG	1k	0.1	0.15	CL	[128]
CING	21k	0.004	0.001	CL	[157]
DRG	80k	0.36	1	CL	[142]
μBRG	70k	0.03	10	CL	[158]
TRG	100k	0.12	0.05	CL	[159]
QMG	1M	<0.0001	0.02	OL	[93]
QMG	2M	<0.0001	0.06	OL/CL	this work
milli-HRG	15M	<0.0001	0.001	N/A	[150, 155]

effort on implementation of the WA-OL and WA-CL modes of operation and the hardware integration for both modes of operation.

4.4.1 Front-end Electronics

The WA mode of operation was implemented on hardware differently, allowing the real-time frequency tracking for the purpose of correct demodulation. The main difference in implementations is in the approach for frequency tracking of the orbital trajectory. In the work by [158], two commercial PLLs along with off-chip circuits were used to track the frequency of the vibration pattern. However by the use of two PLLs, one will always lose its lock state, either at $\theta = 0$ or at $\theta = 90$ degree, due to a momentary loss of the amplitude in the drive- or sense- modes when one axis is fully excited and the other is nulled. Therefore, the use of two PLLs is not optimal. The work by [93] uses only one commercial PLL for pattern tracking on a high Q-factor device, limited to measurements of the decay time constant, and not allowing for sustaining the energy of the system for continues operation. Besides conventional methods for implementation of PLL with internally set VCO (Voltage-Controlled Oscillator), the reference signal to the PLL implementation in this work was based on [154], shown in Eq. (4.2), where L was used as the reference phase point of the PLL block (see Fig. 4.6). With this model, only one PLL can lock to different frequencies

when switching between modes, without losing its locked condition. For example, the model was implemented in the work by [160], where the gyro code was programmed on a laptop, which controlled a universal software radio peripheral. However, the performance of the WA in this implementation was limited by delay in the communication between the computer and device. In a study by [161], a universal architecture using commercial off-the-shelf electronics was developed in which the forcer feedback uses resonator position and velocity feedback instead and implemented in an audio codec with a PC running Matlab.

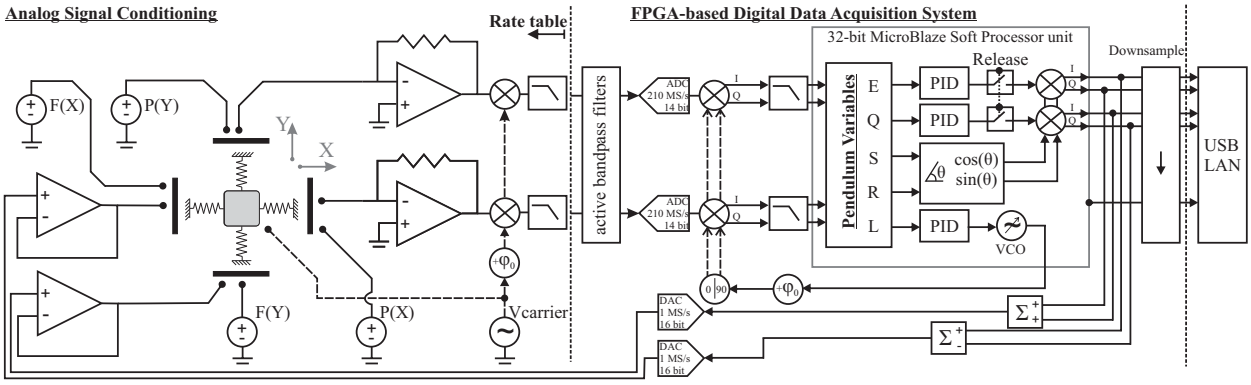

Figure 4.6: Control loops involved in operating WA mode. Block diagram of the system, including analog signal conditioning and digital control loops for estimating the direct angle by demodulating the pendulum variables. The DC electrostatic voltages were applied to x and y axis, where P stands for "pickoff" and F stands for "forcer" electrode pairs.

The entire system architecture used for WA in this study is shown in Fig. 4.6. The sensor was interfaced to the buffer electronics mounted on the high-speed rate table (Ideal Aerosmith 1571), which signals passed through the slip-rings to the FPGA system located outside of the rate table. The rate table was rotated with a constant angular rate of rotations. The buffer electronics comprised of biasing circuits, charge amplifiers (AD8034 Op Amps), forcer buffer amplifiers with low offset voltage (AD8639), modulation of the proof-mass carrier, differential demodulation of the delayed carrier, and with active filters. The parasitic feedthrough path from the drive to sense electrodes was canceled by the carrier demodulation scheme, [99]. This also required the phase compensation at the output of the current-to-voltage amplifier to account for the system phase delay. The carrier amplitude applied to

the proof-mass as voltage was optimized to utilize the full-scale analog electronic reading of the output current-to-voltage transformation after demodulation at the resonance condition, set to be at 1.2 V. In our experiments, the carrier frequency was selected at 100 kHz, which is 50 times greater than the resonator's resonance frequency of the device, which was at 1.6 kHz. No dependency was observed between device characteristics (resonance frequency and amplitude of vibration) and the carrier frequency from 40 kHz to 150 kHz, under the hardware constraints of the current-to-voltage amplifier with the gain of 1 MΩ. Initially, the delayed carrier was verified for optimal phase setting and kept fix for the rest of the characterization. To further remove any unwanted noise from the slip-rings and setup, active lowpass filters (Butterworth with 36 dB/octave slope set at 5 kHz) were presented before input to the FPGA signal acquisition system. For WA operation, to relax the load on the implemented algorithm, the gain mismatch between X-axis and Y-axis was compensated using external hardware. The gain-balance for X-axis and Y-axis was achieved by scaling amplifiers and monitoring input amplitude errors, and making them equal for an equal amplitude command on the X-axis (at 0°) and the Y-axis (90°) by steering the amplifier gains.

An FPGA-based digital data acquisition system processed the input and returned output waveforms. The in-phase and in-quadrature demodulation at the oscillation frequency, followed by low-pass filters at 2 Hz, were all implemented on FPGA. The slow convergence pendulum variables (c_x, c_y, s_x, s_y) were estimated using the demodulated pickoff signals and used to establish the feedback control loops, which were equivalent to the estimation of precession parameters under the release condition of free vibration. These control loops, including the estimation of pendulum variables, with three PID controllers (energy, quadrature, and PLL) and an in-phase and an in-quadrature coordinate transformation, were implemented on a Xilinx MicroBlaze 32-bit processor. The processor was used for engaging and disengaging the loops, selecting control gains, adjusting controller set points, and real-time angle measurement. In this study, the complete architecture was run with a set sampling

frequency of 998 Hz, which is more than three times higher than the Nyquist sampling rate selected relative to the input rate of rotation. These parameters were then down-sampled at 224 Hz for data recording and real-time visualization on a computer. The gyroscope readout signals were digitized by 14-bit ADCs at 210 MS/s with an input range of 0 to 1.5 V returns the output waveform through 2-channel 16-bit DACs at 1 MS/s. The selection procedure of the PID parameters for E, Q, and phase loops for the high Q-factor device under the test were similar to that described in the rate mode operation of the same device [162].

The as-fabricated frequency mismatch of 15 Hz was tuned electrostatically to 0.12 Hz, using 16.6 V DC bias on differential parallel electrodes. A constant DC bias was applied to the drive forcer electrodes (F(X)=F(Y)=6.1 V), the pickoff electrodes were used for DC electrostatic tuning (P(X)=2.05 V, P(Y)=16.85 V).

4.4.2 Whole-Angle Open-Loop Operation

For operating the gyroscope in the Whole-Angle Open-Loop (WA-OL) configuration, a long ringdown time constant (τ) for the X-axis and Y-axis resonators is preferred over lower frequency mismatch, as the duration of experiment would be limited by the decay time constant duration and not by frequency mismatch. Low energy dissipation rate enables instrumentation of QMG in the WA mode without the energy control feedback loop, eliminating any interference with the gyroscope's output [163]. The damping symmetry of $\Delta(1/\tau)<0.0001$ Hz translates to a theoretical angle error of less than 5° making the device suitable for the WA operation in free vibrations.

To avoid the overlapping patterns of precession, a few milli-second of the X- and Y-axes pickoff signals of the device rotated at the 100 °/s angular velocity of rotation is plotted in Fig. 4.3a. This plot illustrates the precession of the vibration pattern in the XY-plane of oscillation. The long energy decay time of the sensor of 300 s enabled the WA operation

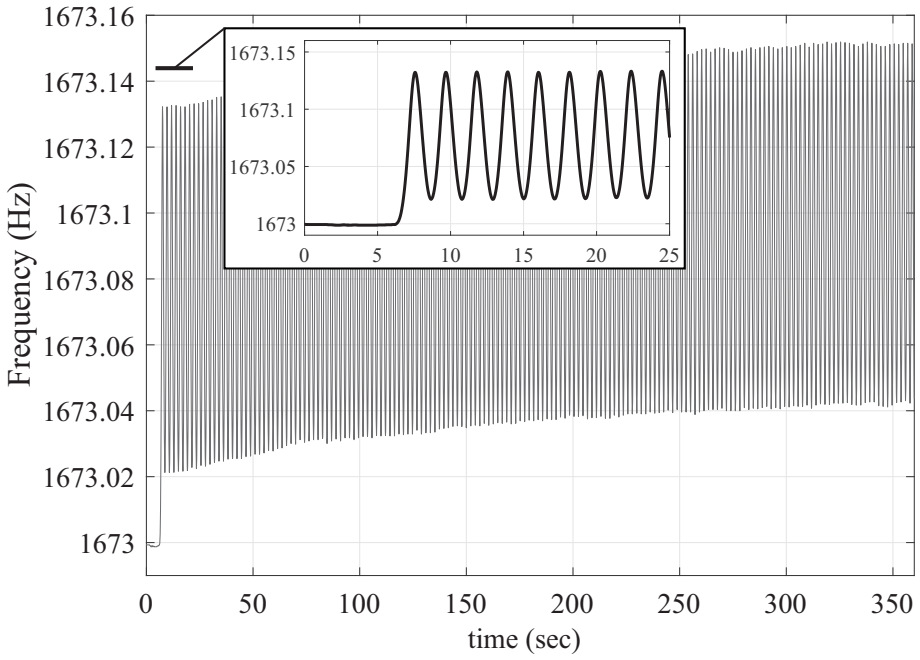

Figure 4.7: PLL output frequency in the WA mode operation during precession of vibration pattern, representing the switching modal frequencies between X- and Y-axes by tracking the phase of the elliptical orbit.

in free vibration without applying any forcer signals to maintain the oscillation for over 30 minutes. The pickoff signals were demodulated at the frequency of oscillation at the instantaneous pattern angle. The slow varying components (c_x, c_y, s_x, s_y) were used to calculate the pendulum variables: energy (E), quadrature (Q), phase (L), and angle of precession (θ). Fig. 4.7 shows how the PLL tracks the frequency of oscillation during precession of the vibration pattern (carouseling), demonstrating the exchange of energy between orthogonal modes, corresponding to $\sim$0.11 Hz frequency mismatch.

The energy (E) and quadrature (Q) were calculated from Eq. (4.2) and normalized to initial energy of oscillation (E_0), Fig. 4.8. The decay in the energy of the system corresponds to the decay of vibration amplitude, as the energy control loop was not engaged. The inset plot demonstrates the energy and quadrature decay for a few cycles, showing the dependency of E and Q on the pattern angle. Finally, the invariant quantities of S and R were calculated.

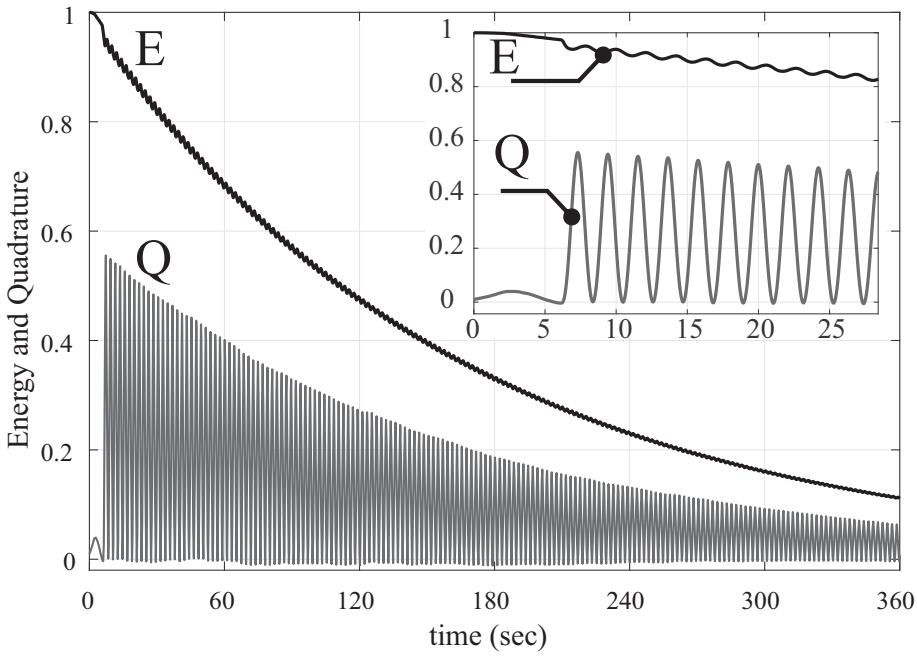

Figure 4.8: Energy (E) and quadrature (Q) extraction from components of the demodulated signals, normalized with respect to the initial energy E_0. The decay in energy corresponds to the decay in the amplitude of vibration.

Fig. 4.9 shows the experimentally measured S and R components after demodulation of the QMG sensor when operated in the WA-OL during an applied input rate of 180 °/s rotation. The S and R components were used for direct angle computation.

The angle output of the sensor operating in free vibration was captured for more than 4 times of the time constant, 4τ, where by definition τ is a characteristic decay time of the system equal to the time where the amplitude was reduced to 37 % of its initial value. Fig. 4.10 shows residuals of the linear fit to the angle output data after 2,200 s of continuous rotation at 180 °/s. The linear fit reveals an angular gain factor of 0.83. The residual errors increased as the amplitude of vibration decayed and the signal-to-noise ratio (SNR) decreased. During this experiment, the local perturbation after τ was less than 3°, and it grew to 10° after 4τ. For any τ second interval, the SNR ratio decays to 37 % of its previous value, therefore after 4τ the amplitude drops to 1 % of its initial value, still slightly above the noise level to directly measure the angle. Although the SNR is relatively low, it confirms that in the

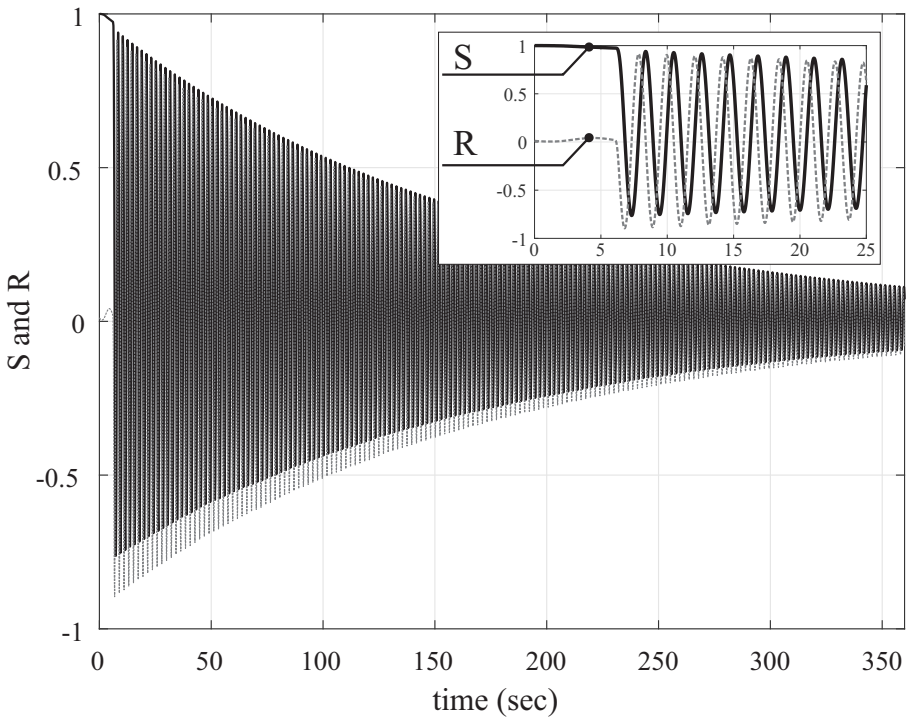

Figure 4.9: Pendulum parameters S and R are proportional to $sin(2\theta)$ and $cos(2\theta)$, and were used to extract the gyro output precession angle, $\theta(t)$.

WA-OL operation with much longer than τ time interval, the angle estimation still resulted in a bounded error.

4.4.3 Whole-Angle Closed-Loop Operation

To improve robustness of the angle output and to reduce the uncertainty of gyro over time, the WA operation was performed in a closed-loop configuration [152]. In the Whole-Angle Closed-Loop (WA-CL) mode of operation, the energy and quadrature control loops were implemented to maintain the oscillation amplitude and to null, or asymptotically minimize, the quadrature error.

In this section, we report the closed-loop experimental analysis on the same device with the same tuned condition, where modal frequency split of the device was closely mode-matched

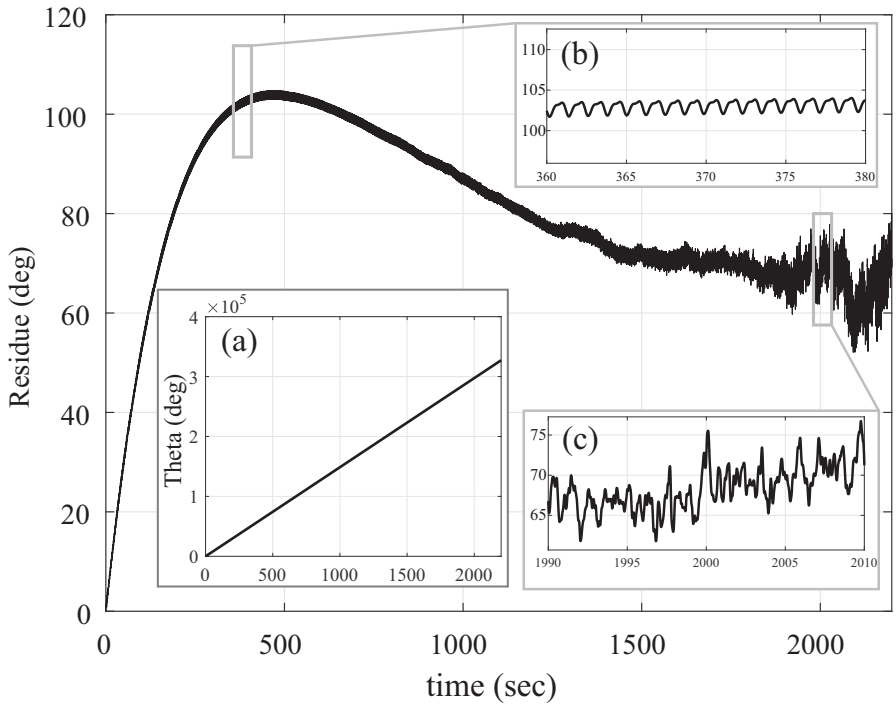

Figure 4.10: 36 minutes of experimental measurements of the gyroscope's precession angle in a free vibration under an input rotation rate of 180 °/s. Inset (a) is the angle output with 0.83 angular gain factor. Inset (b-c) are local perturbations at 1τ and after 4τ.

(<120 mHz). The feedback control signals were applied to the excitation electrodes of the two orthogonal modes, based on the estimated precession angle, to maintain the amplitude and null the quadrature errors.

The sensor was rotated with a constant input rate of +180 °/s and the pendulum variables were estimated using the demodulated pickoff signals and used to establish feedback control loops. The 2θ dependency patterns of command signals were correlated to an uncompensated aniso-elasticity and aniso-damping, as analytically predicted, [92]. The energy and quadrature errors were estimated from the demodulated pickoff signals and plotted in Fig. 4.11. The insets of plot revealed the dependency of energy and quadrature on the precession angle. Fig. 4.12 shows the estimated output angle from the whole-angle gyro. A linear fit to the precession angle data revealed an angular gain factor of 0.84. The RMS error of the fit residuals was calculated and shown in Fig. 4.13, to be 11° over 10,000 seconds of rotation,

with the total accumulated angle of 1.8 million degrees, showing the angular gain variation of less than 7 ppm RMS (with a local perturbation less than 2.5°).

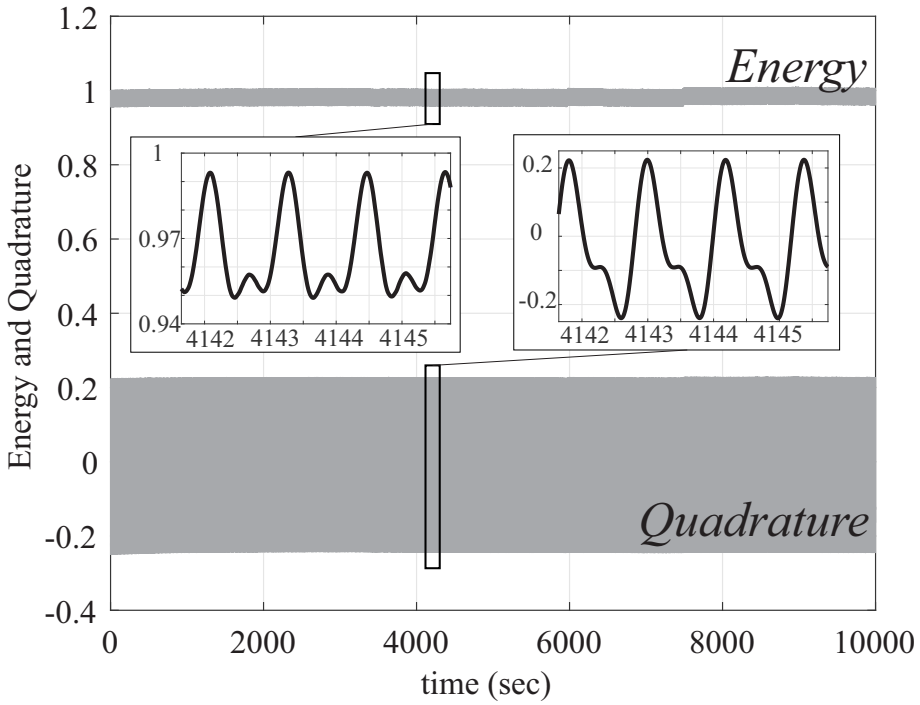

Figure 4.11: Experimental measurement of closed-loop energy loop and quadrature error loop over 10,000 s normalized to the maximum energy.

In summary, for a high Q-factor device the implementation of WA-OL configuration in hardware is simpler to develop than WA-CL, wherein the parameters are being directly observed and the θ is being estimated in real-time without feedback control. In the WA-CL in addition to real-time θ estimation, a proper operation of control loops to provide proportional forcer signals are necessary for continuous operation.

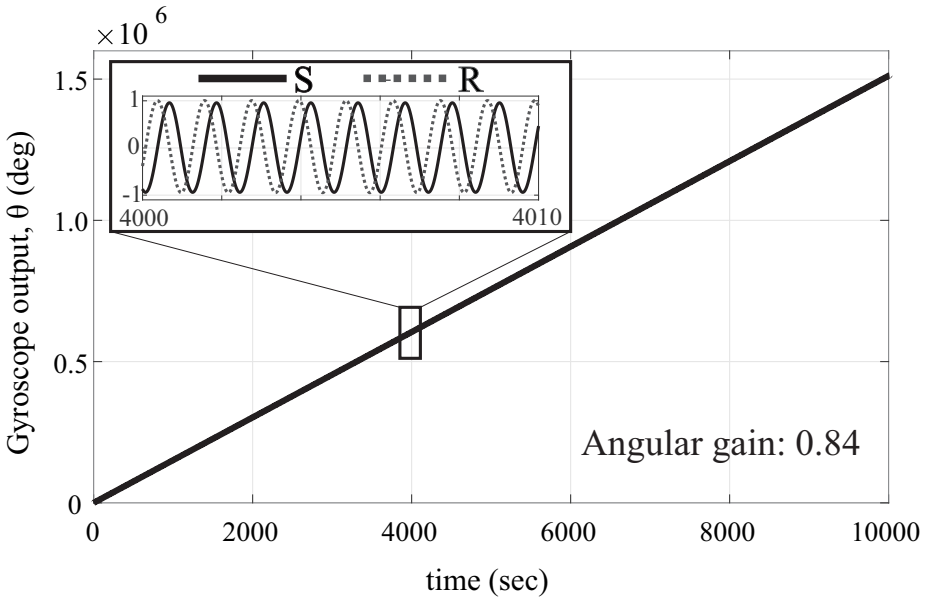

Figure 4.12: Output of the whole-angle gyroscope (angle θ) over 10,000 s of continuous rotation at +180 °/s. The angular gain factor of 0.84 was estimated from the linear fit. The inset plot shows graphically the demodulated components (S and R) involved in derivation of the output angle.

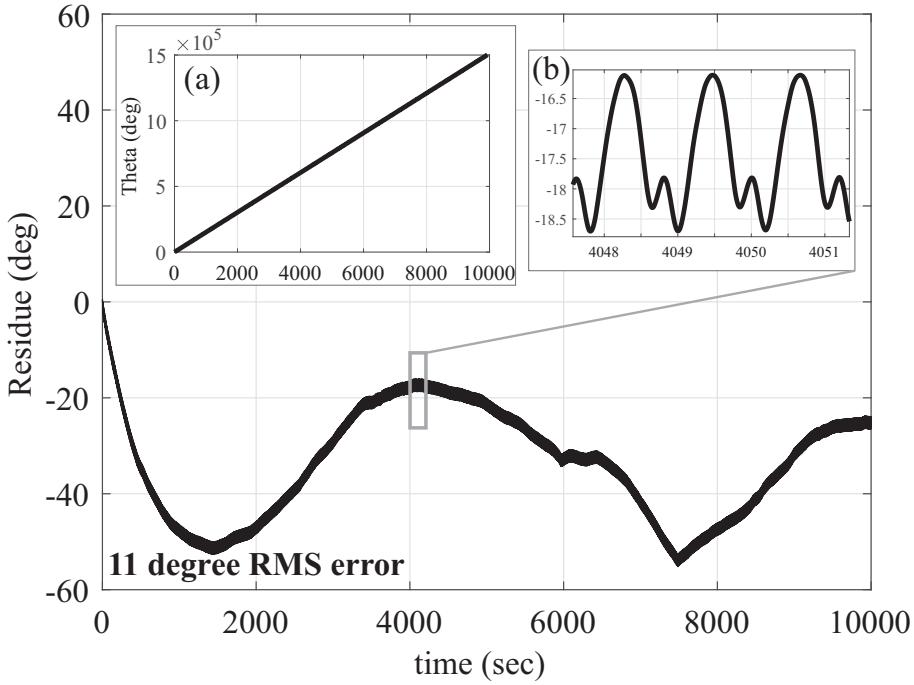

Figure 4.13: A residual fit of over 10,000 s of the output measurement of the angle of rotation, showing 11° RMS error, corresponding to 7 ppm angular gain variation with local perturbation error <2.5°. Inset (a) is a direct angle measurement with 0.84 angular gain. Inset (b) is a 4 s local perturbation.

4.5 Identification of Errors

To identify the device error parameters without physical rotation, we used an electrostatically emulated virtual rotation. The model is similar to that described in WA operation, but with different notations, to emphasize the digital implementation of the control hardware. The effectiveness of the approach was validated by a physical input rotation stimulus provided by a rate table. Virtual Carouseling (VC) allows for self-test and self-identification functionalities without relying on any external physical stimuli to the device. The block diagram of the implemented algorithm is shown in Fig. 4.14, with a full representation of the closed-loop angle estimation and VC controls. Due to Virtual Carouseling, a frequency mismatch, a damping mismatch, and gain errors were made observable. The measured angle of precession θ was estimated from the rate signal output at every incremental precession ($\Delta\theta$), and it was used as the direct output angle of measurement and also as an input to the system to sustain the line of oscillation (an analogy of a standing wave in continues systems). The Angular Gain (AG) was estimated from the precession angle of the gyro subjected to a known continuous external rotation. In the WA mode, the input rotations of θ are controlled by a rate table, whereas in the VC operation the precession is controlled by a forcing function supplied to the device simulating the Coriolis force.

The trajectory of a standing wave pattern at any given angle θ can be described by an in-phase, $I(t)$, and in-quadrature, $Q(t)$, components of the oscillation frequency ω, which is in the rotating frame can be expressed as $I(t) = cos(\omega t + \phi_0)$ and $Q(t) = sin(\omega t + \phi_0)$.

The control command signals, $F_{x(t)}$ and $F_{y(t)}$, required to sustain such a pattern with PID set values of amplitude (a), phase (p), quadrature (q), and rate (r) are expressed in terms of in-phase $(x_i(t), y_i(t))$ and in-quadrature $(x_q(t), y_q(t))$ components, following notations in

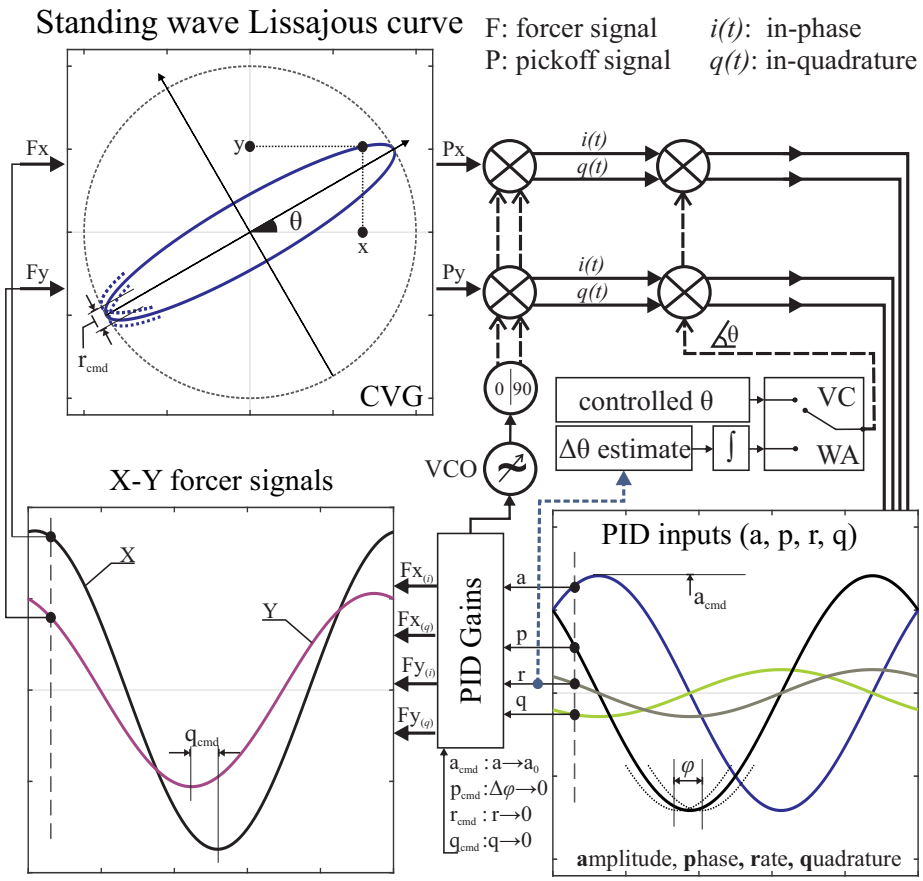

Figure 4.14: Graphical representation of the implemented control loops for the WA mode of operation, or VC control. The input to the PID controllers and forcer signals to the device is shown for one full wave cycle of the oscillation.

[154]:

$$
\begin{aligned}
\mathrm{F}_{x_i(t)} &= a_{cmd} \cdot Q(t) \cdot cos\theta - (q_{cmd} \cdot I(t) + r_{cmd} \cdot Q(t))\ sin\theta, \\
\mathrm{F}_{x_q(t)} &= a_{cmd} \cdot I(t) \cdot cos\theta + (q_{cmd} \cdot Q(t) - r_{cmd} \cdot I(t))\ sin\theta, \\
\mathrm{F}_{y_i(t)} &= a_{cmd} \cdot Q(t) \cdot sin\theta + (q_{cmd} \cdot I(t) + r_{cmd} \cdot Q(t))\ cos\theta, \\
\mathrm{F}_{y_q(t)} &= a_{cmd} \cdot I(t) \cdot sin\theta - (q_{cmd} \cdot Q(t) - r_{cmd} \cdot I(t))\ cos\theta.
\end{aligned}
\tag{4.4}
$$

In the expressions, index *cmd* represents the output command of the PID controller and

indexes x and y denote the X-axis and Y-axis of the device defined by the layout (which are intended by design the principal axes of elasticity of the device). The main loops are Phase-Locked Loop (PLL), amplitude, quadrature, and rate controls. The discrete-time control sequence input at time k for each PID controller with filters can be expressed by U(k) as follow:

$$\begin{aligned}
\mathrm{U}(k)_a &= +x(k)_i \cdot cos\theta + y(k)_i \cdot sin\theta, \\
\mathrm{U}(k)_r &= -x(k)_i \cdot sin\theta + y(k)_i \cdot cos\theta, \\
\mathrm{U}(k)_p &= +x(k)_q \cdot cos\theta + y(k)_q \cdot sin\theta, \\
\mathrm{U}(k)_q &= -x(k)_q \cdot sin\theta + y(k)_q \cdot cos\theta.
\end{aligned} \tag{4.5}$$

After the PID loops are established, the gyro is capable of operating in the Open-loop Rate, Rate FRB, or WA modes. In the WA case, the FRB control in the rate loop is turned off. In all of the operational modes, a Voltage-Controlled Oscillator (VCO) was used to track the oscillation frequency, the quadrature command was used to null the quadrature signal, and the rate command was used to estimate $\Delta\theta$.

The command signals to maintain the amplitude, the quadrature errors, and the resonator frequency are plotted versus the precession angle in Fig. 4.16. The data suggested the dependency of control loop signals on the pattern angle. The variation in frequency and gain mismatches originated from uncompensated structural asymmetry and the gain mismatch of the electronics.

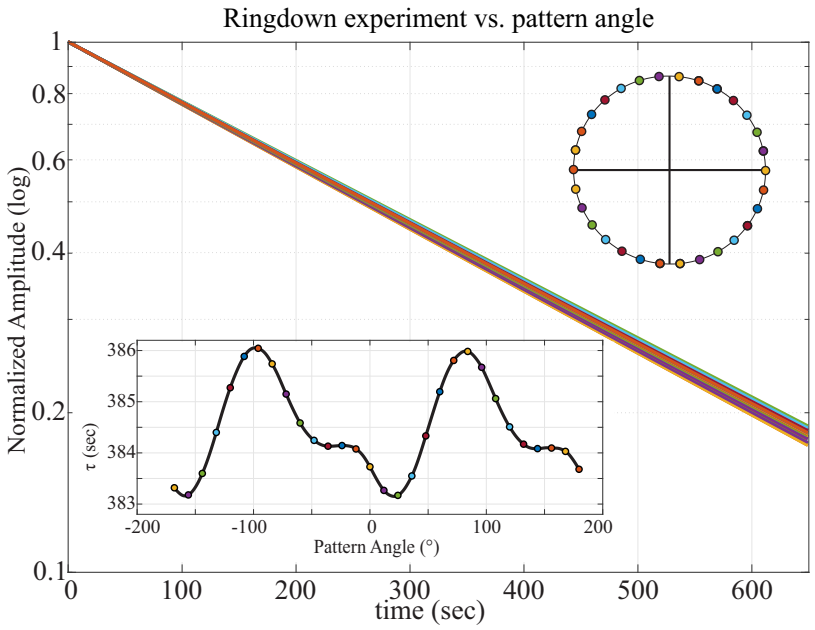

Figure 4.15: Identification of $\Delta(1/\tau)$ under tuned condition at each angle by disengaging the amplitude control loop, while other control loops, such as phase, quadrature, and rate, were still engaged.

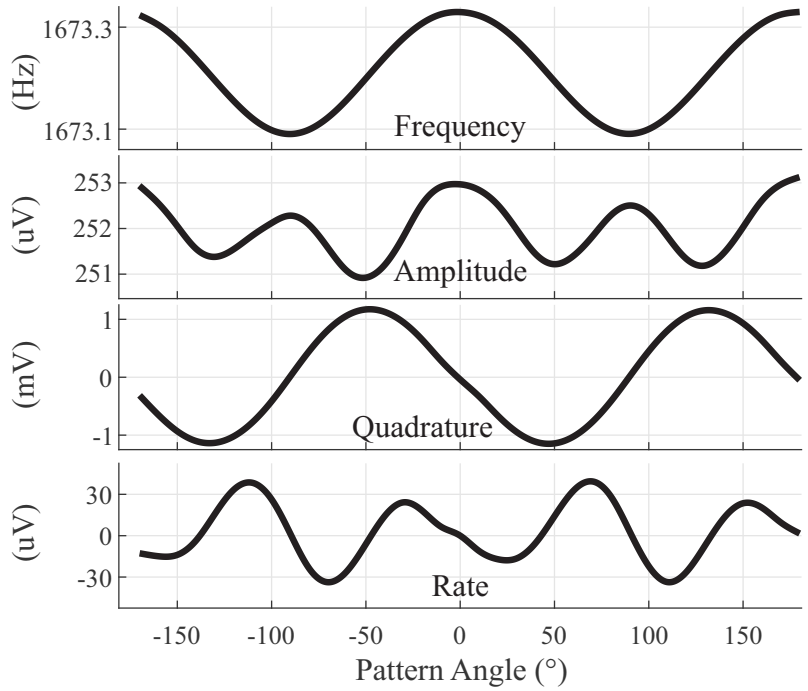

Figure 4.16: Experimental error identification using virtual carouseling of the vibration pattern in response to electrostatic force mimicking the rotation. The frequency mismatch and the orientation of principle axes of elasticity were observed from the PLL frequency, amplitude, quadrature, and rate command signals, showing 2θ and 4θ dependency of errors on the pattern angle.

4.6 Effect of Imperfections

Many of the effects of imperfections that result in errors of the output when operating in the WA mode have been reported in [151, 164]. For example, large displacements result in duffing nonlinearity causing angle dependent errors in WA mode of operation [165]. Ideal WA mode can theoretically track the input rotation angle with an unlimited dynamic range. Non-idealities from fabrication imperfections will limit the detection range of input rates above a certain threshold [166]. The uncompensated frequency mismatch Δf and anisodamping $\Delta(1/\tau)$ are the two major sources of drift, limiting the minimum detectable rate in the WA mode of operation [154, 167, 168]. Thus, maximization of the energy dissipation time constant, damping symmetry, and matching modal frequencies are the defining factors for the angle error in an angle measuring gyroscope. The high Q-factor QMG device is a good candidate to investigate the isolated effects of frequency mismatch on the precession drift in the WA mode of operation. For the high Q-factor device to identify the errors, three conditions were experimented with and verified numerically: (A) estimation of angle output with a fixed frequency mismatch, (B) estimation of angle output with varying frequency mismatch, and (C) validation in angle output to extract the bandwidth and linearity.

4.6.1 Rate-dependency Error

The angle measurement drift in a WA mode was derived in [154]. The drift model is described by a set of nonlinear coupled ordinary differential equations. In the WA mode under free

vibration, the drift equations have a form:

$$\begin{aligned}
\dot{\theta} &= -k\Omega + \frac{1}{2}\Delta\left(\frac{1}{\tau}\right) sin2(\theta - \theta_\tau)\frac{E}{\sqrt{E^2 - Q^2}} \\
&\quad + \frac{1}{2}\Delta\omega\ cos2(\theta - \theta_\omega)\frac{Q}{\sqrt{E^2 - Q^2}}, \\
\dot{E} &= -\frac{2}{\tau}E - \Delta\left(\frac{1}{\tau}\right) cos2(\theta - \theta_\tau)\sqrt{E^2 - Q^2}, \\
\dot{Q} &= -\frac{2}{\tau}Q - \Delta\omega\ sin2(\theta - \theta_\omega)\sqrt{E^2 - Q^2},
\end{aligned} \tag{4.6}$$

where E is the vibration energy, Q is the quadrature, θ is the output angle, and θ_τ and θ_ω are the primary axes of damping and elasticity, respectively. The uncompensated anisoelasticity ($\Delta\omega$) and anisodamping $\Delta(1/\tau)$ of the sensor introduce an angle-dependent perturbation in E, Q, and θ, limiting the measurement resolution of the gyroscope. For the systems of nonlinear coupled ordinary differential equations above, the E and Q can be approximated by [154]:

$$\begin{aligned}
&\Delta\left(\frac{1}{\tau}\right) \neq 0 \rightarrow E \propto \frac{\Delta(1/\tau)}{\Omega}, \\
&\Delta\omega \neq 0 \rightarrow \quad Q \propto \frac{\Delta\omega}{\Omega}.
\end{aligned} \tag{4.7}$$

Thus, maximization of the energy dissipation time constant, damping symmetry, and matching modal frequencies ($\Delta\omega = 2\pi(f_x - f_y)$) are the defining factors for the angle error in an angle measuring gyroscope. The drift equations were numerically solved for Δf =0.1 Hz and $\Delta(1/\tau)$ =0.0001 Hz, and the normalized energy and quadrature are plotted over time for different input rotation rates in Fig. 4.17. The results demonstrated the dependency of the quadrature error amplitude from the input rate rotation. At higher rates, the quadrature error decreased, resulting in a smaller perturbation of the angle measured. Larger quadrature errors are expected at lower input rates due to uncompensated frequency mismatch in

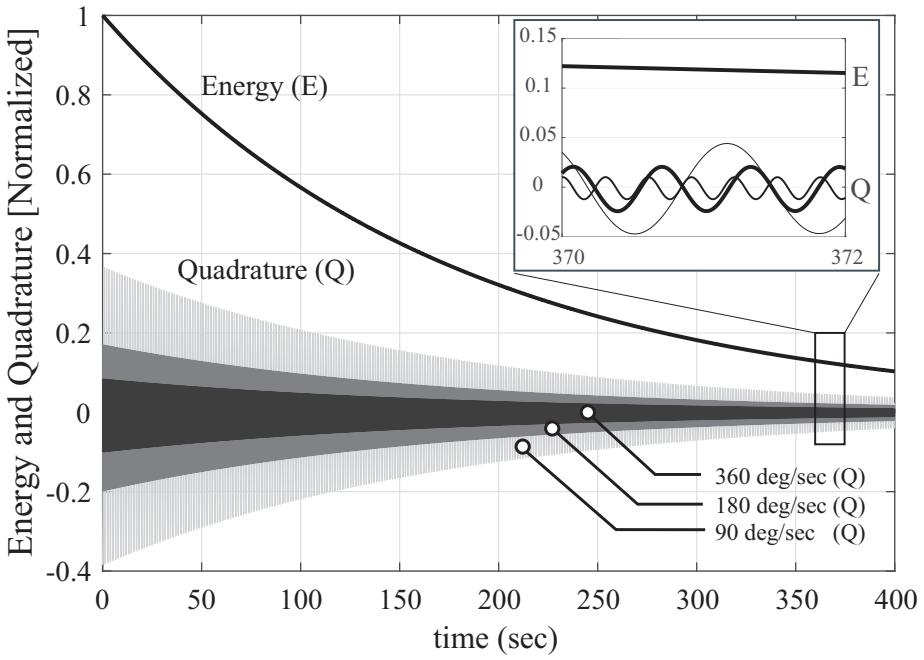

Figure 4.17: Numerical simulation of energy and quadrature under continuous rotation of a sensor with Δf =0.1 Hz and $\Delta(1/\tau)$ =0.0001 Hz. The values are normalized with respect to the maximum energy, corresponding to the maximum amplitude of vibration.

the sensor.

The energy and quadrature variables were collected and estimated in real-time during the continuous rotation, Fig. 4.18. As it was predicted from simulation results, the dependency of quadrature error on the input rotation rate was observed experimentally. The uncompensated anisoelasticity introduced a rate-dependent quadrature error, which couples to the angle drift, Eq. (4.6), resulting in a local perturbation in angle measurements and an error in the angular gain factor of the gyroscope operating in the WA mode.

For the same dataset, the direct angle measurement with associated errors was analyzed. Fig. 4.19 shows the angle output of the sensor under 0.5, 1 and 2 Hz input rotations. The sensor output was collected for a time constant (τ) of one amplitude decay cycle. A linear fit to the output data showed an angular gain factor of 0.83. The residuals of the fit revealed a rate-dependent angle estimation error. The local perturbation in the estimated angle was

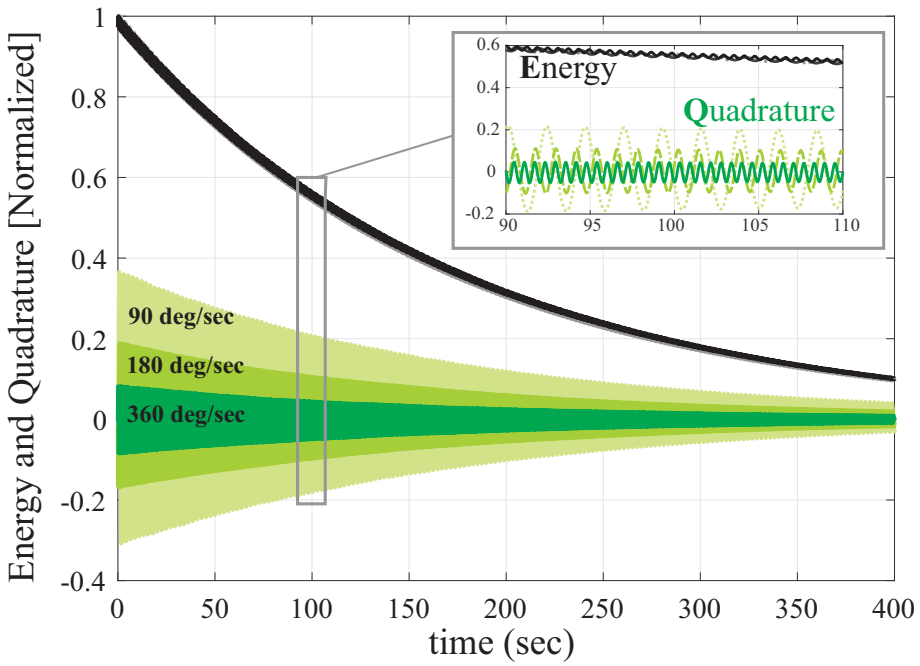

Figure 4.18: Experimental measurement of E and Q in WA under free vibration at three different clockwise input rotation rates: 90, 180 and 360 °/s.

less than 1° at 2 Hz input rotation, while the error increased to more than 2° at 0.5 Hz input rotation. As described earlier, the rate-dependent growth of errors is explained to be originated from an uncompensated frequency mismatch of the gyroscope, resulting in a lower error for higher input speed rotation.

4.6.2 Anisoelasticity Error (Δf)

In WA mode of operation, there is a better quadrature nulling control and therefore a reduced error in measured angle. Thus, an improved performance can be achieved by correction of the frequency split, [164, 169].

A closed-loop controlled thermal stage was developed for ovenization of the gyro in an LCC package as well as a direct recording of temperature fluctuations during the experiments, Fig. 4.20. The stage was composed of a temperature controller, a thermoelectric cooler (TEC),

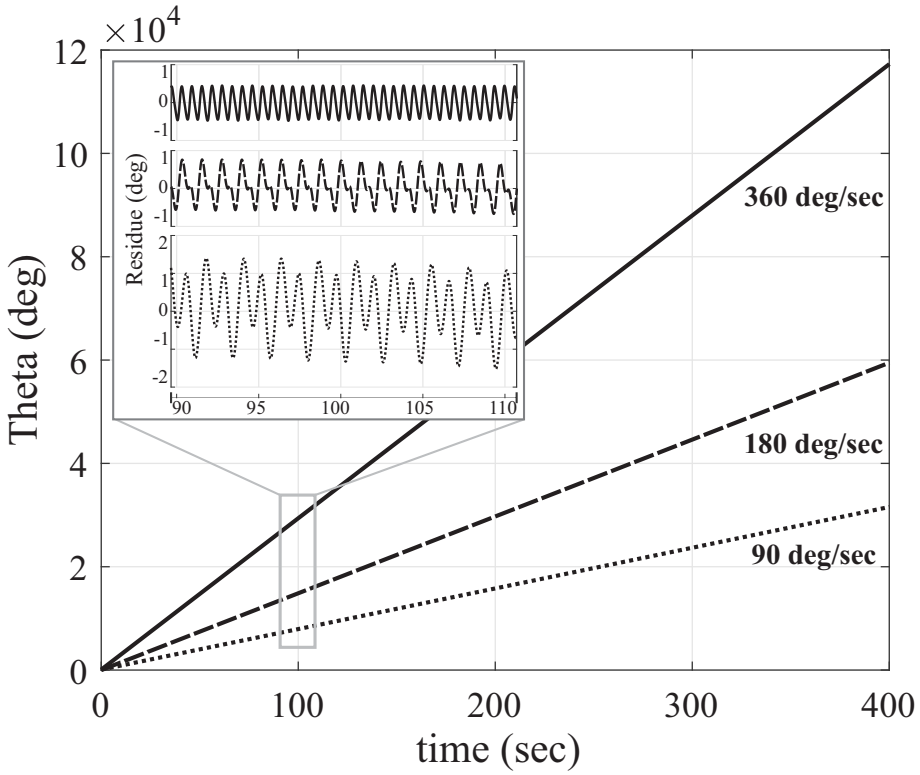

Figure 4.19: Experimental measurement of the angle directly and the error in the WA operation under a free vibration at three different input rotations: 90, 180 and 360 °/s. The inset shows residuals of the linear fit.

and a thermistor, with a temperature range from 20°C to 85°C. The events of temperature variations were recorded during the experiments. The temperature of the LCC package slowly rose up to about 32°C as a result of electronics power-up (Fig. 4.21a). As the rate table rotation started, the temperature dropped by 1°C due to convective cooling of the rate table (Fig. 4.21b). Fig. 4.21c illustrates the closed-loop ovenization and stability of temperature for the calibration purpose, demonstrating the stability of temperature fluctuations within 0.04 °C.

Fig. 4.22 shows frequency mismatch variations at different temperatures through virtual carouseling. At every temperature, the frequency mismatch was estimated from a range of frequency parameters extracted experimentally as a maximum deviation in peak-to-peak values. The results show 160 mHz variations in frequency mismatch Δf over 20 °C temper-

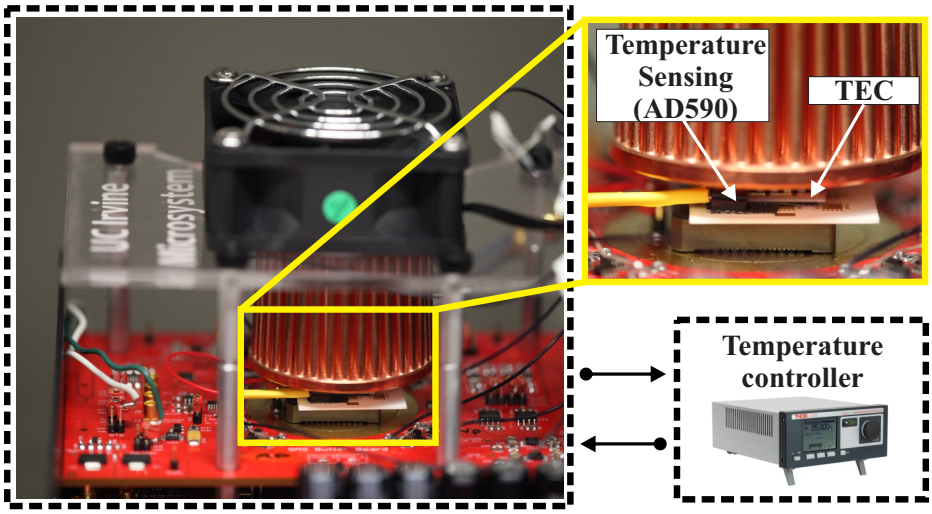

Figure 4.20: Experimental setup of the localized closed-loop controlled cooling/heating for a vacuum sealed device in LCC package.

ature change. The phenomenon was only observed experimentally on this particular high Q-factor device. We expect the trend will be different through different samples.

To observe the effect of temperature on the angular gain, the gyro was operated in the WA mode. A constant angular rate of 180 °/s (well above the minimum detectable angle for this device) was applied to the rate table and the angular gain was calculated at different temperatures set by the thermal controller. The effective angular gain as a function of temperature of the LCC package is plotted in Fig. 4.23. Each measurement point represents an average of roughly 100s of continuous rotation. In the WA mode, at a given temperature T, the frequency mismatch can be calculated from the fluctuation range of the VCO frequency output (similar to VC). The frequency mismatch extracted in the WA mode matches closely the frequency mismatches measured by the VC operation. The results demonstrate a strong correlation between the angular gain drift and the temperature-induced frequency mismatch. The exact trend of frequency mismatches might be unique to the studied sample, but the phenomena is universal.

To support numerically the experimental observation of drift in angular gain, we applied virtual carouseling, described in section 4.5, to the device by controlling the θ and observing

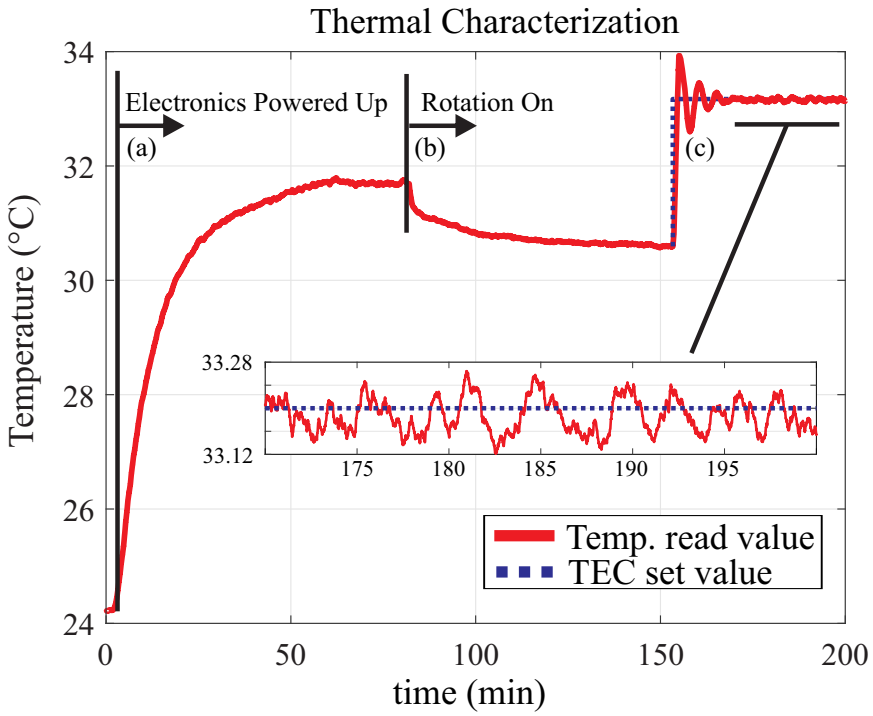

Figure 4.21: Illustration of temperature events for one complete characterization cycle from room temperature: a) front-end electronics powered up, b) start of rate table rotation at 180 °/s, c) closed-loop controlled thermal ovenization.

the E and Q parameters to estimate the error. While applying virtual carouseling, the parameter Q showed a significant dependency to the harmonics, Fig. 4.24. Since the $\Delta(1/\tau)$ is small, the error Eq. (4.6) can be rewritten as, [154]:

$$\dot{\theta} = -k\Omega + \frac{1}{2}\Delta\omega \; cos2(\theta - \theta_\omega)\frac{Q}{\sqrt{E^2 - Q^2}} \tag{4.8}$$

By extracting E and Q from virtual carouseling measurements, the coefficient $Q/\sqrt{E^2 - Q^2}$ can be estimated and it is shown in Fig. 4.25. This estimated coefficient shows as a sum of the sinusoidal harmonics. Therefore the estimated angular gain can be written as:

$$\hat{k} = [k \pm \Delta k] + \left\{ \frac{B}{2}\frac{\Delta\omega}{\Omega} cos(2\theta) * \sum a_n cos(n\theta) \right\} \tag{4.9}$$

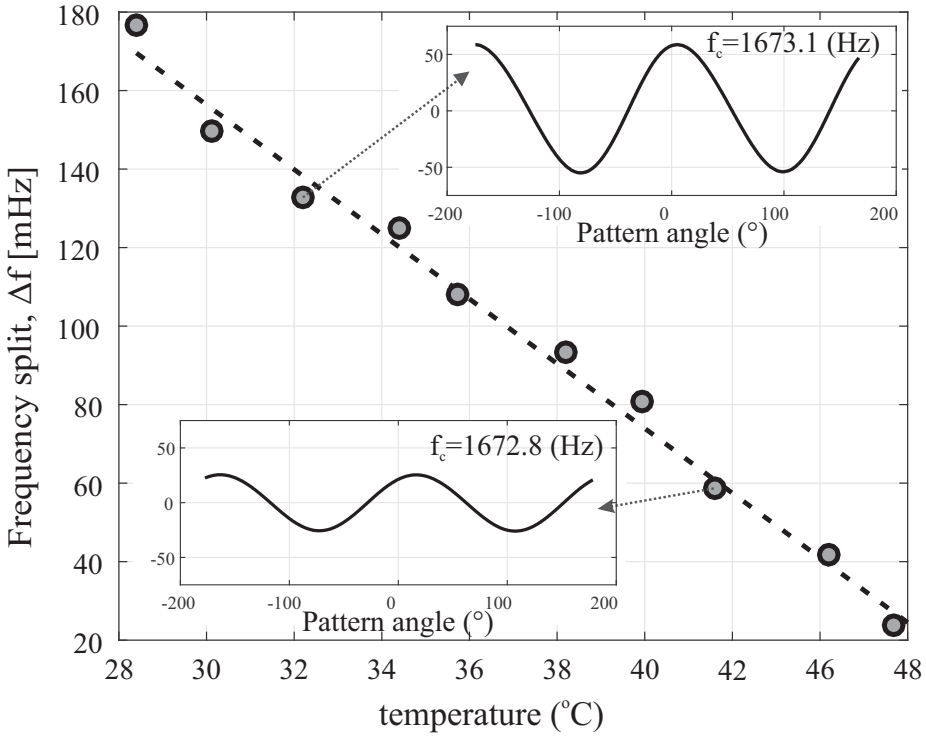

Figure 4.22: Experimental characterization of the frequency split through virtual carouseling vs. temperatures set by TEC. Inset figures: two examples of virtual carouseling of the gyroscope at 30°C and 37°C temperatures, observing changes in frequency split and shift in the drive center frequency (f_c).

It is estimated that changes in the angular gain (effective angular gain) $\hat{k}$ is proportional to $(\Delta\omega)/\Omega$. For this device, due to uncompensated anisoelasticity, and under a fixed input rotation, we experimentally observed a drift in the angular gain as a function of temperature.

The drift in the angular gain was corrected by the least-squares linear fit between the measured dependence of the frequency mismatch and the temperature. An algorithm was implemented to correct the drift by sensing the frequency mismatch variation. Fig. 4.26 shows schematics of the correction procedure applied in this section. Two examples are provided to show fluctuations of the frequency mismatch during experiments. In the first experiment, a rotation was applied in a closed environment inside a high speed centrifuge system to observe a baseline angular gain drift, and in the second experiment, the temperature of the LCC package was increased during rotation and a retrospective correction was applied.

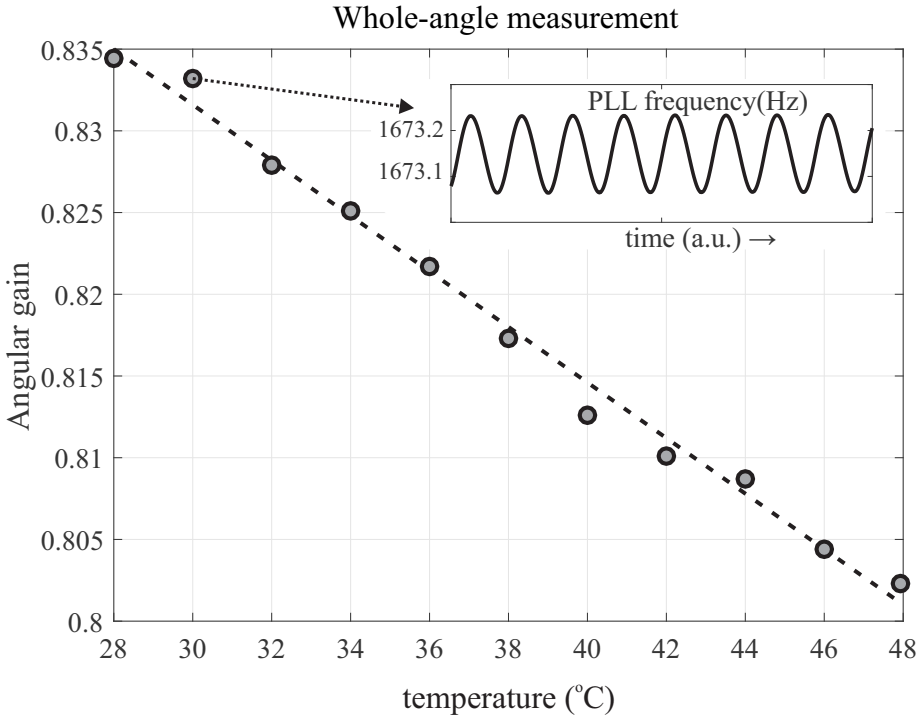

Figure 4.23: Experimentally extracted angular gain under different temperatures in WA mode, illustrating 4 % deviation of the angular gain over 20°C temperature change. The inset shows an example of the corresponding frequency of the PLL control over time at a fixed 30°C temperature.

The input rate rotation of 180 °/s was applied to the rate table. The WA mode algorithms were enabled when the temperature of the electronics reached a plateau, to eliminate the observed changes. Fig. 4.27 shows the extracted frequency tracking from the PLL loop under continuous rotation without thermal control (the first experiment). The result showed a shift of 1.5 mHz for 400s as a baseline angular gain drifts. Fig. 4.28 demonstrates experimentally the measured angular gain drift for an accumulated input rotation of 1.8×10^5 degree (the second experiment). An external temperature cycle was applied to the device during the WA operation using the closed-loop thermal stage. The frequency mismatch was calculated using the recorded VCO, which was an output from the PLL loop. The correction was made by the identified virtual carouseling coefficients between frequency mismatch and angular gain by a look-up table. The 2.2 % drift of the angular gain was corrected in post-processing and shown in Fig. 4.28.

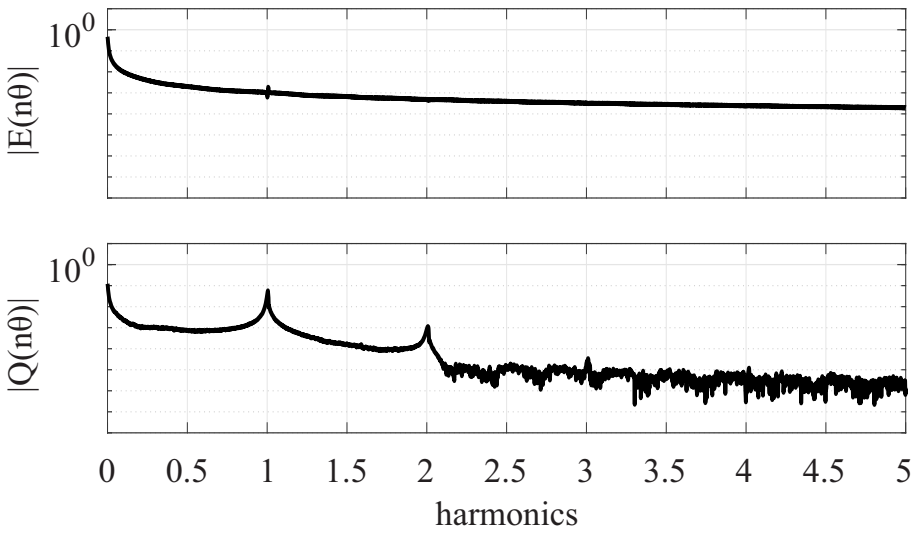

Figure 4.24: Power spectrum density of the energy and quadrature as a function of harmonics, showing a harmonic dependency of the quadrature profile.

4.6.3 Linearity and Bandwidth in WA Instrumentation

The QMG device with the Q-factor of 2 million was tested by applying a linear sweep and sinusoidal angular velocities to extract the full scale and the dynamic range properties of the device, respectively. The device operated in the WL-CL configuration mode, with the description provided in section 4.4.3. The nonlinearity of the device was extracted experimentally and shown in Fig. 4.29. As expected, the high Q-factor device in the WL-CL mode shows a perfect linearity for the high-speed input rotation, whereas for low-speed input of rotation the uncompensated frequency mismatch limited the minimum detectable input rotation, causing the precession pattern angle to lock along the orientation defined by a principal axis of elasticity [170].

To examine the bandwidth of the device, we varied the angular velocity profile of the rate table. From the direct angle measurement output, the −3 dB range resolution was extracted experimentally and estimated to be at 4 Hz, see Fig. 4.30. In the plot, at every input speed the angular gain was estimated from the linear fit of the output over input $\mathrm{dB}(\theta_{out}/\theta_{in})$,

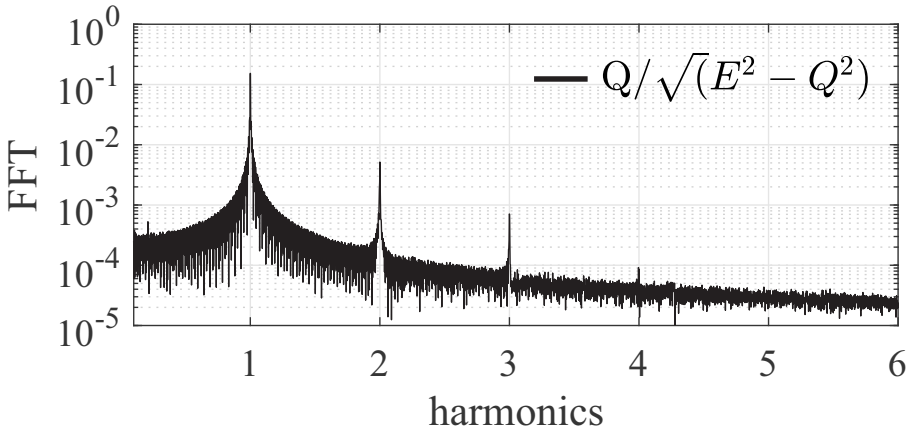

Figure 4.25: FTT of the estimated coefficient $Q/\sqrt{E^2-Q^2}$. Revealing the strong rate dependency, which contributes to the angular gain drift in a non-ideal CVG.

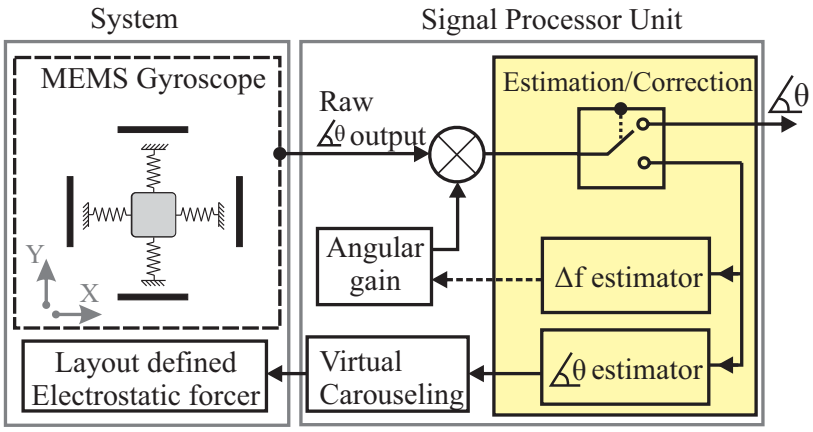

Figure 4.26: Schematics of the proposed error identification technique in the whole-angle mode of operation of a MEMS gyroscope.

where all measurement points were normalized to the response at 0.05 Hz input. Even though we examined the linearity and bandwidth in WL-CL, the result from WL-OL was the same. For the high Q-factor device, a significant improvement in linearity for low input rotation range was demonstrated when the device operated in the rate or FRB modes, and discussed in Chapter 3. Therefore, a CVG system with single sensor and interchangeable mechanization of control algorithms [128], or a CVG system with multiple sensors where each sensor operates with a dedicated mechanism are more suitable to achieve unlimited bandwidth and linearity.

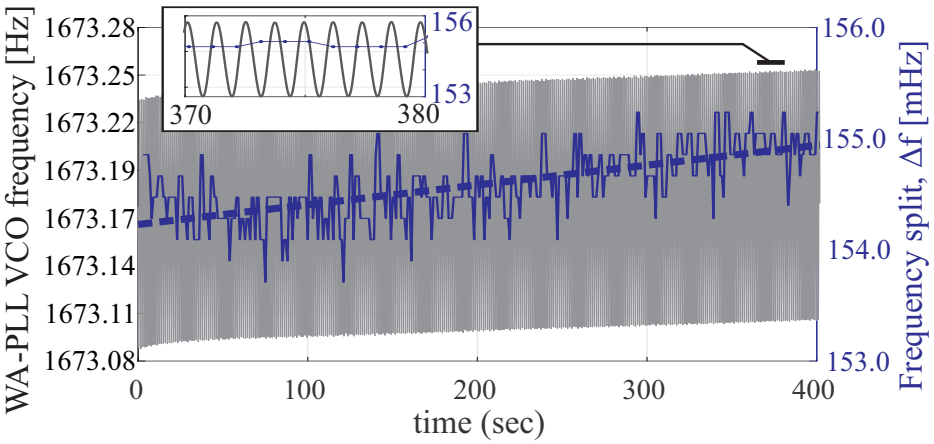

Figure 4.27: Experimental tracking of PLL's VCO frequency in the WA mode of operation. The inset figure demonstrates a periodic function of the standing Lissajous curve frequency. The frequency mismatch was estimated over a sliding 3s window with the step of 1s.

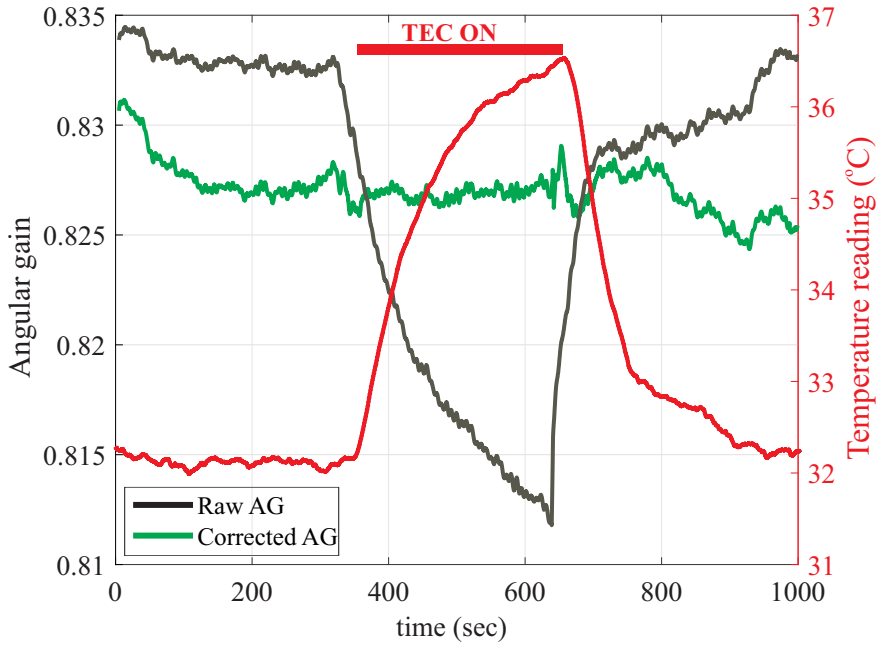

Figure 4.28: Deviation of the gyroscope angle output over 10,000 s without temperature control (black). Correction of the angular gain drift demonstrates a scale-factor improvement of direct measurements of the angle from precession (green).

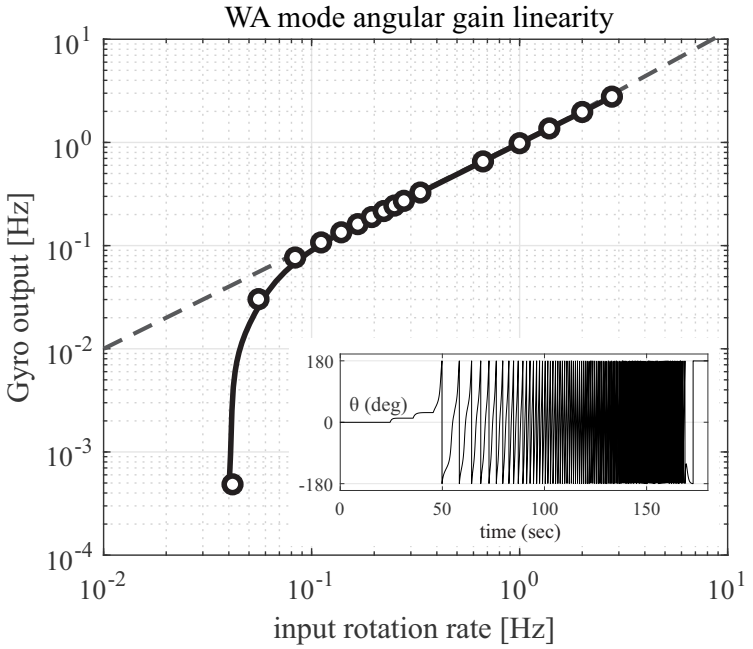

Figure 4.29: Linearity of direct angle measurement of a non-ideal QMG device in WA mode. The inset plot shows the raw output angle from the device while applying linear sweep of input angular velocities to the rotary stage.

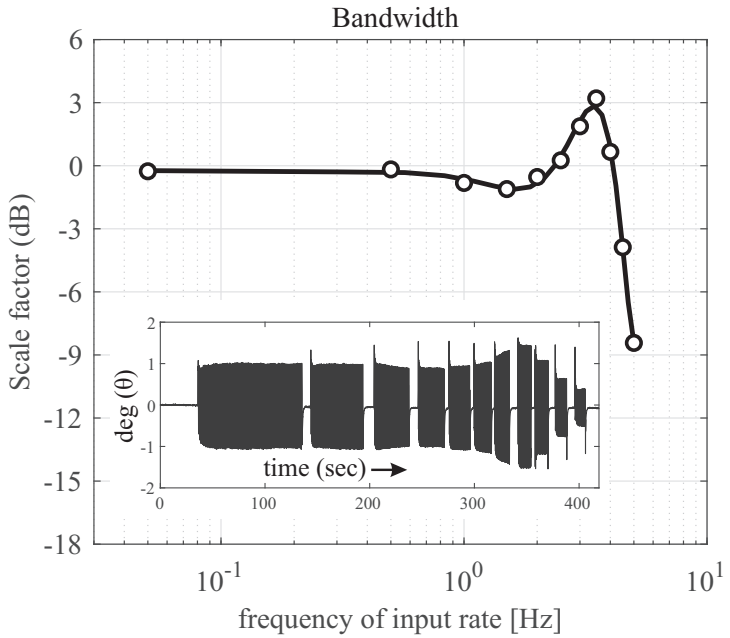

Figure 4.30: Experimental estimation of gyroscope's output angle bandwidth operating in the WA mode. The inset plot shows the raw output angle from the device in response to a sequences of rapid rotation followed by a stop at different speeds.

4.7 Conclusion

The importance of long-term drift on the MEMS gyroscope used for vestibular prosthesis was demonstrated, where this drift changes the scale-factor resulting in a shift in Allan variance of the device. Using low-cost MEMS device for vestibular prosthesis require frequent calibration or additional methods for long-term calibration. We demonstrated that the thermal calibration is important for the device to preserve the long-term drift. Without this technique, the operation time is limited for the prosthesis, e.g., 5.5 hours before it enters into the vestibular dysfunction region for tactical grade gyroscope without calibration (Chapter 1-Fig. 1.3).

We experimentally demonstrated a vacuum sealed silicon Quad Mass Gyroscope (QMG) in the whole-angle mode of operations with the Q-factor on the level of higher than 2 million. The sensor was operated for more than 30 minutes under free vibration without any excitation signals, allowing to estimate the angle output without interferences of the electrostatic compensation loops, only involving dynamics of the gyroscope itself. Due to the long decay time constant of 300 s and damping symmetry of the device, the effect of anisoelasticity on the precession angle was isolated and the contributing effects of imperfects on drift were investigated directly. We presented the performance analysis of the direct angle output of the precession under free vibration. The result coincided with equations of the linearized Foucault pendulum in 2D approximation. The amplitude of the energy loop is an important key parameter in determining the accuracy of the angle estimation. In the closed-loop configuration, we demonstrated the continuous operation of the sensor in the whole-angle mode for 10,000 s, resulting in bounded residual error over a long time, where the duration of experiment was not a limit.

The rate-dependency of quadrature error was predicted numerically from the error model and observed experimentally. The quadrature error resulted in a rate-dependent error in the

angle estimation, which was mainly the result of structural imperfections in the system. We experimentally demonstrated the effect of quadrature and thermal variations on the drift of the estimated angular gain in a non-ideal high-Q gyroscope operating in the whole-angle mode. The frequency mismatch variations were identified by virtual carouseling and used as an input to the feed-forward correction algorithm to retrospectively correct for the drift of angular gain in the whole-angle mode of operation. The frequency mismatch limit the minimum detectable input rotation causing WA to fail to operate and locking the precession pattern into a geometrically defined orientation. An uncompensated frequency mismatch result in rate-dependency of angular gain and output measurement error in WA mode operation. Even though the presented results were specific for the the QMG architecture, the observations are general and can be applied to a broad class of Coriolis Vibratory Gyroscopes instrumented to operate in the whole-angle mode.

Chapter 5

Event Detection for Aiding Calibration

A learning-based calibration algorithm for a vestibular prosthesis with the long-term goal of reproducing error-free vestibular system dynamic responses was developed. Our approach uses an additional IMU to detect the head acceleration of a patient and to correct the corresponding drift in the vestibular prosthesis. The algorithm includes four major parts. First, we extract features from the shoe-mounted IMU to classify human activities through convolutional neural networks. Second, we fuse data from the head-mounted IMU (vestibular prosthesis). Third, we artificially create additional data samples from a small pool of training data for each classification class. Fourth, we use the classified activities to calibrate the reading from the head-mounted IMU. The results indicate that during daily routine activities the firing rate baseline of a vestibular prosthesis system without calibration fluctuates between 100 pulses/s to 150 pulses/s; in contrast, an appropriate calibration to human activity results in correction of 4 pulses/s in extreme cases, providing a stable baseline firing rate while the head is not moving. In this chapter, we specifically study the contribution of gyroscope scale factor on the drift of the vestibular prosthesis system and propose a corresponding

calibration method.

5.1 Introduction

Proprioception of the body and control of eye movement are supported by the vestibular system of both inner ears. Impairment of one or both sides of vestibular systems, were reported to be caused by, for example, aging, toxic reaction to medications, tumors, or brain injury, resulting in loss of balance, vertigo, abnormal gait, and visual instability [171, 172]. Rotational movements are captured by three semicircular canals and the vector of acceleration (or gravity) is sensed by the otolith organs. Together, the semicircular canals and otolith organs, provide the three-dimensional rotation and translation information of human body to the brain. This information is integrated by the brain with other sensory information and is used for a number of functions, including the posture control and balance, stabilization of images on the retina, and more. For people who have lost vestibular functions, with the help of MEMS inertial sensing technology, position and orientation can be substituted by gyroscopes and accelerometers, which are low in price and small in size, making them suitable for biomedical applications [173]. Vestibular prosthesis uses MEMS Inertial Measurement Unit (IMU) and the corresponding signal processing, which transmits human head rotation to neuronal firing pulses. While MEMS-based Vestibular Prosthesis (VP) has theoretically a potential to restore the balance function, the effect of drift in the sensor on the performance of the vestibular prosthesis may present a major roadblock for acceptance of the technology.

We have demonstrated a VP prototype using a single axis commercial grade gyroscope to mimic the dynamics of a vestibular system, [34]. Johns Hopkins University developed a semi-implantable unit with 3 MEMS gyroscopes to restore the vestibular function, [4], and its clinical study is underway to evaluate the unit [174]. Generally, an IMU consists of three orthogonal pairs of gyroscopes and accelerometers to capture the orientation of

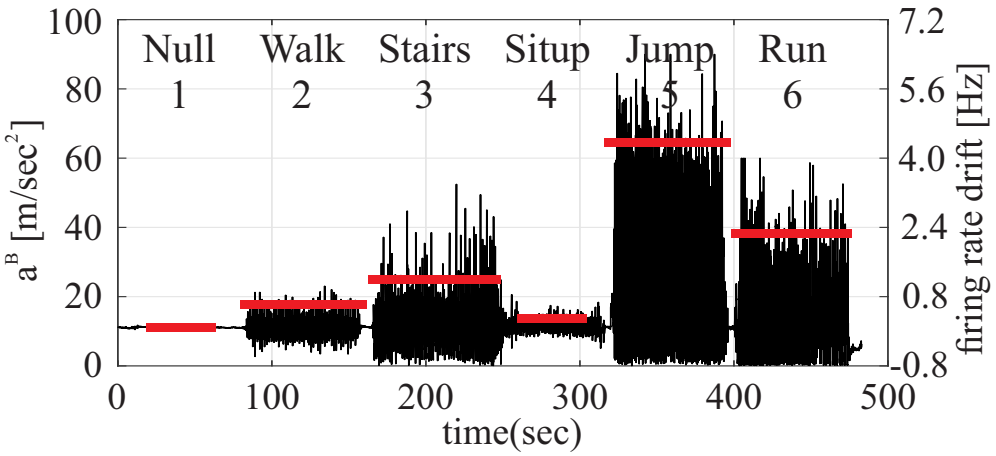

Figure 5.1: Acceleration magnitude sensed on head-mounted IMU due to different human activities. Horizontal bar line represents the firing rate drift due to the effect of acceleration, as predicted by the vestibular dynamic model.

the sensor with respect to an inertial coordinate frame. For a gyroscope, the scale factor corresponds to sensor's sensitivity, the ratio from a readable output to the input physical rate of rotation, measured in (Volt or LeastSignificantBit)/(°/s). The scale factor of a MEMS gyroscope itself is also sensitive to many factors, such as temperature [175], repeatability (turn-on to turn-on) [176], linearity [177], and acceleration force [178]. For a long duration of operation, inertial sensors require an in-situ multi-dimensional calibration functionality to avoid erroneous signals to be sent to the brain.

The study in [4] proposed a nonlinear dynamic model defining the relationship between head's angular velocity Ω in [°/s], and the neuron's firing rate in [pulses/s or Hz] as follows:

$$f = \frac{1}{2} \times f_{max} \times (1 + tanh(tanh^{-1}(2 \times \frac{f_0}{f_{max}} - 1) + C(\frac{\Omega}{450}))), \tag{5.1}$$

where f_0 is a baseline firing rate at 100 Hz, f_{max} at 450 Hz, C is compression factor of 10 and Ω is input head velocity in [°/s] with a range between -450 to 450 °/s. According to the model, a typical scale factor sensitivity of 0.1 °/s/g, significantly alters the intensity of the firing rate and could cause an additional vestibular damage or ill-signaling of the vestibular activities. Over daily routine activities, the human body undergoes different accelerations

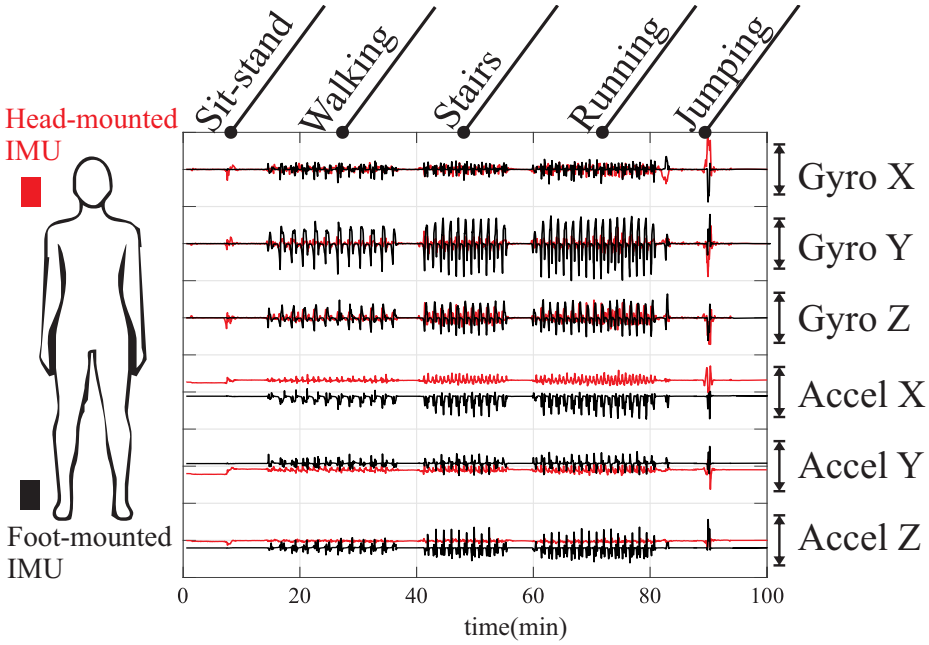

Figure 5.2: Demonstration of human daily routine activities recorded by two IMUs, located on foot and head. Each IMU provides 6 parameters.

[179], this also applies to the head-mounted IMU, or VP sensor. Fig. 5.1 demonstrates the corresponding accelerations through the daily routine activities. For the IMU, the sum of magnitudes squared of the acceleration along three axes *(x, y, z)* in the sensor's body coordinate B can be represented as:

$$a^B = \sqrt{(a_x^B)^2 + (a_y^B)^2 + (a_z^B)^2}, \tag{5.2}$$

where a^B refers to the magnitude of acceleration experienced by the IMU during each activity. The gyroscope's g-sensitivity is about 0.3 °/s/g [180], which for VP translates in a drift of 4 Hz as a result of applied 6.1 g acceleration, e.g., in the event of jumping, shown also on the plot.

5.2 Design

5.2.1 Data Collection

MEMS IMU sensors are categorized into different grades depending on their sensitivity, representing consumer, industrial, tactical, navigation, and space-grades. The consumer grade is easily accessible, smaller in size, low in cost, and often used for biomedical motion applications. The inherent bias and scale factor drifts of such sensors result in a faulty output and corrections become necessary. A major contributing factor to these drifts is environmental changes, such as shock, vibration, and temperature.

In our experiments, data was recorded using three different hardware platforms: a) a custom foot-mounted inertial navigation system (INS) [104], b) a miniature GPS-Aided INS, VN-200 [181], and c) a flexible laboratory INS testbed [182]. The IMUs for each platform were selected to represent different sensor grades, based on their sensitivity and noise characteristics reported by the corresponding manufacturer, including consumer, industrial, and tactical grades, respectively. The head-mounted IMU was mounted behind the ear using straps. Depending on the platform, we attached the foot-mounted IMU either to a custom shoe or strapped on the shoe. Data recorded across platforms and experiments were recorded with different sampling frequencies ranging from 100 Hz to 450 Hz. To achieve a uniform database, each time series data were then resampled at 200 Hz using linear interpolation techniques. The first 10 s of each IMU recording from these platforms were used for calibration as described in Appendix B. Human daily activities were recorded from three different subjects on different days and occasions. An example of motion captured by two IMUs with their location is shown in Fig. 5.2. Motion signals captured from the two IMUs were different from each other, e.g., more fluctuation in the gyroscope readout was sensed by the foot due to dynamics of the gait and the acceleration pattern across classes (events)

was easily distinguishable.

5.2.2 Data Augmentation

The mounting position and the sensor grade of IMU resulted in different accuracy, [183, 184], and the dataset collected for this study was a combination of both approaches. Therefore, the training dataset was rich enough in features. Consequently, to artificially increase the number of training datasets we proposed a data augmentation process inspired by a study in [185]. For every gyroscope and accelerometer recording data in the sensor body-frame coordinates *(x, y, z)*, we applied the Euler rotation, with the corresponding angles ϕ, θ and ψ about the sensor axes using the following sequence of rotations:

$$R_x(\phi,\theta,\psi) = (R_x(\phi)\cdot R_y(\theta)\cdot R_z(\psi)) = \left(\begin{bmatrix} 1 & 0 & 0 \\ 0 & c(\phi) & s(\phi) \\ 0 & -s(\phi) & c(\phi) \end{bmatrix}\cdot\begin{bmatrix} c(\theta) & 0 & -s(\theta) \\ 0 & 1 & 0 \\ s(\theta) & 0 & c(\theta) \end{bmatrix}\cdot\begin{bmatrix} c(\psi) & s(\psi) & 0 \\ -s(\psi) & c(\psi) & 0 \\ 0 & 0 & 1 \end{bmatrix}\right), \tag{5.3}$$

where c and s represent *cos* and *sin* functions, respectively. For each dataset, the angles were randomly selected and repeated three times. Fig. 5.3 illustrates this process visually of the data for one gait cycle.

5.2.3 Convolutional Neural Network

Deep learning or multiple-layer neural networks has been successfully applied for image, video, speech, and audio processing [186, 187]. Convolutional Neural Network (CNN) is

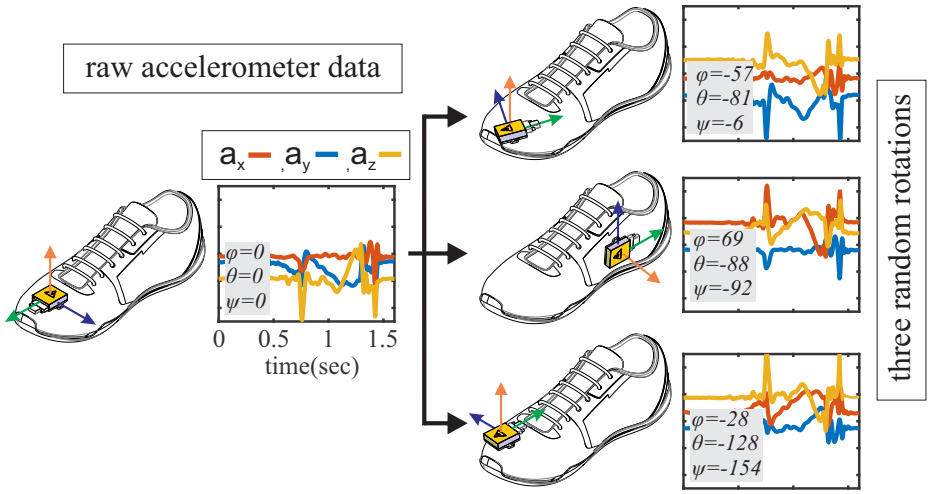

Figure 5.3: Data augmentation by 3D rotation of the raw data. Original data (left) compared to rotation angles of ϕ, θ and ψ (right). Only *(x, y, z)* accelerometers from the shoe-mounted IMU are shown for one gait cycle.

the first layer in an artificial neural network. The word deep refers to multiple layers of CNN in the network. CNNs for human event classification using accelerometer alone was demonstrated by [188], and using smartphone IMU by [189]. This study, focuses particularly on shoe-mounted IMU for classification, with expanding the model by fusing the data from a head-mounted IMU. The architecture used for our algorithms is a standard 2D CNNs layer with Rectified linear Unit (RelU) activation followed by a max-pooling layer to train the model [190]. Compared to an image classification, where R, G, B layers are stacked to form a 3D volume with 3 layers depth. In this architecture, the *x, y, z* of gyroscope and accelerometer parameters of both IMUs form a 2D matrix with 1 layer depth, 12 rows and N samples are presented as a column. Therefore, a standard 2D CNN was considered.

The width of the matrix represents a sequence in time series extracted from a moving window size of 1.5 s with an overlap of 0.1 s, which is corresponded to 300 samples at any step. The convolutional layer convolves a matrix weights window *(w)* of unit size of $(i \times j)$ on the input temporal sequence (v_i) of IMU data to its neighborhood time window with 64 filters and finally added a bias *(b)*. The RelU layer maps the features from the previous neuron with the following activation function:

A convolutional network has n number of filters f_n with a predefined matrix weights *(w)*. These layers are trained one by one in order to extract features from the input data. The convolutional layer *($conv_i$)* convolves a window of unit size of *($i \times j$)* on the input temporal sequence *(v_i)* of IMU data to its neighborhood time window and finally added a bias *(b)* with the following expression, [191]:

$$conv_i = b_i + w_{ij} * v_i = b_i + \sum_{j=1}^{H} \sum_{i=1}^{W} w_{ij} \cdot v_i \tag{5.4}$$

After performing the convolution an activation function, RelU maps features from the previous neuron with the following function:

$$RelU(conv)\ ,\ RelU(x) = \begin{cases} 0 & if \quad x < 0 \\ x & if \quad x >= 0 \end{cases} \tag{5.5}$$

Followed by the activation function, a 2D global average maximum pooling were employed to perceive features from the signal [192]. Each layer of the feature maps will be partitioned into multiple areas with the size of $(H \times W)$, each area will be represented by a maximum value, which resulted in dimension reduction. The dataset was split into two parts, 70 % to be used to train the model and 30 % to be used to test the model, total of 226 independent recordings. The developed architecture was trained and tested using TensorFlow in Google's Colaboratory framework, [193]. We used Python programming language for implementation of the algorithm, the NumPy library for pre-processing and matrix manipulation and the Pandas library for data wrangling.

5.2.4 Architecture

The generalized layer architecture of a deep CNN for a time series input was implemented, and is shown in Fig. 5.4. Each layer consists of many neurons. The layers are stacked upon each other, and the sizing of each layer was determined based on how the neurons in one layer are connected to concurrent and sequential layers. The sizing is also noted in the graph. The architecture presented here is similar to image classification [194], where the main layers are: input, CNN, Fully Connected (FC) and output, with the following description:

- ***Input layer*** has a shape of (h, w, d)=(12, 300, 1), where the layer is a 2D matrix of the horizontally stacked *x, y, z* parameters of the gyroscopes followed by *x, y, z* parameters of the accelerometers. The width of the matrix represents a sequence in time series extracted from a moving window size of 1.5 s with an overlap of 0.1 s.

- ***CNN layer 1*** has a weight matrix W^1 with *64* features with the shape of $(L1_W \times L1_H \times f_1) = (11 \times 290 \times 64)$, where $W = 11, H = 2$, with the stride size of 1×1, zero padding and RelU.

- ***CNN layer 2*** has a weight matrix W^2 with the shape of $(L2_W \times L2_H \times f_1) = (10 \times 145 \times 64)$, where $W = 18, H = 2$. The pooling stride of size (2×1) and dropout probability of 20 %.

- ***CNN layer 3*** has a weight matrix W^3 with *128* features with the shape of $(L3_W \times L3_H \times f_2) = (9 \times 128 \times 128)$, where $W = 18, H = 2$, with the stride size of 1×1, zero padding and RelU.

- ***CNN layer 4*** has a weight matrix W^4 with the shape of $(L4_W \times L4_H \times f_2) = (8 \times 64 \times 128)$, where $W = 18, H = 2$. The pooling stride of size (2×2) and dropout probability of 20 %.

- ***FC flatten layer*** passes through the previous 2D weights and connected them all to form a $1 \times f_n$ hidden features. For the two CNN implemented, $f_2 = 128$.
- ***FC dense layer*** has the same size as input, and performs a linear operation and connects the neurons.
- ***FC fully connected layer*** has the same size as input, and reshapes the layers to prediction values.
- ***Output layer:*** maps the final prediction (classification) with f_n size output, here 6 classes for the human activity recognition.

5.3 Experimental Results

A human gait cycle was extracted experimentally using two IMUs placed on the forefoot and the heel of the shoe. Vector Nav (VN-200) inertial sensors were used due to the high dynamic range of $2000 deg/sec$ in angular rotation and $\pm 16g$ in acceleration. Experimental data shows a complete gait cycle with a duration of around ~ 1.6 second, under walking at fast speed, with the stance and swing phases each occupy 50% of the gait cycle. However during a normal speed, the ratio of the stance-to-gait cycle was 60%. The swing phase was a major focus when analyzing the hardware requirement to capture the dynamic range. During this phase alone, the motion divides into four segments: 1) heel-off, 2) toe-off, 3) heel-contact and 4) toe-contact. Fig. 5.5 shows an example of raw data extracted from the foot motion by IMUs during a walking scenario. Regardless of IMU placement, the maximum instantaneous rotation sensed by IMU mounted on the forefoot and the heel area are 600 and 250 deg/sec, respectively. This significant difference in angular rotation occurs only during the toe-off segment. However, the maximum instantaneous acceleration magnitude are during two-phases: toe-off $40 m/s^2$ and heel contact $76 m/s^2$. The IMU mounted on heel

area experiences more shock during the heel contact, which is 3 times more as compared to the IMU mounted on the forefoot area.

Table 5.1 summarizes the tradeoff between the IMU noise, cost and dynamic range among the considered 4 IMU sensors, arranged in ascending order of their accelerometer noise. ADIS16490 and ADIS16485 IMUs are categorized as tactical, VN-200 IMU as industrial and MPU9150 IMU as consumer grade sensors. The platform ID corresponded to the ones assigned in section 5.2.1. The data collected under these different scenarios represent different dynamic ranges, therefore not all IMUs are suitable to capture all human activities. This table is useful for verifying that the sensor meets system requirements for activity recognition during a particular activity. The result shows that as the speed of gait cycle increases or an activity with anticipated jumping, the sensed acceleration and angular motion during the gait cycle increases, which requires a higher dynamic for the IMU specification. Although IMU with better resolution is desirable for activity recognition, their dynamic range gets limited as higher resolution is possible. In the table, these activities were mapped to the considered four IMUs.

Table 5.1: IMU used with their corresponding full scale dynamic range

Plat.	IMU	price $	gyro bias (^{o}/hr)	gyro ARW (^{o}/sec)/rt(hr)	gyro full scale	accel bias (ug)	accel full scale
c	ADIS16490	2472	1.8	0.0020	±100	3.6	±8g
c	ADIS16485	1645	6.25	0.0066	±450	32	±5g
b	VN-200	2465	5	0.0035	±2000	40	±16g
a	MPU9150	14	40	0.2000	±2000	150000	±16g

In order to have a sense of features extracted by classification, some basic statistics was computed and correlated with the result from CNNs. Two parameters were extracted from

gyroscope and accelerometer datasets: the standard deviation and maximum range (instantaneous difference values across three axes during the full gait cycle). These parameters were reported for different activities, as summarized in Table 5.2. The results show that as the speed of the gait cycle increases, e.g., jumping activity, the sensed acceleration and angular motion during the gait cycle increased, which was associated with the signal edges identified by the CNNs.

Table 5.2: Features extracted from foot-mounted IMU for classification

	gyroscope (deg/sec)		accelerometer-g (m/s^2)	
Activity/Parameters	max range	std	max range	std
Walking	329.64	185.3	5.48	10.44
Running	567.7	293.89	7.5	14.67
Jumping	938.96	527.02	11.16	22.32
Sit to stand	10.3	3.5	0.5	0.2
Stairs(up & down)	841.3	437.7	6.9	12.90

Four different configurations were considered for classification using the described CNNs: 1) only head-mounted IMU, 2) only foot-mounted IMU, 3) both head- and foot-mounted IMUs, and 4) the same as 3, but with added data augmentation. The visualization of performance of the classification (confusion matrix) is shown in Fig. 5.6. The head-mounted IMU alone revealed difficulty of distinguishing between walking and running activities, as well as sitting and running activities. The shoe-mounted IMU alone revealed difficulty of distinguishing between standing still from sitting activities, and vice versa. The usage of both IMUs together showed an improvement with the help of data augmentation. The learning rate also increased when utilizing two IMUs, as compared to an individual IMU. The developed model was applied to the dataset shown earlier in Fig. 5.1 and the correction was made on

the Z-axis gyroscope of the head-mounted IMU. The firing rate proportional to the angular velocity before and after correction is shown in Fig. 5.7. The major benefit of the calibration is to correctly generate firing rate for such activities, e.g., in the running activity the largest acceleration force occurs and the necessary corrections are introduced.

Training Accuracy: The accuracy of the training progress is shown in Fig. 5.8, revealing that the learning rate increases when utilizing two IMUs, as compared to an individual IMU. Therefore multiple IMUs are desirable in human activity classification. Foot-mounted IMU has higher accuracy as compare to head-mounted IMU for human activity classification.

5.4 Conclusion

In this section we present the need for long-term calibration of IMU sensors for vestibular prosthesis. We proposed a calibration algorithm for the sensor under varying dynamics and environmental conditions. We used convolutional neural networks to classify human activity based on inertial sensor data captured from foot- and head-mounted IMUs. The classification based on a single sensor is shown to be effective, however, fusing multiple sensors resulted in an improved classification. We implemented a data augmentation algorithm for inertial sensors to extend the small dataset and to consider different scenarios of an IMU placement. We showed that selection (or design) of IMUs is important to capture the dynamic range of human activity. For example, a near tactical grade IMU with the range limit of 450 °/s is within the dynamic range of walking activity of 330 °/s.

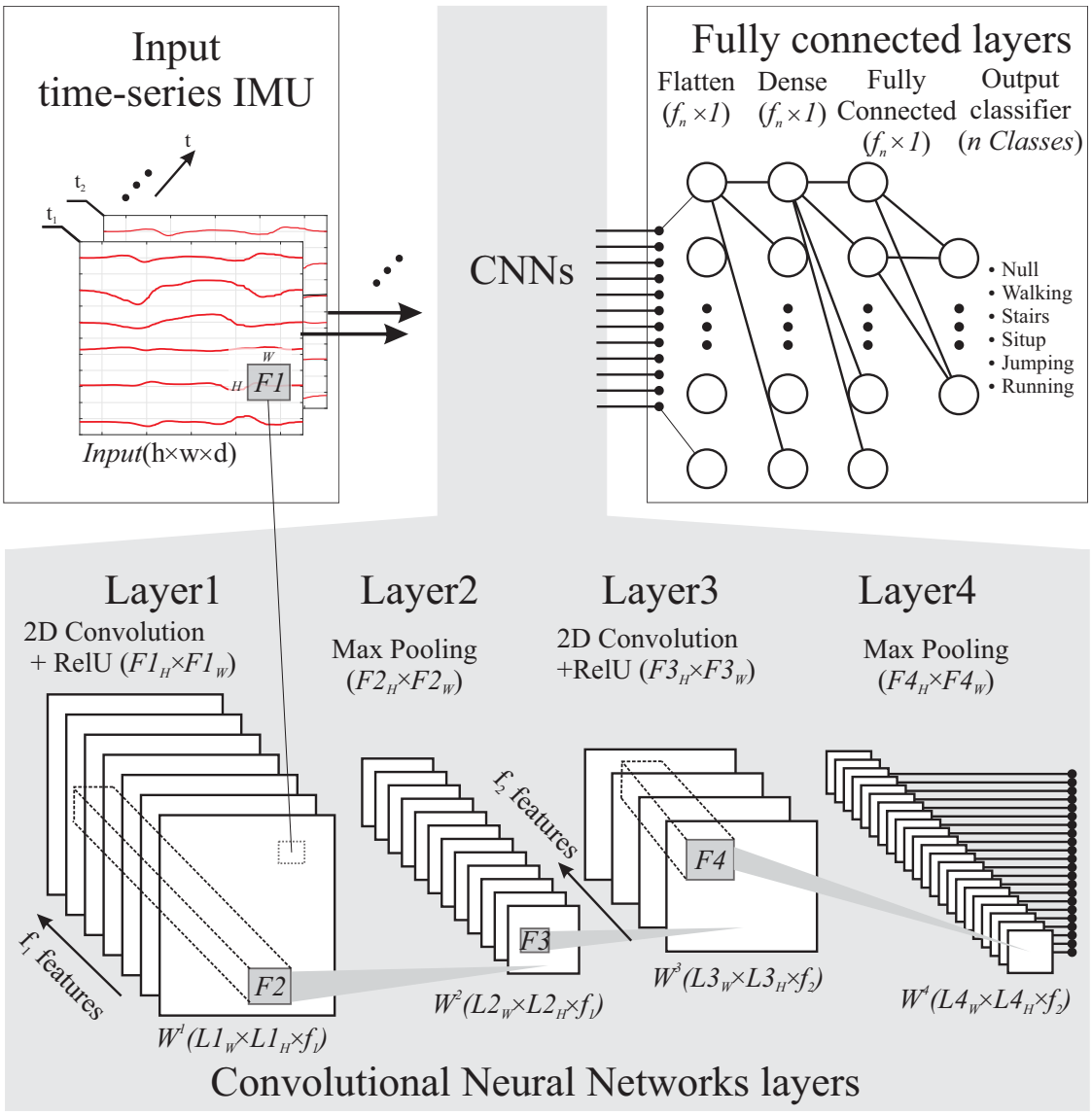

Figure 5.4: The implemented deep CNN architecture for classification

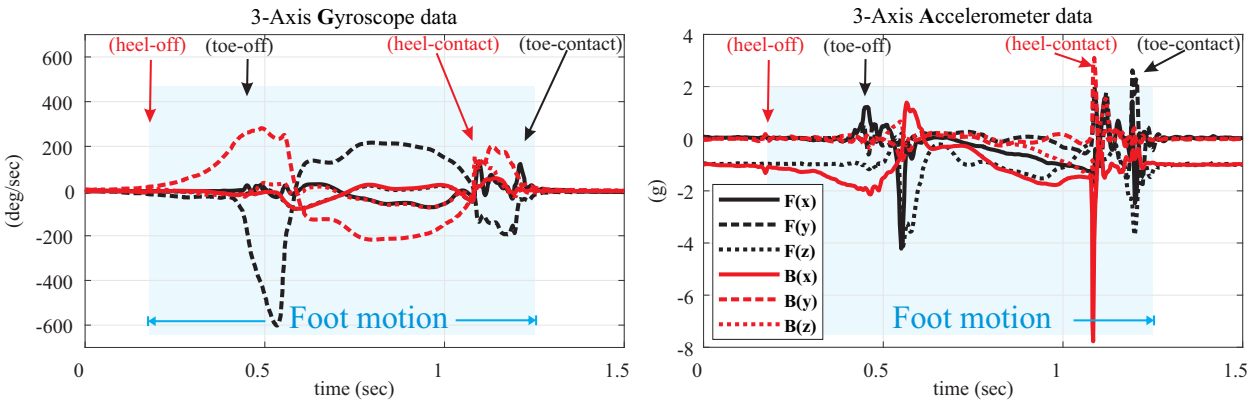

Figure 5.5: Experimental raw data from two IMUs of walking (3-axis gyroscope and 3-axis accelerometer) mounted to forefoot (F) and heel (B) area of the shoe (swing phase shown here).

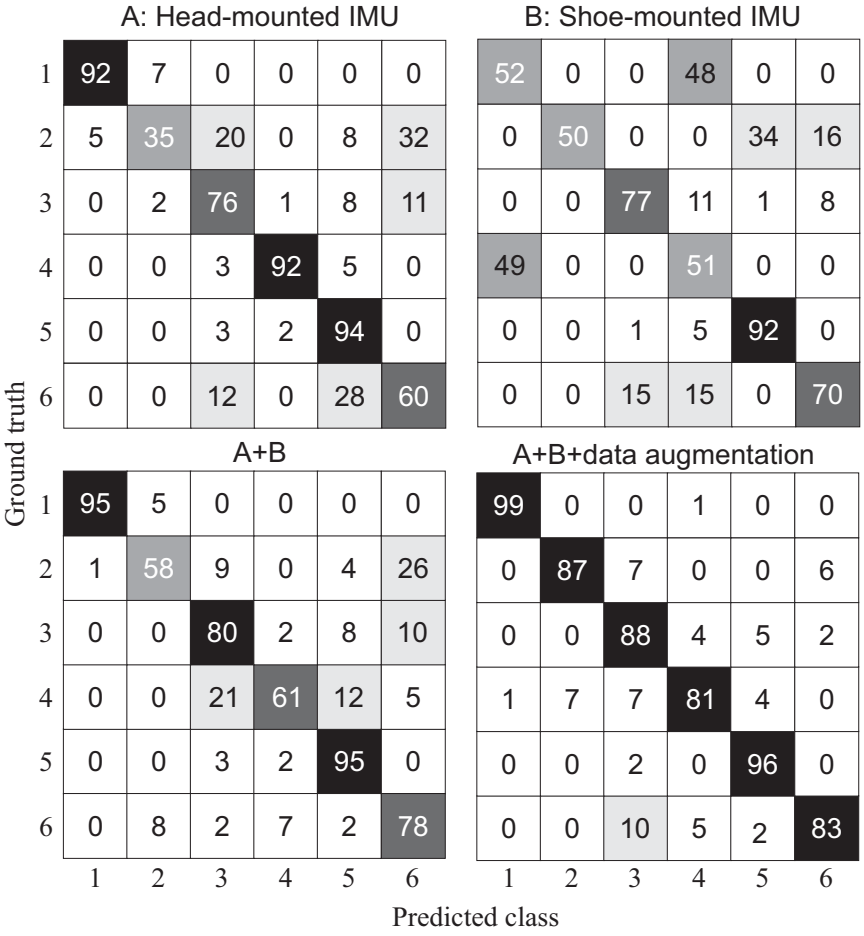

Figure 5.6: Confusion matrix on the data set considering four different configurations. Classes are 1)standing still, 2)walking, 3)walking up and down stairs, 4)standing up and sitting down, 5)jumping, and 6)running. Due to rounding of percentages, the summation of each row might not add up to 100.

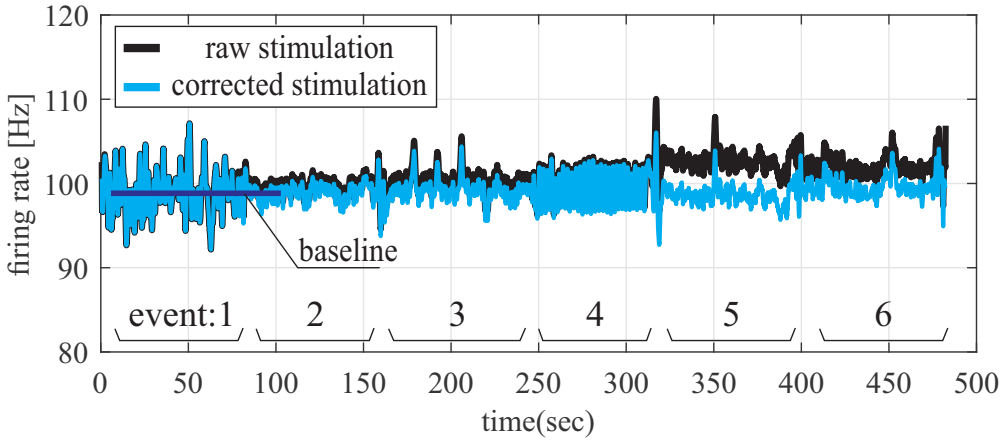

Figure 5.7: An example showing a correction of sensitivity of head-mounted IMU using activities, labeled 1 through 6 classifications, to calibrate the Z-axis (perpendicular to the transverse plane of the body) proportional to the firing rate.

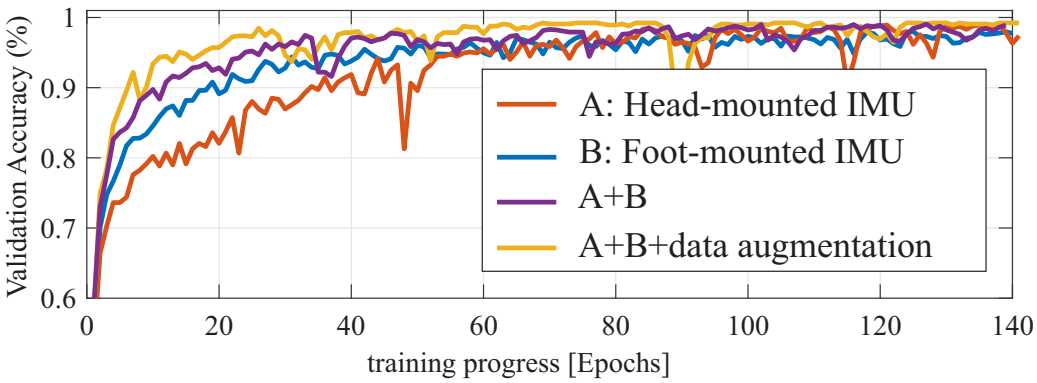

Figure 5.8: Normalized accuracy of the implemented CNN on the recorded dataset.

Chapter 6

An Electrical Stimulation Platform with Cuff Electrode

In previous chapters, we discussed the structure, the electronics, the control algorithms, and calibration methods needed for a MEMS gyroscope to be used for a vestibular prosthesis. In this chapter, we look into the development of the prosthesis as a system for delivering current pulses to the nerve.

6.1 Introduction

A closed-loop vestibular prosthesis unit requires an IMU for sensing rotation, a controller for implementation of the algorithm, and an electrical stimulating circuit to deliver stimulus pulses. Fig. 6.1 shows the conceptual schematic of the electrical current stimulation triggered by an input rotation. Due to challenges involved in locating the vestibular nerve in an animal model, a platform was then designed with an extra purpose on facial reanimation that utilizes electromyographic (EMG) input coupled to a chronically implanted multichannel cuff electrode (MCE). This was done to restore instantaneous, volitional, and selective hemifacial movement in a feline model, where the animal model has been pursued in a different laboratory. Therefore, a neuroprosthetic prototype approach with a switching mechanism between input rotation and EMG input for both vestibular prosthesis and facial reanimation was developed, to be described next.

The translation of 3D rotation using an IMU with 3-gyroscope and 3-accelerometer to biphasic current stimulation pulses was first integrated into the "MPU-9250 CA-SDK" evaluation board. The experimental result of this implementation on gyroscope data and its corresponding stimulus is shown in Fig. 6.2. X, Y, and Z denote the gyroscope sensing axes. The highest sensitivity is on the axis where the rotation is being applied, where each gyroscope encodes its sensing information to pulses using the model introduced by [4] described Chapter 1.

Facial nerve (FN) injury can cause permanent facial paralysis or paresis (FP), which can result in substantial clinical impairment, [195–197]. Deficits include dysfunctions with facial expression, proper enunciation and communication, proper blink function and corneal protection, and maintenance of oral competency. One approach to facial reanimation is the application of neuroprosthetic technologies to facial reanimation. In such a system, detection of movement from the normal hemiface could instantaneously activate the same muscles on

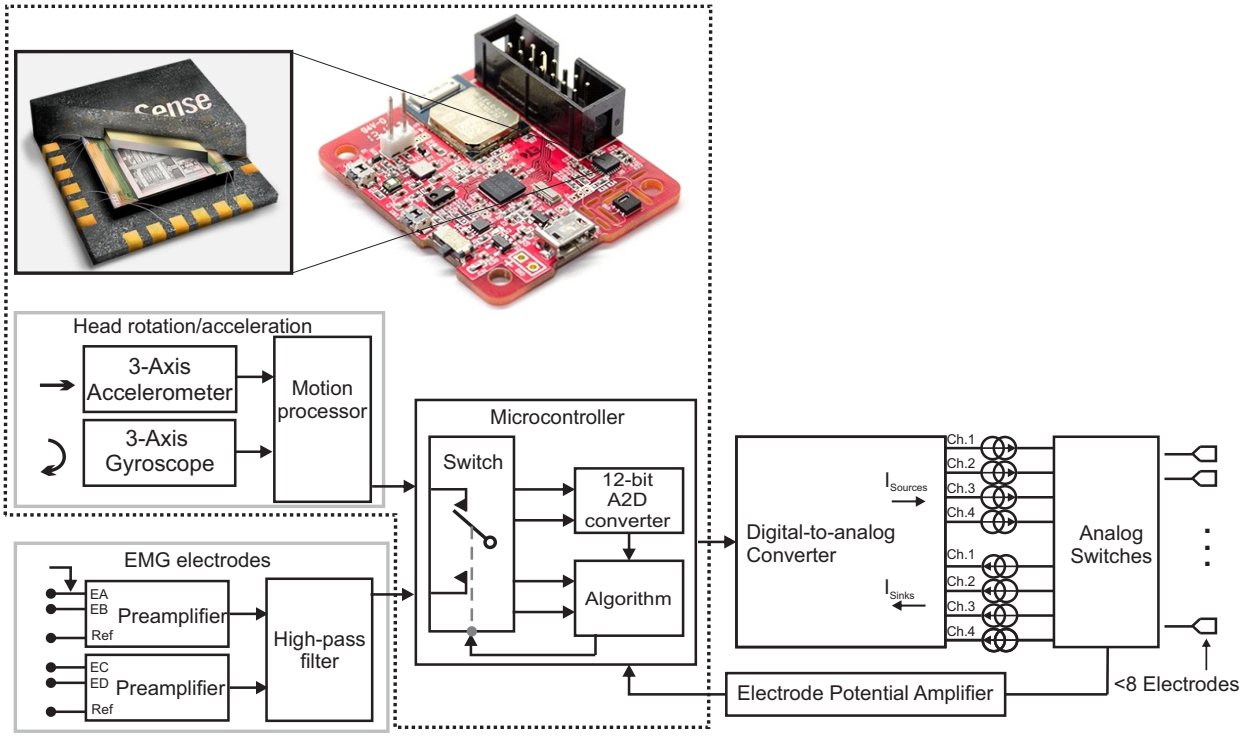

Figure 6.1: Block diagram of the proposed architecture to investigate the integration with implantable electrode, where the algorithm implementation was integrated in the microcontroller, and the system as whole was evaluated in facial reanimation.

the contralateral paralyzed hemiface. Therefore a neuroprosthetic devices that can directly stimulate cranial nerves is needed. Furthermore, we aim to expand the functionality of existing cuff electrode approaches by taking advantage of the ability of multichannel cuff MCEs to selectively stimulate motor nerve fascicles and subsequently result in selective muscle activation. To demonstrate the feasibility of a closed-loop device for stimulation, we detect and process human EMG input through a developed prototype, and deliver current to a MCE chronically implanted on a feline FN that subsequently results in concentric hemifacial contraction of discrete muscles.

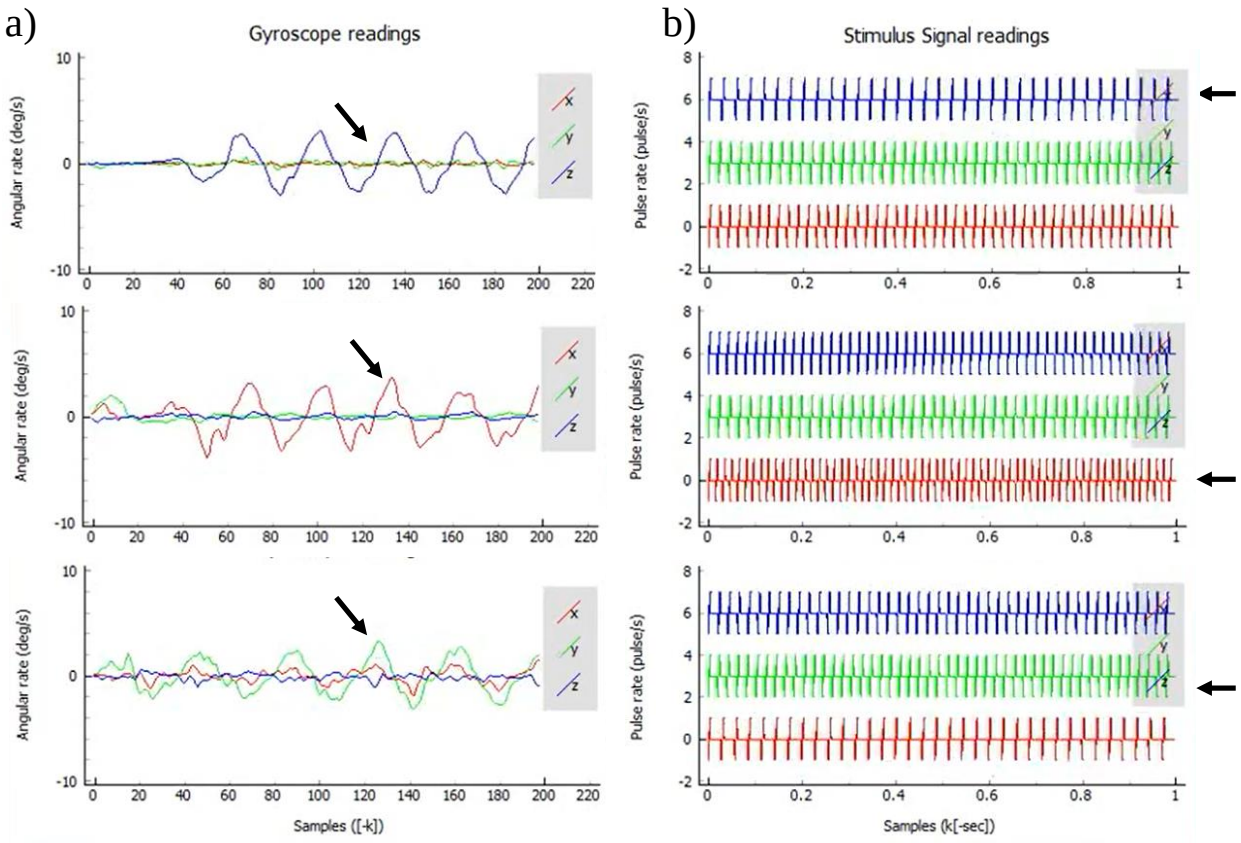

Figure 6.2: Experimental results of multichannel rotation to biphasic pulses: a) gyroscope reading in (deg/sec), b)corresponding biphasic stimulus. Each rows shows different response to physical rotation applied to the prototype. From top to bottom, Z-axis, X-axis and Y-axis rotations. The arrow represents the axis with the highest rotation and dense train of pulses.

6.2 Method

6.2.1 Animals

All procedures were conducted in accordance with the NIH Animal Welfare Guidelines and with a protocol approved by the Institutional Animal Care and Use Committee at the University of California at Irvine. One female domestic shorthaired cats (Felis catus) was obtained from a research breeding colony at the University of California at Davis. The cat was recorded for seven months post-electrode implantation.

6.2.2 Anesthesia

A light level of anesthesia was induced with an intramuscular injection of 0.7 mL of ketamine (20 mg/kg) and 0.3 mL of acepromazine (1 mg/kg); with a booster dose of 0.3 mL of ketamine given when necessary to maintain stable sedation.

6.2.3 MCE Specifications

A custom 8-channel MCE (MicroProbes for Life Science, Gaithersburg, MD, USA) with an inner diameter of 1.5 mm was used. The MCE contained two "rings" of electrodes with each ring containing 4 individual 100 µm rectangular (tripolar) platinum contacts housed within a silicon enclosure. Each electrode was positioned at 0°, 90°, 180° and 270° around the ring, and perpindicular to the neural epineurium (Fig. 6.3). This configuration allowed for monopolar stimulation of four discrete neural locations within each ring, which ultimately allowed for eight individual contact points with the nerve. Field steering allowed for stimulation of 2 (or more) contacts simultaneously.

6.2.4 Surgical Implantation

A pre-auricular incision was made under sterile conditions and dissection through the parotid gland proceeded until the FN trunk was identified and skeletonized. The MCE was positioned at the main trunk of the FN, and fastened shut with incorporated nylon sutures.

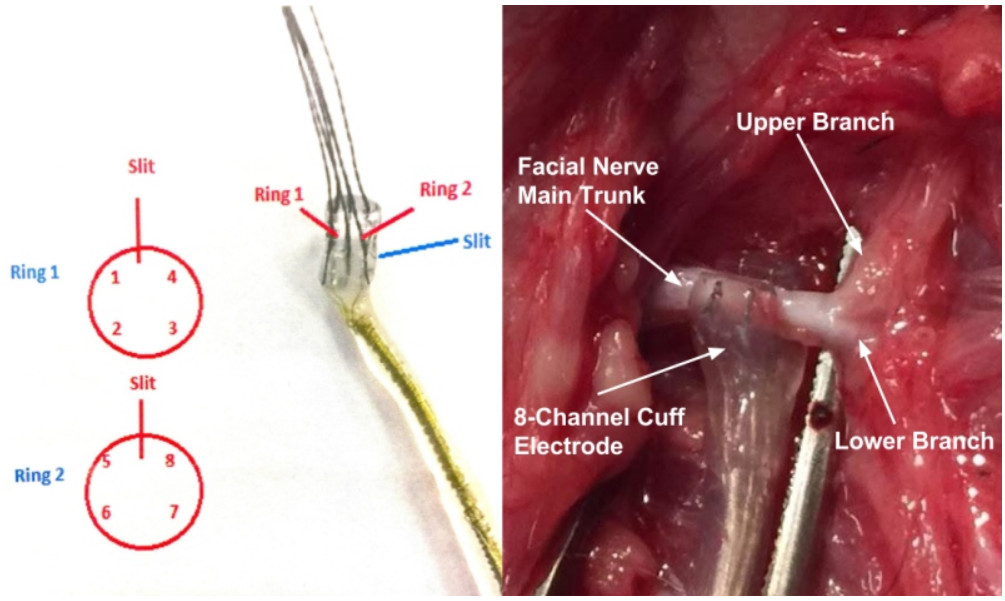

Figure 6.3: Integrated platform with cuff electrode. a) 8-channel MCE with 2 electrode "rings", each with 4 rectangular platinum electrodes in a silicon enclosure 90° apart, b) An intraoperative image of the implanted MCE, [198].

6.2.5 Stimulus Generation

Two different set-ups were used to generate biphasic electrical pulses (82 µs duration/phase). In the first set-up, a commercially off the shelf analog and digital controller (*TDTCS*), electrical pulses were generated by a custom optically isolated 16-channel current sources controlled by 16-bit digital-to-analog converters (TDT RX8). Each channel had a maximum output of 1 mA and four different current intensity were tested: ∼(1, 0.56 and 0.36) mA. In order to better investigate EMG responses, in this phase of our study we presented only a single biphasic pulse rather than train of pulses. This allowed us to have artifact-free EMG, as the stimulus artifact was confined to the first 1 ms of data.

In the second set-up (*Portable Platform*), a miniaturized EMG-driven current source was developed, Fig. 6.4. This platform includes an EMG pre-amplifier, analog EMG signal conditioning, an 8-bits microcontroller, buffer electronic circuitry, current source, and digital switches to generate a biphasic current stimulus and with an onboard Li-ion battery for

power management. The platform is capable of mapping EMG data to biphasic electrical current pulses in response to detection of EMG activity. Raw EMG activity from volitional human muscle activity was detected and recorded by three surface skin electrodes (one active and one reference electrode were used for recording the signal and the third was used as a ground electrode), and enhanced by an EMG preamplifier (INA333). The EMG activity was high-pass filtered to eliminate DC voltage (cut-off frequency = 1 Hz) and was connected to the 10-bit Analog-to-Digital converter of the ATmega32U4 microcontroller (MCU). The microcontroller was programmed to read and process EMG input data every 16 µs and to control the current source and the frequency of the digitally controlled switch arrays (ADG611). The platform, therefore, becomes a closed loop EMG feedback controller which is capable of delivering biphasic current pulses when EMG activity surpasses a certain threshold. For this study, the maximum current level up to ∼1.33 mA was utilized. Circuit power consumption including the microcontroller at full operation under EMG activity was measured to be 330 mW. For the purpose of this study, which was to compare EMG recorded between the developed *Portable Platform* and *TDTCS*, we limited the stimulation to a single biphasic pulse, even though the platform has the flexibility to generate a train of pulses to any rate, the only limitation being the ADC frequency conversion, see AppendixC-PCBC.1.5 for detailed development of this prototype.

6.2.6 Electromyography (EMG)

Following biphasic current delivery to a MCE channel, EMG activity from concentric muscle contraction in the feline hemiface was detected and recorded using TDT hardware with clinical sub-dermal electrodes. Four active electrodes were used to record from four different facial muscles: *levator, orbicularis oris, orbicularis oculi* and *nasalis*. The reference and the ground were placed in the lateral/long *triceps* head on the front limb of the cat. The sampling frequency was 24,414 Hz. The TDTCS set-up included a high-pass digital filter

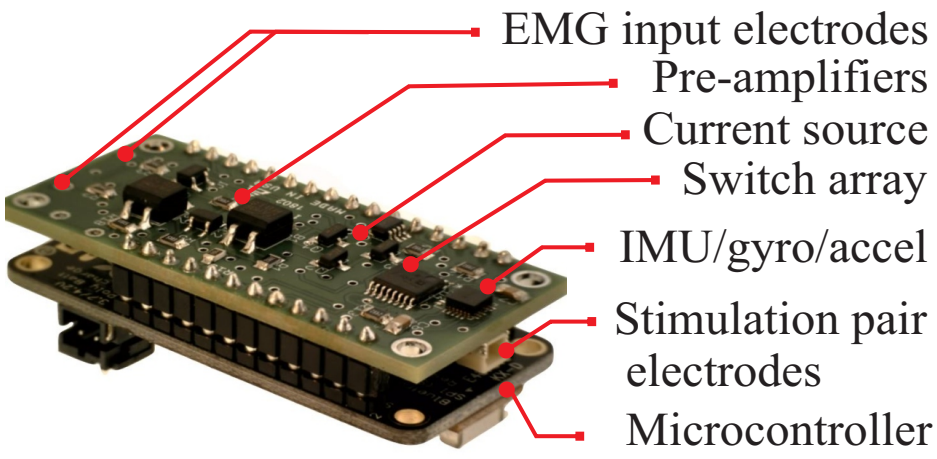

Figure 6.4: The developed dual purpose input rotation and EMG-driven nerve stimulation prototype. A custom daughter board was developed to interface with the commercially available Adafruit Feather 32u4 microcontroller.

with a cut-off frequency at 10 Hz, while the prototype set-up included a high-pass digital filter with a cut-off frequency at 1 Hz. The signal was down-sampled in real-time to 3,052 Hz and then band-pass filtered offline using a 4th order Butterworth filter (100 to 1,500 Hz).

6.3 Experimental Results

TDTCS set-up

Fig. 6.6a, shows the results when using the TDTCS set-up and stimulating facial muscles through channel 1 of the MCE. The first 1 ms of the waveform represents stimulus artifact elicited by the biphasic electrical pulse. *Levator* and *nasalis* were activated when applying a current of 1 mA and resulting EMG activity was observed at around 5 ms following stimulus onset. Conversely, no EMG was detected from *oris* and *oculi*. As the intensity of the current was decreased down to 0.56 mA, excellent muscle selectivity was achieved. At this current level, EMG activity from only the *levator* muscle was recorded, while the other three muscles

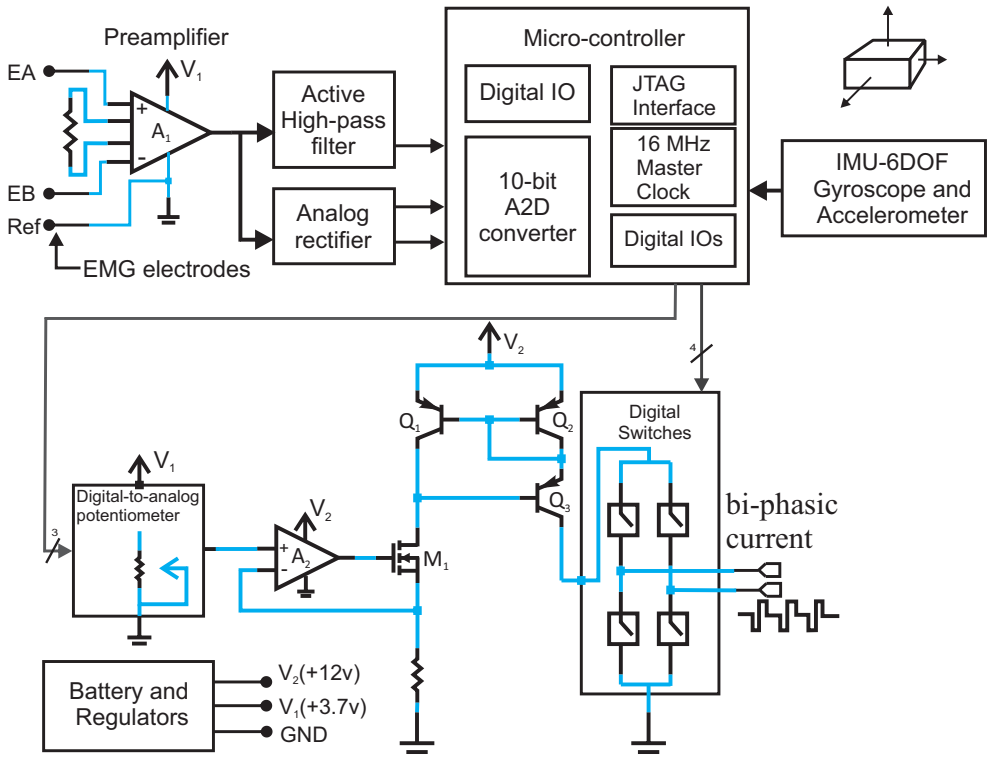

Figure 6.5: Detailed circuit schematic of the EMG-driven biphasic current stimulator. Input EMG data are processed and translated to output-current stimulus amplitude which ultimately activated feline facial muscles.

remained "silent".The current intensity of 0.3 mA was not sufficient to stimulate any of the four muscles and only stimulus artifact was recorded.

Developed set-up vs. TDTCS set-up:

Figure 6.6b shows the EMG responses recorded from a representative muscle (*nasalis*) elicited by current delivered by the TDTCS set-up (panel A) and the developed prototype (panel B). The waveform generated from the prototype demonstrates good agreement with the waveform triggered by the TDTCS set-up, in terms of both the strength of the response (similar amplitude values) and the latency (∼5 ms) of the most prominent positive peak post stimulus onset. As we increased the current level up to ∼1 mA, this selectivity is partially lost and EMG from the *nasalis* is also detected. The activation of two muscles

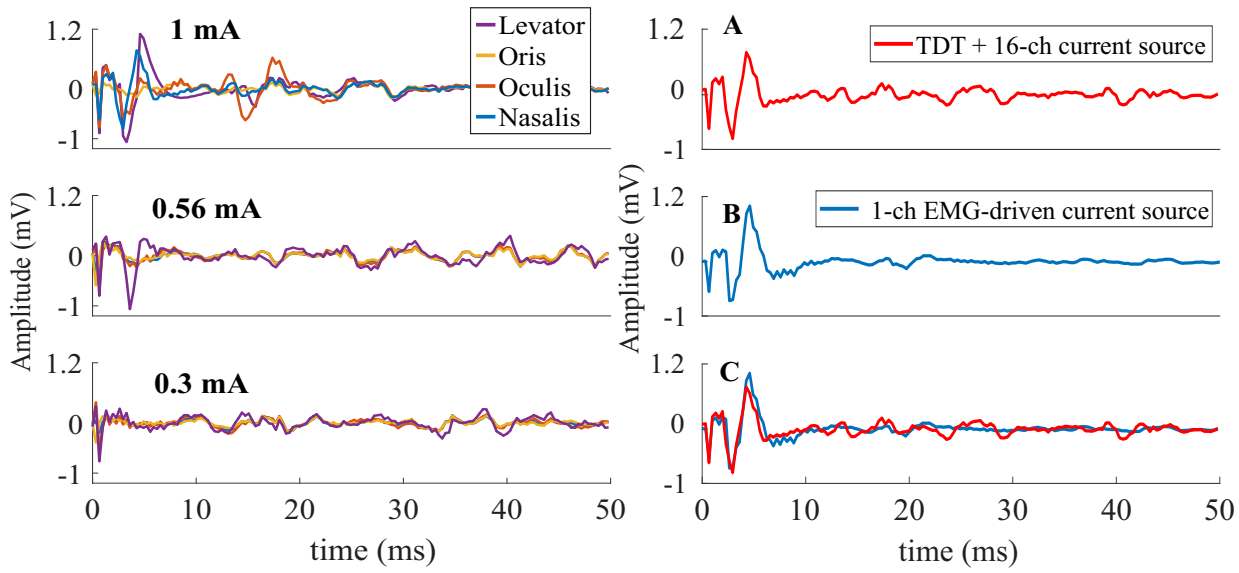

(a) Increase in stimulation current amplitude. The best selectivity was achieved at 0.56 mA, where only *levator* was activated.

(b) Response elicited by the TDTCS set-up (A), by the developed prototype (B), comparison of both comparable (C).

Figure 6.6: Demonstration of functionality of the prototype with integrated with electrodes, a)EMG recorded simultaneously during the first 7 months from four muscles: *levator, oris, oculi* and *nasalis* b) EMG responses recorded at month 7 from *nasalis*

at 1 mA is likely due to the spread of excitation elicited by the increase in current being delivered.

6.4 Conclusion

This chapter explored facial nerve stimulation and emphasized its similarities with a vestibular prosthesis. These similarities include the following: sensing input, analog readout electronics, microcontroller, biphasic pulse generator, and cuff electrodes. We presented the development of a miniaturized neuroprosthetic device to provide both vestibular nerve stimulation and closed-loop facial reanimation system. We demonstrated the feasibility of the prototype integrated for nerve stimulation, where the implanted MCE to the prototype device utilizes volitional EMG input to deliver biphasic current pulses to specific MCE channels. We described the architecture implemented on electronics to interfere with multichannel cuff

electrodes. In parallel, we validated the encoding process of multiple channel rotation to biphasic current pulses using the same MCU. Following the validation of both functionalities, we expect that the developed platform could ultimately be used for the vestibular nerve when an animal model is available.

Chapter 7

Conclusion

This dissertation reports on the algorithm design and calibration requirements for a MEMS gyroscope sensor used for a vestibular prosthesis. We approach this problem by first understanding the contribution of drift on the existing neural dynamic model in literature and identifying the requirements. A MEMS gyroscope structure with highly symmetric features was used as a test structure to investigate the sensitivity limit of the prosthesis. The device was instrumented in both rate and rate integrating mode of operations to identify the algorithm limitations on the dynamic response of the prosthesis and the challenges involved in the implementation are studied. The primary focus of this thesis was to develop different characterization platforms to investigate and identify sources of error resulted from short-term (in-run) and long-term drifts, whether on a fabricated sensor or a commercially available IMU. An aiding calibration for vestibular prosthesis was proposed by fusing external sensors reading from foot-mounted IMU. The work presented focuses on the sensor and system-level characterizations on control of MEMS gyroscopes sensors. The specific contributions are detailed next.

7.1 Contributions of the Dissertation

- It has been analyzed in this thesis that utilizing low-cost MEMS gyroscope for vestibular prosthesis has played a significant role in drifting of the produced electrical stimulation pulses. The design requirement for utilizing a MEMS gyroscope for the prosthesis was identified and the in-run bias instability is set to be $0.02\,^{\circ}/\mathrm{s}$ at 15 ms averaging time to mimic the sensitivity and latency of the VOR.

- Demonstrated experimentally a miniaturize MEMS gyroscope sensor can detect the sensitivity needed for the prosthesis. To achieve required sensitivity a vacuum sealed silicon Quad Mass Gyroscope (QMG) with the Q-factor on the level of higher than 2 million was utilized and noise performance was investigated. The short-term stability parameters of the device were compared to 1,000 and 25,000 Q-factor devices of the same design. We demonstrated a possibility of achieving with MEMS devices $0.09\,^{\circ}/\mathrm{hr}$ bias instability and a $0.01\,^{\circ}/\sqrt{\mathrm{hr}}$ ARW in the rate mode of operation with no thermal compensations on the device level. We demonstrated that a higher Q-factor resulted in higher frequency stability, thus in lower rate random walk. These outcomes were predicted by our analytic analysis and supported in this paper experimentally. We showed that a higher Q-factor and a lower frequency split can lead to noise performance improvement by >100 fold in ARW, bias, and RRW.

- Demonstrated that the sensor scale-factor nonlinearity on the dynamic range is an important characteristic in vestibular prosthesis for use in operation. The dependency of the scale-factor nonlinearity on control loops was investigated in different combinations of algorithms. We demonstrated that force-to-rebalance resulted in a linear full-scale dynamic range. The tradeoff between bandwidth and sensitivity was shown experimentally on a CVG with different Q-factors operating in the open-loop rate mode. We showed that a realistic MEMS gyroscope with imperfections (nearly matched, but non-

zero frequency asymmetry), a higher Q-factor would increase the frequency stability of the drive axis resulting in improved noise performance.

- For the studied device considered for the prosthesis, it was demonstrated that the rate and rate integrating mode of operations complement each other in the dynamic range of operation. The developed architecture for each mode was described and the hardware requirements were defined and designed.

- A long-term calibration algorithm was proposed by virtual carouseling mechanism. The algorithm were implemented for error identification on a device with Q-factor of above 2 million. The frequency mismatch variations were identified by virtual carouseling and used for compensation. A feed-forward correction algorithm was implemented to retrospectively correct for the drift of angular gain in the whole-angle mode of operation.

- Demonstrated that vestibular prosthesis can benefit from multi-sensor fusion for event detection. An event-based detection algorithm was proposed for the correction of the device scale factor for the vestibular prosthesis. As a result, a flexible platform was developed for integration and processing data from multiple foot-mounted inertial sensors. The architecture to fused multiple sensors was described. The limitation imposed on sampling and noise performance of the system was reported.

- A standalone characterization electronics platform was developed for full gyroscope characterization to identify the needed algorithms for a prosthesis. A multi-stage approach was considered for this universal architecture, provides flexibility to different characterization methods and adaptability to different sensor configurations. The platform enables investigation of control algorithms in an evaluation DSP controller for ease of integration and reduced design time. The limitation on performance was discussed by the selection of different components. The design challenges related to analog and digital signal conditioning as well as the power consumption were reported.

- A dual-purpose electrical current stimulation platform integrated with an implantable multichannel cuff electrode was developed for the prosthesis. The prototype was designed to translate motion reading from IMU or electromyographic (EMG) reading from muscle activity into biphasic pulses. This neuroprosthetic prototype enabled closed-loop current stimulation to the nerve. The prototype enabled the selectivity of the multichannel electrode simulation. The functionality of this miniaturized prototype was also validated against in custom off the shelf electrical stimulation.

7.2 Future Research Directions

7.2.1 Animal experiments

One avenue for future research is to answer research questions arising from the animal model. The efficacy of the calibration methods suggested for the vestibular system in the animal model needs to be investigated.

7.2.2 Miniaturization of Vestibular Prosthesis

The integration of silicon MEMS gyroscopes along with the requirement of front-end circuits with necessary digital control algorithms as a system for vestibular prosthesis was demonstrated as part of this thesis. The analog parts and the described digital controllers parts, PLL and AGC can be realized by circuit components using CMOS technology. Therefore, the system can be realized in a CMOS/MEMS technology which leads to the miniaturization of the vestibular prosthesis for implantation. The research on the sensitivity of this miniaturization is still unknown and yet to be explored.

7.2.3 Custom Microelectrode Array

Surgery in proximity to the inner ear bones can cause scarring and damage to the tissue. Complication as a result of cochlear surgery in animal studies shows impairment of hearing organs and remains an important concern [49, 199]. Due to the difficulties with the microsurgery and precision of implantable microelectrode surgery, the bioelectrical current that travels through the vestibular nerve may cause hearing loss [200]. To overcome this limitation, a custom microelectrode array with functional selectivity is needed to be developed for stimulating precisely the vestibular organ. Recent patents of design methodology on electrode structure [201–206] suggest a more flexible electrode in terms of placement and number of contacts is needed. Therefore the development of a custom electrode for selectivity of the vestibular nerve branch puts a present immerse challenge in system development for future research.

7.2.4 Embedded Calibration Algorithms with Motion Sensor

The developed calibration algorithm with the fusion of multiple IMUs for vestibular prosthesis presented in this dissertation uses a centralized approach, where huge data was acquired and prepossessed by single controller and features were ultimately extracted using machine learning techniques. However in the vestibular prosthesis, fast response and low latency are needed, so the computing must be done locally. From a system-level point of view, dealing with huge data at once is complex and not optimized in power and performance. By bringing the computation to the edge, the IMU motion pre-processing and extraction of features can be done locally in one single unit without any controller using finite state machines [207]. This not only benefits the power optimization but also opens the possibility to explore new research areas on high-level features extracted from multiple sensor fusion.

7.2.5 Enhancement of Calibration Performance

The calibration algorithm developed for a vestibular prosthesis in this thesis uses sensor fusion from multiple mounted IMUs. The training coefficients can be trained to the individual patients; therefore, augmentation on the small dataset is needed. For example, in image classification tasks, recent literature reports the use of "Hide-and-Seek" to existing data augmentation methods, which benefits the performance of the classification [208]. The technique works by hiding randomly different areas in each image to force the network to seek features when the most discriminative feature is hidden. This technique or based on similar algorithms could be adopted on event identification on time series data for classification and calibration. For example, in a representation of stacked IMU data, an algorithm can randomly hide regions of step in motion, so the network is forced to train its coefficients in areas of non-motion.

7.2.6 Overcoming Algorithmic Limitations

As demonstrated in this dissertation, fabrication imperfection sets a limit on full-scale sensitivity in the rate mode or sets a minimum detection in the WA mode of operations. Therefore, control algorithms functioned in the complement of each other. Some literature suggest simultaneously operating control loops or a stage platform that switches between modes of operation in the application [166]. However, these techniques have not been explored for a prosthesis application application in which the latency is important and would need to be explored in the future.

Bibliography

[1] A. Talasaz and R. V. Patel. Integration of force reflection with tactile sensing for minimally invasive robotics-assisted tumor localization. *IEEE Trans. Haptics*, 6(2):217–228, 2012.

[2] J. Shih and A. Dunn. Pressure sensing in implantable drug pumps, June 2019. US Patent 10,307,530.

[3] A. M. Shkel. Precision navigation and timing enabled by microtechnology: Are we there yet? In *IEEE Sensors Conf.*, Kona, HI, USA, Nov. 1–4, 2010.

[4] C. C. Della Santina, A. A. Migliaccio, and A. H. Patel. A multichannel semicircular canal neural prosthesis using electrical stimulation to restore 3-D vestibular sensation. *IEEE Trans. Biomed. Eng.*, 54(6 Pt 1):1016–1030, 2007.

[5] W. Gong and D. M. Merfeld. Prototype neural semicircular canal prosthesis using patterned electrical stimulation. *Ann. Biomed. Eng.*, 28(5):572–581, 2000.

[6] A. Shkel, J. Liu, C. Ikei, and F.-G. Zeng. Feasibility study on a prototype of vestibular implant using MEMS gyroscopes. In *IEEE Sensors Conf.*, Orlando, FL, USA, June 12–14, 2002.

[7] N. Yazdi, F. Ayazi, and K. Najafi. Micromachined inertial sensors. *Proc. IEEE*, 86(8):1640–1659, 1998.

[8] J. M. Goldberg and C. Fernandez. Physiology of peripheral neurons innervating semicircular canals of the squirrel monkey. I. Resting discharge and response to constant angular accelerations. *J. Neurophysiology*, 34(4):635–660, 1971.

[9] Y. Valko, R. F. Lewis, A. J. Priesol, and D. M. Merfeld. Vestibular labyrinth contributions to human whole-body motion discrimination. *J. Neuroscience*, 32(39):13537–13542, 2012.

[10] G. Wilson. Cardiac implantable demand pacemaker, Nov. 1969. US Patent 3,478,746.

[11] T. Cameron. Safety and efficacy of spinal cord stimulation for the treatment of chronic pain: A 20-year literature review. *Journal of Neurosurgery: Spine*, 100(3):254–267, 2004.

[12] R. V. Shannon. Multichannel electrical stimulation of the auditory nerve in man. I. basic psychophysics. *Hearing Research*, 11(2):157–189, 1983.

[13] A. L. Benabid. Deep brain stimulation for parkinsons disease. *Current Opinion in Neurobiology*, 13(6):696–706, 2003.

[14] O. N. Markand, J. C. Kincaid, R. A. Pourmand, S. S. Moorthy, R. D. King, Y. Mahomed, and J. W. Brown. Electrophysiologic evaluation of diaphragm by transcutaneous phrenic nerve stimulation. *Neurology*, 34(5):604–614, 1984.

[15] Y. Agrawal, J. P. Carey, C. C. Della Santina, M. C. Schubert, and L. B. Minor. Disorders of balance and vestibular function in US adults: Data from the national health and nutrition examination survey, 2001-2004. *Arch. Intern. Med.*, 169(10):938–44, 2009.

[16] F. Lin. *One in Five Americans Has Hearing Loss*, 2011. `http://www.hopkinsmedicine.org/`.

[17] Y. Agrawal, J. P. Carey, C. C. Della Santina, M. C. Schubert, and L. B. Minor. Diabetes, vestibular dysfunction, and falls: Analyses from the national health and nutrition examination survey. *Otology and Neurotology*, 31(9):1445–1450, 2010.

[18] J. P. Boyle, A. A. Honeycutt, K. V. Narayan, T. J. Hoerger, L. S. Geiss, H. Chen, and T. J. Thompson. Projection of diabetes burden through 2050. *Diabetes Care*, 24(11):1936–1940, 2001.

[19] F. Martini, M. J. Timmons, R. B. Tallitsch, W. C. Ober, C. W. Garrison, K. B. Welch, and R. T. Hutchings. *Human anatomy*. Pearson Education, Inc., publishing as Pearson Benjamin Cummings, San Francisco, CA, 2011. ISBN: 978-0-321-68815-6.

[20] C. Fernandez and J. M. Goldberg. Physiology of peripheral neurons innervating otolith organs of the squirrel monkey. I. Response to static tilts and to long-duration centrifugal force. *J. Neurophysiology*, 39(5):970–984, 1976.

[21] L. Grabherr, K. Nicoucar, F. W. Mast, and D. M. Merfeld. Vestibular thresholds for yaw rotation about an earth-vertical axis as a function of frequency. *Experimental Brain Research*, 186(4):677–681, 2008.

[22] G. M. Jones and L. R. Young. Subjective detection of vertical acceleration: a velocity-dependent response? *Acta Otolaryngolica*, 85(1-2):45–53, 1978.

[23] G. M. Jones and J. H. Milsum. Frequency-response analysis of central vestibular unit activity resulting from rotational stimulation of the semicircular canals. *J. Physiology*, 219(1):191–215, 1971.

[24] V. A. Sadovnichii, V. V. Aleksandrov, T. B. Aleksandrova, A. A. Konik, B. V. Pakhomov, G. Y. Sidorenko, E. Soto, K. V. Tikhonova, and N. E. Shulenina. Mathematical simulation of correction of output signals from the gravitoinertial mechanoreceptor of a vestibular apparatus. *Moscow University Mechanics Bulletin*, 68(5):111–116, 2013.

[25] D. M. Merfeld, C. Haburcakova, W. Gong, and R. F. Lewis. Chronic vestibulo-ocular reflexes evoked by a vestibular prosthesis. *IEEE Trans. Biomed. Eng.*, 54(6):1005–1015, 2007.

[26] F. Corradi, D. Zambrano, M. Raglianti, G. Passetti, C. Laschi, and G. Indiveri. Towards a neuromorphic vestibular system. *IEEE Trans. Biomed. Circuits Syst.*, 8(5):669–680, 2014.

[27] T. A. K. Nguyen, M. Ranieri, J. DiGiovanna, O. Peter, V. Genovese, A. P. Fornos, and S. Micera. A real-time research platform to study vestibular implants with gyroscopic inputs in vestibular deficient subjects. *IEEE Trans. Biomed. Circuits Syst.*, 8(4):474–484, 2014.

[28] C. Mack. Headgear position and impact sensor, Aug. 2012. US Patent App. 13/354,003.

[29] D. M. Merfeld, A. Priesol, D. Lee, and R. F. Lewis. Potential solutions to several vestibular challenges facing clinicians. *J. Vestibul. Res. Equil.*, 20(1):71–77, 2010.

[30] S. C. Kim, J. Y. Kim, H. N. Lee, H. H. Lee, J. H. Kwon, N. B. Kim, M. J. Kim, J. H. Hwang, and G. C. Han. A quantitative analysis of gait patterns in vestibular neuritis patients using gyroscope sensor and a continuous walking protocol. *J. Neuroeng. Rehabilitation*, 11:58, 2014.

[31] A. Pérez Fornos, N. Guinand, R. van de Berg, R. Stokroos, S. Micera, H. Kingma, M. Pelizzone, and J. P. Guyot. Artificial balance: Restoration of the vestibulo-ocular reflex in humans with a prototype vestibular neuroprosthesis. *Frontiers in Neurology*, 5:66, 2014.

[32] J. Hegeman, F. Honegger, M. Kupper, and J. H. Allum. The balance control of bilateral peripheral vestibular loss subjects and its improvement with auditory prosthetic feedback. *J. Vestibul. Res. Equil.*, 15(2):109–117, 2005.

[33] J. T. Rubinstein, S. Bierer, C. Kaneko, L. Ling, K. Nie, T. Oxford, S. Newlands, F. Santos, F. Risi, P. J. Abbas, and J. O. Phillips. Implantation of the semicircular canals with preservation of hearing and rotational sensitivity: A vestibular neurostimulator suitable for clinical research. *Otology and Neurotology*, 33(5):789–796, 2012.

[34] A. M. Shkel and F.-G. Zeng. An electronic prosthesis mimicking the dynamic vestibular function. *Audiology and Neurotology*, 11:113–122, 2006.

[35] R. F. Lewis. Vestibular prostheses investigated in animal models. *J. Oto-Rhino-Laryngology (ORL)*, 77(4):219–226, 2015.

[36] C. Haburcakova, R. F. Lewis, and D. M. Merfeld. Frequency dependence of vestibuloocular reflex thresholds. *J. Neurophysiology*, 107(3):973–983, 2012.

[37] C. Wall, D. M. Merfeld, S. D. Rauch, and F. O. Black. Vestibular prostheses: The engineering and biomedical issues. *J. Vestibul. Res. Equil.*, 12(2–3):95–113, 2002.

[38] V. Rodionov, J. Elidan, M. Nitzan, M. Sela, and H. Sohmer. Vertical plane short and middle latency vestibular evoked potentials in humans. *Annals of Otology, Rhinology & Laryngology*, 105(1):43–48, 1996.

[39] C. Della Santina. A device to restore balance. *Scientific American*, 302:68–71, 2010.

[40] K. Nie, L. Ling, S. M. Bierer, C. R. Kaneko, A. F. Fuchs, T. Oxford, J. T. Rubinstein, and J. O. Phillips. An experimental vestibular neural prosthesis: Design and preliminary results with rhesus monkeys stimulated with modulated pulses. *IEEE Trans. Biomed. Eng.*, 60(6):1685–1692, 2013.

[41] B. Chiang, G. Y. Fridman, C. Dai, M. A. Rahman, and C. C. D. Santina. Design and performance of a multichannel vestibular prosthesis that restores semicircular canal sensation in rhesus monkey. *IEEE Trans. Neural Syst. Rehabil. Eng.*, 19(5):588–598, 2011.

[42] C. C. Della Santina, A. A. Migliaccio, R. Hayden, T. A. Melvin, G. Y. Fridman, B. Chiang, N. S. Davidovics, C. Dai, J. P. Carey, L. B. Minor, I. C. Anderson, H. Park, S. Lyford-Pike, and S. Tang. Current and future management of bilateral loss of vestibular sensation - an update on the Johns Hopkins Multichannel Vestibular Prosthesis Project. *Cochlear Implants Int.*, 11 Suppl 2:2–11, 2010.

[43] R. C. Fitzpatrick and B. L. Day. Probing the human vestibular system with galvanic stimulation. *Journal of Applied Physiology*, 96(6):2301–2316, 2004.

[44] Y. P. Danilov, M. E. Tyler, K. L. Skinner, R. A. Hogle, and P. Bach-y Rita. Efficacy of electrotactile vestibular substitution in patients with peripheral and central vestibular loss. *J. Vestibul. Res. Equil.*, 17(2–3):119–130, 2007.

[45] A. C. Nau, C. Pintar, A. Arnoldussen, and C. Fisher. Acquisition of visual perception in Blind Adults Using the BrainPort Artificial Vision Device. *Am J Occup Ther*, 69(1):1–8, 2015.

[46] N. Vuillerme, N. Pinsault, A. Fleury, O. Chenu, J. Demongeot, Y. Payan, and P. Pavan. Effectiveness of an electro-tactile vestibular substitution system in improving upright postural control in unilateral vestibular-defective patients. *Gait & Posture*, 28(4):711–715, 2008.

[47] B. D. Lawson, A. H. Rupert, and S. M. Legan. Vestibular Balance Deficits Following Head Injury: Recommendations Concerning Evaluation and Rehabilitation in the Military Setting, 2012.

[48] R. Van De Berg, N. Guinand, J.-P. Guyot, H. Kingma, and R. J. Stokroos. The modified ampullar approach for vestibular implant surgery: Feasibility and its first application in a human with a long-term vestibular loss. *Frontiers in Neurology*, 3:18, 2012.

[49] M. Pelizzone, A. P. Fornos, N. Guinand, R. van de Berg, I. Kos, R. Stokroos, H. Kingma, and J. P. Guyot. first functional rehabilitation via vestibular implants. *Cochlear Implants Int.*, 15 Suppl. 1:S62–S64, 2014.

[50] N. Guinand, R. Van de Berg, S. Cavuscens, R. Stokroos, M. Ranieri, M. Pelizzone, H. Kingma, J.-P. Guyot, and A. Pérez Fornos. Restoring visual acuity in dynamic conditions with a vestibular implant. *Frontiers in Neuroscience*, 10(577), 2016.

[51] N. Guinand, R. Van de Berg, S. Cavuscens, M. Ranieri, E. Schneider, F. Lucieer, H. Kingma, J.-P. Guyot, and A. Pérez Fornos. The video head impulse test to assess the efficacy of vestibular implants in humans. *Frontiers in Neurology*, 8:600, 2017.

[52] L. A. Thompson, C. Haburcakova, and R. F. Lewis. A distinctive platform system to study the effects of a vestibular prosthesis on nonhuman primate postural control. *Journal of Engineering and Science in Medical Diagnostics and Therapy*, 1(2), Feb. 2018.

[53] W. Jiang and S. M. Rajguru. Eye movements evoked by pulsed infrared radiation of the rat vestibular system. *Ann. Biomed. Eng.*, 46(9):1406–1418, 2018.

[54] C. Fernandez and J. M. Goldberg. Physiology of peripheral neurons innervating semicircular canals of the squirrel monkey. II. Response to sinusoidal stimulation and dynamics of peripheral vestibular system. *J. Neurophysiology*, 34(4):661–675, 1971.

[55] T. G. Constandinou, J. Georgiou, and C. Toumazou. A neural implant ASIC for the restoration of balance in individuals with vestibular dysfunction. In *IEEE Int. Symp. Circuits and Syst.*, Taipei, Taiwan, May 24–27 2009.

[56] C. M. Andreou, Y. Pahitas, and J. Georgiou. Bio-inspired micro-fluidic angular-rate sensor for vestibular prostheses. *Sensors*, 14(7):13173–13185, 2014.

[57] H. Töreyin and P. T. Bhatti. A low-power ASIC signal processor for a vestibular prosthesis. *IEEE Trans. Biomed. Circuits Syst.*, 10(3):768–778, 2016.

[58] K. N. Hageman, Z. K. Kalayjian, F. Tejada, B. Chiang, M. A. Rahman, G. Y. Fridman, C. Dai, P. O. Pouliquen, J. Georgiou, C. C. D. Santina, and A. G. Andreou. A CMOS neural interface for a multichannel vestibular prosthesis. *IEEE Trans. Biomed. Circuits Syst.*, 10(2):269–279, 2016.

[59] A. Gonshor and G. M. Jones. Extreme vestibulo-ocular adaptation induced by prolonged optical reversal of vision. *J. Physiology*, 256(2):381–414, 1976.

[60] G. Y. Fridman, N. S. Davidovics, C. Dai, A. A. Migliaccio, and C. C. Della Santina. Vestibulo-ocular reflex responses to a multichannel vestibular prosthesis incorporating a 3D coordinate transformation for correction of misalignment. *J. Assoc. Res. Otolaryngol.*, 11(3):367–381, 2010.

[61] J. DiGiovanna, J. Carpaneto, S. Micera, and D. M. Merfeld. Alignment of angular velocity sensors for a vestibular prosthesis. *J. Neuroeng. Rehabilitation*, 9(1):14, 2012.

[62] E. Soto-Eguibar, M. De Miera, T. Alexandrova, V. Aleksandrov, M. Romero, A. Carrillo, and W. Sanchez. Vestibular prosthesis, 2014. US Patent 8,855,774.

[63] D. Jiang, D. Cirmirakis, and A. Demosthenous. A vestibular prosthesis with highly-isolated parallel multichannel stimulation. *IEEE Trans. Biomed. Circuits Syst.*, 9(1):124–137, 2015.

[64] P. J. Boutros, N. Valentin, K. N. Hageman, D. Roberts, C. Dai, and C. C. Della Santina. Temporal discretization errors produce minimal effects on vestibular prosthesis performance. *J. Medical Devices*, 10(3/030958):1–3, 2016.

[65] R. Vivacqua, R. Vassallo, and F. Martins. A low cost sensors approach for accurate vehicle localization and autonomous driving application. *Sensors*, 17(10), 2017.

[66] R. Neul, U. Gomez, K. Kehr, W. Bauer, J. Classen, C. Doring, E. Esch, S. Gotz, J. Hauer, B. Kuhlmann, C. Lang, M. Veith, and R. Willig. Micromachined angular rate sensors for automotive applications. *IEEE Sensors J.*, 7(2):302–309, 2007.

[67] R. Xu, S. Zhou, and W. J. Li. MEMS accelerometer based nonspecific-user hand gesture recognition. *IEEE Sensors J.*, 12(5):1166–1173, 2012.

[68] P. Daponte, L. D. Vito, F. Picariello, and M. Riccio. State of the art and future developments of the augmented reality for measurement applications. *Measurement*, 57:53–70, 2014.

[69] T. Li, G. Yuan, and W. Li. Particle filter with novel nonlinear error model for miniature gyroscope-based measurement while drilling navigation. *Sensors*, 16(3):371, 2016.

[70] L. I. Iozan, M. Kirkko-Jaakkola, J. Collin, J. Takala, and C. Rusu. Using a MEMS gyroscope to measure the earth's rotation for gyrocompassing applications. *Meas. Sci. Technol.*, 23(2/025005):1–8, 2012.

[71] T. K. Tang, R. C. Gutierrez, J. Z. Wilcox, C. Stell, V. Vorperian, R. Calvet, W. J. Li, I. Charkaborty, R. Bartman, and W. J. Kaiser. Silicon bulk micromachined vibratory gyroscope. In *Solid-State Sensors, Actuators, and Microsystems Workshop*, Hilton Head Island, SC, USA, June 3–6, 1996.

[72] Z. Wang, M. Poscente, D. Filip, M. Dimanchev, and M. P. Mintchev. Rotary in-drilling alignment using an autonomous MEMS-based inertial measurement unit for measurement-while-drilling processes. *IEEE Instrum. Meas. Mag.*, 16(6):26–34, 2013.

[73] A. A. Trusov, A. R. Schofield, and A. M. Shkel. Micromachined tuning fork gyroscopes with ultra-high sensitivity and shock rejection, Dec. 2012. US Patent 8,322,213.

[74] B. R. Simon, A. A. Trusov, and A. M. Shkel. Anti-phase mode isolation in tuning-fork MEMS using a lever coupling design. In *IEEE Sensors Conf.*, Taipei, Taiwan, Oct. 28–31 2012.

[75] B. R. Simon. *Mode Ordering in Anti-Phase Driven MEMS Gyroscopes and Accelerometers*. PhD dissertation, University of California, Irvine, 2014.

[76] B. R. Simon, A. A. Trusov, and A. M. Shkel. Lever mechanisms for anti-phase mode isolation in MEMS tuning-fork structures, Dec. 2015. US Patent 9,217,756.

[77] B. R. Simon, S. Khan, A. A. Trusov, and A. M. Shkel. Mode ordering in tuning fork structures with negative structural coupling for mitigation of common-mode g-sensitivity. In *IEEE Sensors Conf.*, Busan, South Korea, Nov. 1–5, 2015.

[78] A. A. Trusov, I. P. Prikhodko, S. A. Zotov, A. R. Schofield, and A. M. Shkel. Ultra-high Q silicon gyroscopes with interchangeable rate and whole angle modes of operation. In *IEEE Sensors Conf.*, Waikoloa, HI, USA, Nov. 1–4, 2010.

[79] C. Acar and A. M. Shkel. *MEMS vibratory gyroscopes – structural approaches to improve robustness*. Springer Science & Business Media, Boston, MA, 2009. ISBN (print): 978-0-387-09535-6.

[80] M. H. Asadian, S. Askari, and A. M. Shkel. An ultrahigh vacuum packaging process demonstrating over 2 million Q-factor in MEMS vibratory gyroscopes. *IEEE Sensors Letters*, 1(6):1–4, 2017.

[81] A. M. Shkel. Type I and type II micromachined vibratory gyroscopes. In *IEEE/ION Position Location and Navigation Symposium*, Coronado, CA, USA, Apr. 25–27, 2006.

[82] M. S. Weinberg and A. Kourepenis. Error sources in in-plane silicon tuning-fork MEMS gyroscopes. *IEEE/ASME J. Microelectromech. Syst.*, 15(3):479–491, 2006.

[83] M. Saukoski, L. Aaltonen, and K. A. I. Halonen. Zero-rate output and quadrature compensation in vibratory MEMS gyroscopes. *IEEE Sensors J.*, 7(12):1639–1652, 2007.

[84] S. E. Alper and T. Akin. A single-crystal silicon symmetrical and decoupled MEMS gyroscope on an insulating substrate. *IEEE/ASME J. Microelectromech. Syst.*, 14(4):707–717, 2005.

[85] M. F. Zaman, A. Sharma, and F. Ayazi. High performance matched-mode tuning fork gyroscope. In *IEEE Int. Conf. Micro Electro Mechanical Systems*, Istanbul, Turkey, Jan. 22–26 2006.

[86] S. Park and R. Horowitz. Adaptive control for the conventional mode of operation of MEMS gyroscopes. *IEEE/ASME J. Microelectromech. Syst.*, 12(1):101–108, 2003.

[87] M. W. Putty. *A micromachined vibrating ring gyroscope*. PhD dissertation, University of Michigan, 1995.

[88] P. Minotti, S. Dellea, G. Mussi, A. Bonfanti, S. Facchinetti, A. Tocchio, V. Zega, C. Comi, A. L. Lacaita, and G. Langfelder. High scale-factor stability frequency-modulated MEMS gyroscope: 3-axis sensor and integrated electronics design. *IEEE Trans. Ind. Electron.*, 65(6):5040–5050, 2018.

[89] A. A. Trusov, A. R. Schofield, and A. M. Shkel. Performance characterization of a new temperature-robust gain-bandwidth improved MEMS gyroscope operated in air. *Sensors and Actuators A: Physical*, 155(1):16–22, 2009.

[90] Y. S. Suh. Attitude estimation using low cost accelerometer and gyroscope. In *Korea-Russia Int. Symp. Sci. Technol. (KORUS)*, Pasadena, CA, USA, June 28–July 6 2003.

[91] L. Joseph and N. Elwood. Rate and attitude indicating instrument, Feb. 1943. US Patent 2,309,853.

[92] D. D. Lynch. Coriolis vibratory gyros. In *Symposium Gyro Technology*, Stuttgart, Germany, Sept. 15–16, 1998.

[93] I. P. Prikhodko, S. A. Zotov, A. A. Trusov, and A. M. Shkel. Foucault pendulum on a chip: Rate integrating silicon MEMS gyroscope. In *Sensors and Actuators A: Physical*, volume 177, pages 67–78, 2012.

[94] A. A. Trusov, G. Atikyan, D. M. Rozelle, A. D. Meyer, B. R. Simon, and A. M. Shkel. Force rebalance, whole angle, and self-calibration mechanization of silicon MEMS quad mass gyro. In *IEEE Int. Symp. Inertial Sensors and Systems*, Laguna Beach, CA, USA, Feb. 25–26, 2014.

[95] ITmems S.r.l. MEMS Characterization Platform, Product Data-Sheet. [Online]. accessed Jan. 2016. `http://www.itmems.it`.

[96] E. Margan. Transimpedance amplifier analysis. *Technical report*, 1:1–19, 2012. `http://www-f9.ijs.si/~margan/Articles/trans_z_amplifier.pdf`.

[97] F. Ayazi and K. Najafi. A HARPSS polysilicon vibrating ring gyroscope. *IEEE/ASME J. Microelectromech. Syst.*, 10(2):169–179, 2001.

[98] J. Y. Cho, J. Woo, J. Yan, R. L. Peterson, and K. Najafi. Fused-silica micro birdbath resonator gyroscope (μ-BRG). *IEEE/ASME J. Microelectromech. Syst.*, 23(1):66–77, 2014.

[99] C. T.-C. Nguyen. *Micromechanical signal processors*. PhD dissertation, University of California, Berkeley, 1994.

[100] D. Senkal, M. J. Ahamed, M. H. A. Ardakani, S. Askari, and A. M. Shkel. Demonstration of 1 million Q-factor on microglassblown wineglass resonators with out-of-plane electrostatic transduction. *IEEE/ASME J. Microelectromech. Syst.*, 24(1):29–37, 2015.

[101] R. McCroskey. Universal inertial testing system (UITS) device under test (DUT) specification. *Honeywell International Inc.*, pages 1–21, 2012. V5.

[102] E. Foxlin. Pedestrian tracking with shoe-mounted inertial sensors. *IEEE Comput. Graph.*, 25(6):38–46, 2005.

[103] M. Romanovas, V. Goridko, A. Al-Jawad, M. Schwaab, M. Traechtler, L. Klingbeil, and Y. Manoli. A study on indoor pedestrian localization algorithms with foot-mounted sensors. In *IEEE Int. Conf. Indoor Positioning and Indoor Navigation*, Sydney, Australia, Nov. 13–15, 2012.

[104] J. Nilsson, A. K. Gupta, and P. Händel. Foot-mounted inertial navigation made easy. In *IEEE Int. Conf. Indoor Positioning and Indoor Navigation*, Busan, South Korea, Oct. 27–30, 2014.

[105] M. Laverne, M. George, D. Lord, A. Kelly, and T. Mukherjee. Experimental validation of foot to foot range measurements in pedestrian tracking. In *Proceedings of the 24th International Technical Meeting of The Satellite Division of the Institute of Navigation (ION GNSS)*, Portland, OR, USA, Sept. 19-23, 2011.

[106] J. Cao and C. T.-C. Nguyen. Drive amplitude dependence of micromechanical resonator series motional resistance. In *Int. Conf. Solid-State Sensors and Actuators (TRANSDUCERS)*, volume 10, Sendai, Japan, June 7–10, 1999.

[107] K. Y. Yasumura, T. D. Stowe, E. M. Chow, T. Pfafman, T. W. Kenny, B. C. Stipe, and D. Rugar. Quality factors in micron- and submicron-thick cantilevers. *IEEE/ASME J. Microelectromech. Syst.*, 9(1):117–125, 2000.

[108] S. Zotov, B. Simon, G. Sharma, J. Han, I. Prikhodko, A. Trusov, and A. Shkel. Investigation of energy dissipation in low frequency vibratory. MEMS demonstrating a resonator with 25 minutes time constant. In *Solid-State Sensors, Actuators, and Microsystems Workshop*, Hilton Head Island, SC, USA, June 8–12, 2014.

[109] S. Askari, M. H. Asadian, K. Kakavand, and A. M. Shkel. Near-navigation grade quad mass gyroscope with Q-factor limited by thermo-elastic damping. In *Solid-State Sensors, Actuators, and Microsystems Workshop*, Hilton Head Island, SC, USA, June 5–9, 2016.

[110] Y. Wang, S. Askari, C.-S. Jao, and A. M. Shkel. Directional ranging for enhanced performance of aided pedestrian inertial navigation. In *IEEE Int. Symp. Inertial Sensors and Systems*, Naples, FL, USA, Apr. 1–5, 2019.

[111] K. V. Poletkin, J. G. Korvink, and V. Badilita. Mechanical thermal noise in micromachined levitated two-axis rate gyroscopes. *IEEE Sensors J.*, 18(4):1390–1402, 2018.

[112] R. P. Leland. Mechanical-thermal noise in MEMS gyroscopes. *IEEE Sensors J.*, 5(3):493–500, 2005.

[113] V. Apostolyuk and F. E. Tay. Dynamics of micromechanical coriolis vibratory gyroscopes. *Sensor Letters*, 2(3–4):252–259, 2004.

[114] A. A. Trusov, A. R. Schofield, and A. M. Shkel. Micromachined rate gyroscope architecture with ultra-high quality factor and improved mode ordering. *Sensors and Actuators A: Physical*, 165(1):26–34, 2011.

[115] M. S. Kranz and G. K. Fedder. Micromechanical vibratory rate gyroscope fabricated in conventional CMOS. In *Symposium Gyro Technology*, Stuttgart, Germany, Sept. 16–17, 1997.

[116] J. A. Geen and J. Kuang. Cross-quad and vertically coupled inertial sensors, Sept. 2008. US Patent 7,421,897.

[117] I. P. Prikhodko, S. A. Zotov, A. A. Trusov, and A. M. Shkel. Sub-degree-per-hour silicon MEMS rate sensor with 1 million Q-factor. In *Int. Conf. Solid-State Sensors and Actuators (TRANSDUCERS)*, Beijing, China, June 5–9, 2011.

[118] D. Senkal, A. Efimovskaya, and A. M. Shkel. Dual foucault pendulum gyroscope. In *Int. Conf. Solid-State Sensors and Actuators (TRANSDUCERS)*, Anchorage, AK, USA, June 21–25, 2015.

[119] M. H. Asadian, S. Askari, I. B. Flader, Y. Chen, D. D. Gerrard, D. D. Shin, H.-K. Kwon, T. W. Kenny, and A. M. Shkel. High quality factor mode ordered dual foucault pendulum gyroscope. In *IEEE Sensors Conf.*, New Delhi, India, Oct. 28–31, 2018.

[120] M. H. Asadian, S. Askari, Y. Wang, and A. M. Shkel. Characterization of energy dissipation mechanisms in dual foucault pendulum gyroscopes. In *IEEE Int. Symp. Inertial Sensors and Systems*, Naples, FL, USA, Apr. 1–5, 2019.

[121] A. D. Challoner, H. H. Ge, and J. Y. Liu. Boeing disc resonator gyroscope. In *IEEE/ION Position Location and Navigation Symposium*, Monterey, CA, USA, May 5–8, 2014.

[122] S. Nitzan, C. H. Ahn, T. H. Su, M. Li, E. J. Ng, S. Wang, Z. M. Yang, G. O'Brien, B. E. Boser, T. W. Kenny, and D. A. Horsley. Epitaxially-encapsulated polysilicon disk resonator gyroscope. In *IEEE Int. Conf. Micro Electro Mechanical Systems*, Taipei, Taiwan, Jan. 20–24, 2013.

[123] R. Mirjalili, H. Wen, D. E. Serrano, and F. Ayazi. Substrate-decoupled silicon disk resonators having degenerate gyroscopic modes with Q in excess of 1-million. In *Int. Conf. Solid-State Sensors and Actuators (TRANSDUCERS)*, Anchorage, AK, USA, June 21–25, 2015.

[124] I. P. Prikhodko, A. A. Trusov, and A. M. Shkel. North-finding with 0.004 radian precision using a silicon MEMS quadruple mass gyroscope with Q-factor of 1 million. In *IEEE Int. Conf. Micro Electro Mechanical Systems*, Paris, France, Jan. 29–Feb. 2, 2012.

[125] S. A. Zotov, B. R. Simon, G. Sharma, A. A. Trusov, and A. M. Shkel. Utilization of mechanical quadrature in silicon MEMS vibratory gyroscope to increase and expand the long term in-run bias stability. In *IEEE Int. Symp. Inertial Sensors and Systems*, Laguna Beach, CA, USA, Feb. 25–26, 2014.

[126] A. A. Trusov, D. M. Rozelle, G. Atikyan, S. A. Zotov, B. R. Simon, A. M. Shkel, and A. D. Meyer. Non-axisymmetric coriolis vibratory gyroscope with whole angle, force rebalance, and self-calibration. In *Solid-State Sensors, Actuators, and Microsystems Workshop*, Hilton Head Island, SC, USA, June 8–12, 2014.

[127] B. R. Simon, G. Sharma, S. A. Zotov, A. A. Trusov, and A. M. Shkel. Intrinsic stress of eutectic Au/Sn die attachment and effect on mode-matched MEMS gyroscopes. In *IEEE Int. Symp. Inertial Sensors and Systems*, Laguna Beach, CA, USA, Feb. 25–26, 2014.

[128] A. A. Trusov, G. Atikyan, D. M. Rozelle, A. D. Meyer, S. A. Zotov, B. R. Simon, and A. M. Shkel. Flat is not dead: Current and future performance of Si-MEMS quad mass gyro (QMG) system. In *IEEE/ION Position Location and Navigation Symposium*, Monterey, CA, USA, May 5–8, 2014.

[129] S. Askari, M. H. Asadian, K. Kakavand, and A. M. Shkel. Vacuum sealed and getter activated MEMS quad mass gyroscope demonstrating better than 1.2 million quality factor. In *IEEE Int. Symp. Inertial Sensors and Systems*, Laguna Beach, CA, USA, Feb. 23–25, 2016.

[130] D. Kim and R. M'Closkey. Noise analysis of closed-loop vibratory rate gyros. In *American Control Conference*, Montreal, QC, Canada, June 27–29, 2012.

[131] *IEEE Standard Specification Format Guide and Test Procedure for Coriolis Vibratory Gyros*, 2004. IEEE Std 1431™-1998 (2004).

[132] S. Olcum, N. Cermak, S. C. Wasserman, and S. R. Manalis. High-speed multiple-mode mass-sensing resolves dynamic nanoscale mass distributions. *Nature communications*, 6(7070), 2015.

[133] J. Cui, X. Z. Chi, H. T. Ding, L. T. Lin, Z. C. Yang, and G. Z. Yan. Transient response and stability of the AGC-PI closed-loop controlled MEMS vibratory gyroscopes. *J. Micromechanics and Microengineering*, 19(12/125015):1–17, 2009.

[134] S. E. Alper, Y. Temiz, and T. Akin. A compact angular rate sensor system using a fully decoupled silicon-on-glass MEMS gyroscope. *IEEE/ASME J. Microelectromech. Syst.*, 17(6):1418–1429, 2008.

[135] A. Sharma, M. F. Zaman, M. Zucher, and F. Ayazi. A 0.1°/hr bias drift electronically matched tuning fork microgyroscope. In *IEEE Int. Conf. Micro Electro Mechanical Systems*, Wuhan, China, Jan. 13–17 2008.

[136] G. Langfelder, S. Dellea, A. Berthelot, P. Rey, A. Tocchio, and A. F. Longoni. Analysis of mode-split operation in MEMS based on piezoresistive nanogauges. *IEEE/ASME J. Microelectromech. Syst.*, 24(1):174–181, 2015.

[137] P. Loveday and C. Rogers. The influence of control system design on the performance of vibratory gyroscopes. *J. Sound and Vibration*, 255(3):417–432, 2002.

[138] *IEEE Standard Specification Format Guide and Test Procedure for Linear Single-Axis, Nongyroscopic Accelerometers*, 2011. IEEE Std 1293™-1998 (R2008).

[139] F. L. Walls and J. Gagnepain. Environmental sensitivities of quartz oscillators. *IEEE Transactions on Ultrasonics, Ferroelectrics, and Frequency Control*, 39(2):241–249, 1992.

[140] I. P. Prikhodko, A. A. Trusov, and A. M. Shkel. Compensation of drifts in high-Q MEMS gyroscopes using temperature self-sensing. *Sensors and Actuators A: Physical*, 201:517–524, 2013.

[141] D. Senkal, E. Ng, V. Hong, Y. Yang, C. Ahn, T. Kenny, and A. M. Shkel. Parametric drive of a toroidal MEMS rate integrating gyroscope demonstrating <20 PPM scale factor stability. In *IEEE Int. Conf. Micro Electro Mechanical Systems*, Estoril, Portugal, Jan. 18–22, 2015.

[142] P. Taheri-Tehrani, O. Izyumin, I. Izyumin, C. H. Ahn, E. J. Ng, V. A. Hong, Y. Yang, T. W. Kenny, B. E. Boser, and D. A. Horsley. Disk resonator gyroscope with whole-angle mode operation. In *IEEE Int. Symp. Inertial Sensors and Systems*, Hapuna Beach, HI, USA, Mar. 23–26, 2015.

[143] D. Senkal, A. Efimovskaya, and A. M. Shkel. Minimal realization of dynamically balanced lumped mass WA gyroscope: Dual Foucault Pendulum. In *IEEE Int. Symp. Inertial Sensors and Systems*, Hapuna Beach, HI, USA, Mar. 23–26, 2015.

[144] V. Zhuravlev. Oscillation shape control in resonant systems. *Journal of Applied Mathematics and Mechanics*, 56(5):725–735, 1992.

[145] S. Askari, M. H. Asadian, and A. M. Shkel. High quality factor MEMS gyroscope with whole angle mode of operation. In *IEEE Int. Symp. Inertial Sensors and Systems*, Lake Como, Italy, Mar. 26–29, 2018.

[146] D. M. Rozelle. The hemispherical resonator gyro: From wineglass to the planets. In *AAS/AIAA Space Flight Mechanics Meeting*, Savannah, GA, USA, Feb. 8–12, 2009.

[147] A. D. Meyer and D. M. Rozelle. milli-HRG inertial navigation system. In *IEEE/ION Position Location and Navigation Symposium*, Myrtle Beach, SC, USA, Apr. 24–26, 2012.

[148] R. L. Kubena, R. J. Joyce, and A. D. Challoner. Correlation of frequency, temperature, and bias stability of a Si ring gyro. In *IEEE Int. Symp. Inertial Sensors and Systems*, Laguna Beach, CA, USA, Feb. 23–25, 2016.

[149] G. Remillieux and F. Delhaye. Sagem Coriolis Vibrating Gyros: A vision realized. In *Inertial Sensors and Systems (Symp. Gyro Techn.)*, Karlsruhe, Germany, Sept. 16–17, 2014.

[150] A. A. Trusov, M. R. Phillips, A. Bettadapura, G. Atikyan, G. H. McCammon, J. M. Pavell, Y. A. Choi, D. K. Sakaida, D. M. Rozelle, and A. D. Meyer. mHRG: Miniature CVG with beyond navigation grade performance and real time self-calibration. In *IEEE Int. Symp. Inertial Sensors and Systems*, Laguna Beach, CA, USA, Feb. 23–25, 2016.

[151] P. Taheri-Tehrani, A. D. Challoner, and D. A. Horsley. Micromechanical rate integrating gyroscope with angle-dependent bias compensation using a self-precession method. *IEEE Sensors J.*, 18(9):3533–3543, 2018.

[152] C. Painter and A. M. Shkel. Experimental evaluation of a control system for an absolute angle measuring micromachined gyroscope. In *IEEE Sensors Conf.*, Irvine, CA, USA, Oct. 31–Nov. 3, 2005.

[153] A. M. Shkel, R. Horowitz, A. A. Seshia, , and R. T. Howe. Dynamics and control of micromachined gyroscopes. In *American Control Conference*, volume 3, San Diego, CA, USA, June 2–4, 1999.

[154] D. D. Lynch. Vibratory gyro analysis by the method of averaging. In *The 2nd St. Petersburg Int. Conf. on Gyroscopic Technology and Navigation*, Saint Petersburg, Russia, May 24–25, 1995.

[155] A. D. Meyer, D. M. Rozelle, A. A. Trusov, and D. K. Sakaida. milli-HRG inertial sensor assembly – A reality. In *IEEE/ION Position Location and Navigation Symposium*, Monterey, CA, USA, Apr. 23–26, 2018.

[156] T. Tsukamoto and S. Tanakaa. Fully-differential single resonator FM/whole angle gyroscope using CW/CCW mode separator. In *IEEE Int. Conf. Micro Electro Mechanical Systems*, Las Vegas, NV, USA, Jan. 22-26, 2017.

[157] J. Cho, J. Gregory, and K. Najafi. Single-crystal-silicon vibratory cylinderical rate integrating gyroscope (CING). In *Int. Conf. Solid-State Sensors and Actuators (TRANSDUCERS)*, Beijing, China, June 5–9, 2011.

[158] J. K. Woo, J. Y. Cho, C. Boyd, and K. Najafi. Whole-angle-mode micromachined fused-silica birdbath resonator gyroscope (WA-BRG). In *IEEE Int. Conf. Micro Electro Mechanical Systems*, San Francisco, CA, USA, Jan. 26–30, 2014.

[159] D. Senkal, S. Askari, M. J. Ahamed, E. J. Ng, V. Hong, Y. Yang, C. H. Ahn, T. W. Kenny, and A. M. Shkel. 100k Q-factor toroidal ring gyroscope implemented in wafer-level epitaxial silicon encapsulation process. In *IEEE Int. Conf. Micro Electro Mechanical Systems*, San Francisco, CA, USA, Jan. 26–30, 2014.

[160] J. A. Gregory, J. Cho, and K. Najafi. MEMS rate and rate-integrating gyroscope control with commercial software defined radio hardware. In *Int. Conf. Solid-State Sensors and Actuators (TRANSDUCERS)*, Beijing, China, June 5–9, 2011.

[161] D. Challoner, J. D. Popp, and P. W. Bond. A universal electronics approach for rate integrating gyroscopes. In *IEEE Int. Symp. Inertial Sensors and Systems*, Kauai, HI, USA, Mar. 27–30, 2017.

[162] S. Askari, M. H. Asadian, and A. M. Shkel. Quad mass gyroscope instrumented to operate in the angular rate mode. *IEEE Sensors J.*, Under review.

[163] B. Friedland and M. Hutton. Theory and error analysis of vibrating-member gyroscope. *IEEE Trans. Autom. Control*, 23(4):545–556, 1978.

[164] Z. Hu and B. J. Gallacher. Precision mode tuning towards a low angle drift MEMS rate integrating gyroscope. *Mechatronics*, 56:306–317, 2018.

[165] S. H. Nitzan, P. Taheri-Tehrani, M. Defoort, S. Sonmezoglu, and D. A. Horsley. Countering the effects of nonlinearity in rate-integrating gyroscopes. *IEEE Sensors J.*, 16(10):3556–3563, 2016.

[166] I. P. Prikhodko, J. A. Gregory, D. I. Bugrov, and M. W. Judy. Overcoming limitations of rate integrating gyroscopes by virtual rotation. In *IEEE Int. Symp. Inertial Sensors and Systems*, Laguna Beach, CA, USA, Feb. 23–25, 2016.

[167] I. P. Prikhodko, J. A. Gregory, and M. W. Judy. Virtually rotated MEMS gyroscope with angle output. In *IEEE Int. Conf. Micro Electro Mechanical Systems*, Las Vegas, NV, USA, Jan. 22–26, 2017.

[168] J. A. Gregory, J. Cho, and K. Najafi. Novel mismatch compensation methods for rate-integrating gyroscopes. In *IEEE/ION Position Location and Navigation Symposium*, Myrtle Beach, SC, USA, Apr. 23-26 2012.

[169] C. C. Painter and A. M. Shkel. Identification of anisoelasticity for electrostatic trimming of rate-integrating gyroscopes. In *Smart Structures and Materials: Smart Electronics, MEMS, and Nanotechnology*, San Diego, CA, USA, Mar. 18–20 2002.

[170] C. C. Painter and A. M. Shkel. Active structural error suppression in MEMS vibratory rate integrating gyroscopes. *IEEE Sensors J.*, 3(5):595–606, 2003.

[171] S. J. Herdman and R. Clendaniel. Bilateral vestibular hypofunction. *Vestibular Disorder Association*, 503:1–8, 2014.

[172] G. Paige. Senescence of human visual-vestibular interactions. I. Vestibulo-ocular reflex and adaptive plasticity with aging. *J. Vestibul. Res. Equil.*, 2(2):133–151, 1992.

[173] C. M. N. Brigante, N. Abbate, A. Basile, A. C. Faulisi, and S. Sessa. Towards miniaturization of a MEMS-based wearable motion capture system. *IEEE Trans. Ind. Electron.*, 58(8):3234–3241, 2011.

[174] J. P. Carey. Multichannel vestibular implant early feasibility study, 2016. `https://clinicaltrials.gov/`, identifier: NCT02725463.

[175] S. Sonmezoglu, S. E. Alper, and T. Akin. A high performance automatic mode-matched MEMS gyroscope with an improved thermal stability of the scale factor. In *Int. Conf. Solid-State Sensors and Actuators (TRANSDUCERS)*, Barcelona, Spain, June 16–20, 2013.

[176] J. G. Hanse. Honeywell MEMS inertial technology & product status. In *IEEE/ION Position Location and Navigation Symposium*, Monterey, CA, USA, Apr. 26–29, 2004.

[177] A. Brown and Y. Lu. Performance test results of an integrated GPS/MEMS inertial navigation package. In *Proceedings of the 17th International Technical Meeting of the Satellite Division of The Institute of Navigation (ION GNSS)*, Long Beach, CA, USA, Sept. 21–24, 2004.

[178] B. S. Park, K. Han, S. Lee, and M. Yu. Analysis of compensation for a g-sensitivity scale-factor error for a MEMS vibratory gyroscope. *J. Micromechanics and Microengineering*, 25(11/115006):1–10, 2015.

[179] N. Ravi, N. Dandekar, P. Mysore, and M. L. Littman. Activity recognition from accelerometer data. In *Innovative Applications of Artificial Intelligence (IAAI)*, Pittsburgh, PA, USA, July 9-13, 2005.

[180] J. M. Hansen, J. Rohác, M. Šipoš, T. A. Johansen, and T. I. Fossen. *Validation and Experimental Testing of Observers for Robust GNSS-Aided Inertial Navigation*. Recent Advances in Robotic Systems, InTech, 2016. ISBN (print): 978-953-51-2570-9.

[181] Vectornav Technologies, Dallas, TX 75238 USA. *VN-200 Development Board User Manual*. `https://www.vectornav.com/products/vn-200/documentation/`.

[182] S. Askari, C.-S. Jao, Y. Wang, and A. M. Shkel. A laboratory testbed for self-contained navigation. In *IEEE Int. Symp. Inertial Sensors and Systems*, Naples, FL, USA, Apr. 1–5, 2019.

[183] Y. Wang, S. Askari, and A. M. Shkel. Study on mounting position of IMU for better accuracy of ZUPT-aided pedestrian inertial navigation. In *IEEE Int. Symp. Inertial Sensors and Systems*, Naples, FL, USA, Apr. 1–5, 2019.

[184] Y. Wang, D. Vatanparvar, A. Chernyshoff, and A. M. Shkel. Analytical closed-form estimation of position error on ZUPT-augmented pedestrian inertial navigation. *IEEE Sensors Letters*, 2(4):1–4, 2018.

[185] L. S. Yaeger, R. F. Lyon, and B. J. Webb. Effective training of a neural network character classifier for word recognition. In *Int. Conf. Neural Inform. Process. Syst. (NeurIPS)*, Denver, CO, USA, Dec. 3–5, 1996.

[186] H. Shin, H. R. Roth, M. Gao, L. Lu, Z. Xu, I. Nogues, J. Yao, D. Mollura, and R. M. Summers. Deep convolutional neural networks for computer-aided detection: CNN architectures, dataset characteristics and transfer learning. In *IEEE Trans. Med. Imag.*, volume 35, pages 1285–1298, 2016.

[187] Y. LeCun, Y. Bengio, and G. Hinton. Deep learning. *Nature*, 521(7553):436–444, 2015.

[188] M. Zeng, L. T. Nguyen, B. Yu, O. J. Mengshoel, J. Zhu, P. Wu, and J. Zhang. Convolutional neural networks for human activity recognition using mobile sensors. In *Mobile Computing, Applications and Services (MobiCASE)*, Austin, TX, USA, Nov. 6-7, 2014.

[189] P. Kasnesis, C. Z. Patrikakis, and I. S. Venieris. Perceptionnet: A deep convolutional neural network for late sensor fusion. In *Intelligent Syst. Conf.*, London, UK, Sept. 6–7, 2018.

[190] Y. LeCun and Y. Bengio. Convolutional networks for images, speech, and time series. In M. A. Arbib, editor, *The Handbook of Brain Theory and Neural Networks*, pages 255–258. MIT Press, 1998.

[191] J. Bouvrie. *Notes on Convolutional Neural Networks*, Nov. 2006. `http://cogprints.org/5869/1/cnn_tutorial.pdf`.

[192] M. Lin, Q. Chen, and S. Yan. Network in network. In *Int. Conf. Learn. Representations (ICLR)*, Banff, Canada, Apr. 14–16, 2014.

[193] Google. *Colaboratory: Frequently Asked Questions.*, accessed 2019. `https://research.google.com/colaboratory/faq.html`.

[194] A. Krizhevsky, I. Sutskever, and G. E. Hinton. Imagenet classification with deep convolutional neural networks. In *Advances in neural information processing systems*, pages 1097–1105, 2012.

[195] M. May, R. Wette, W. B. Hardin, and J. Sullivan. The use of steroids in Bell's palsy: A prospective controlled study. *The Laryngoscope*, 86(8):1111–1122, 1976.

[196] M. May, S. R. Klein, and F. H. Taylor. Idiopathic (Bell's) facial palsy: Natural history defies steroid or surgical treatment. *The Laryngoscope*, 95(4):406–409, 1985.

[197] E. Peitersen. Bell's palsy: The spontaneous course of 2,500 peripheral facial nerve palsies of different etiologies. *Acta Oto-Laryngologica*, 122(7):4–30, 2002.

[198] R. Sahyouni. *Neuroprosthetic Approaches to Selective Facial Nerve Stimulation*. PhD dissertation, University of California Irvine, 2018.

[199] C. Dai, G. Y. Fridman, and C. C. Della Santina. Effects of vestibular prosthesis electrode implantation and stimulation on hearing in rhesus monkeys. *Hearing Research*, 277(1-2):204–210, 2011.

[200] T. G. Constandinou, J. Georgiou, C. C. Doumanidis, and C. Toumazou. Towards an implantable vestibular prosthesis: The surgical challenges. In *Int. IEEE/EMBS Conf. Neural Eng.*, Kohala Coast, HI, USA, May 2–5 2007.

[201] D. Mechlenburg and S. Lattner. Vestibular stimulation system and method, Jan. 2013. US Patent 8,355,788.

[202] A. Ramachandran, S. Nielsen, C. Jolly, and M. Zimmerling. Ear implant electrode and method of manufacture, June 2013. US Patent 8,457,764.

[203] A. Shalev. Electrical stimulation in the middle ear for treatment of hearing related disorders, May 2014. US Patent 8,718,786.

[204] J. Webb, M. Bendett, H. Ralph, and J. WELLS. Vestibular implant and method for optical stimulation of nerves, Nov. 2012. US Patent 8,317,848.

[205] P. Berrang, H. Bluger, H. Klosowski, and A. Lupin. Modiolar hugging electrode array, Apr. 2002. US Patent 6,374,143.

[206] C. Jolly and S. Nielsen. Cochlear implant electrode with adjustable subdivision for middle ear functions, Feb. 2012. US Patent 8,126,572.

[207] STMicroelectronics, Geneva, Switzerland. *iNEMO inertial module: Always-on 3D accelerometer and 3D gyroscope Rev. 3.* `https://www.st.com/en/mems-and-sensors/lsm6dsox.html`.

[208] K. K. Singh and Y. J. Lee. Hide-and-Seek: Forcing a network to be meticulous for weakly-supervised object and action localization. In *IEEE Int. Conf. Computer Vision*, Venice, Italy, Oct. 22–29, 2017.

[209] P. D. Groves. *Principles of GNSS, inertial, and multisensor integrated navigation systems*. Artech house, Norwood, MA, 2013. ISBN (print): 978-1608070053.

Appendices

A Development of a Flexible Platform

A.1 Introduction

The specific components of the laboratory testbed system consisted of a National Instruments CompactRIO (NI-cRIO) with programmable FPGA/CPU controller, a wireless communications system, and a laptop (or a tablet) for data display, sending and receiving commands. In this section, we discuss the description of the integration process on the developed hardware architecture for sensor fusion. The communication interfaces used for simultaneous collection of data from two IMUs and two SONARs, the wireless control of the flexible laboratory testbed and the internal network architecture implemented for data transmission are described. The developed architecture offers a wireless communication (802.11b/g standard) for control of the algorithm parameters, data logging, and visualization.

A.2 Decide on a Flexible Hardware, Parts and Interconnects

Activity recognition or monitoring tasks deemed necessary to interact with multiple sensors, such as IMU, ranging and GPS. These sensors vary in their provided output signals (analog or digital) with different communication configurations (SPI, I2C, PWM, or serial). Table A.1, summarizes the available sensors to be used for integration and their manufacture communication protocol. To select a core platform to interact with these sensors, we have selected a National Instruments CompactRIO (NI-9039) system with user-programmable real-time processor and FPGA. The platform was configured per our requirement request as follow: CPU processor with 1.91 GHz Intel quad-core, 2 GB DDR3 RAM and FPGA Xilinx Kintex-7 series 325T in a single chassis. Four digital input/output modules were selected for this system, each with 8 -bit uni-directional I/O channel with resolution speed of 100 ns good enough to establish communication clock speed as high as 15 MHz. A serial module interface was added to the platform with four output ports which will be used for UART communication through RS232 port. Fig. A.1, shows the considered architecture for this

integrated system with multiple sensors.

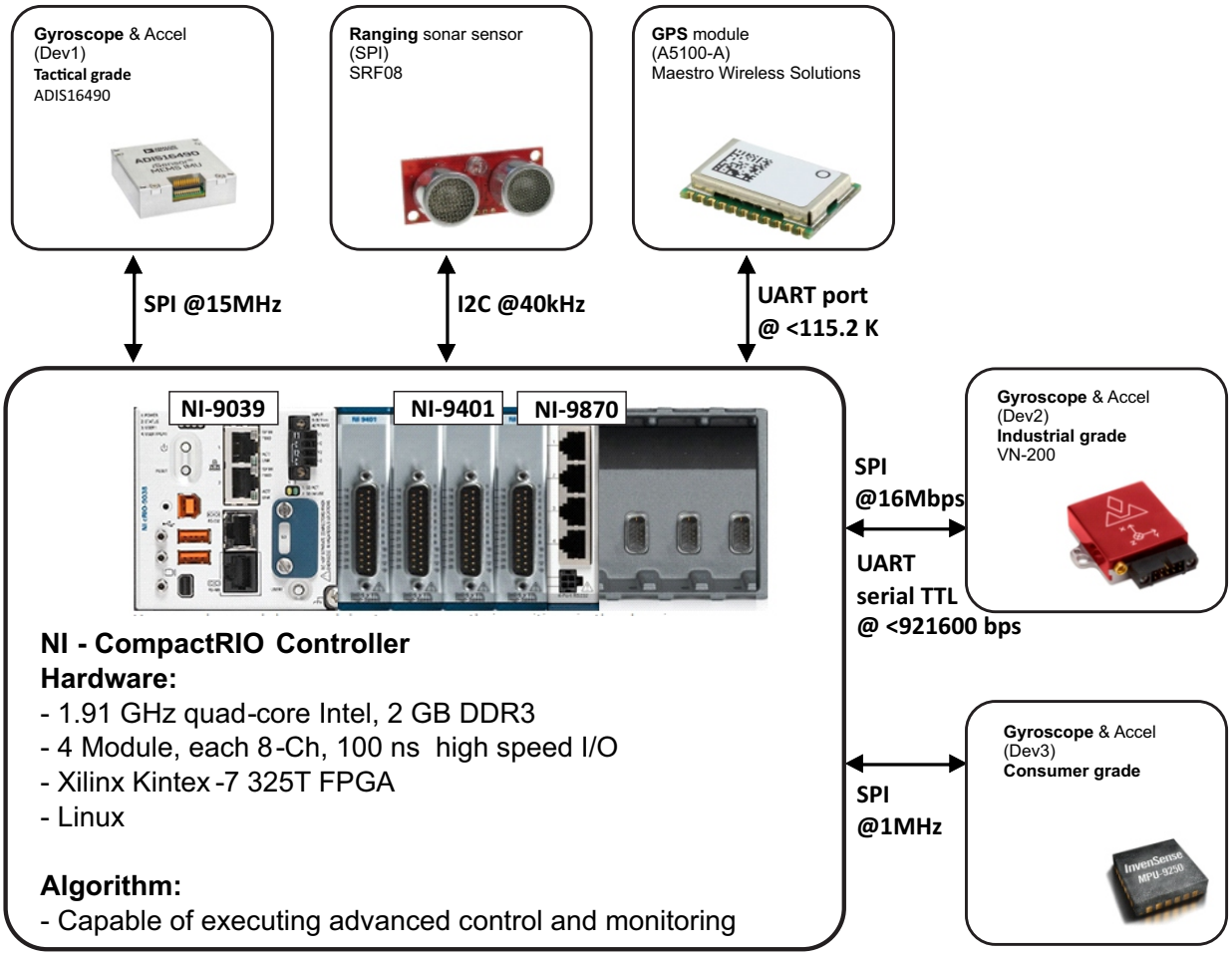

Figure A.1: Hardware architecture for integration with multiple sensors. The firmware for the data acquisition will be implemented on the FPGA part, while the algorithm for signal processing will be implemented on the CPU real-time processor.

The whole system is under control of the main station NI-cRIO 9039, where the LabVIEW algorithm is programmed. Algorithms are implemented in LabVIEW environment Virtual Instruments (VI). The rest of the algorithms depending on the speed and complexity of the calculation can be divided into three parts. 1) Sensor Communication: data acquisition, 2) Equations: such as orientation/position/velocity estimations, and 3) Visualization: Monitor and control of filter parameters. The data acquisition algorithm was implemented on the FPGA-VI to access high-speed data transfer. After acquiring data from the IMU, filtration such as moving average and motion detection is being applied. ZUPT detection is estimated by comparison between the amplitude of the X-Y-Z acceleration with a predefined level adjusted by the user, these algorithms were implemented in the CPU-VI, while data logging, visualization, and control of the filter parameters were implemented in the computer-VI.

Table A.1: Available sensors and their communication protocol.

Sensor	Description	Communication Protocol
IMU-(VN-200)	VectorNav industrial grade	UART serial TTL 921600 bps
IMU-(ADIS16490)	Analog devices tactical grade	SPI @15 MHz
IMU-(MPU-9250)	Invensense consumer grade	SPI / I2C @1 MHz
Ranging (SRF08)	Ultra sonic range finder	I2C @40 kHz
GPS (A5100-A)	Maestro GPS module	UART port @ 9.6 kHz

A.3 FPGA and CPU Configurations

The NI-9401 digital input/output module is used to connect the ADIS16490 IMU to the CompactRIO platform. Fig. A.2, shows the schematic of the SPI integration for this sensor. The IMU interacts with flex cable (ADIS1644X/FLEX) to an adapter board (ADIS16IMU1/PCB), and connected through a cable to the terminal block of the digital module. A pin map of this communication is shown in Table A.2. Configurable input/output control ports of the IMU (e.g., FIR filter) are available through four additional pins (DIO1, DIO2, DIO3 and DIO4).

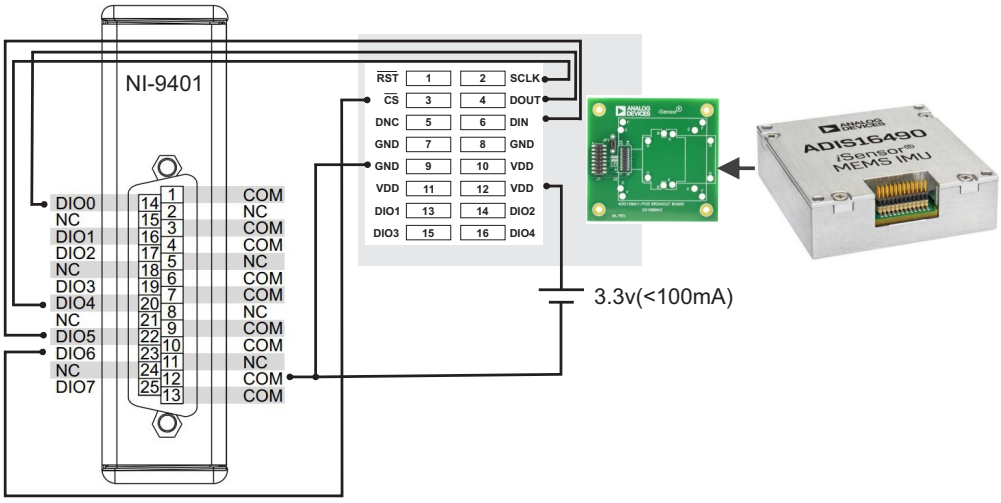

Figure A.2: Wiring connection between the cRIO and the ADIS IMU.

The low-level abstraction of data and clock transmission is programmed on the FPGA part of the platform. The FPGA-VI reference performs sensor communication in three stages. They are, 1) select the specific measurement type (temperature, gyroscope, accelerometer), 2) communicate with the sensor and acquire the binary data, 3) Apply the appropriate bias and scale factor conversion to the received binary data. Fig. A.3 shows an example of this implementation. In this configuration, 32 -bit resolution was selected by stacking 3 SPI VI blocks. The first VI is responsible for register address, the second and the third VIs are responsible for the high and low byte of the data responded to the requested address, respectively. In the case of 16 -bit it only requires 2 SPI VI blocks. The CPU part of the platform gathered data from the FPGA by first calling individual sensor and second

Table A.2: Connection diagram for simple read/write IMU data

PIN label	NI 9401 DIO	ADIS16IMU1/PCB
SCLK	20	2
MOSI	22	6
MISO	14	4
CS	23	3
Ground	12	7
DIO1	(Configure register)	13
DIO2	(Configure register)	14
DIO3	(Configure register)	15
DIO4	(Configure register)	16

requesting the specific data from the individual axis of the IMU sensor. Fig. A.4 shows this implemented sequence calling algorithm of how IMU data is being concatenated and stored and its corresponding block diagram.

The flexible hardware (National Instruments-CompactRIO) was developed further to acquire

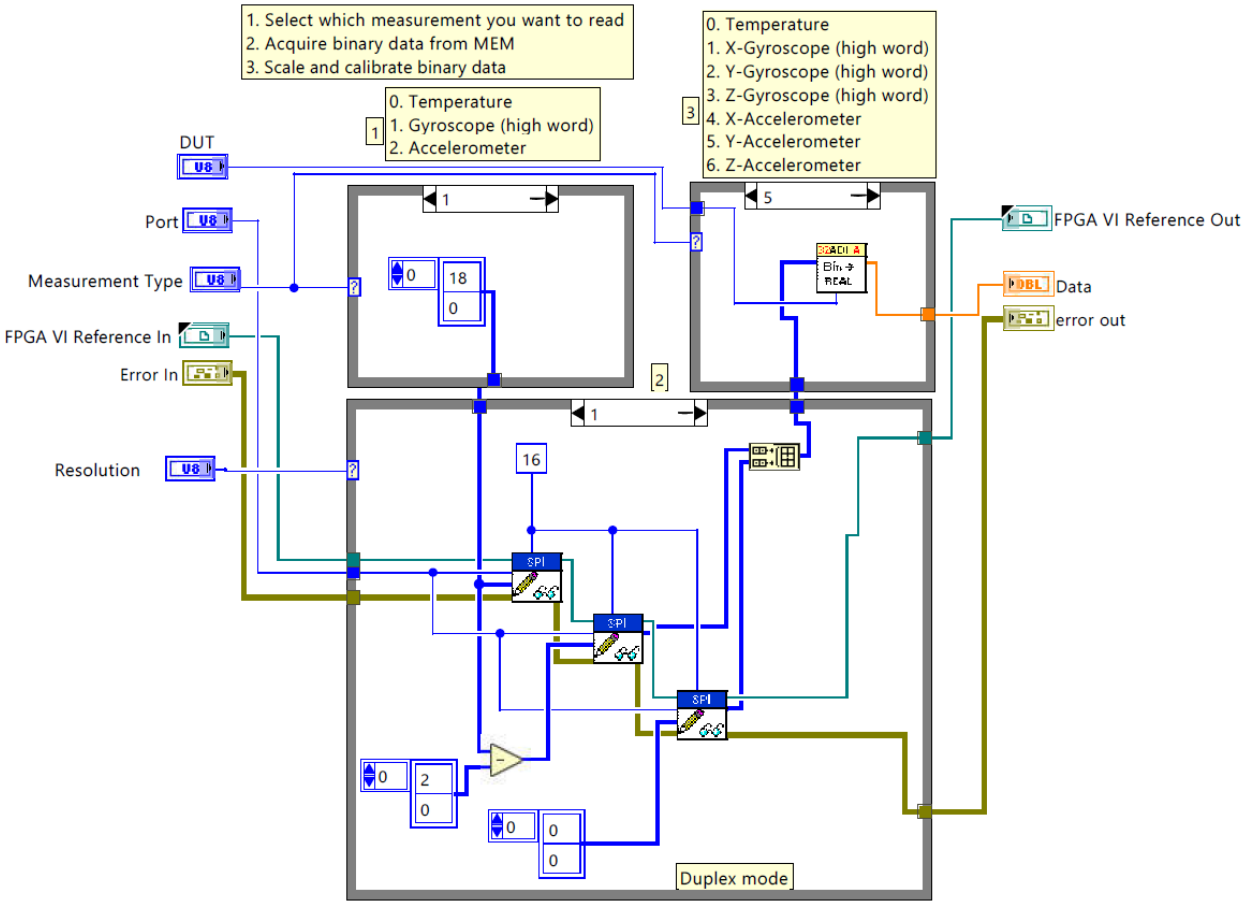

Figure A.3: SPI firmware protocol for send command and request data packet.

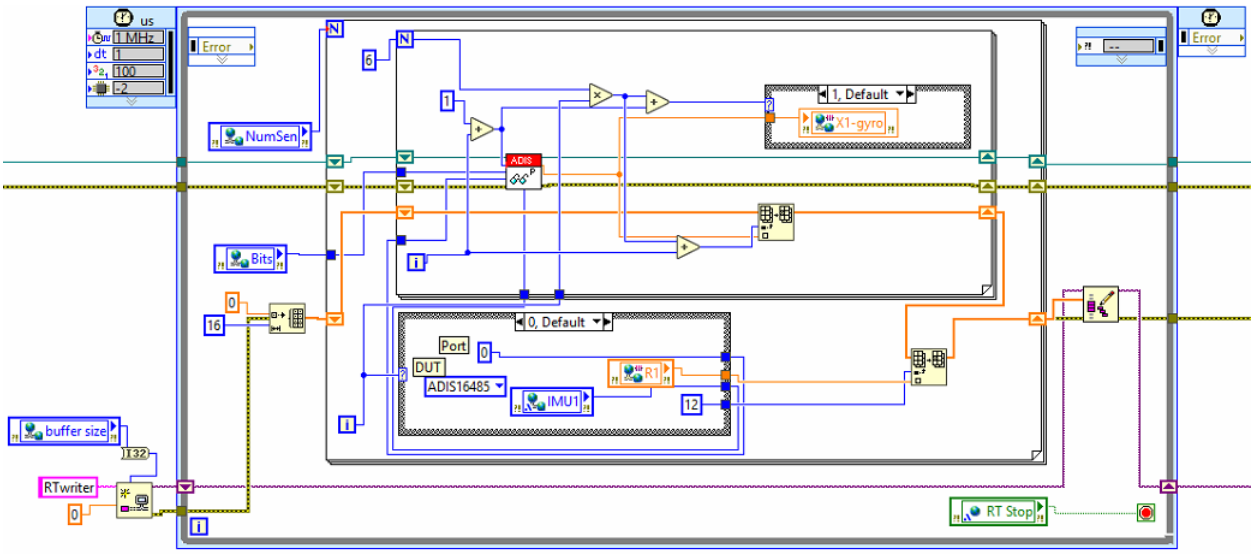

(a) From left to right: assigned the number of IMUs, select the bit resolution, retrieve the (x,y,z) gyroscope parameters followed by (x,y,z) accelerometer parameters, concatenate the data with other sensors and data transmission through the network.

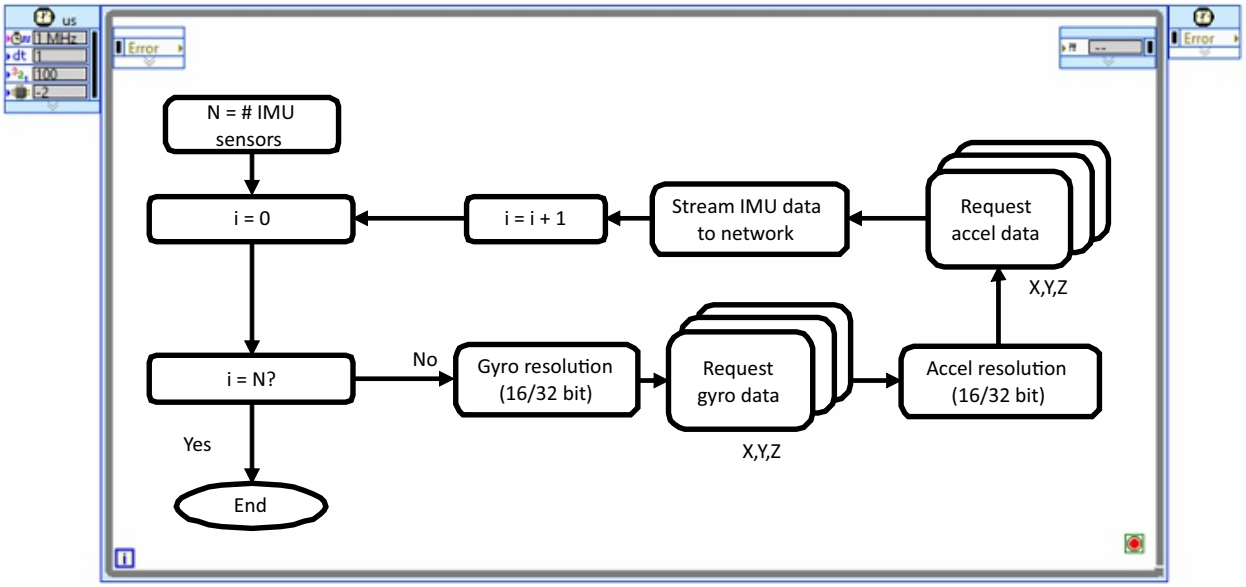

(b) The corresponding SPI flowchart implementation.

Figure A.4: SPI packet format and its communication by the controller (LabVIEW RT and FPGA) to the IMU sensors (ADIS), a) graphical programming, b) the block diagram.

signals related to distance information between the two feet. A Devantech (SRF08) high-performance ultrasonic ranger was selected for this purpose. The communication to this sensor is via Inter-Integrated Circuit (I2C) bus. C-series digital module 4-channel (NI-9402) with the resolution speed of 55 ns were used to achieve bi-directional digital communication to send and receive commands. Fig. A.5 shows the architecture of this integration in which each channel may be used to extend up to 16 sonar sensors.

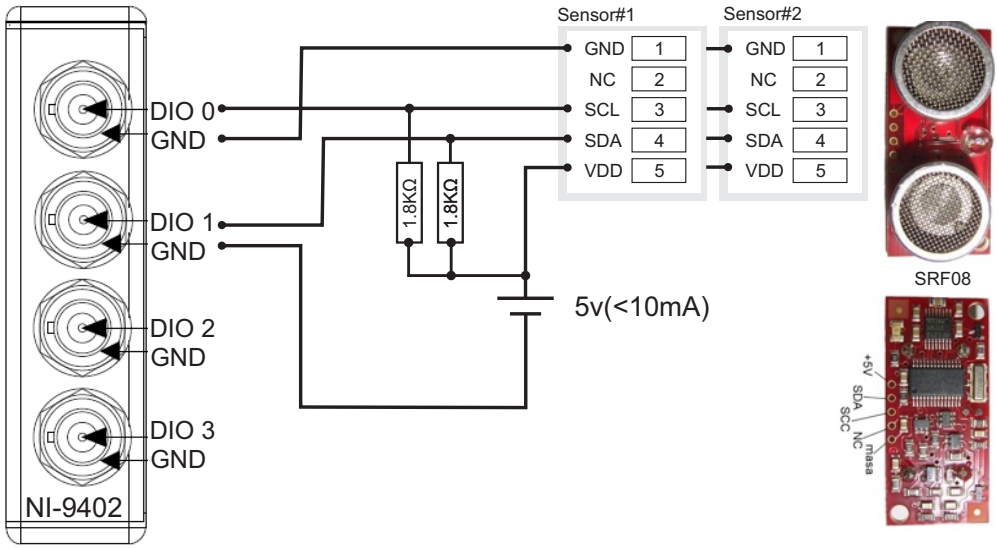

Figure A.5: Hardware architecture between CompactRIO controller and sonar sensors.

Two ranging sensors were used for this development (unique address of 0xF0 and 0xF1), each mounted to the midfoot area of the left and right shoe facing each other. The controller sends a command packet (write or read) containing two bytes to set the read distance configuration in metric system and request the start of a ranging session. The sensor listens to the 1st echo range that the controller requested by pointing to 0x2 location. Table A.3 summarizes the sequence of these commands and Fig. A.7 shows its graphical programming implementation in LabVIEW Real-Time (RT) and LabVIEW FPGA targets. A timed loop configuration with a specified period of 10,000 µs between each iteration was used to execute the bi-directional communication to both sensors. In order to fire the sonar rapidly, one can set a limit to the maximum analog gain and ranging distance, so that the next session can get started immediately. This results in a delay between the start of the session and the received echo, which sets a limit to the system for recording distance information. By default, 15 Hz output is available after sensor powered-up with manufacture gain and ranging configurations. Here the gain limit was set to 94(0x00) and the maximum distance register was set to 49(0x37), providing a readable ranging distance of $(49 * 43) + 43 = 2150mm$ with 100 Hz available on output. This sensor initialization and its LabVIEW environmental representation are shown in Fig. A.6.

Table A.3: I2C packet commands "read" and "write" to the sensor memory locations.

Address	Data Byte	Data Byte	Data Byte	Data Byte
F0, F1	0x0 (cmd)	0x51(request cm)	0x0 (cmd)	0x2 (1st echo packet)

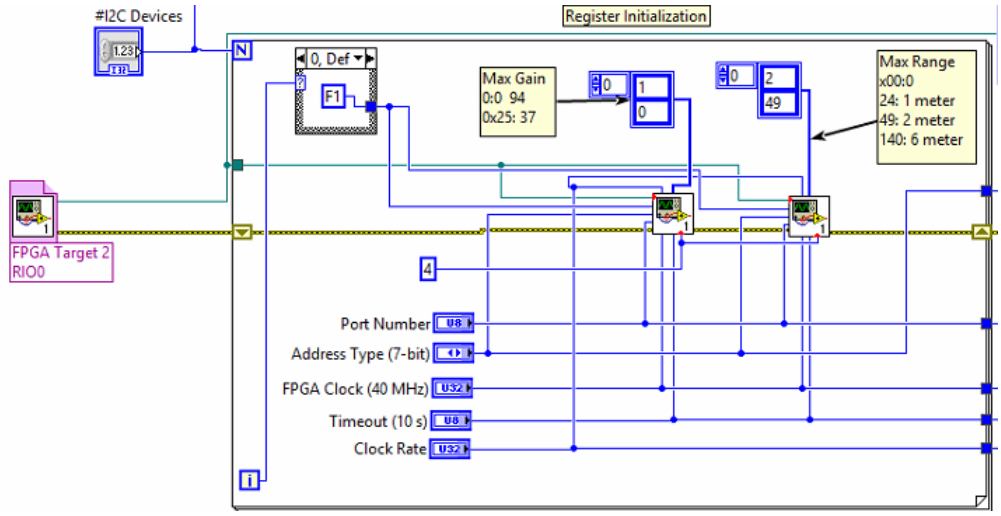

Figure A.6: Initialization of maximum level of analogue gain and distance range of the SRF08 through LabVIEW VI.

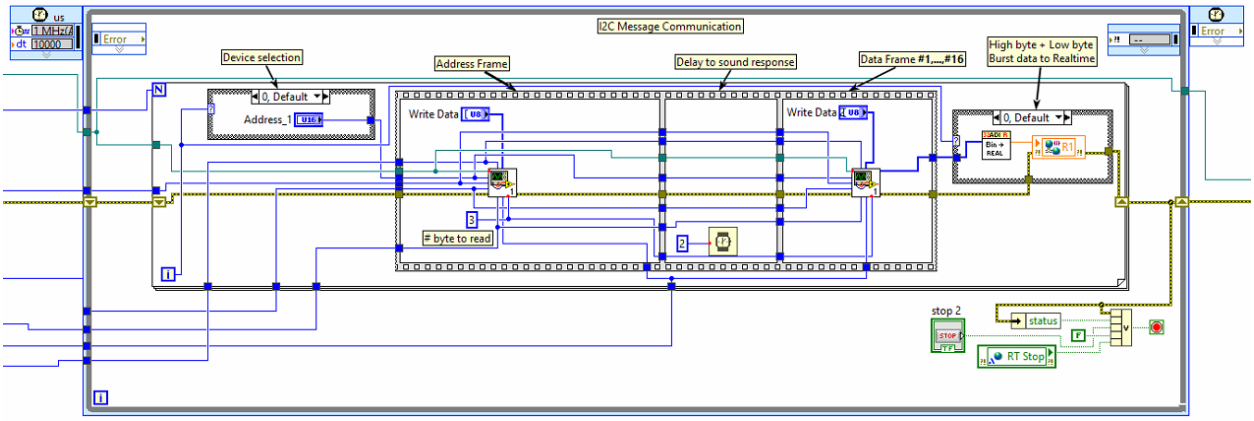

(a) From left to right: selection of the device address, sends the first byte for read/write command, necessary delay to wait for the 1st distance echo from the object, send data and command.

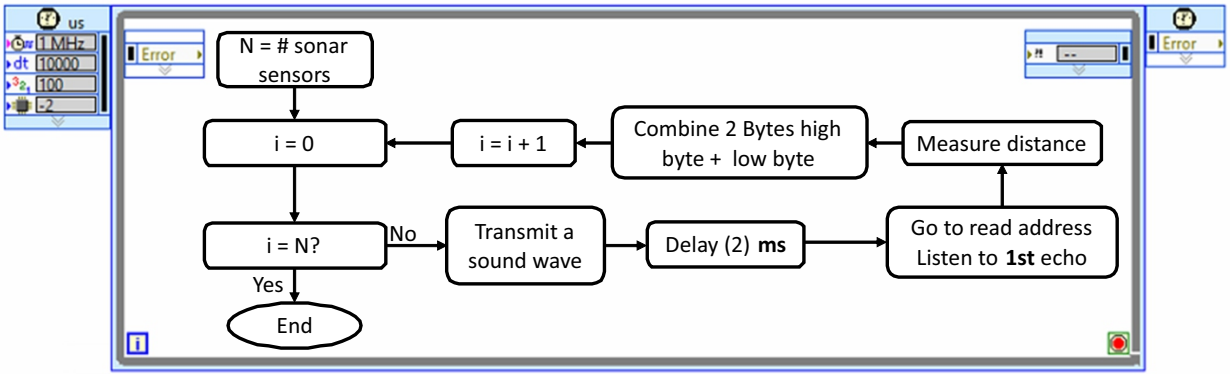

(b) The corresponding I2C flowchart implementation.

Figure A.7: I2C packet format and its communication by the controller (LabVIEW RT and FPGA) to the SONAR sensors (SRF08), a) graphical programming, b) the block diagram.

A.4 Network Architecture

The developed controller was interfaced with multiple sensors and was programmed in LabVIEW, the architecture was discussed in the previous quarters. The wireless communication system was added as a part of the development. The wireless system consisted of a wireless router and a wireless Ethernet adapter. For the router ASUS RT-AC66R 802.11ac with dual-band channel capability, and for the adapter, the industrial wireless network Moxa AWK-3131A were selected. This combination enabled the IEEE 802.11a/b/g/n standard wireless communication protocol under 5 GHz channel, which translates to communication bandwidth of 54Mbps between the NI-cRIO and the laptop. The FPGA is responsible for data acquisition from sensors and runs in parallel to the real-time CPU controller, therefore high-throughput data obtained from the sensors needed to transfer to the real-time CPU for navigational algorithm and downsampled to the laptop for visualization. To off-load the CPU update rate, we considered network architecture for transferring data between FPGA and CPU which allows the processor to perform the navigational algorithm at a higher rate, resulting in higher performance of real-time computation. The CPU then downsamples and transmits the data through wireless channel to the laptop. The network architecture was implemented including the wireless protocol as described next:

The adapter provides a wireless access point to the controller. An Ethernet port for wireless programming of the Moxa controller provided a direct connection between the NI-cRIO and the adapter. The voltage regulator on the PCB inside the backpack provided a 12V/0.6A power for the adapter. Two wireless infrastructure modes are possible, a) "access point mode" using built-in WiFi for one connection only, or b) "client mode" where the platform is connected to the network cloud. In the latter mode, the wireless router served as a link

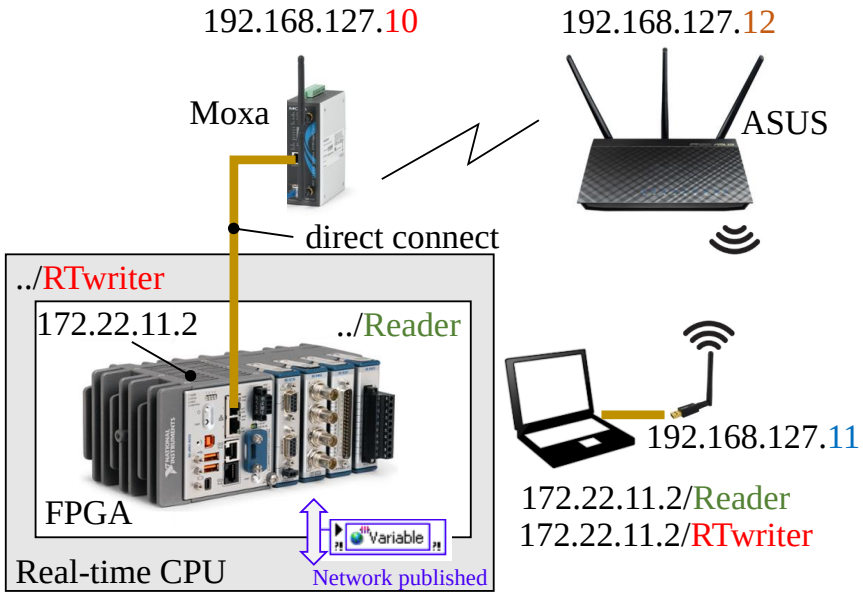

Figure A.8: Allocated IP addresses for the system.

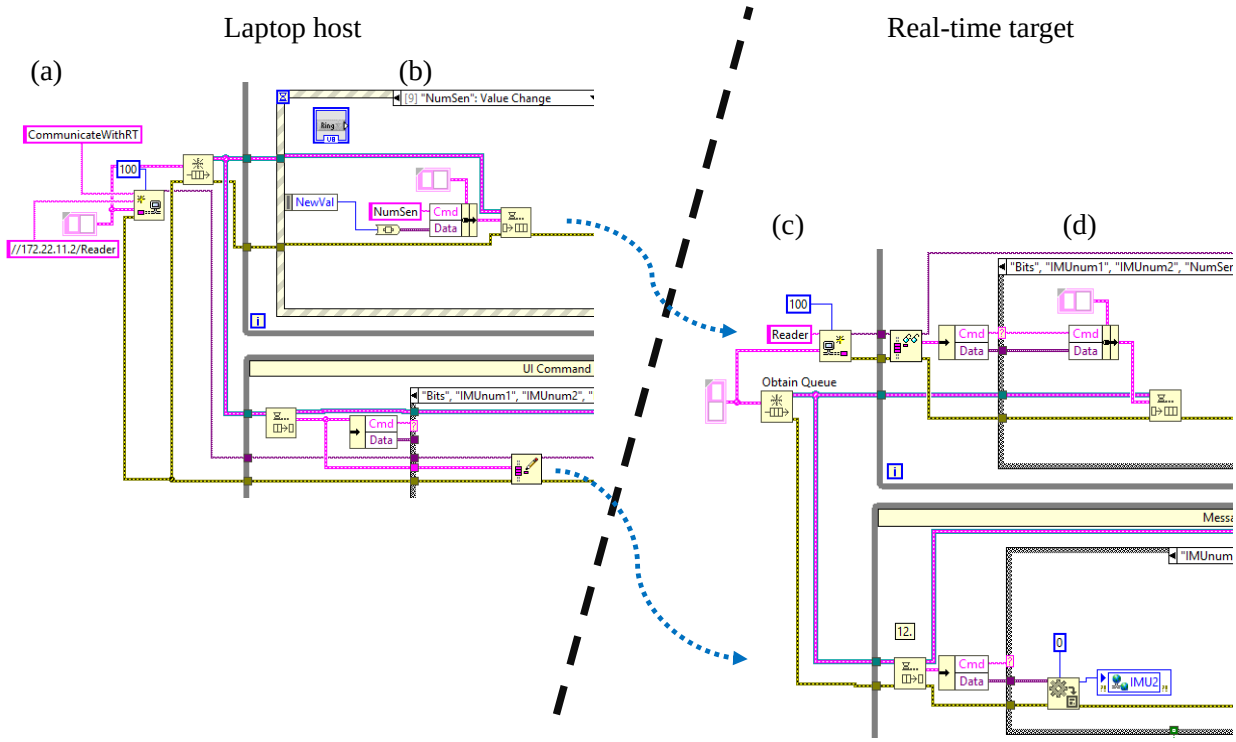

Figure A.9: Left side: writing elements to the stream, laptop host to the cRIO, a) reference to the reader URL IP address, b) start of the stream with specified header and command data value. Right side: reading elements from the stream on cRIO, c) create stream reader endpoint, d) read event specific handler and decompose the data value from the stream.

between the laptop and the adapter and any client can access the data, or remote control, and tune the algorithms on the platform. Unique static IP addresses were assigned to each component of the flexible INS system: NI-cRIO controller, wireless adapter, router, and the laptop display, as indicated in Fig. A.8. Individual sensor data on different time instances are streamed from FPGA to CPU over internal server communication called NI Publish-Subscribe Protocol (NI-PSP), the CPU processor fuses the data, resamples at a fixed timing intervals and publishes into the network where it is accessible on the dedicated IP address. The header value of "Reader" indicates the stream coming from the client and transferred to the platform. The header value of "RTwriter" indicates the stream coming from the CPU processor transmitting to the client.

The network protocol for writing/reading elements to/from the data stream between the laptop and the controller is shown in Fig. A.9. A buffer with a waiting timeout on both sides of the stream data was implemented and provides a lossless transfer protocol even if a connection is lost. Different commands associated with algorithm have been implemented on the stream protocol which is controllable by the client on the front panel display, e.g., calibration sensitively threshold, gravity value, selection of 16 -bit or 32 -bit IMU data, sonar-data, reset free inertial integration. After successful communication through the wireless network, the stream data is being decomposed to command and data value. At the end of every stream execution and read, the stream endpoint is destroyed. An example of the

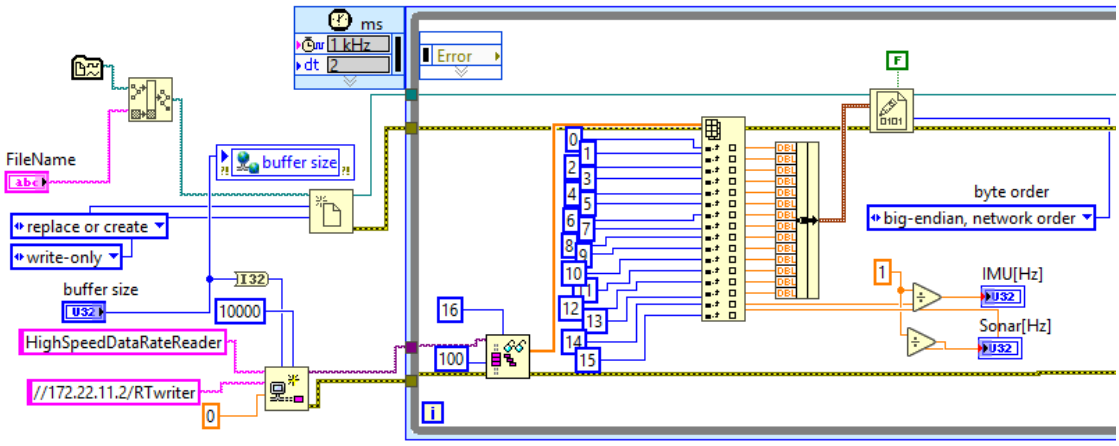

Figure A.10: Data stream communication protocol from controller to laptop for data logging.

stream from the NI-cRIO to the laptop for data logging is shown in Fig. A.10. A buffer size of 100 s is implemented on the wireless network, with a stream of sixteen parameters with execution time at every 2 ms.

A.5 GUI Software Control

An example of the implemented front panel software graphical user interface (GUI) is shown in Fig. A.11. The GUI is controlling the three main VIs. The window-VI sets the initial condition, scaling, 3D demonstration of the IMU sensor, and LEDs to interacts with the algorithm for debugging and development. The front panel of the FPGA-VI is demonstrating the real-time data captured from the sensors, here the instantaneous value of the only one IMU. The front panel CPU-VI is demonstrating the visual representation of the implemented algorithm, here the orientation value of the IMU. The there parts can work simultaneously, or they can be turned on and off and controlled by the user.

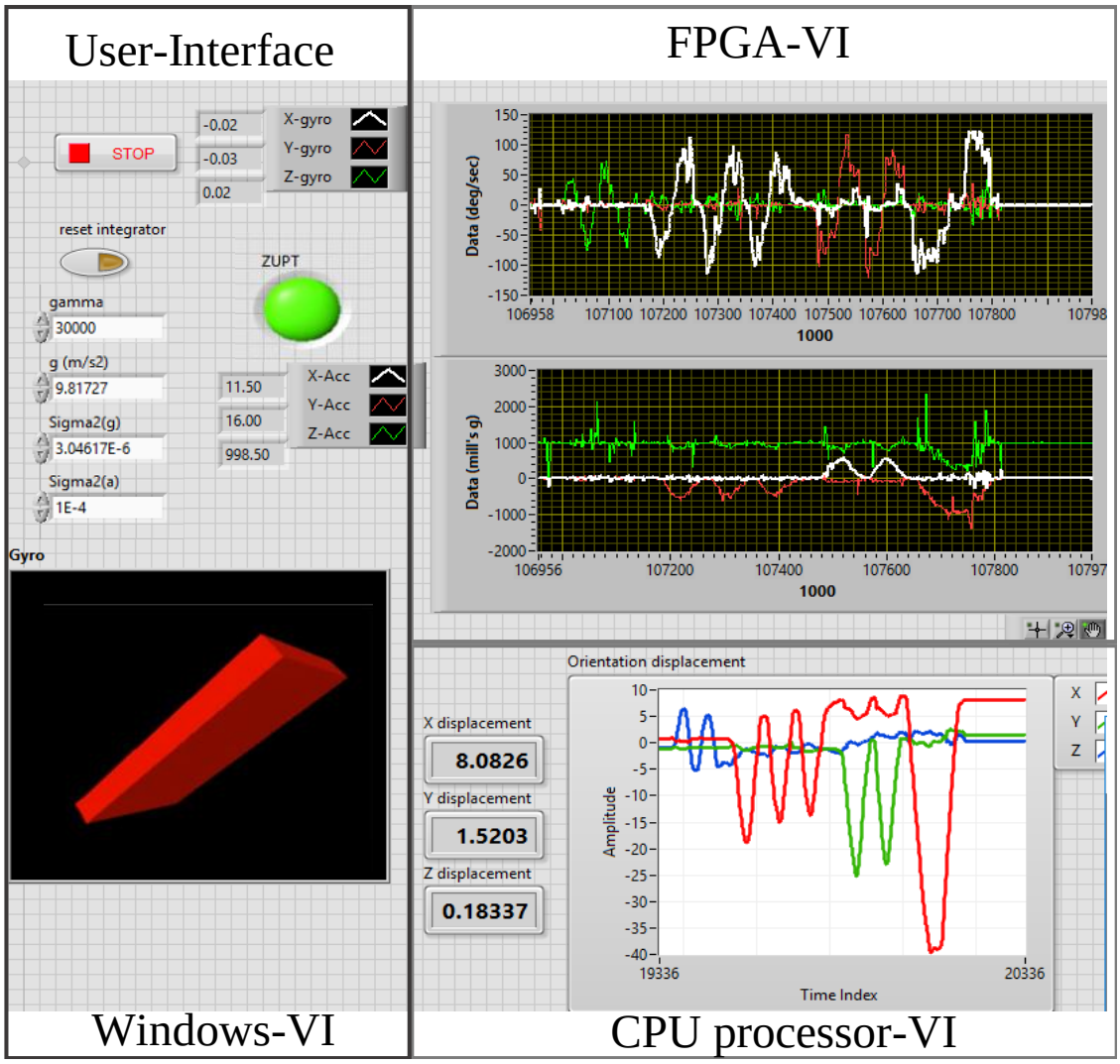

Figure A.11: The developed GUI for control and visualization of the acquired data, single IMU sensor shown here. User-interface includes: LED indicator to flag stationary motion events, control parameter to change the detector sensitivity and filter reset. CPU-VI shows the algorithm applied on IMU output.

A.6 Conclusion

The hardware integration between the flexible platform, IMUs and the sonar sensors were discussed. The gain of the sonar sensors was optimized to record data rate of 100 Hz for the ranging distance of 2 m, enough to capture the maximum feet displacement in normal walking of 1 m. The implementation of the network architecture for the stream of data between the controller and the laptop was described. The flexible platform in conjunction with wireless communication will assist to ease the process of in-field data recording during experimental recording.

B Calibration of IMU's Systematic Errors

B.1. Purpose

This document describes a typical example of a calibration procedure performed on an IMU measurement.

B.2. Scope

IMU measurement brakes down to accelerometer and gyroscope measurements. The main systematic errors (known as deterministic) are fixed biases, scale factor, and misalignment. This document briefly discusses the procedure to extract and to calibrate these error from the IMU measurement.

B.3. Error characteristics

B.3.1. Accelerometer measurement of an IMU reading can be represented by a 3×1 matrix as, [209]:

$$\tilde{\vec{f}} = b_{accel,fix} + (I_{3\times3} + M_a)\hat{\vec{f}}\,,$$

where the $\tilde{\vec{f}}$ is the specific forcer sensed by the accelerometer of an IMU measurement, $\hat{\vec{f}}$ is the estimate of the IMU true value, $I_{3\times3}$ is a 3×3 identity matrix, $b_{accel,fix}$ represented the fixed bias error and matrix M represents the error model including both scale factor and misalignment.

B.3.2. The characteristic can be rewritten for gyroscope measurement $\vec{\Omega}$ for each axis, with a matrix size of 3×1 as, [209]:

$$\tilde{\vec{\Omega}} = b_{gyro,fix} + (I_{3\times3} + M_g)\hat{\vec{\Omega}}\,.$$

B.3.3. The error model matrix M for accelerometer is "M_a" and for gyroscope is "M_g", as follows:

$$M_a = \begin{bmatrix} SF_{a,x} & m_{a,xy} & m_{a,xz} \\ m_{a,yx} & SF_{a,y} & m_{a,yz} \\ m_{a,zx} & m_{a,zy} & SF_{a,z} \end{bmatrix},\; M_g = \begin{bmatrix} SF_{g,x} & m_{g,xy} & m_{g,xz} \\ m_{g,yx} & SF_{g,y} & m_{g,yz} \\ m_{g,zx} & m_{g,zy} & SF_{g,z} \end{bmatrix},$$

where SF stands for Scale Factor, and m stands for misalignment coefficient.

B.3.4. After extraction of errors *(b,SF,m)*, the true value of an IMU can be estimated from measurement data for accelerometer as:

$$\hat{\vec{f}} = (I_{3\times3} + \hat{M}_a)^{-1}(\tilde{\vec{f}} - \hat{b}_{fixed}),$$

and similarly for gyroscope as:

$$\hat{\vec{\Omega}} = (I_{3\times3} + \hat{M}_g)^{-1}(\tilde{\vec{\Omega}} - \hat{b}_{fixed}).$$

Test procedure:

B.4. Setup equipment and device

B.4.1. Prepare the physical setup for IMU characterization.

B.4.2. Select a rate table with 3-axis rotation, and secure the IMU sensor along with its electronic at the center of the table (pivot point).

B.4.3. If rate table with 3-axis rotation is not available, use a 2-axis rate table along with a 2-axis tilt table to be seated on the pivot point. The tilt table will be used for accelerometer characterization for changing orientation.

B.4.4. Note the +/− direction of the IMU sensor for each three axes *(x, y, z)*. The are denoted as (x^+, y^+, z^+) or (x^-, y^-, z^-).

B.4.5. Record the measurement on each axis as specified.

B.5. Accelerometer (force measurement):
IMU has three accelerometers oriented perpendicular to each other, where each axis's coordinate frame is the one orthogonal to the device structure noted as + direction. Measure the force sensed on the individual axis of the IMU by changing the orientation of the platform setup and observe the response. For the 3-axis rate table, use the outer axis of the rate table to change the orientation. If the tilt table is being used, turn the stage from one position (e.g., facing upwards) to another (e.g., facing downwards), and then rotate back to the original position. Local gravity (g) will be used as a reference for input applied force. Once all measurements are complete, the following procedure extracts the accelerometer errors.

Bias:

B.5.1. For each axis of the accelerometer, perform two measurements to measure local gravity (g).

B.5.2. Measure the opposite orientations, where the normal force of that axis is aligned with the local gravity (g).

B.5.3. By summing the average measurements $\bar{f}$ for +/−, the gravity component will get canceled.

B.5.4. The results of summation is two times the fixed bias on that particular axis of the device structure.

B.5.5. The following equation extracts the fixed bias of the accelerometer.

$$b_{accel,fix} = \frac{1}{2}\begin{bmatrix} \bar{f}_{x^+} + \bar{f}_{x^-} \\ \bar{f}_{y^+} + \bar{f}_{y^-} \\ \bar{f}_{z^+} + \bar{f}_{z^-} \end{bmatrix}$$

Scale factor:

B.5.1. For each axis of the accelerometer, perform two measurements to measure local gravity (g).

B.5.2. Measure the opposite orientations, where the normal force of the that axis is aligned with the local gravity (g).

B.5.3. By subtracting the average measurements $\bar{f}$ for +/−, the fixed bias component sensed on that axis will get canceled.

B.5.4. The results of subtraction is two times the fixed local gravity value.

B.5.5. The following equation extracts the scale factor error of the accelerometer.

$$\begin{bmatrix} \hat{SF}_{a,x} & 0 & 0 \\ 0 & \hat{SF}_{a,y} & 0 \\ 0 & 0 & \hat{SF}_{a,z} \end{bmatrix} = \frac{1}{2g} \begin{bmatrix} \bar{f}_{x^+} - \bar{f}_{x^-} & 0 & 0 \\ 0 & \bar{f}_{y^+} - \bar{f}_{y^-} & 0 \\ 0 & 0 & \bar{f}_{z^+} - \bar{f}_{z^-} \end{bmatrix} - I_{3\times 3}$$

Misalignment:

B.5.1. For each axis of the accelerometer (e.g., X-axis), perform two measurements to measure cross axis sensitivity (e.g., Y- and Z-axes corresponding to $m_{a,xy}$ and $m_{a,xz}$).

B.5.2. Similar to B.5.2 align the normal force of one axis with the local gravity (g) to measure the opposite orientations.

B.5.3. While changing the orientation record the response of the other two axes and report as cross axis sensitivity.

B.5.4. By subtracting the average measurements $\bar{f}$ for +/−, the fixed bias components sensed on that axis will get canceled.

B.5.5. The result of cross axis sensitivity subtraction is two times the fixed local gravity value.

B.5.6. Repeat steps B.5.1 through B.5.3 for the other two axes.

B.5.7. The following equation extracts the misalignment errors of the accelerometer.

$$\begin{bmatrix} 0 & m_{a,xy} & m_{a,xz} \\ m_{a,yx} & 0 & m_{a,yz} \\ m_{a,zx} & m_{a,zy} & 0 \end{bmatrix} = \frac{1}{2g} \begin{bmatrix} 0 & \bar{f}_{y^+} - \bar{f}_{y^-} & \bar{f}_{z^+} - \bar{f}_{z^-} \\ \bar{f}_{x^+} - \bar{f}_{x^-} & 0 & \bar{f}_{z^+} - \bar{f}_{z^-} \\ \bar{f}_{x^+} - \bar{f}_{x^-} & \bar{f}_{y^+} - \bar{f}_{y^-} & 0 \end{bmatrix}$$

B.6. Gyroscope (angle measurement):
IMU has three gyroscopes oriented perpendicular to each other, where each axis's coordinate frame is the one orthogonal to the device structure and noted as + direction. Measure the displacement angle rate sensed on the individual axis of the IMU by applying input rotation to the rate table. Rotate the rate table with a known input rotation in one direction (e.g., clockwise with fix angular rate). Repeat the measurement for the opposite direction (e.g., counter-clockwise with a fix angular rate). Change the

orientation of the device and measure the rotation along the other two axes. Once all measurements are complete, the following procedure extracts the gyroscope errors.

Bias:

B.6.1. For each axis of the gyroscope, perform two measurements.

B.6.2. Measure gyroscope response to opposite directions with a fix angular rate Ω applied to the rate table +/−.

B.6.3. By summing the average measurements Ω for +/−, the known input rotation will get canceled.

B.6.4. The results of summation is two times the fixed biased on that particular axis to the device structure.

B.6.5. The following equation extracts the fixed bias of the gyroscope.

$$b_{gyro,fix} = \frac{1}{2}\begin{bmatrix} \bar{\Omega}_{x^+} + \bar{\Omega}_{x^-} \\ \bar{\Omega}_{y^+} + \bar{\Omega}_{y^-} \\ \bar{\Omega}_{z^+} + \bar{\Omega}_{z^-} \end{bmatrix}$$

Scale factor:

B.6.1. For each axis of the gyroscope, perform two measurements to measure applied known input rotation Ω.

B.6.2. Measure the opposite input rate rotations, where the normal force of that axis is perpendicular to the rotating rate-table.

B.6.3. By subtracting the average measurements $\bar{\Omega}$ for +/−, the fixed bias component sensed on that axis will get canceled.

B.6.4. The results of subtraction is two times the input rotation rate.

B.6.5. The following equation extracts the scale factor error of the gyroscope.

$$\begin{bmatrix} \hat{SF}_{g,x} & 0 & 0 \\ 0 & \hat{SF}_{g,y} & 0 \\ 0 & 0 & \hat{SF}_{g,z} \end{bmatrix} = \frac{1}{2\Omega}\begin{bmatrix} \bar{\Omega}_{x^+} - \bar{\Omega}_{x^-} & 0 & 0 \\ 0 & \bar{\Omega}_{y^+} - \bar{\Omega}_{y^-} & 0 \\ 0 & 0 & \bar{\Omega}_{z^+} - \bar{\Omega}_{z^-} \end{bmatrix} - I_{3\times 3}$$

Misalignment:

B.6.1. For each axis of the gyroscope (e.g., X-axis), perform two measurements to measure cross axis sensitivity (e.g., Y- and Z-axes corresponding to $m_{g,xy}$ and $m_{g,xz}$).

B.6.2. Similar to B.6.2 align the normal force of one axis with the rotating rate-table and measure the opposite input rate rotation.

B.6.3. While rotating the rate-table either + or −, record the response of the other two axes and report as cross axis sensitivity.

B.6.4. By subtracting the average measurements $\bar{\Omega}$ for +/−, the fixed bias components sensed on that axis will get canceled.

B.6.5. The result of cross axis sensitivity subtraction is two times the input rotation rate.

B.6.6. Repeat steps B.6.1 through B.6.3 for the other two axes.

B.6.7. The following equation extracts the misalignment errors of the gyroscope.

$$\begin{bmatrix} 0 & m_{g,xy} & m_{g,xz} \\ m_{g,yx} & 0 & m_{g,yz} \\ m_{g,zx} & m_{g,zy} & 0 \end{bmatrix} = \frac{1}{2\Omega} \begin{bmatrix} 0 & \bar{\Omega}_{y^+} - \bar{\Omega}_{y^-} & \bar{\Omega}_{z^+} - \bar{\Omega}_{z^-} \\ \bar{\Omega}_{x^+} - \bar{\Omega}_{x^-} & 0 & \bar{\Omega}_{z^+} - \bar{f}_{z^-} \\ \bar{\Omega}_{x^+} - \bar{\Omega}_{x^-} & \bar{\Omega}_{y^+} - \bar{\Omega}_{y^-} & 0 \end{bmatrix}$$

C Electronics Schematic Development

Following circuits were developed and used for characterization of the sensors in this dissertation. Circuit schematics were grouped into blocks based on their functionality. The schematic and layout implemented are shown and a list of bill of materials is provided, linked to each sub-circuits.

C.1. Printed Circuit Boards (PCBs)

The developed PCBs falling under the following categories:

C.1.1. Resonator

Functionality: compatible for resonators, accelerometers and piezoelectric sensors, operation in open-loop or closed self-oscillating loop, vacuum chamber compatible.

C.1.2. Gyroscope analog buffer card

Functionality: differential drive and sense analog buffer electronics, quadrature DC and AC drive channel, single rail power supply, vacuum chamber compatible.

C.1.3. Inertial measurement unit readout

Functionality: three channel fully differential input output for gyroscope and accelerometer characterization together, vacuum chamber compatible.

C.1.4. Gyroscope standalone control platform (analog/digital)

Functionality: single supply standalone full gyroscope characterization platform DSP + microcontroller + analog signal conditioning. Modes of operations: open-loop rate mode, closed-loop rate or rate integrating gyroscope. Temperature reading with heather control.

C.1.5. Angular motion and EMG driven electrical stimulation

Functionality: single channel EMG activity input reading and single channel stimulation output for nerve stimulation. Closed-loop driven by input rotation or EMG activity for nerve stimulation. Microcontroller for implementation of custom algorithm on stimulation, processing EMG data, acquiring commercial IMU data.

C.1.6. Miscellaneous adapters:

C.1.6.1. Centrifuge system feedthrough

Functionality: used for digital and analog interface with the developed platform on rate table and instrument for signal conditioning.

C.1.6.2. Si-Ware systems ASIC interconnects

Functionality: used for ASIC characterization and programming on in-house vaccum sealed fabricated gyroscope.

C.2. PCB Input/Outputs (I/Os) identification

A summary of common I/O notations used for labeling across the developed PCBs are listed in Table. C.4.

Table C.4: PCB I/Os identification

Name	Alt.	Axis	Description
NODE	X	X-axis	Layout defined X-axis
ANODE	Y	Y-axis	Layout defined Y-axis
CARRIER	Carr	-	Proof mass applied voltage
NODEF(EXT)	FX	X-axis	Drive mode applied signal
ANODEF(EXT)	FY	Y-axis	Drive mode applied signal
NODE+	FX+	X-axis	Drive mode applied diff. signal (+)
NODE−	FX−	X-axis	Drive mode applied diff. signal (−)
ANODE+	FY+	Y-axis	Drive mode applied diff. signal (+)
ANODE−	FY−	Y-axis	Drive mode applied diff. signal (−)
NODEP+	PX+	X-axis	Sense mode readout diff. signal (+)
NODEP−	PX−	X-axis	Sense mode readout diff. signal (−)
ANODE+	PY+	Y-axis	Sense mode readout diff. signal (+)
ANODE−	PY−	Y-axis	Sense mode readout diff. signal (−)
DC_NODE_F_BIAS	DCX	X-axis	Drive mode DC voltage bias
DC_NODE_P_BIAS	DCX1	X-axis	Sense mode DC voltage bias
DC_ANODE_F_BIAS	DCY	Y-axis	Drive mode DC voltage bias
DC_ANODE_P_BIAS	DCY1	Y-axis	Sense mode DC voltage bias
SCK	CLK	-	clock signal generated by MCU
MOSI	-	-	Master Output Slave Input, MCU to IMU
MISO	-	-	Master Input Slave Output, MCU to IMU
I+	Curr+	-	Current nerve stimulation drive source
I−	Curr−	-	Current nerve stimulation sink signal

C.3. PCB schematics

C.3.1. Sensor package adapter:
This circuit serve as a bridge between device sealed package and the signal routing on the PCB layers, drive or sense channels. The implemented schematic of the LCC-44pin package is shown in Fig. C.12.

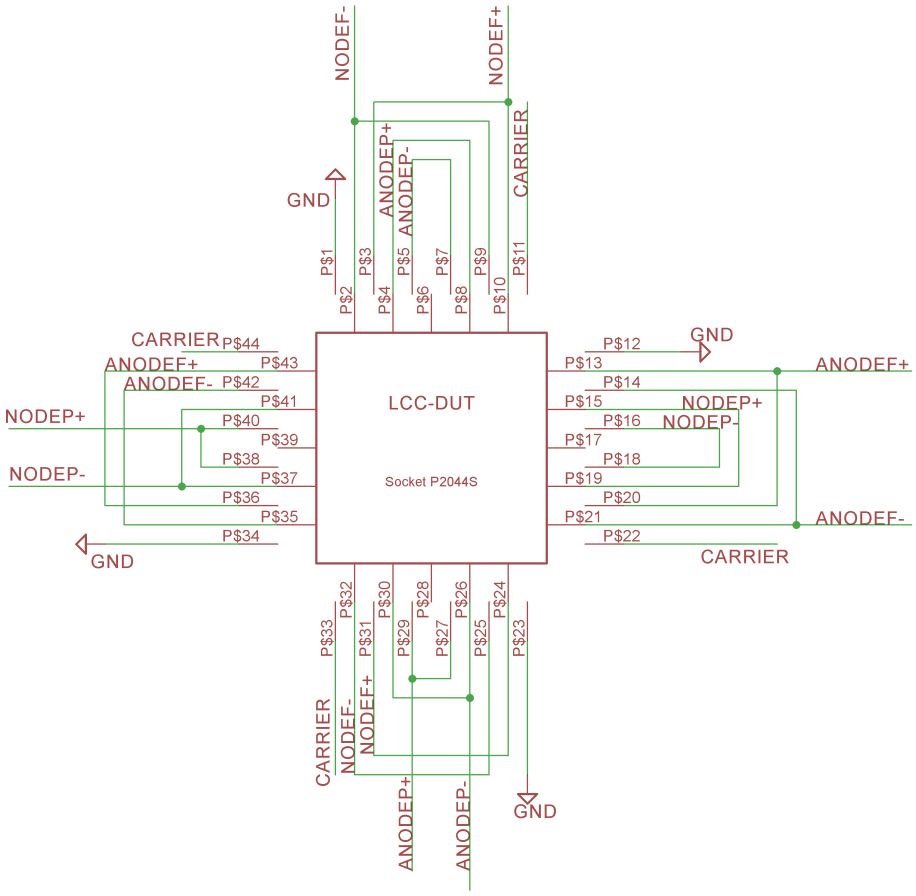

Figure C.12: Schematic for device under test to 44 pin LCC package.

C.3.2. Front-end detection:
Two circuit topologies were implemented to achieve differential input to differential output.

C.3.2.1. Differential detection using two transimpedance amplifiers. The implemented schematic is shown in Fig. C.13.

C.3.2.2. Differential detection using one fully differential input/output amplifier configured as transimpedance amplifier, cascaded with a buffer fully differential input/output amplifier is shown in Fig. C.14.

C.3.3. MCU Interfaces to IMU and analog signals:
The interface from integrated MCU to biphasic current control, IMU readout, and EMG amplitude readout. The schematic of this interface is shown in Fig. C.15.

C.3.4. Centrifuge system feedthrough:
Analog and digital signals were combined and passed through sliprings with configuration shown in Fig. C.16.

C.3.5. Forcer signals:
Single-ended input to differential drive for excitation of MEMS devices. The schematic of using dual buffer amplifiers is shown in Fig. C.17, and using dual instrumentation amplifiers is shown in Fig. C.18.

C.3.6. Carrier signal demodulator:
Analog demodulation of the carrier signal on pick-off channels, by analog signal multiplication unit. The demodulation process breaks down to two parts, 1) analog multiplication, the schematic is shown in Fig. C.19, and 2) low-pass filtering after demodulation to remove harmonics, the schematic is shown in Fig. C.20.

C.3.7. Power management:
For denoising PCB power supply lines, positive and negative low noise voltage regulators were considered and implemented. The schematic is shown in Fig. C.21.

C.3.8. EMG reading:

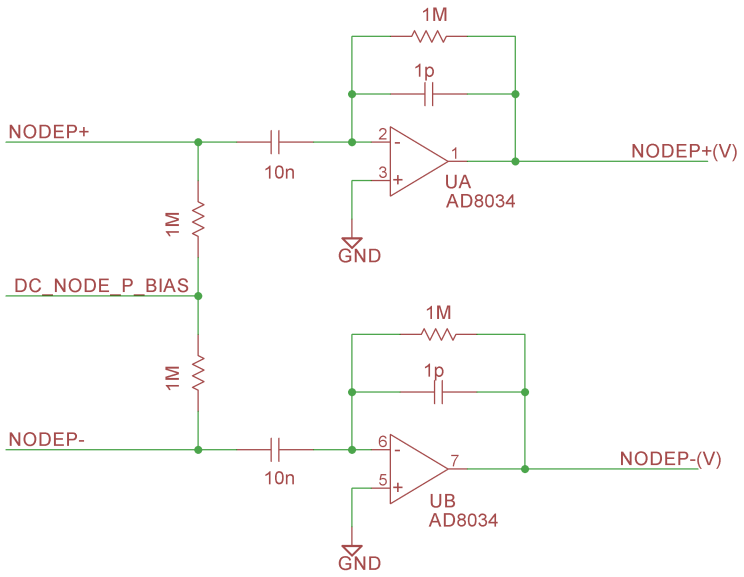

Figure C.13: Transimpedance amplifier with differential input and output.

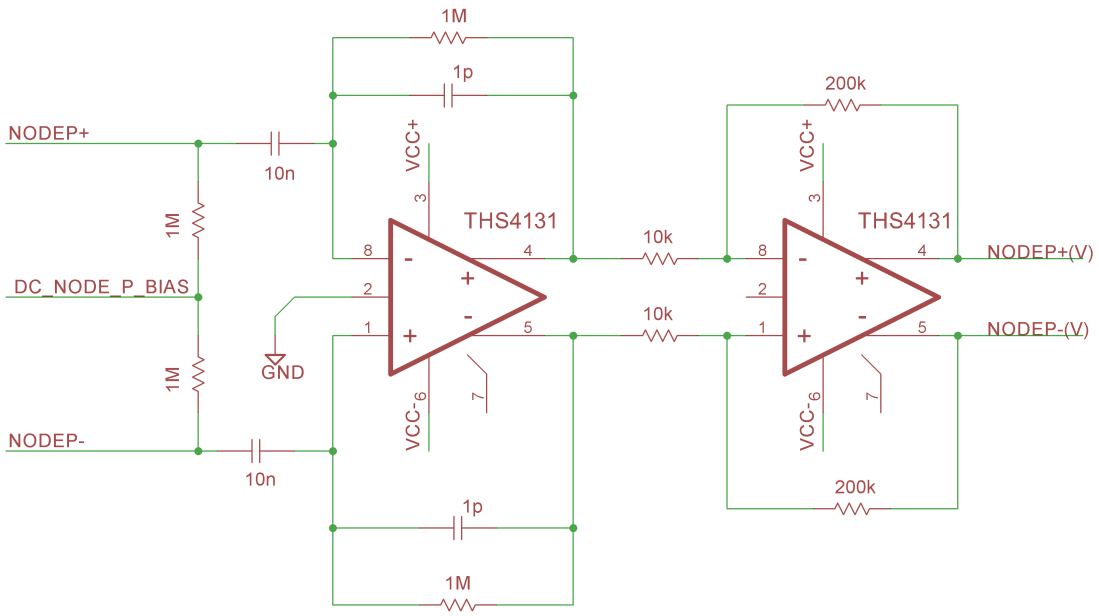

Figure C.14: Fully differential input-output transimpedance amplifier.

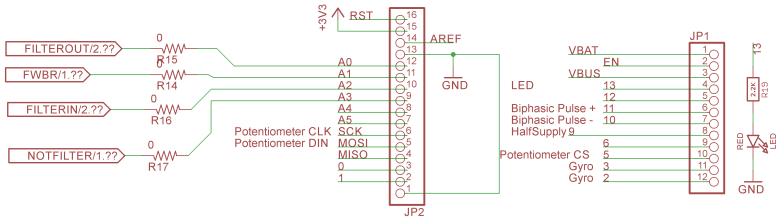

Figure C.15: Schematic of interface of MCU to IMU/Current generator/EMG used in the PCB C.1.5.

The schematic of recording EMG activity consists of ESD electrode protection, instrumentation amplifier, filter followed by waveform rectifier. This is shown in Fig. C.22.

C.3.9. Current stimulation:
Current stimulation consists of the following parts: digital potentiometer, buffer circuit, current mirror, biphasic switches. The schematic of the integration of digital potentiometer controlled by MCU is shown in Fig. C.23. The output of digital potentiometer goes directly into the buffer amplifier where it adjusts the current amplitude of the current mirror branch. The schematic of this integration is shown in Fig. C.24.

C.3.10. Function generator:
Schematic implementation of function generator to achieve 1x (for proof mass) and 4x for differential in-phase/in-quadrature modulation) carrier frequency for demodulation is shown in Fig. C.25.

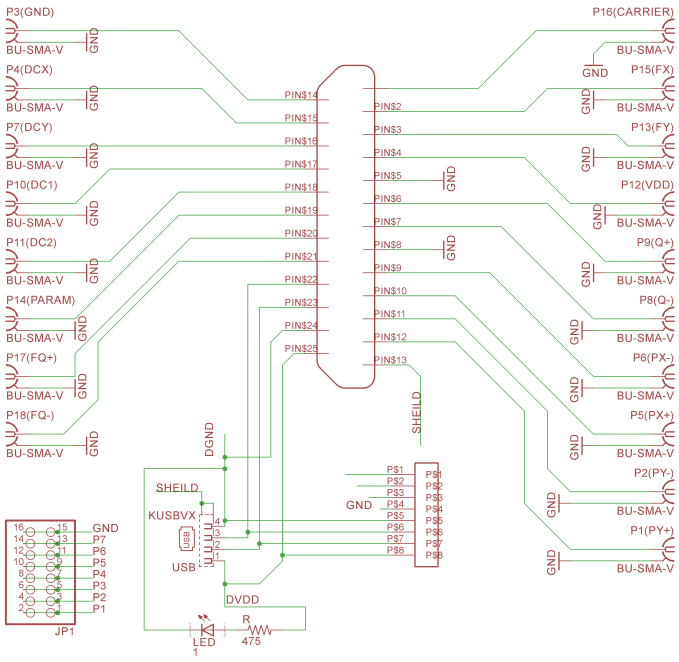

Figure C.16: Schematic of the Centrifuge system feedthrough, used in PCB C.1.6.1.

C.3.11. Commercial IMU readout:
Schematic of MPU9150 IMU digital routing to MCU used in PCB C.1.5 is shown in Fig. C.26.

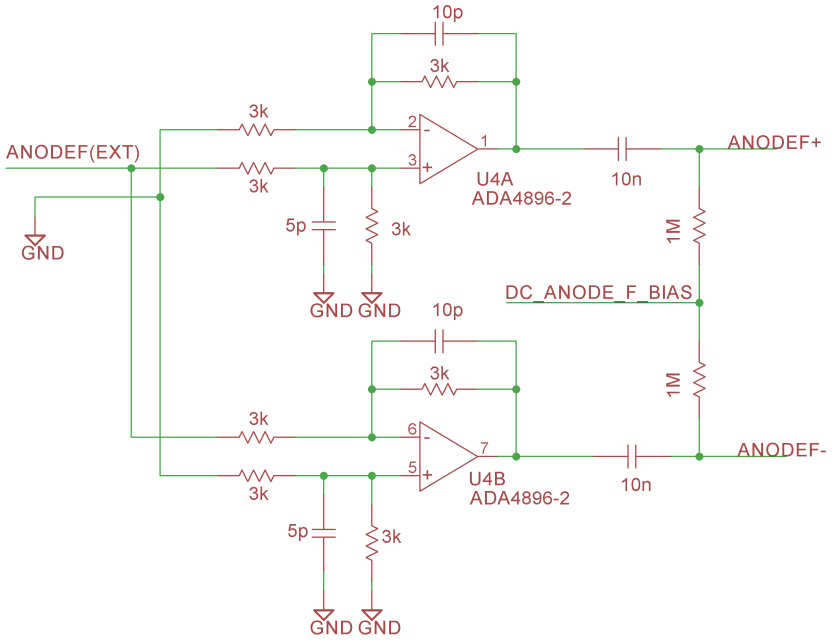

Figure C.17: Single-ended to differential drive using buffer amplifiers, implemented in PCB C.1.4.

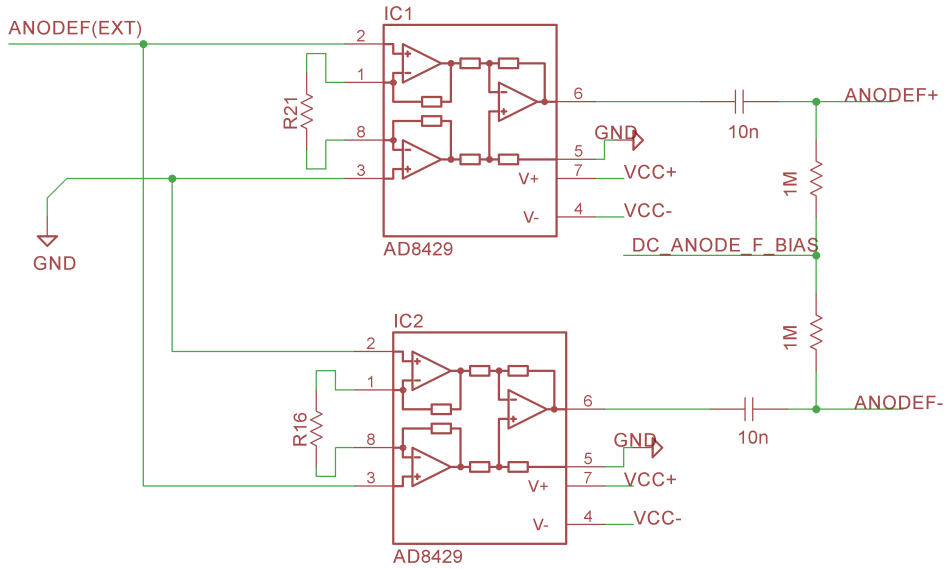

Figure C.18: Single-ended to differential drive using instrumentation amplifiers, implemented in PCB C.1.4.

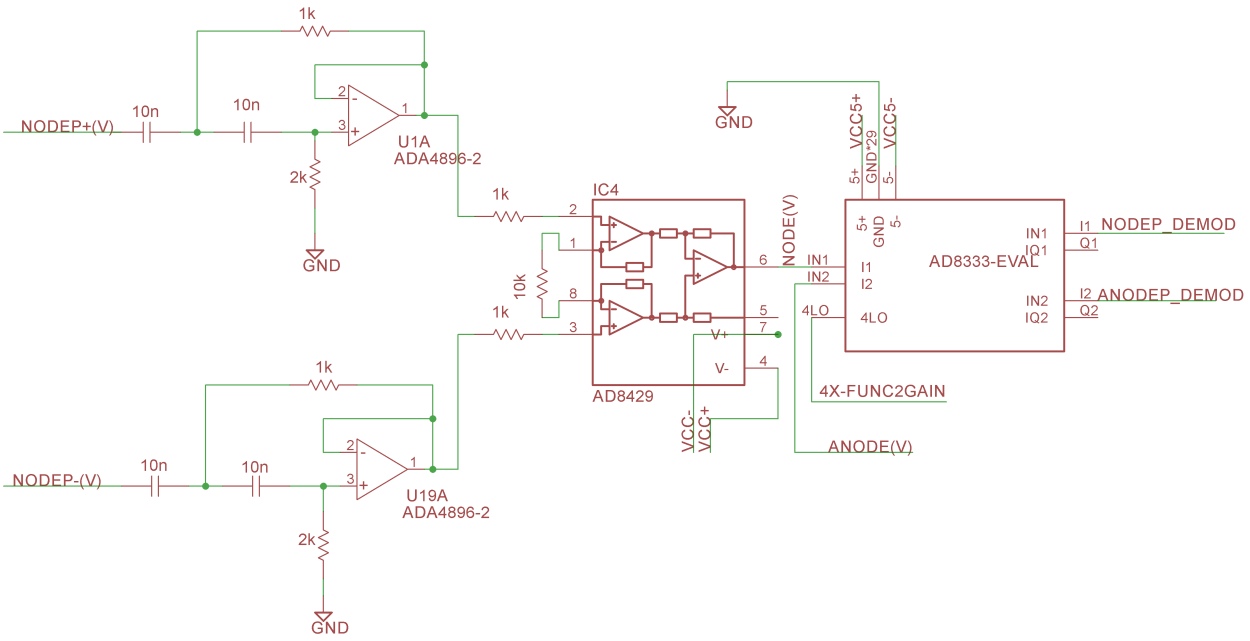

Figure C.19: Sallen-Key high-pass filter and carrier demodulation scheme implemented in PCB C.1.4.

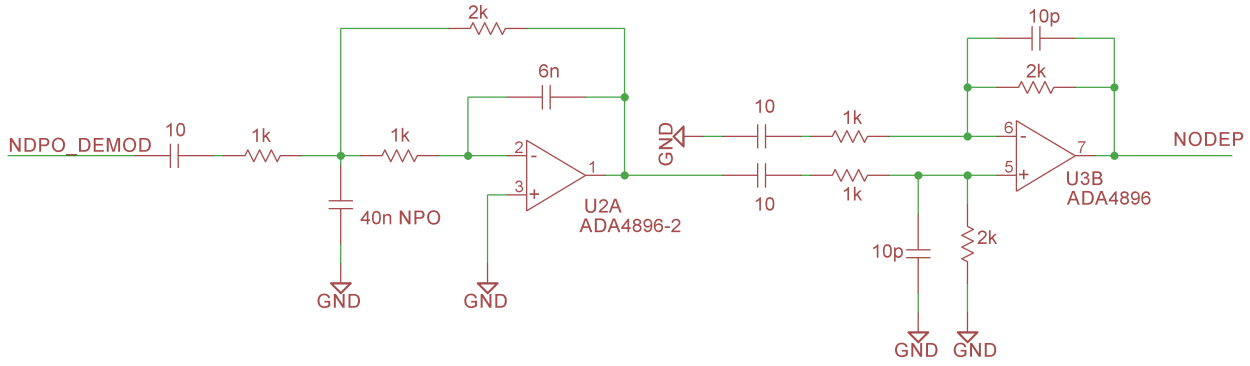

Figure C.20: Multiple feedback low-pass filter after carrier demodulation, implemented in PCB C.1.4.

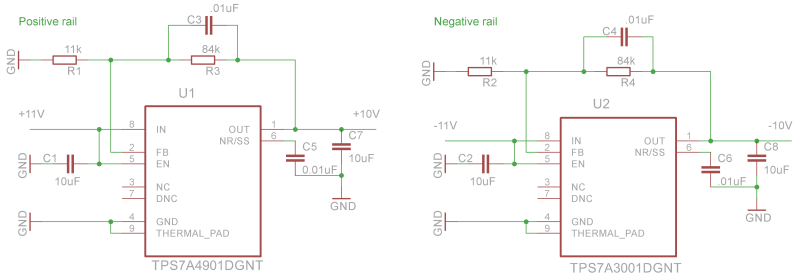

Figure C.21: Schematic of LDO voltage regulators used for denoising power rails, implemented in PCB C.1.4.

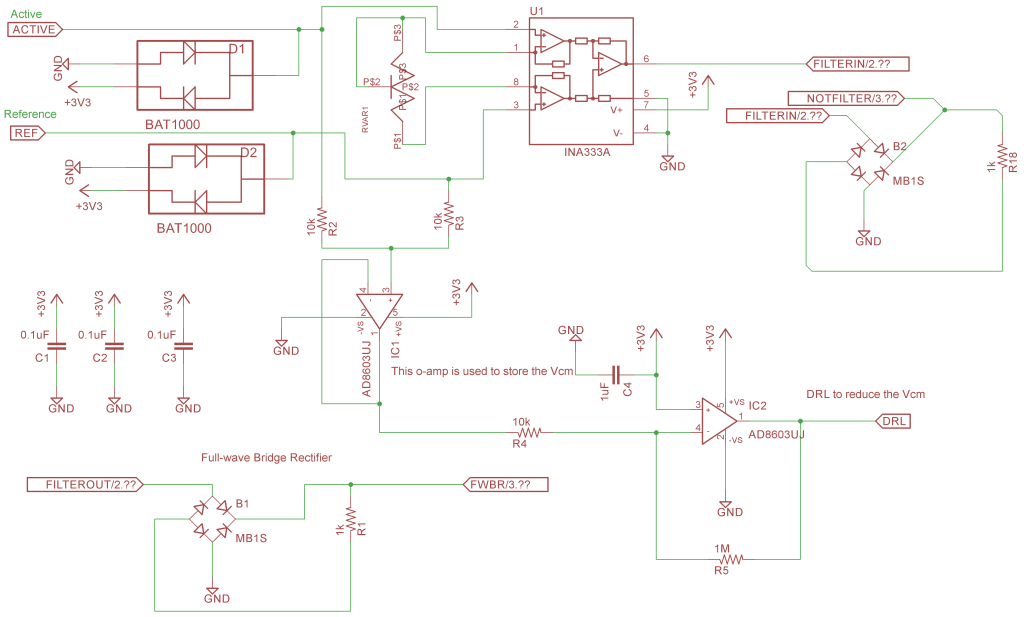

Figure C.22: Schematic of EMG readout used in the PCB C.1.5.

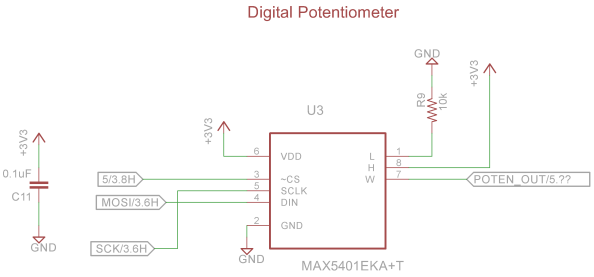

Figure C.23: Schematic of digital potentiometer used in the PCB C.1.5.

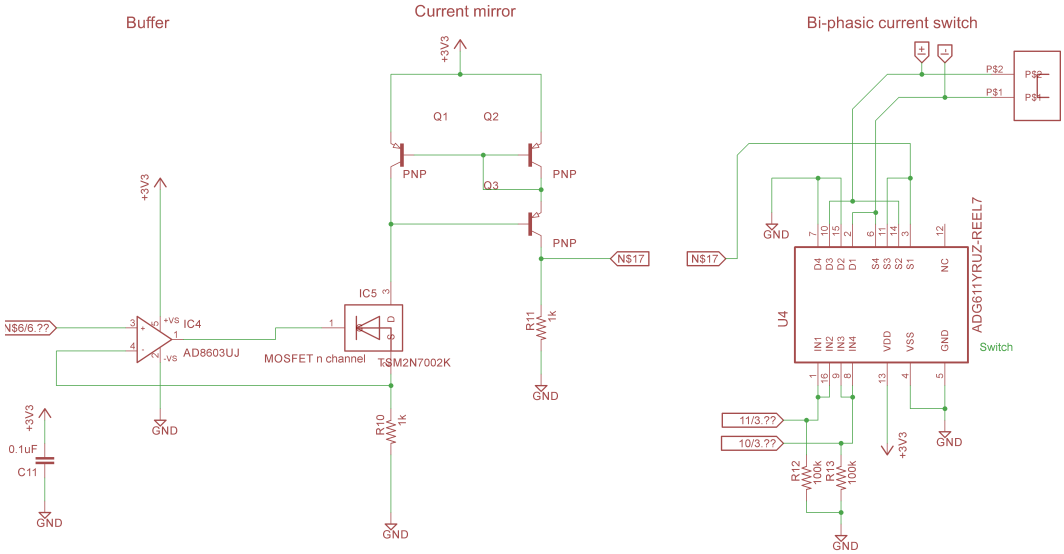

Figure C.24: Schematic of digital after potentiometer used in the PCB C.1.5.

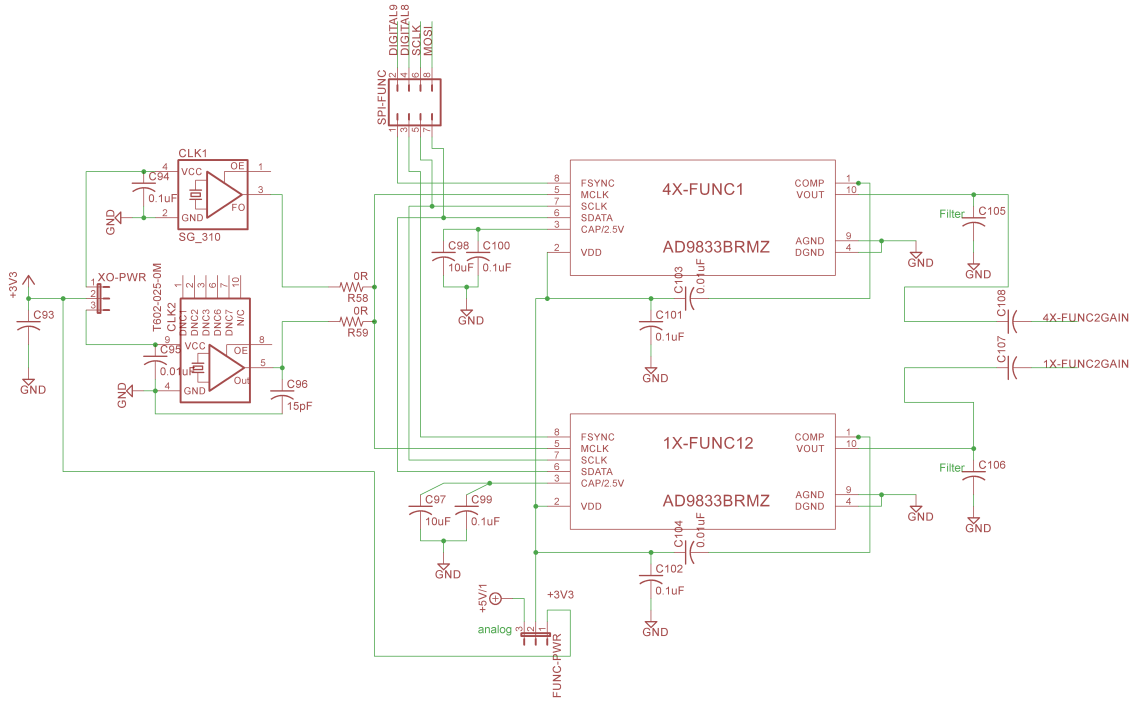

Figure C.25: Function generator feed to I/Q demodulator, implemented in PCB C.1.4.

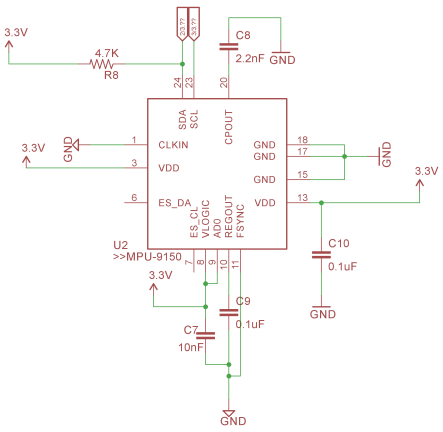

Figure C.26: Wiring of digital IMU readout to MCU used in the PCB C.1.5.

C.3.12. Magnetic reading:

To measure the magnitude of the magnetic field, a miniaturized Hall effect sensor was placed underneath the sensor packaged. The corresponding schematic is showing in Fig. C.27.

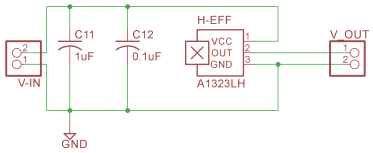

Figure C.27: Magnetic sensor reading used in the PCB C.1.6.2.

C.3.13. Si-Ware adapter (ASIC characterization solution):

A custom made adapter was developed to characterize the fabricated sensors with Si-Ware ASIC platform front-end. The schematic of this adapter is shown in Fig. C.28.

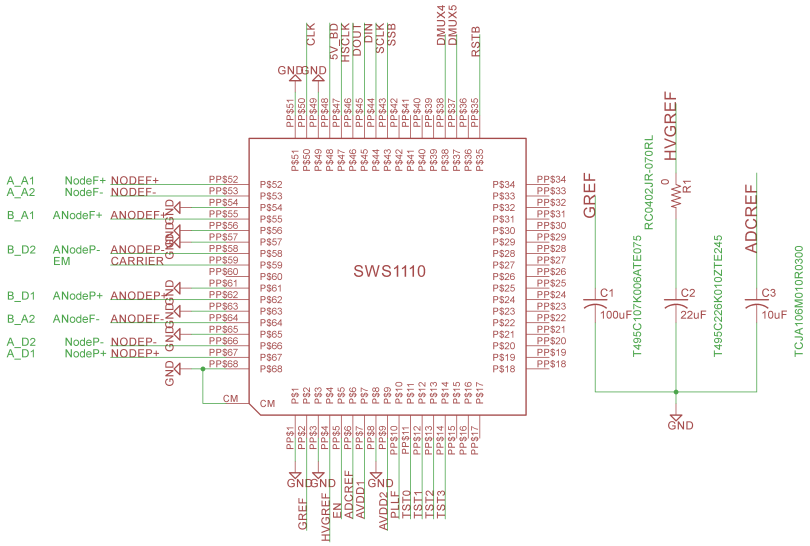

Figure C.28: Integration of Si-Ware chip to fabricated packaged gyroscope device.

C.4. Layouts

The described PCBs were fabricated in two-layer or multi-layer PCB configuration, depending on their complexity, analog and digital and number of components. The layouts and component placements are shown next:

C.4.1. First stage amplification for resonator or gyroscope:

For PCB C.1.1, a two layer PCB were fabricated and it is shown in Fig. C.29. The ground shielding for first stage active components is considered on the bottom layer. This technique isolates the current from the ground plane and to avoid any unwanted potential differences, which this will reduce down the electromagnetic interference on the sensed current.

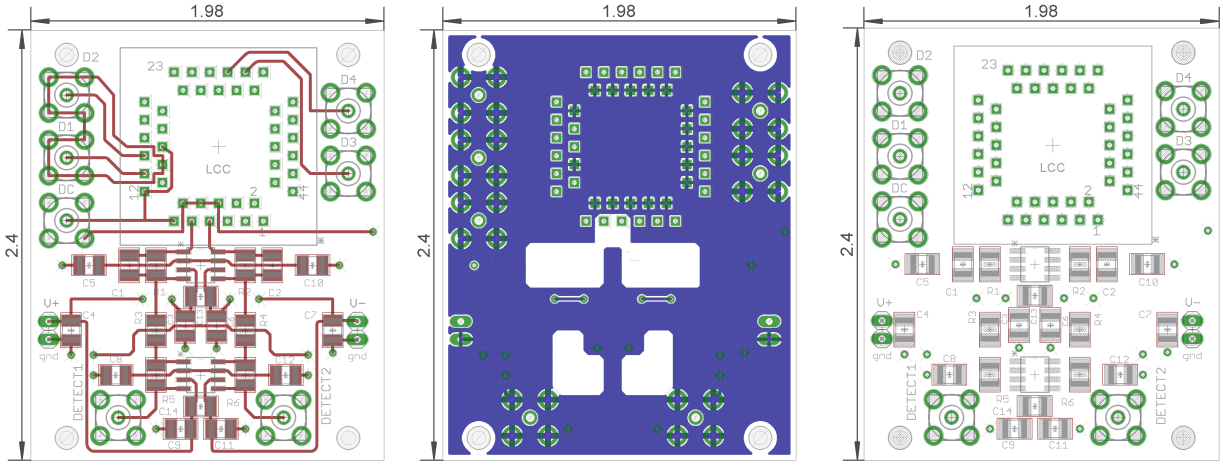

(a) top layer (b) bottom layer (c) component placement

Figure C.29: Layout of resonator characterization PCB, scale (1:1).

C.4.2. Gyroscope analog buffer card:

A two layer PCB was developed for PCB C.1.3 and the top layer routing layout is shown in Fig. C.30, the bottom routing layer layout in Fig. C.31, and the component placement in Fig. C.32.

C.4.3. Miscellaneous adapters and feedthrough:

Multiple adapters were developed and their layouts are shown next:

C.4.3.1. Single gyroscope adapter:

The PCB C.1.2, as described earlier provides the first stage amplification for the gyroscope, reroute the drive, sense and carrier signals to the package pins. The layout is shown in Fig. C.33.

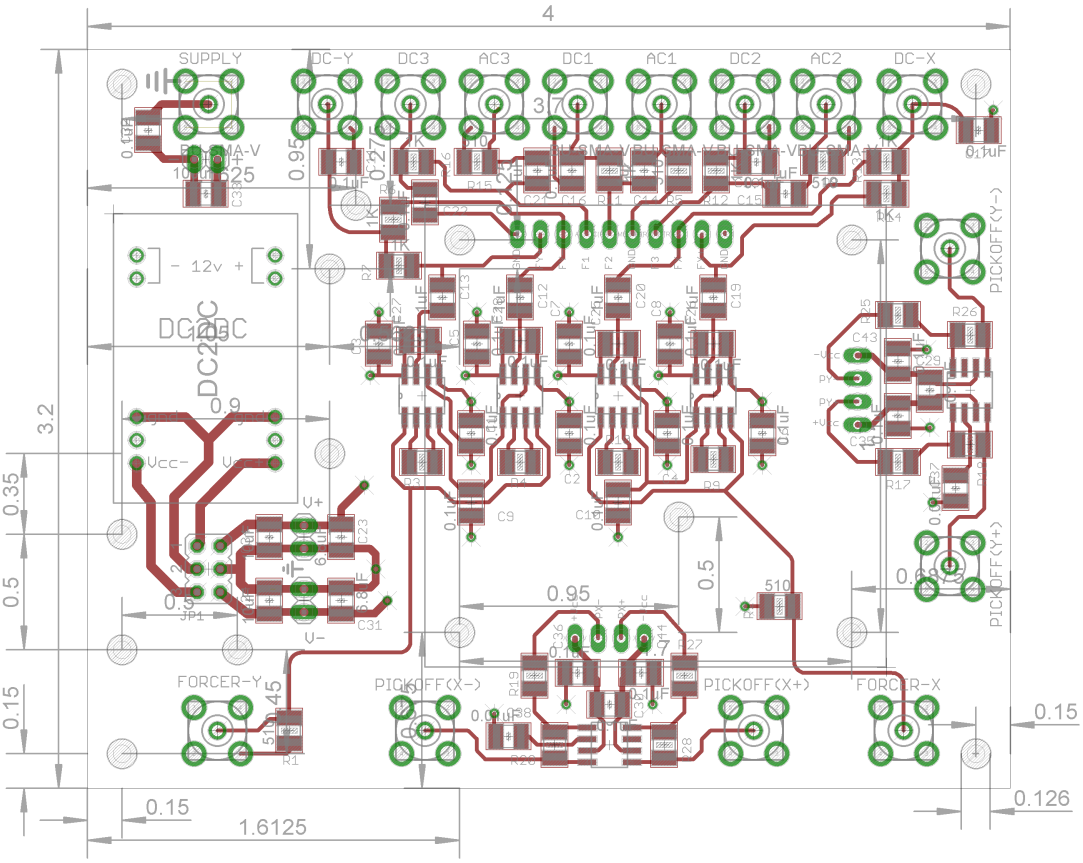

Figure C.30: Top layer layout of the gyroscope signal conditioning, scale (1:1).

C.4.3.2. IMU adapter adapter:
For PCB C.1.3 the implemented layout is shown in Fig. C.34.

C.4.3.3. Feedthrough adapter:
For PCB C.1.6.1 the implemented layout is shown in Fig. C.35.

C.4.3.4. Power regulator adapter:
An extra module for noise cancellation and to be seated on PCB C.1.2 and PCB C.1.4 is shown Fig. C.36.

C.4.3.5. Si-ware:
For PCB C.1.6.2, multi-layer configuration were considered and it is shown in Fig. C.37.

C.4.4. IMU/EMG current stimulation:
For PCB C.1.5, the implemented layout is shown in Fig. C.38.

C.4.5. Main board:

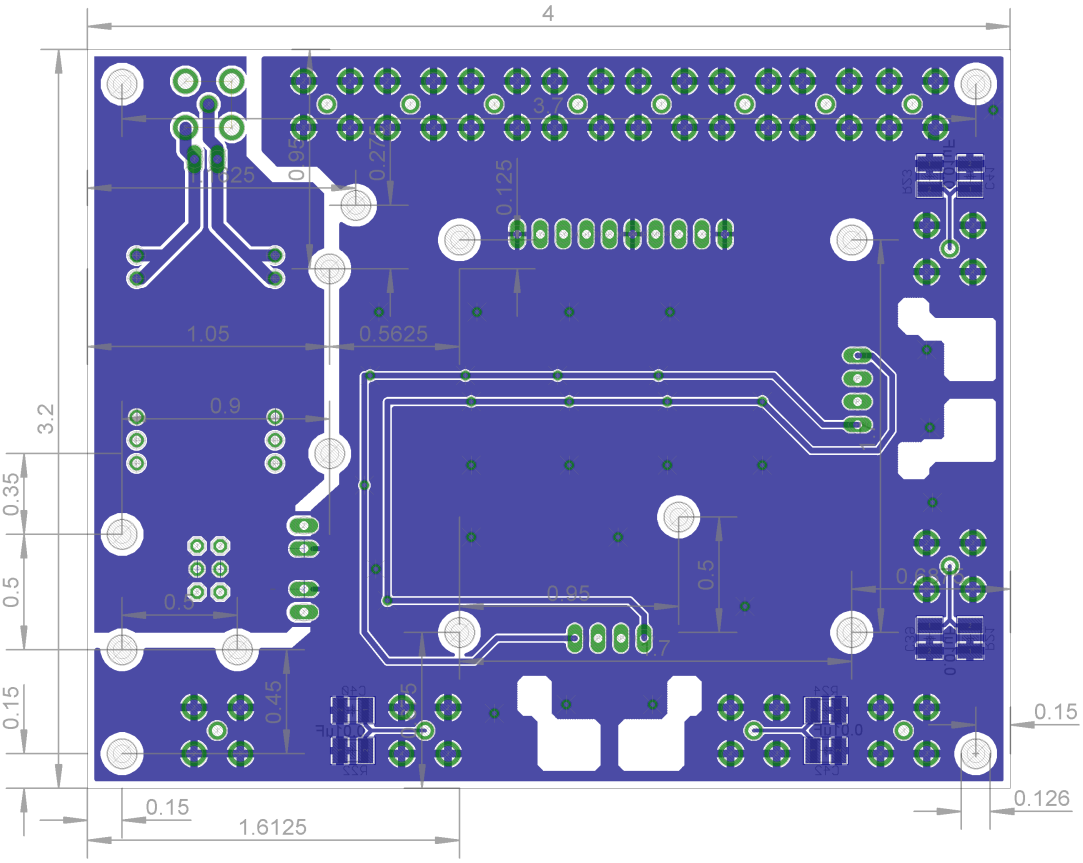

Figure C.31: Bottom layer layout of the gyroscope signal conditioning, scale (1:1).

For PCB C.1.4 the top layer is shown in Fig. C.41. The bottom layer considering the ground return path for digital and analog is shown in Fig. C.39, and the component placement is shown in Fig. C.40.

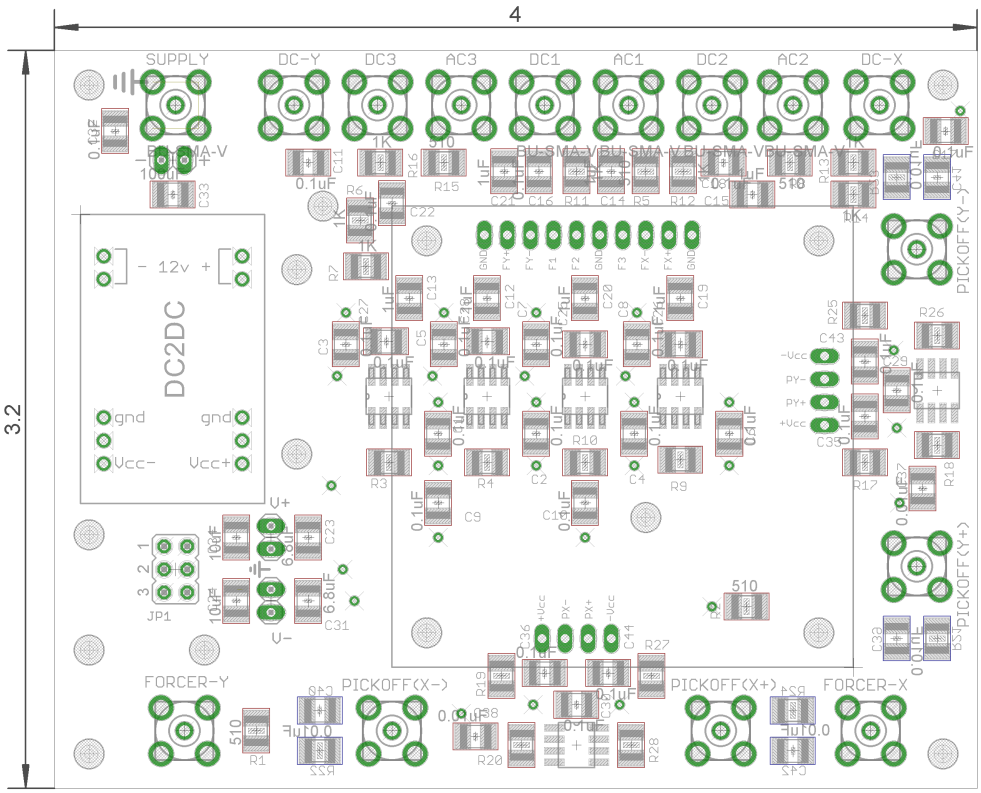

Figure C.32: Layout of component layer and its functionality, scale (1:1).

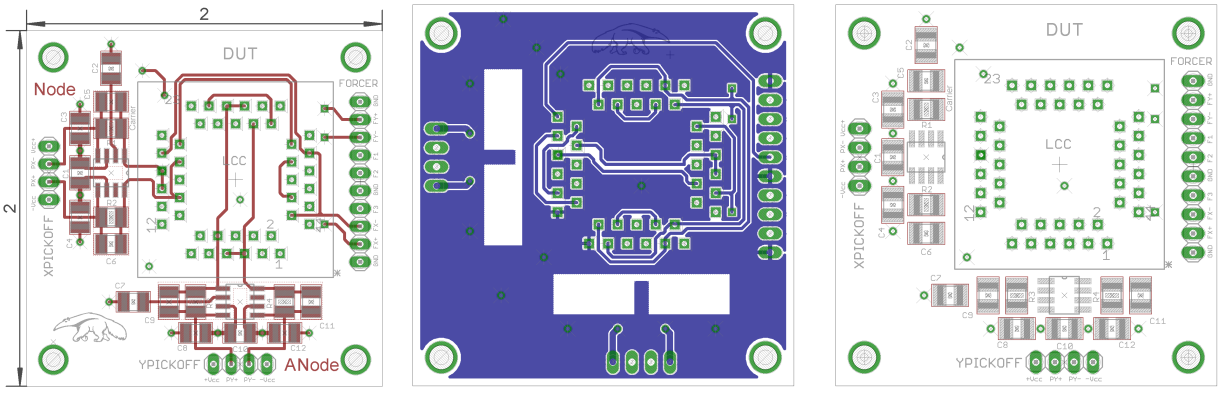

(a) top layer (b) bottom layer (c) component placement

Figure C.33: Layout of gyroscope device adapter, scale (1:1)

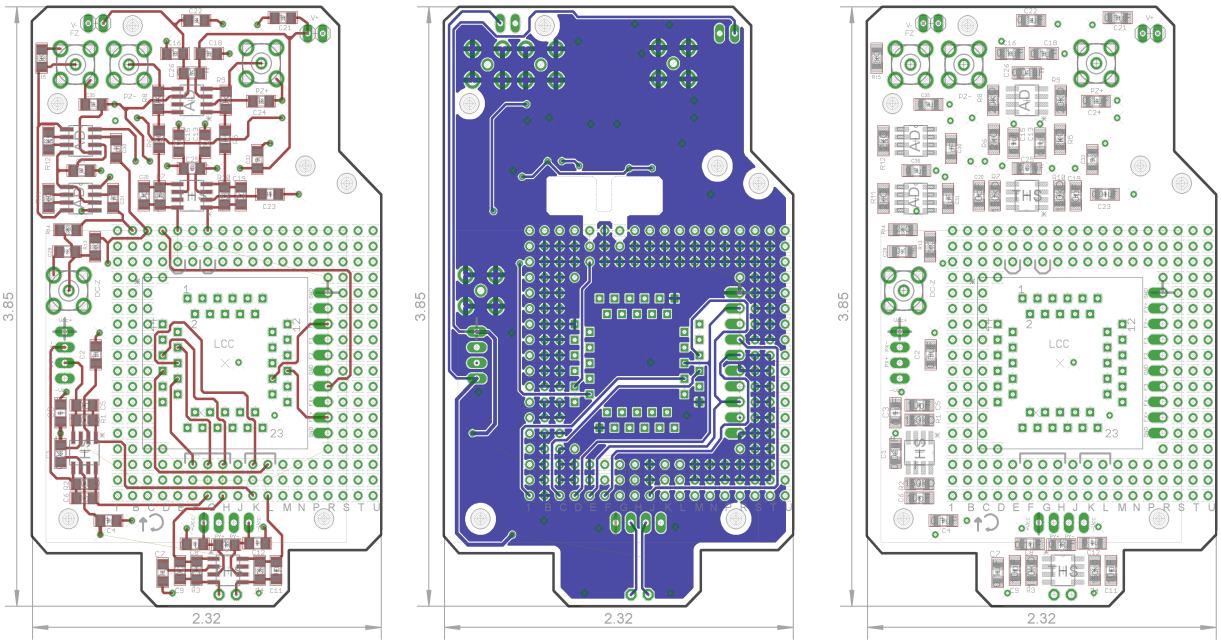

(a) top layer (b) bottom layer (c) component placement

Figure C.34: Layout of gyroscope device adapter, scale (1:1.7).

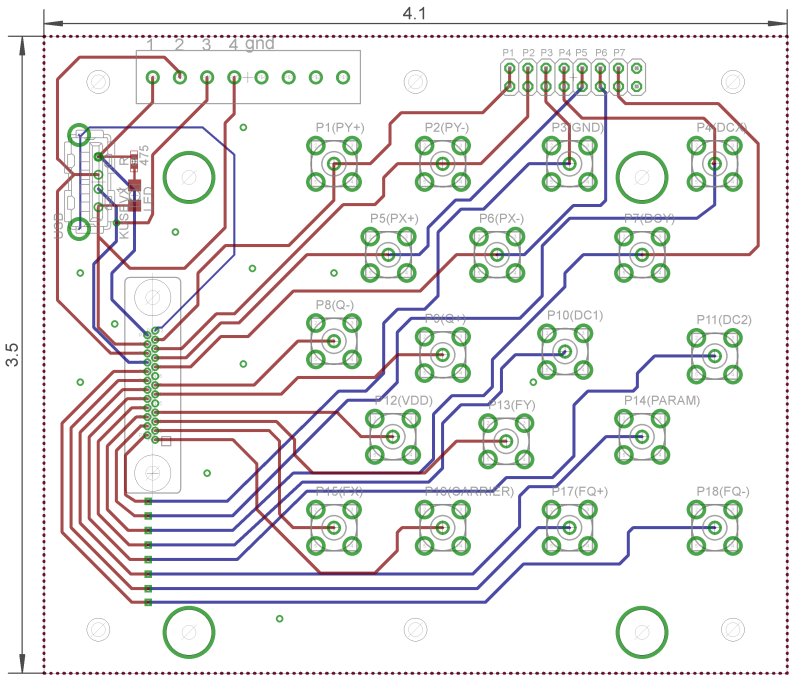

Figure C.35: Layout of the PCB interconnect top(red traces) and bottom(blue traces) layers, scale (1:1).

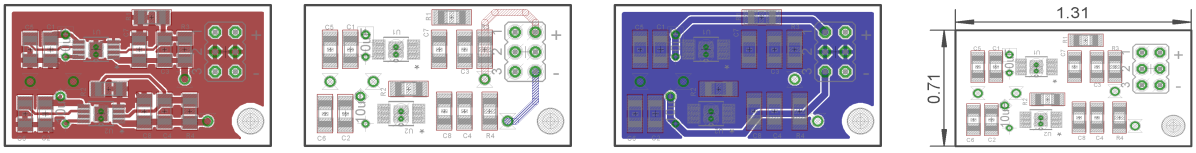

(a) top layer (b) mid layers (c) bottom layer (d) placements

Figure C.36: Layout of Low-dropout voltage regulator, scale (1:1).

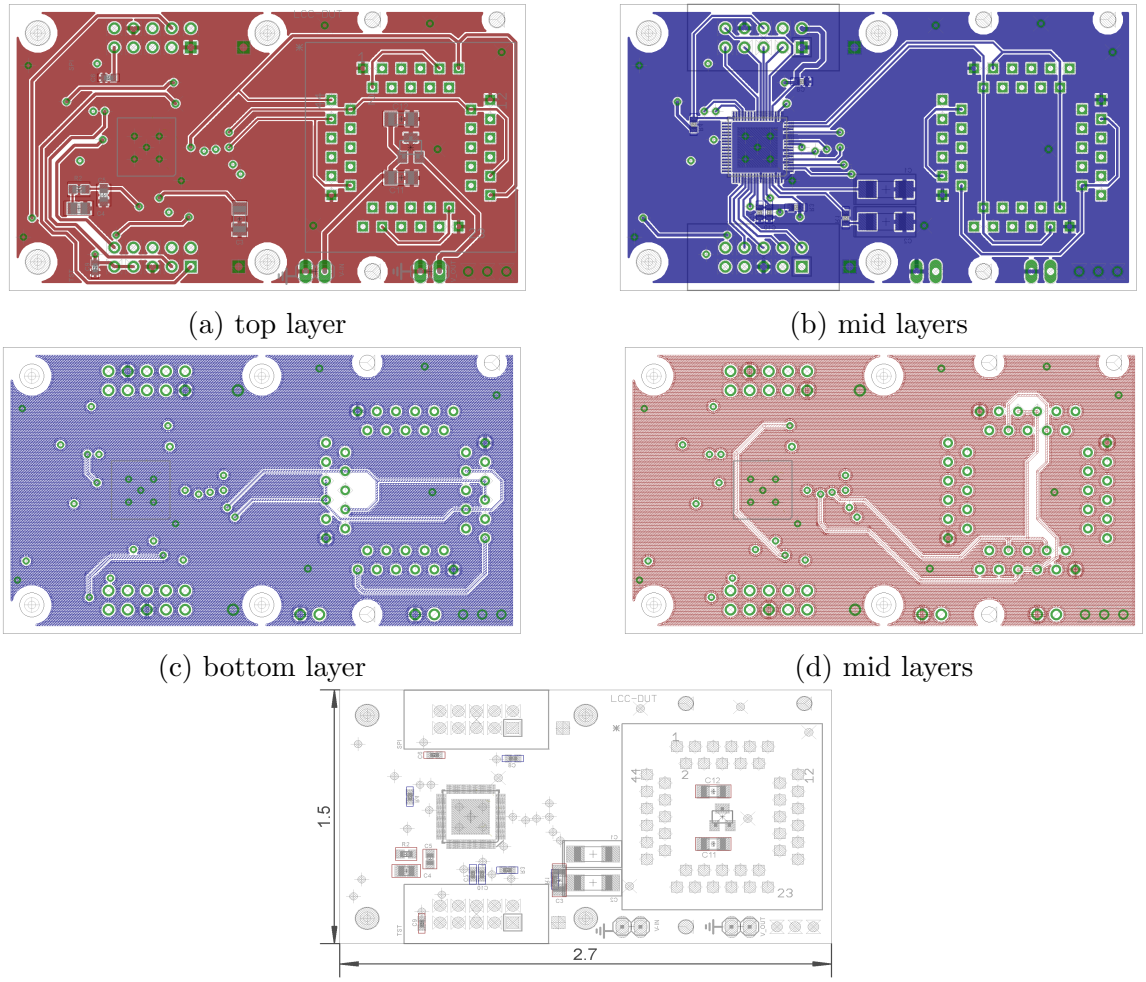

(a) top layer (b) mid layers

(c) bottom layer (d) mid layers

(e) component placements top

Figure C.37: Layout of ASIC solution characterization for gyroscope devices, scale (1:1).

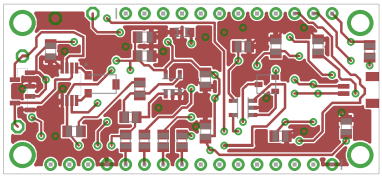

(a) top layer

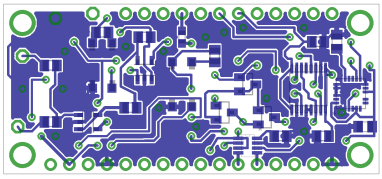

(b) bottom layer

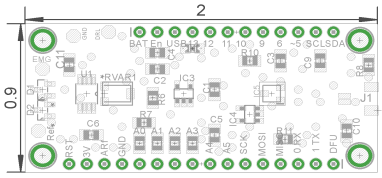

(c) component placement top

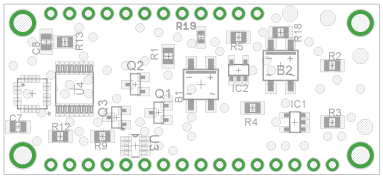

(d) component placements bottom

Figure C.38: Layout of IMU/EMG driven voltage regulator, scale (1:1).

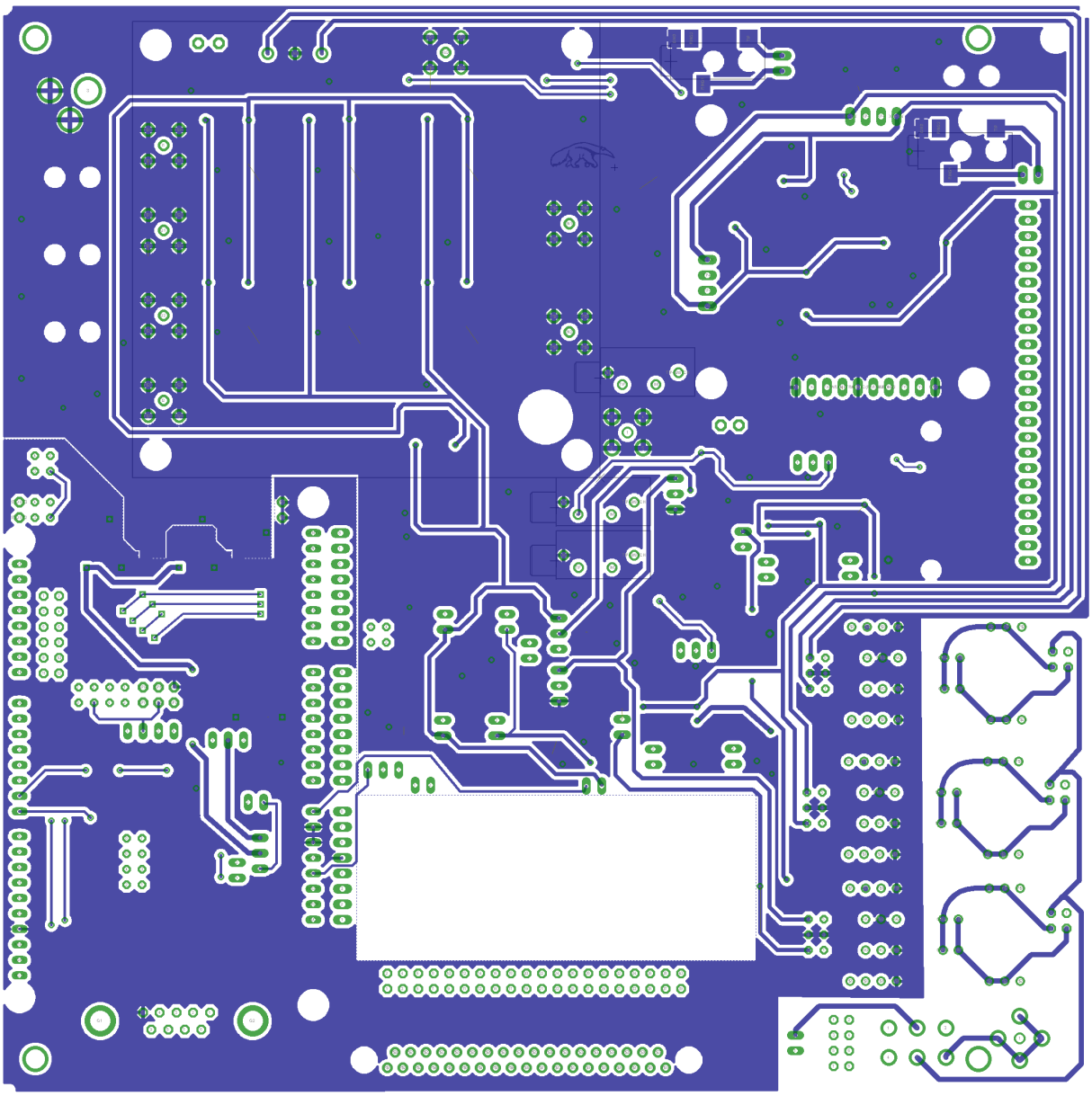

Figure C.39: Layout of the bottom layer (virtual ground), scale (1:1).

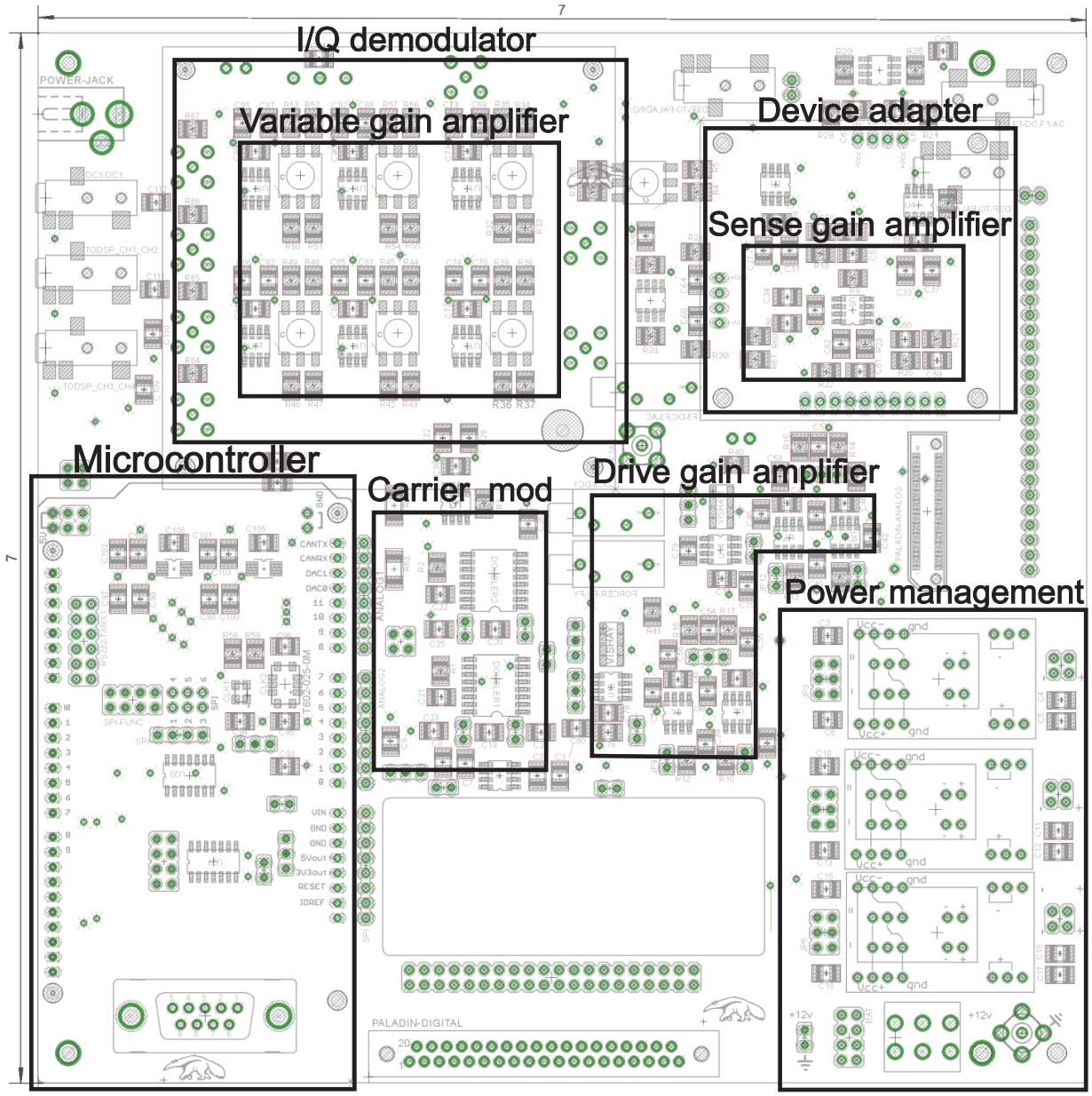

Figure C.40: Components placement and block functionality, scale (1:1).

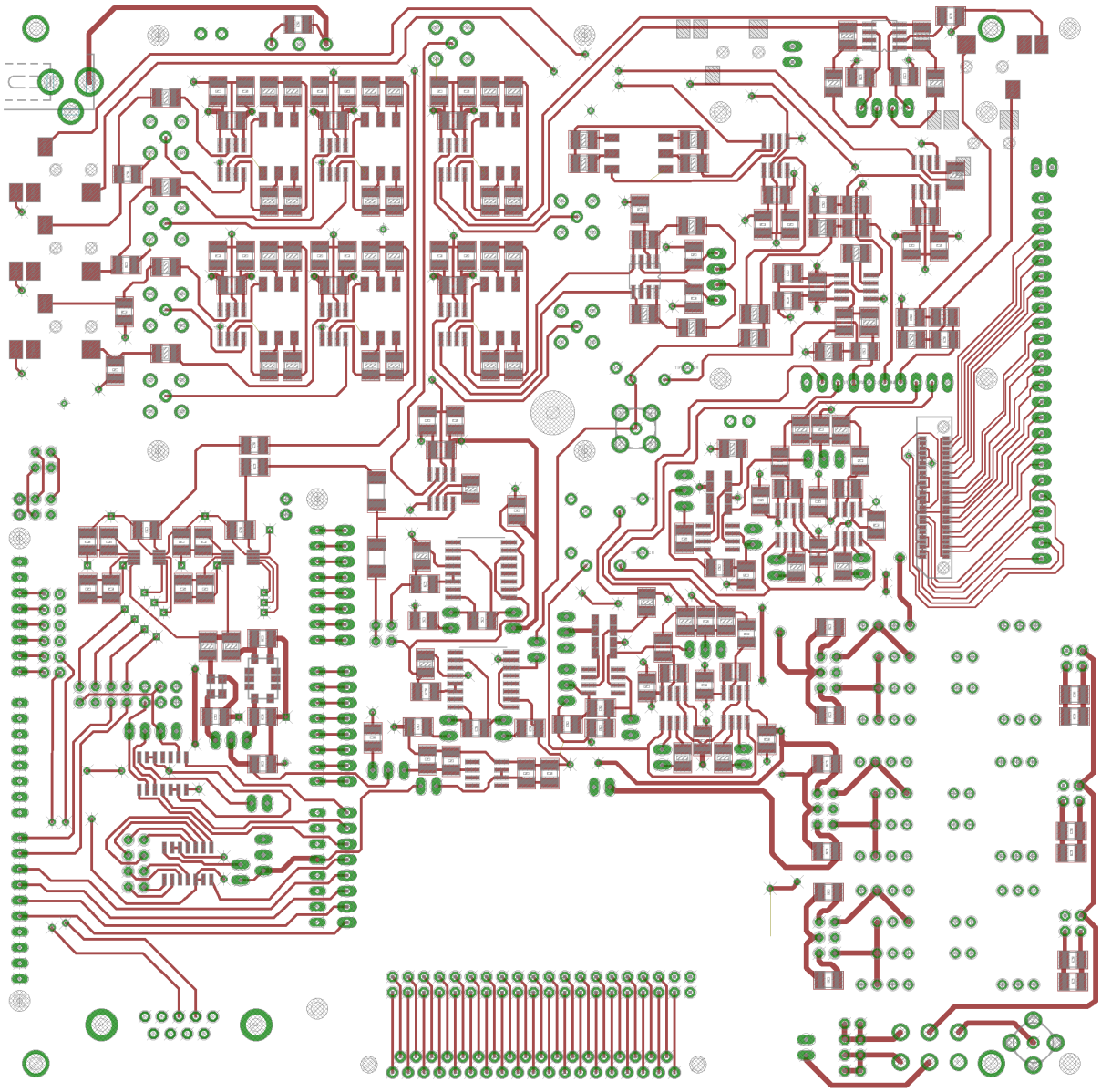

Figure C.41: Layout of the top layer (signal routing), scale (1:1).

C.5. Analog front-end bill of materials (BOM)
Main active components used in above circuits

Manufacture	Part number	Description	Pins	PCB
Texas Instruments	THS4131	Fully differential input/output low noise amplifier	8	C.1.1 C.1.2 C.1.3 C.1.4
Plastronics	P2044S-B-AU	Open top castellated LCC package	44	C.1.1 C.1.3
-	Resistors	$0\,\Omega$ to $1 \times 10^6\,\Omega$(SMD)	2	all
-	Capacitors	10×10^{-12} F to 1×10^{-1} F (SMD)	2	all
Mill-max	Connectors	Precision-machined interconnect	2-64	all
Molex	0836149016	conn microD Plug vertical sldr	25	C.1.6
Kycon	KUSBVX-AS1N-B	USB Connectors A type vertical	4	C.1.4 C.1.6
Kingbright	APHBMURKC	LED green/red clear	2	C.1.4 C.1.5 C.1.6
Analog Devices	AD8429ARZ	IC instrumentation amplifier circuit	8	C.1.2 C.1.3 C.1.4
Texas Instruments	INA333AIDGKR	IC instrumentation amplifier circuit	8	C.1.5
NKK Switches	MS22ANA03/UC	Switch slide 6A 125V	6	C.1.4
Analog Devices	REF196GSZ	Precision micropower, low dropout voltage references	8	C.1.3
TE Connectivity	-	SMA connectors	1	C.1.1 C.1.2
Texas Instruments	TPS7A4901	IC positive linear regulator	8	C.1.2
Texas Instruments	TPS7A3001	IC negative linear regulator	8	C.1.2
Analog Devices	AD835ARZ	IC multiplier 4-Quadrant	8	C.1.4
ON Semi.	MB1S	Bridge rectifier 500MA 4SOIC	4	C.1.5
ON Semi.	BAT54SLT1G	Diode array schottky	3	C.1.5
Maxim Integrated	MAX5401EKA	IC digital potentiometer $100\,\mathrm{k}\Omega$	8	C.1.5
Analog Devices	AD8638ARJZ	IC operational amplifier	5	C.1.5
Micro Commercial	MMBTA56-TP	Transistor PNP	3	C.1.5
Analog Devices	AD8603AUJ	IC operational amplifier	5	C.1.5
Taiwan Semi.	TSM2N7002KCX	Transistor MOSFET N-CH	3	C.1.5
Analog Devices	AD8034ARZ	IC FastFET operational amplifier	8	C.1.3
Analog Devices	ADA4896-2ARMZ	Rail-to-rail output amplifiers	8	C.1.4
TDK InvenSense	MPU-9150	IMU Accel/gyro/mag I2C	24	C.1.5
Diodes Inc.	BAT1000-7-F	Diode schottky		C.1.5
Analog Devices	ADG611YRUZ	IC switch quad	16	C.1.5
Allegro Micro.	A1323LH	Linear hall effect sensor IC	3	C.1.3

Si-Ware Systems	SWS1110	ASIC for capacitive MEMS	68	C.1.6
Analog Devices	AD8333	Dual I/Q demodulator and phase shifter	32	C.1.4
Arduino	A000062	Arduino Due ATSAM3X8E	54	C.1.4
CUI Inc.	PUZ3-D12-D5-D	DC DC converter +/-5V 3W	10	C.1.4
CUI Inc.	PUZ3-D12-D12-D	DC DC converter +/-12V 3W	10	C.1.4
CUI Inc.	PUZ3-D12-S24-D	DC DC CONVERTER 24V 3W	10	C.1.4
Texas Instruments	MPY634_DW_16	IC analog multiplier	16	C.1.4
Analog Devices	OP177GSZ	IC operational amplifier	8	C.1.4
Analog Devices	AD9833BRM	IC waveform generator	10	C.1.4
Connor-Winfield	T602-025-0M	Xtal osc TCXO 25MHZ	10	C.1.4
EPSON	SG-310SCF	Xtal osc XO 11.2896MHZ CMOS	4	C.1.4

PCBs BOM configurations

C.6. PCB fabrication material selection:
For regular PCBs FR4 material were selected for fabrication and for PCBs with vacuum chamber compatibility, ceramic material Roger 4350B laminates material (refer to Rogers' Corporation technical papers `www.rogerscorp.com`). This material also provides increase in thermal stability.

C.7. PCB assembly:
In-house PCB assembly were performed by using the WestBond epoxy die bonder machine. The XG-50 leaded solder paste were used for the assembly process using prototype Kapton stencils on the leads. Bare printed circuit boards were placed on the hot plate holder which has the vacuum on the center. The vacuum sucks down the board to hold it firmly. The vacuum tube on tip of the bonder machine sucks up the component and the controller moves the tip for the purpose of placing the component on top of the indicated area. By moving the tip down for the final placement, the machine releases the component when the tip senses back a small force from the board. For the reflow process a temperature of 220 F for the duration of 120 s applied to the bottom of board. The researcher should consider the safety operation of the high temperature for each active component reading from datasheet, lowering the temperature requires more time of heat to be applied on the board.

D Frequency Response Test

D.1. Purpose

This document described the basic steps needed on extraction of frequency sweep of a resonator. The following items are required: 1) A packaged resonator device for testing (with both X- and Y-modes operational), 2) Electronics for characterization. Actuation will be performed by the network analyzer, the carrier demodulation will be performed by the lock-in amplifier. PCB has been considered as forcer and detection analog circuit. The AC and DC actuation and carrier voltages will be adjusted and set by the user based on the device parameter. The device outputs current which is a function of both the carrier signal and motion of the resonator. The PCB converts this current to voltage. The voltage output is then fed back into the device for excitation.

D.2. Scope

This document described the test procedure on extraction of frequency response of a simple resonator. Previously released document D.3.1.

D.3. Applicable document

D.3.1. Revised version of "Breadboard front-end electronics" using PCB developed previously by [75].

D.3.2. Appendix. C: Electronics Schematic Development

D.4. Required components and equipment

Following list summarizes the components required for this measurement:

Components TYPE	MINIMUM SPEC	RECOMMENDED
Resonator device	Differential I/O (4-pins) Carrier port(1-pin) Ground port(1-pin)	Single mass resonator A device with min 6 electrodes A gyroscope device
Electronics	AC/DC Drive AC/DC Sense Carrier	D.3.2: PCB C.1.2 D.3.2: PCB C.1.3

Table D.6: Components required for frequency response test measurement

Following list summarizes the equipment required for this measurement:

INSTRUMENT TYPE	MINIMUM SPEC	RECOMMENDED
Power supplies	Supply 15 Volts, 0-3Amp	BK Precision 1672 triple output (Agilent E3612A)
Lock-in amplifier	Ametek signal recovery	Model 7270

Spectrum analyzer	FFT-Based network analyzer (51.2 kHz at 2 channel, swept-sine mode)	Agilent HP 35670A

Table D.7: Instruments required for frequency response test measurement

Test procedure:

D.4.3. Equipment and device connection diagram

D.4.3.1. Collect the components as described in Table. D.6.

D.4.3.2. Determine the orientation of the resonator device by confirming the electrode pin and layout connection of the package.

D.4.3.3. Confirm the wirebonding of the device with PCB schematic.

D.4.3.4. Place the resonator device inside the LCC socket. If a gyroscope is being tested, make sure the drive and sense pin corresponded to the electrical connection of the PCB.

D.4.3.5. Collect all instruments as described in Table. D.7.

D.4.3.6. Make sure the ground signal between SMA cables and different instruments are all connected externally.

D.4.3.7. Connect PCB drive SMA signal to network analyzer output (channel 1).

D.4.3.8. Connect channel 1 to input channel 2 (use BNC splitter), where it will be use as a reference for spectrum analyzer to perform the sweep measurement.

D.4.3.9. Connect PCB sense SMA signal to lock-in amplifier input.

D.4.3.10. Connect the lock-in amplifier oscillator output to the PCB carrier SMA port. This will be use for carrier modulation.

D.4.3.11. Connect from the back of the lock-in amplifier, the first modulation amplitude "R" to the network analyzer. This will be used to measure the amplitude of the frequency response of the device.

D.4.3.12. Power up the PCB with +12 Volt and ground connections.

D.4.4. Lock-in amplifier setup parameters

D.4.4.1. Turn on the lock-in amplifier wait for the initial boot up.

D.4.4.2. Set the "DAC 1" output to "X%". Press Menu → Main menu 2 → DAC Menu. The value for "DAC1 SETUP" should be set to "X% (2.5 V fs)". Press the Main Display button to exit.

D.4.4.3. Set the Oscillator frequency to 50 kHz and amplitude of 0.5 V to 2 V. Press Menu → Oscillator. "OSC FREQUENCY" should be set to "50,000.00 Hz" and "OSC AMPLITUDE" should be set to "2 V". Press the Main Display button to exit.

D.4.4.4. The main display screen should display "R" and "Θ" on the right in a large font. If it does not, press the buttons next to each until the top value is set to "R" and the bottom value is set to "Θ".

D.4.4.5. Set “AC Gain” to “0dB, DR 20” on the main display.

D.4.4.6. A green light at the top of the display should read “LOCKED”.

D.4.5. Network analyzer setup parameters

D.4.5.1. Turn on the network analyzer wait for initial boot up.

D.4.5.2. Press “Inst Mode”→ “SWEPT SINE”.

D.4.5.3. Press “Meas Data”→ “FREQ RESP 2/1”.

D.4.5.4. Press “Trace Coord”→ “dB MAGNITUDE”.

D.4.5.5. Press “Scale”→ “Y PER DIV (DECADES)”.

D.4.5.6. Press “Scale”→ “Autoscale ON”.

D.4.5.7. Press “Active Trace”→ “A”.

D.4.5.8. Press “Display Format”→ “Single”.

D.4.5.9. Set the AC signal amplitude. Press “Source” → “LEVEL” → “5” → “Vpk”. Change “5” to whatever amplitude of AC signal is desired.

D.4.5.10. Set the settling and integration time. Settling time determined how much time passes between actuation and measurement. Increasing settling time can help with sweeping high-Q devices. Integration time determined the number of averages that is collected for each measurement. Press “Avg” → “SETTLE TIME” → “2” → “0” → “CYCLES” for 20 frequency cycles between actuation and measurement. Press “Avg” → “INTEGRATE TIME” → “2” → “0” → “CYCLES” for 20 averages for each data point. For a cleaner sweep, increase both of these values to 200.

D.4.5.11. Set the number of data points collected. Press “Freq” → “RESOLUTN SETUP” → “RESOLUTN” → “2” → “0” → “1” → “POINT / SWEEP” for 201 data points. Press “Rtn” to return to the main screen.

D.4.5.12. Set the frequency range of measurement. Press “Freq” and set the range by either selecting a center frequency and frequency span around it (by setting “SPAN” and “CENTER”), or by setting a start and stop frequency (by setting “START” and “STOP”). For low-frequency devices, this should be below 5 kHz.

D.4.6. Frequency response characterization

D.4.6.1. Turn on DC power supplies for PCB active components and biasing drive axis.

D.4.6.2. On the lock-in amplifier, change “SENSITIVITY” until the value of “R” is close to 100%. The “SENSITI VITY” value should be close to “200 mV”. If not, the parasitic capacitance of the device may be far from 10pC.

D.4.6.3. On the lock-in amplifier, press Menu → Auto functions → AUTO PHASE. The main display should not be seen on the screen and “Θ” should be close to zero.

D.4.6.4. On the spectrum analyzer, press "Start" to begin the frequency sweep. At any point, "Pause Cont" can be pressed to pause or continue the sweep, or "Start" to begin the sweep again.

D.4.6.5. Sweep the device multiple times until the frequency response is found. Typically, simply changing the frequency range will suffice; however, the driving force can also be manipulated by changing both the AC and DC driving voltages.

D.4.6.6. To help identify if a magnitude peak is truly a mechanical resonance, the phase of the response can also be examined. Press "Trace Coord" → "PHASE" to examine the phase response, which should shift by roughly 180 degrees for a mechanical response. The magnitude response can be displayed againe by pressing "Trace Coord" → "dB MAGNITUDE".

D.4.6.7. Save the response once one has been found.

D.4.6.8. Press "Save / Recall" → "SAVE DATA" as a single file.

D.4.6.9. Transfer the saved files to the hard drive of the computer.

D.4.6.10. Open Matlab and go to "File" → "Import Data" and save the variables as "time" and "data".

D.4.6.11. Magnitude and phase can then be plotted using the following lines.

a. Magnitude: plot(time,20*log10(abs(data)))

b. Phase: plot(time,phase(data)*180/pi)

E Frequency Split of CVG

E.1. Purpose

This document described the basic steps needed on extraction of frequency split of a MEMS Coriolis Vibrating Gyroscope (CVG). The following items are required: 1) A packaged MEMS gyroscope device for testing (with both X- and Y-modes operational), 2) The full setup to extract frequency response of the device. Actuation will be performed by the network analyzer, the carrier demodulation will be performed by the lock-in amplifier. PCB electronics for characterization has been considered as forcer and detection circuits. The AC and DC actuation and carrier voltages will be adjusted and set by the user based on the device parameter.

E.2. Scope

This document described the test procedure on extraction of frequency split of a simple gyroscope with X- and Y-modes operational.

E.3. Applicable appendix

For the procedure described in this document, characterization of a frequency response is necessary in order to measure the frequency split of a MEMS CVG, for the procedure refer to:

E.3.1. Appendix. D: Frequency Response Test

E.3.2. Appendix. C: Electronics Schematic Development

E.4. Required components and equipment

Following list summarizes the components required for this measurement:

Components TYPE	MINIMUM SPEC	RECOMMENDED
Gyroscope device	Differential I/O (8-pins) Carrier port(1-pin) Ground port(1-pin)	A device with min 10 electrodes
Electronics	AC/DC Drive AC/DC Sense Carrier	E.3.2: PCB C.1.3

Table E.8: Components required for frequency split measurement

Following list summarizes the equipment required for this measurement:

INSTRUMENT TYPE	MINIMUM SPEC	RECOMMENDED
Power supplies	Supply ±15 Volts, 0-3Amp	BK Precision 1672 triple output (Agilent E3612A)
Lock-in amplifier	Ametek signal recovery	Model 7270

Spectrum analyzer	FFT-Based network analyzer (51.2 kHz at 2 channel, swept-sine mode)	Agilent HP 35670A

Table E.9: Instruments required for frequency split measurement

Test procedure:

E.4.3. Prepare test setup

E.4.3.1. Collect the PCB electronic for gyroscope characterization (see. E.3.2).

E.4.3.2. Place your device under the test into the socket mounted on the PCB.

E.4.4. Equipment connection

E.4.4.1. Implement the diagram similar to Appendix. D section D.4.3

E.4.5. Lock-in amplifier setup parameters

E.4.5.1. Repeat the procedure in Appendix. D section D.4.4

E.4.6. Network analyzer setup parameters

E.4.6.1. Repeat the procedure in Appendix. D section D.4.4

E.4.7. X-mode frequency response characterization

E.4.7.1. Check that both DC power supplies are off.

E.4.7.2. Identify the X-mode layout pins of the CVG device, see Fig. E.42.

E.4.7.3. Insert MEMS device into socket in X-mode configuration.

E.4.7.4. Turn on power supplies and perform the sweep and save the sweep as describe in Appendix. D section D.3.1

E.4.7.5. Repeat the procedure in Appendix. D section D.4.6

E.4.7.6. Report the X-mode center frequency as $f_{x-center}$.

E.4.8. Y-mode Resonant Frequency Sweep and Save Response

E.4.8.1. Check that both DC power supplies are off.

E.4.8.2. Identify the Y-mode layout pins of the CVG device, see Fig. E.42.

E.4.8.3. Insert MEMS device into socket in Y-mode configuration.

E.4.8.4. Turn on power supplies and perform the sweep and save the sweep as describe in Appendix. D section E.3.1

E.4.8.5. Repeat the procedure in Appendix. D section D.4.6

E.4.8.6. Report the Y-mode center frequency as $f_{y-center}$.

E.5. Example Calculations

E.6. Frequency split calculation Δf

E.6.1. The frequency split can be extracted using the following simple math by extracting the values reported earlier:

$$\Delta f(Hz) = |f_{x-center} - f_{y-center}|$$

where $f_{x-center}$ represents the center frequency of the X-mode and $f_{y-center}$ represents the center frequency of the Y-mode.

E.6.2. Report the above calculated number as your frequency split of your CVG under test.

E.6.3. The frequency split of the data reported in Fig. E.43 is measured to be 50 Hz.

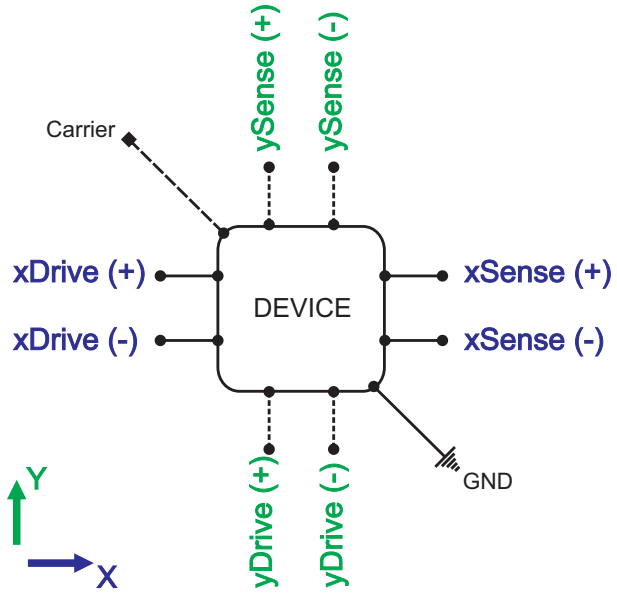

Figure E.42: Gyroscope device differential pins for X-axis and Y-axis drive and sense

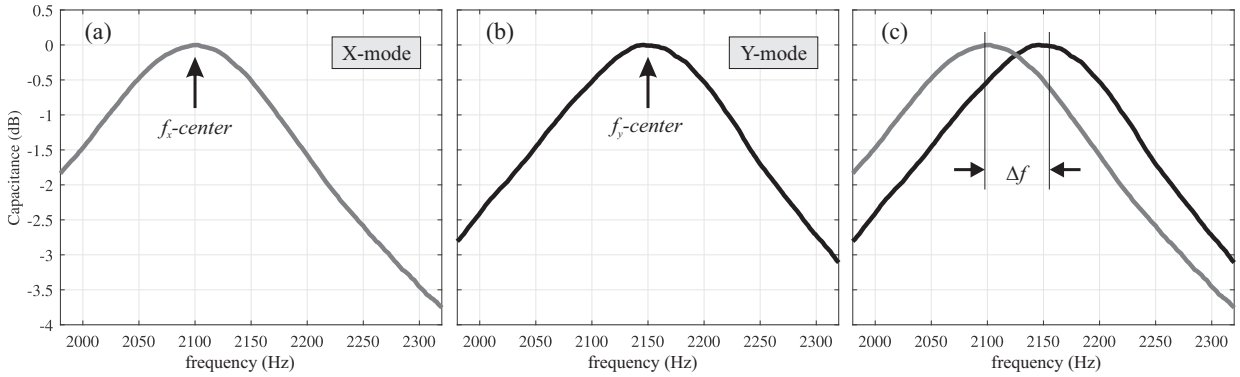

Figure E.43: An example of frequency sweep of a CVG device. a) Drive and sense on X-mode, b) Drive and sense on Y-mode, c) frequency split measurement given the experimental result

F Drive Loop of CVR (PLL and AGC)

F.1. Purpose

This document described the steps needed to track the resonance frequency of a MEMS Coriolis Vibrating Resonator (CVR) using Zurich UHF Look-in Amplifier. The following items are required: 1) A LCC packaged MEMS resonator device for testing (with X-mode operational), 2) Off the shelf lock-in amplifier with a nearby PC with USB port for implementation of the loops, 3) Standalone electronics with necessary power supplies for drive and sense interface. UCI/NGC electronic has been considered here in this document as the front-back end electronics. The AC actuation will be adjusted and set by the user based on the device parameter, the implementation of the loops will be done afterwards.

F.2. Scope

This document described the procedure on driving a resonator into its resonance while keeping the amplitude of the drive motion constant. The frequency tracking can be achieved by implementation of Phase Locked Loop (PLL), and maintaining amplitude by implementation the Amplitude Gain Control (AGC).

F.3. Required and Recommended equipment

Table F.10 summarizes the components required for this measurement:

COMPONENTS TYPE	MINIMUM SPEC	RECOMMENDED
A resonator	A Single X-axis resonator Sealed LCC/DIP package Q-factor of 1k	both modes operational Q-factor of 1M resonance frequency <4 kHz

Table F.10: Component required for this test measurement

Table F.11 summarizes the instruments required for this measurement:

Table F.12 summarizes the software required for this measurement:

Test procedure:

F.4. Equipment connection diagram

F.4.1. Interface device package on the tested PCB for X-mode resonator characterization
Select an electronic of your choice (PCB/breadboard) which you can drive with an external AC-voltage and sense your device externally with cables.

F.4.1.1. It is assumed that the selected electronic would actuate the resonator drive electrodes with a fix DC voltage and bias the proof mass with a modulated carrier frequency of your choice.

INSTRUMENT TYPE	MINIMUM SPEC	RECOMMENDED MODELS
Power supplies	Supply ±15 Volts, 0-3Amp	BK Precision 1672 Triple Output
Lock-in Amplifier	Zurich Lock-in Amplifier	Model UHF, HF2LI
Drive Electronic	DC drive voltage, included Carrier modulation, included	Standalone electronics Custom electronics
Sense Electronic	Carrier demodulation, included	Standalone electronics Custom electronics
Scaling Amplifier (optional)	Any COTS component. Matching the impedance of the buffer board	Stanford research system (SIM983)
Analog Limiter (optional)	Any COTS component. Matching the impedance of the buffer board	Stanford research system (SIM964)
Analog Filter (optional)	Any COTS component. Matching the impedance of the buffer board	Stanford research system (SIM965)

Table F.11: Instruments required for this test measurement

SOFTWARE TYPE	MINIMUM SPEC	RECOMMENDED MODELS
FPGA Control	Implementation of loops	LabOne UI (UHF) Zi Control (Zi2LI)

Table F.12: Software required for this test measurement

F.4.1.2. It is assumed that the carrier frequency is being demodulated internally or externally with another lock-in amplifier (not described here in this procedure).

F.4.2. Check that DC power supplies, and all instruments are off.

F.4.3. Place your device under the test into the socket mounted on the PCB.

F.4.4. Place necessary buffer cards (analog limiter, analog amplifier, low-pass filter) in between the UHF and PCB, and adjust the required parameters (Optional).

F.4.5. Connect the output 2 of the UHF to the input AC drive of the PCB (see Fig. F.44).

F.4.6. Connect output sense of the PCB to the input 2 of the UHF (see Fig. F.44).

F.5. Equipment setup parameters

F.5.1. Make sure that the DC power supply is current limited, to prevent any damage as a result of testing a bad/short device.

F.5.2. Set the higher and lower limit of the limiter based on the device under the test. To prevent any over drive in loop processing select a low value for high quality factor devices and high value for low quality factor devices (optional).

F.5.3. Set the low-pass filter cutoff frequencies to the desire value based on your resonance frequency (optional).

F.6. Procedure

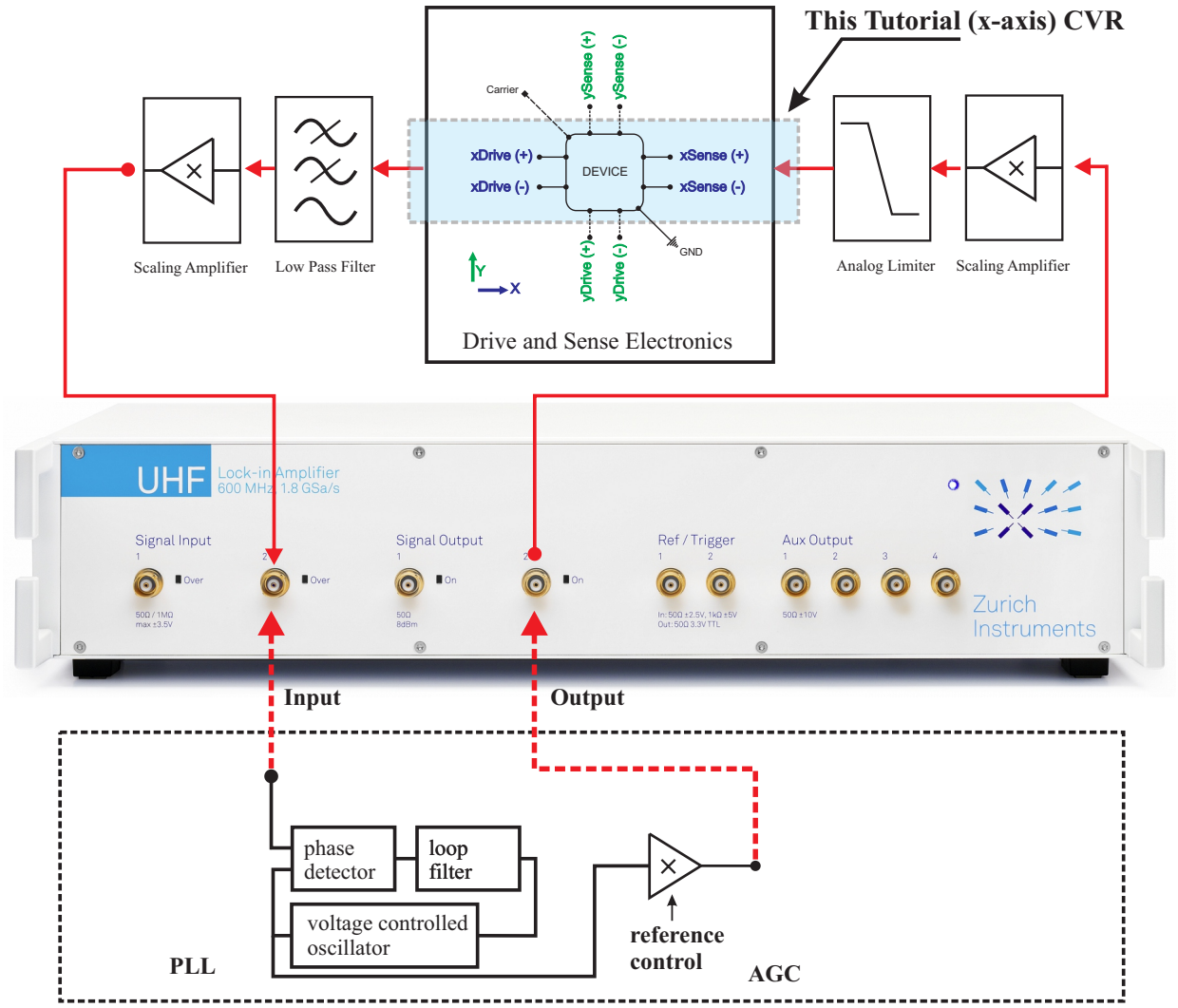

Figure F.44: Resonator device with X-mode under test and necessary interface with instrument for characterization

F.6.1. Check that DC power supplies are ON.

F.6.2. Verify that PCB is powered on with no indication of short in current consumption of the power supply.

F.6.3. Open the UHF user interface software.

F.6.4. From the lock-in tab, follow these steps (see Fig. F.45):

F.6.4.1. In this procedure, we are only working on input signal#2, and output signal#2, and the osc #8 (also called demodulation#8), row#8.

F.6.4.2. For osc#8, select the input signal to “Sig In 2”.

F.6.4.3. For osc#8, set the output Amp 2 (Vpk) to a desire value based on your device, e.g., 8mV.

F.6.4.4. Enable the output Amp 2 and data transfer of osc#8.

F.6.4.5. Select the osc frequency to 8, by dropping down the menu under the frequencies.

F.6.4.6. Make sure that the signal input#2 configuration is set based on your interface, for example here the interface did not require any 50 ohm input impedance to match the scaling amplifier output impedance.

F.6.4.7. For input#2 configuration select AC coupling.

F.6.4.8. Select the appropriate parameter for output#2 configuration, e.g., 50 ohm output impedance was required to match the input impedance of the scaling amplifier.

F.6.4.9. Select the data transfer to 13.41 sample/s for acquisition and visualization of the data.

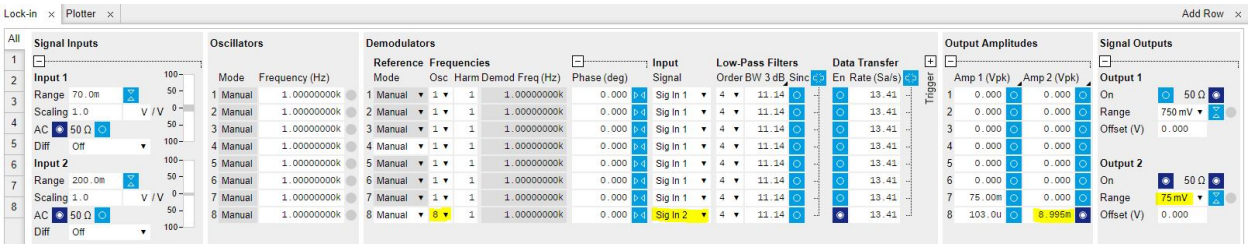

Figure F.45: User interface software configuration to control the output and input excitation of the device under test

F.6.5. From the sweeper tab follow these steps (see Fig. F.46):

F.6.5.1. Type in the start and stop frequency to sweep the frequency (0 Hz to 4 kHz)

F.6.5.2. From the "vertical axis to view" select the R value of the osc#8.

F.6.5.3. Perform the sweep once by clicking the single button, 4 kHz bandwidth.

F.6.5.4. From the amplitude response note the center frequency of the device.

F.6.5.5. Observe the dual plot to see the phase different of the system at the resonance peak, note this number as it would be needed later for PLL settings, e.g., 36° here

F.6.5.6. Perform the sweep once more with a narrower bandwidth 100 Hz, (see Fig. F.47).

F.6.5.7. Note down the phase shift at the resonance frequency, e.g., the shift with respect to zero 0 deg is 110 deg (Optional: In order to get a more accurate number repeat the sweep once again with a narrower bandwidth of around 2 Hz).

F.6.6. The UHF has 4 independent PID loops pre-programmed, with user adjustable parameter. Here in this procedure we only use PID#2, and PID#4.

F.6.7. PID#2 will be used for PLL and PID#4 will be used for AGC.

F.6.8. **Implementation of phase locked loop**

F.6.8.1. From the PID/PLL tab follow these steps: (see Fig. F.48)

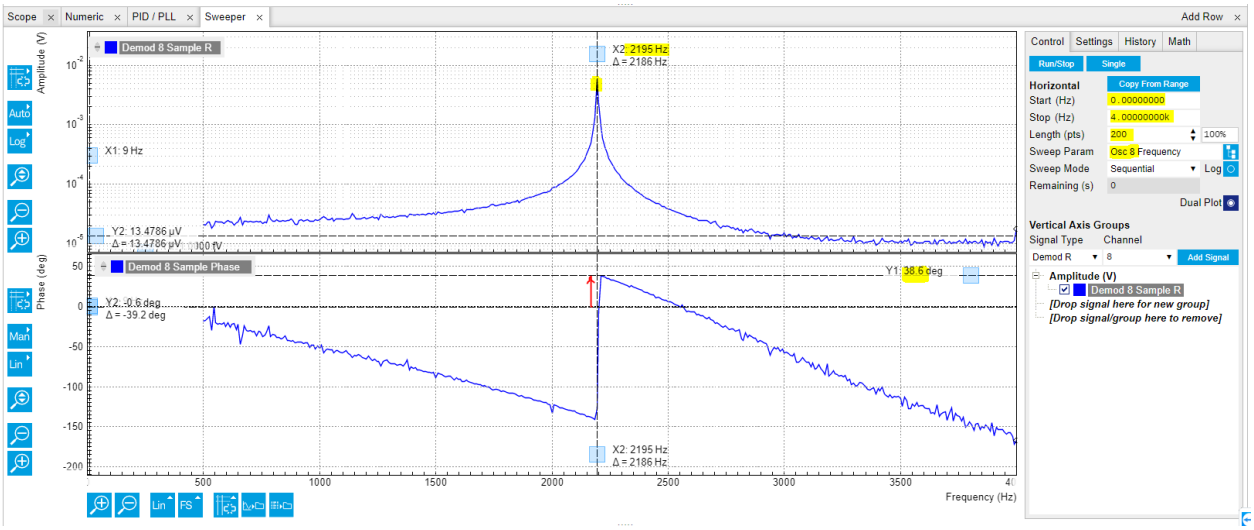

Figure F.46: Initial characterization of the device to obtain the frequency/phase response

i) Type in the center frequency of the device from F.6.5.4 in PID#2 output center frequency.

ii) Type in the desire bandwidth based on the resonance frequency and quality factor into the lower and upper Hz, e.g., 50 Hz here.

iii) Adjust the P, and I value of the loop setting to have a stable phase margin which can satisfy the bandwidth of the resonator, e.g., P:-254 Hz/deg, I:-32 Hz/(deg s).

iv) Select the input phase to osc#8 from the drop-down menu.

v) Type in the noted phase from the sweep F.6.5.5 into the set-point, e.g., a rough estimation with 100 Hz bandwidth it around 110 deg, we will adjust this number in the next step.

F.6.8.2. From the plotter tab observe the R value of the demodulation#8.

F.6.8.3. Adjust the setpoint to find where the R value increases. Fig. F.49, shows this output on different setpoint values, e.g., 130° is where the demodulation R value is maximum.

F.6.8.4. PLL is called locked when the error is within the desire bandwidth and the loop is critically damped, in this condition the LED indicator next to error is green.

F.6.9. **Implementation of amplitude gain control**

F.6.9.1. From the PID/PLL tab follow these steps: (see Fig. F.50)

i) Type in the output amplitude from F.6.4.3 to the output center of the PID#4

ii) Type in the desire upper and lower limit of your excitation amplitude.

iii) Adjust the P, and I value of the loop setting to have a stable phase margin which can satisfy the bandwidth of the resonator, e.g., P: 100m, I: 300m(1/s).

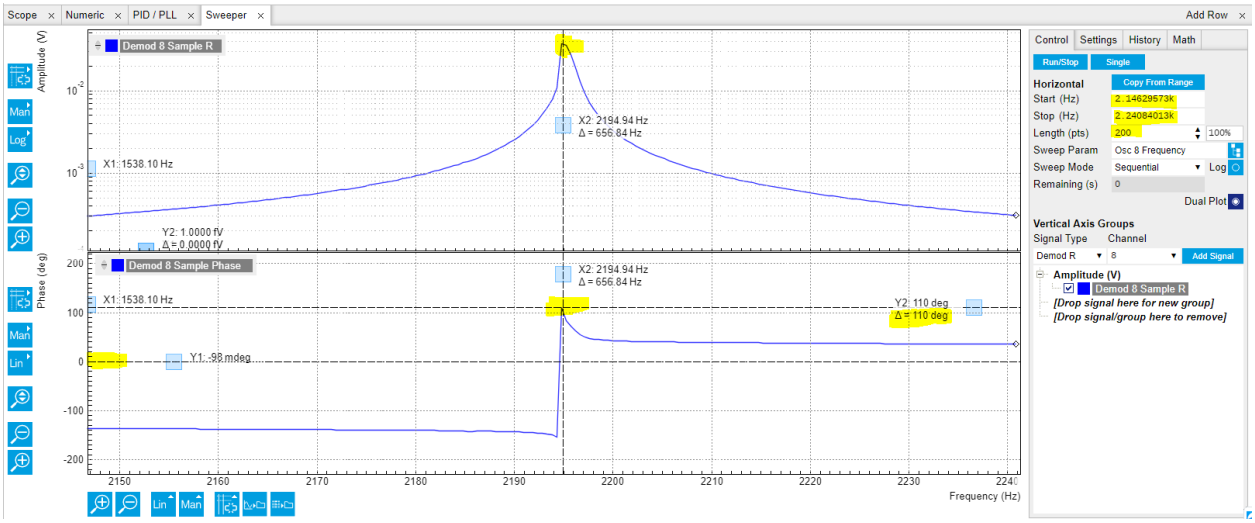

Figure F.47: Zoomed-in view of the sweep to extract the phase different between output and input of the system at the resonance peak

F.6.9.2. From the plotter tab observe the R value of the demodulation#8.

F.6.9.3. Adjust the P and I value to have a critically damped amplitude by changing the set point (see Fig. F.51).

F.6.10. **Observe the CVR oscillation**

F.6.10.1. Select the scope tab and observe the wave#2, which is the input#2 of the UHF.

F.6.10.2. A sinusoidal which tracks the resonance frequency of the device with a fixed amplitude can be seen for further analysis, see Fig. F.52.

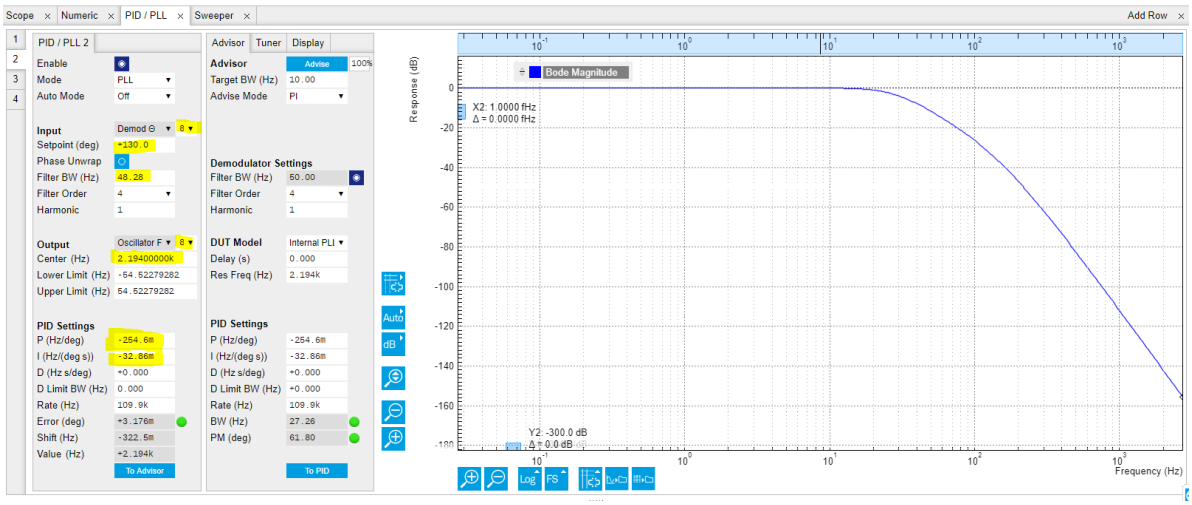

Figure F.48: PLL parameter configuration

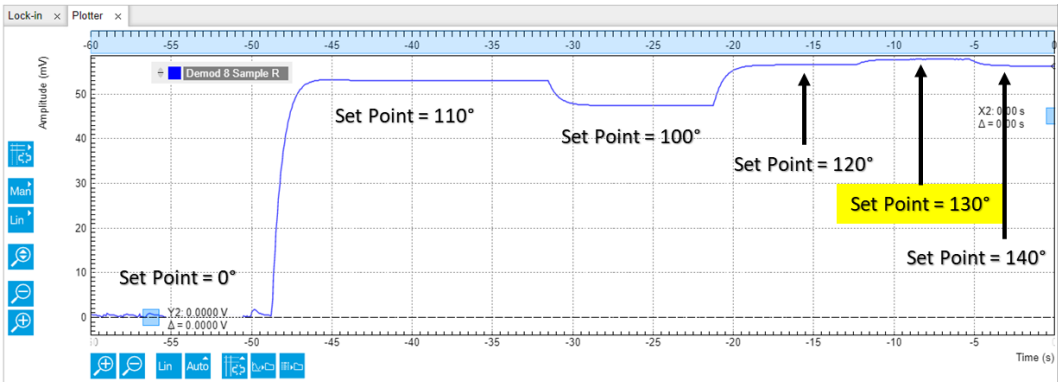

Figure F.49: Resonator output amplitude response as a result of changing/optimizing the set point (PLL ON)

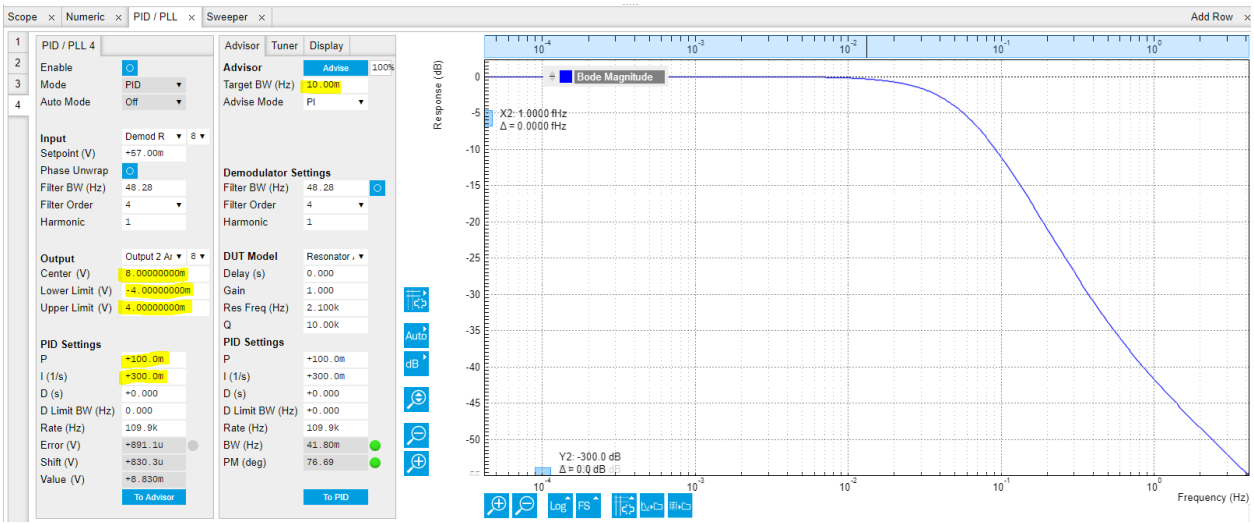

Figure F.50: AGC loop parameter configuration

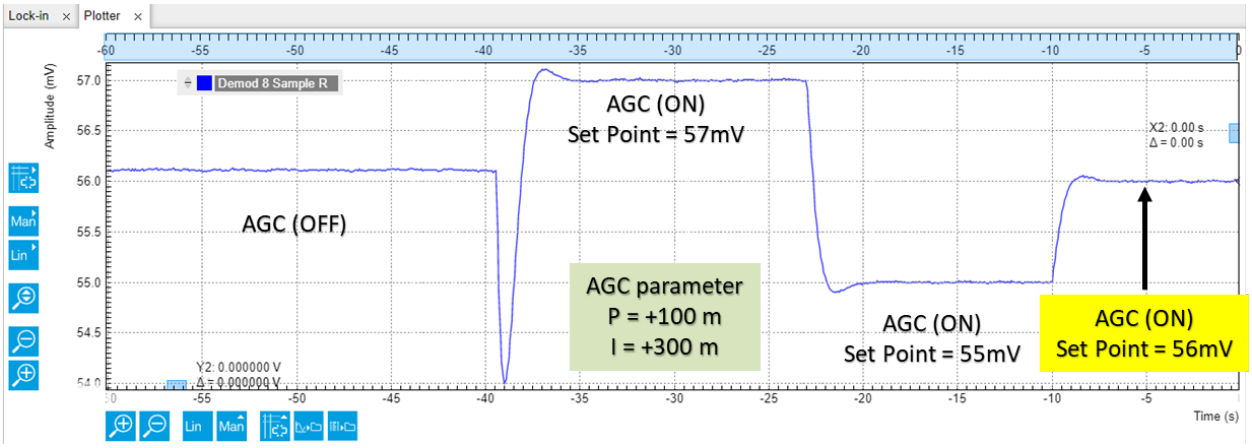

Figure F.51: Resonator output amplitude response as a result of changing/optimizing the AGC set point (AGC/PLL ON)

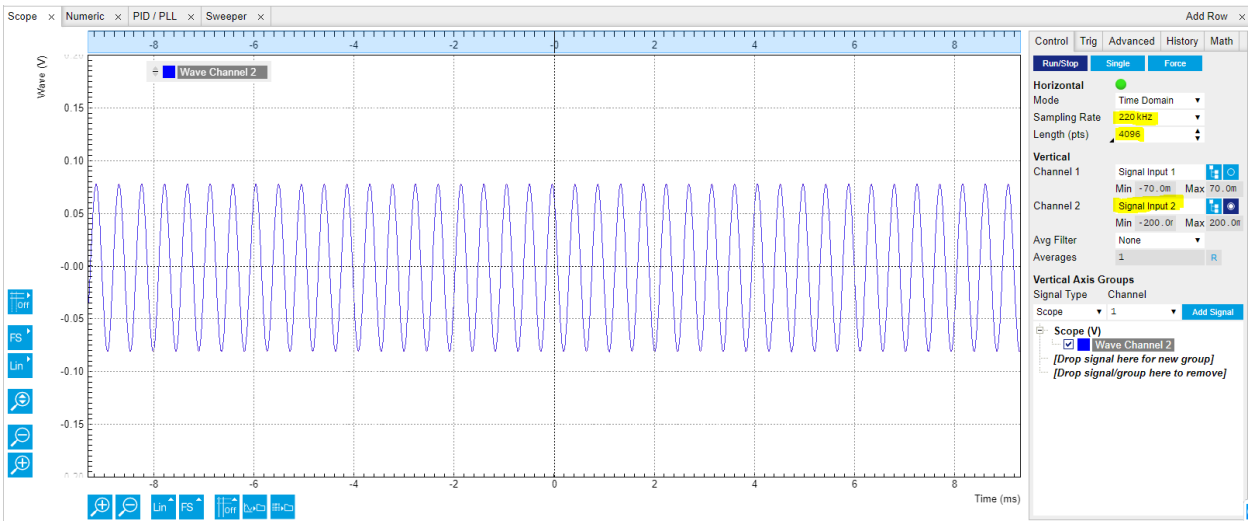

Figure F.52: Realtime measurement of the CVR oscillator while PLL and AGC is being implement

G Scale-Factor for CVG

G.1. Purpose
This document describes the procedure for estimation the Scale-factor (SF) of a single-axis MEMS Coriolis Vibratory Gyroscopes (CVG) using rate table.

G.2. Scope
This document described the procedure on estimating the SF by implementation of the demodulation loop on the sense axis.

G.3. Applicable appendix
For the procedure described in this document, implementation of PLL and AGC control loops are necessary in order to estimate the scale-factor of a MEMS CVG in the rate mode configuration, for the implementation of these loops refer to:

G.3.1. Appendix. F: Drive Loop of CVR (PLL and AGC)

G.4. Required and Recommended equipment
The following items are required: 1) An LCC packaged MEMS gyroscope device for testing (with X- and Y-modes both operational), 2) Off the shelf lock-in amplifier with a nearby PC with USB port for implementation of the loops, 3) Standalone electronics with necessary power supplies for drive and sense interface. UCI/NGC electronics has been considered here in this document as the front-back end electronics. Following components are required for this measurement:

Table G.13 summarizes the components required for this measurement:

Components TYPE	MINIMUM SPEC	RECOMMENDED
A MEMS CVG device	A single yaw axis CVG Sealed LCC/DIP package Quality factor of above 1k	both modes operational

Table G.13: Component required for this test measurement

Table G.14 summarizes the instruments required for this measurement:

Table G.15 summarizes the software required for this measurement:

Test procedure:

G.5. Equipment connection diagram
Interface device package on the tested PCB for CVG characterization

G.5.1. Select the electronic of your choice. (Ref. G.3.1).

INSTRUMENT TYPE	MINIMUM SPEC	RECOMMENDED MODELS
Power supplies	Supply ±15 Volts, 0-3Amp	BK Precision 1672 Triple ch.
Lock-in Amplifier	Modulation, demodulation, data acquisition, digital Filter, arithmetic logic unit	Zi Lock-in Amplifier (UHF), Zi Lock-in Amplifier (HF2LI), evaluation DSP, FPGA, dSPACE
Drive electronic PCB: back-end amplifiers	DC drive voltage, Carrier modulation, Voltage buffer amplifier	Standalone electronics, Custom electronics
Sense electronic PCB: front-end amplifiers	Carrier demodulation Current buffer amplifier	Standalone electronic Custom electronics
Position and rate table system	±1 deg/sec yaw axis rotation	Ideal Aerosmith 1571, Ideal Aerosmith 1291BR, Ideal Aerosmith 1270VS, Ideal Aerosmith 2102 (two axis)
Slip ring adapter (optional for rate table)	10 analog signal connectors from rate table to the outside	Custom made for table 1571
Scaling amplifier (optional)	Any COTS component. Matching impedance	Stanford research system (SIM983)
Analog limiter (optional)	Any COTS component. Matching impedance	Stanford research system (SIM964)
Analog filter (optional)	Any COTS component. Matching impedance	Stanford research system (SIM965)

Table G.14: Instruments required for this test measurement

G.5.2. Place your device under the test into the socket mounted on the PCB (Ref. G.3.1).

G.5.3. (Optional) Place necessary buffer cards (analog limiter, analog amplifier, low-pass filter) in between the UHF and PCB, and adjust the required parameters (Ref. G.3.1).

G.5.4. Connect carrier signal and necessary amount of DC voltages to the PCB (Ref. G.3.1).

G.5.5. Connect the output 1 of the UHF instrument to the forcer X-axis drive of the PCB (see Fig. G.53).

G.5.6. Connect the output of X-axis sense of the PCB to the input 1 of the UHF (see Fig. G.53).

G.5.7. Connect the output of Y-axis sense of the PCB to the input 2 of the UHF (see Fig. G.53).

G.6. Equipment setup parameters
Modify current limit of the power supply

Software TYPE	MINIMUM SPEC	RECOMMENDED MODELS
FPGA Control	Implementation of loops	LabOne UI (UHF) Zi Control (Zi2LI)
RS232 terminal (optional)	RS232 COM port terminal, commands to the rate table	Termite v3.4: a simple RS232 terminal

Table G.15: Software required for this test measurement

G.6.1. Make sure that the DC power supply is current limited, to prevent any damage as a result of testing a bad/short device (Ref. G.3.1).

Modify Analog limiter/scaling/filter Settings (optional)

G.6.1. Set the higher and lower limit of the limiter based on the device under the test to prevent any over drive condition (Ref. G.3.1)

G.6.2. Set the low-pass filter cutoff frequencies to the desire value based on your device resonance frequency, rule of thumb 10x larger than your device resonance (Ref. G.3.1).

G.7. Algorithm for rate mode

G.7.1. Open the UHF user interface software.

G.7.2. Two demodulators are necessary to operate the CGV in the rate mode, here we used demodulator#1 and#4 from the front panel (see Fig. G.54 for the default settings).

G.7.3. Implement the PLL and AGC as described in Ref. G.3.1 on oscillator 1 and output 1 on demodulator#7.

G.7.4. Under stationary condition from the plotter tab observe the in-phase (X) and in-quadrature (Y) component of the demodulator#4.

G.7.5. Adjust the phase between these two to minimize the X component value as possible, preferably close to zero (see Fig. G.54, phase column of demod#4). Here experimentally measured to be 140 deg.

G.7.6. Under this condition the data reported on X-component of demod#4 is called to be CVG output.

G.8. Algorithm for FRB or WA mode (optional)

G.8.1. The UHF user interface software can be configured to operate the CVG device in FRB or WA modes (see Fig. G.55).

G.9. Procedure

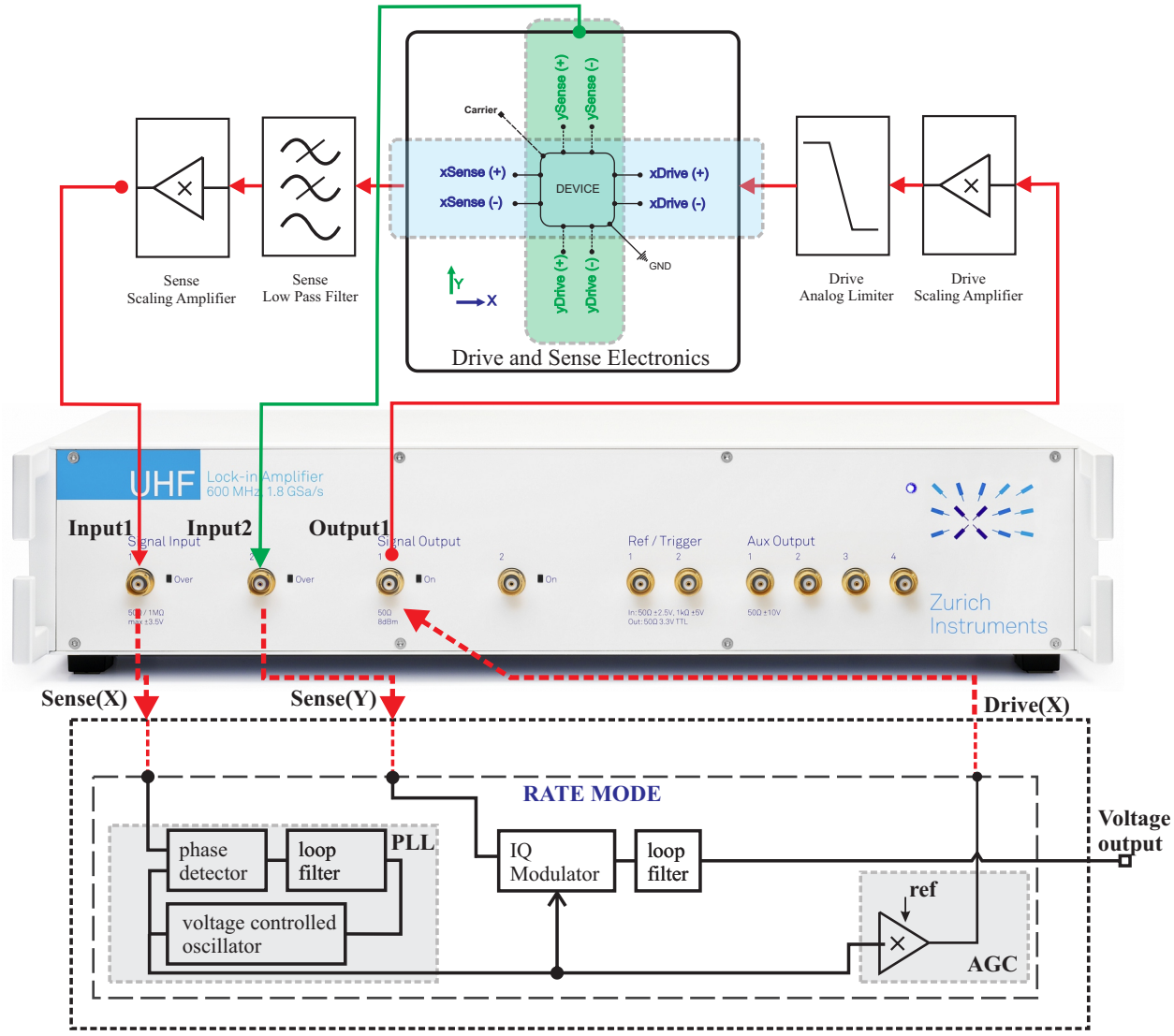

Figure G.53: MEMS CVG device under the test and necessary interface with instrument for rate configuration SF characterization

G.9.1. Mounting the unit

G.9.1.1. Mount the sensor in a package and the electronics onto the rate table stage. Make sure the rate table can be rotated fully at ±360 deg rotation around Z axis (Yaw axis). Use slip ring to pass signals from the rate table to the instrument outside for conditioning.

G.9.2. Instrument setup

G.9.2.1. Verify that PCB is powered on with no indication of short in current consumption of the power supply.

G.9.2.2. Turn on the UHF and implement the algorithm described above G.7.

G.9.3. Duration of the test

Figure G.54: User interface software configuration to extract the output of the CVG device under the test

G.9.3.1. The test is conducted by applying constant rate motion to the stage by inserting the command JOG followed by the rate value on the screen of the controller or software on the PC with RS232 terminal.

G.9.3.2. Due to the Coriolis effect, the gyroscope proof mass senses a force results in change of the capacitance of the sense electrodes and translated into voltage being sensed in X component of the demod#4 (step G.5.7).

G.9.3.3. The CVG output data should be recorded continuously while device is being operated.

G.9.3.4. While the platform is secure apply precise input rotation stimuli of your choice to the platform (see on rate table operation)

G.9.3.5. here we used 60 °/s every 30 s. An example of final output is shown in Fig. G.56.

G.10. Example Calculations

G.10.1. Scale-factor calculation

G.10.1.1. After recording the CVG output from the above procedure. The scale-factor of the device can be calculated as follow:

$$Scale - factor = \frac{\Delta V}{\Delta \Omega}$$

where ΔV represents the change in voltage unit corresponding to the input applied rotation to the stage and $\Delta\Omega$ is the true input rotation commanded to the stage in (deg/sec).

G.10.1.2. The final unit of the scale-factor measured to be V/deg/sec. Report the scale-factor after estimating the number.

G.10.1.3. The scale-factor of the data reported in Fig. G.56 for this device is estimated to be $6/60 = 0.1\,\mathrm{mV}/^\circ/\mathrm{s}$.

G.11. Test Data Requirements/Suggestions

G.11.1. To apply physical input stimuli to the sensor (i.e. rate rotation) here we use single axis Ideal Aerosmith 1270VS (see Fig. G.57)

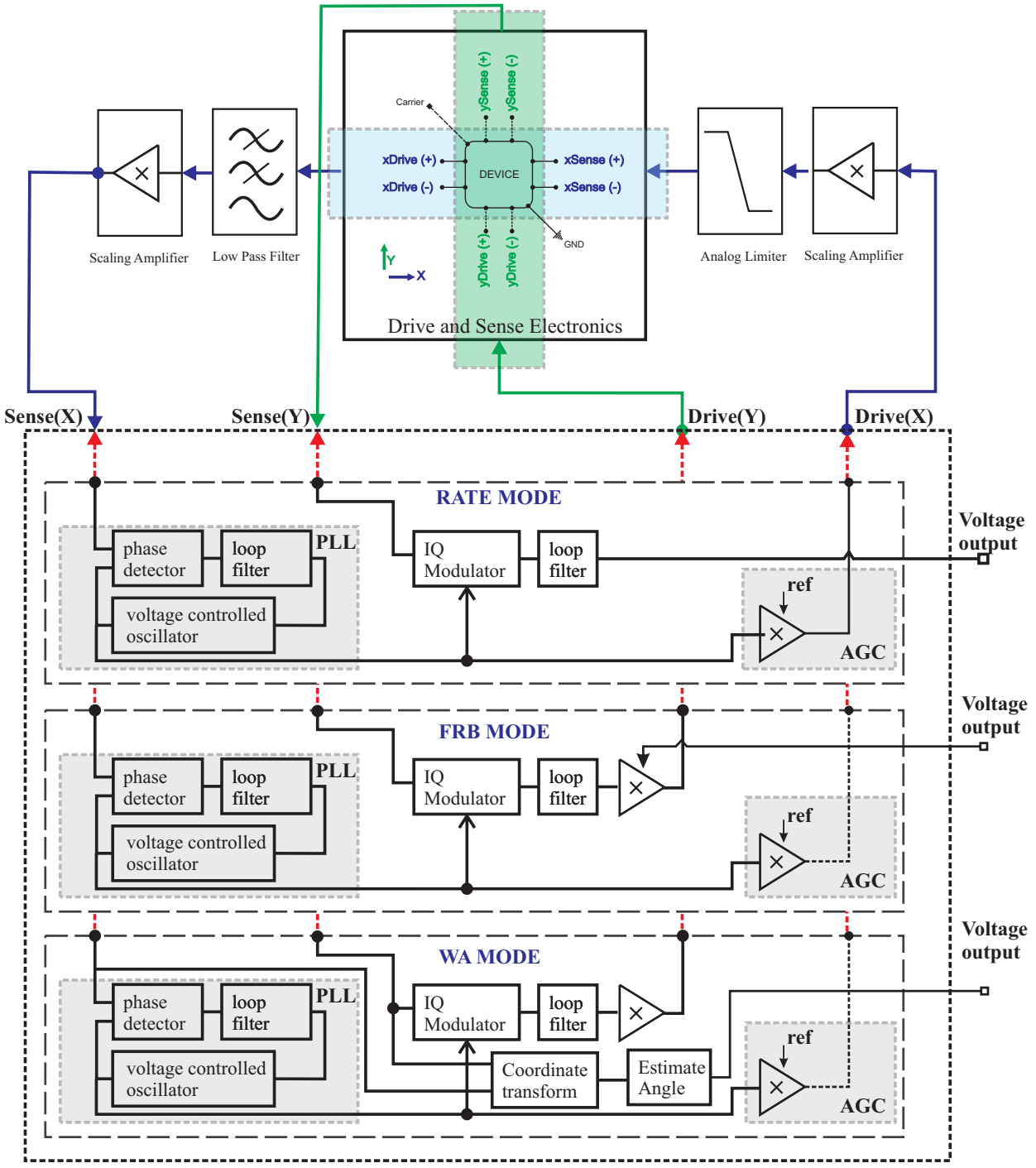

Figure G.55: MEMS CVG device under the test and necessary interface with instrument for rate and whole-angle SF characterization

G.11.2. The table is capable to rotate fully clockwise and/or counter clockwise. The protocol is similar across different model of rate tables.

G.11.3. Secure the electronic platform with sensor on the top of the table using predefined screws on the plate. Use any adapter in between to find the best adjustment to

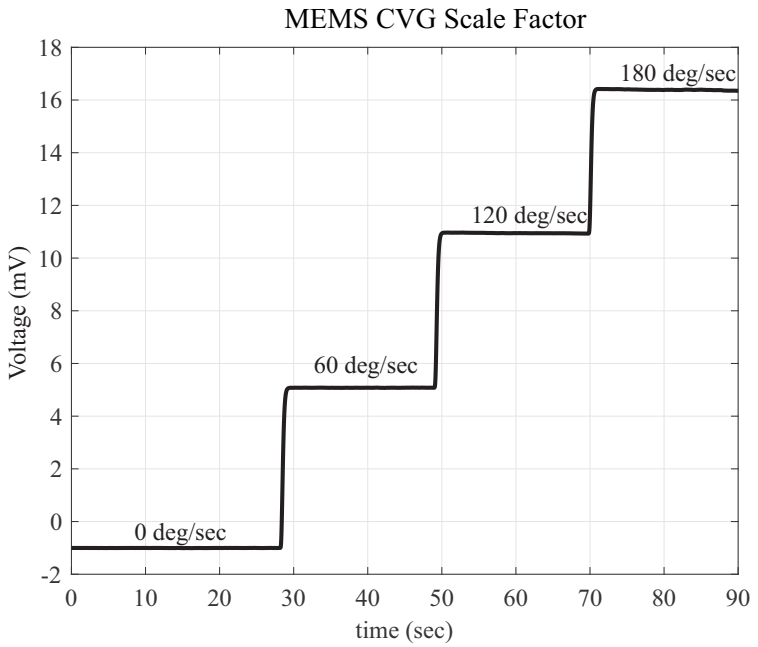

Figure G.56: Example of output response to input rotation of a CVG device under the test in rate mode

your platform/electronic.

G.11.4. Plug the rate table power cable to the electrical outlet.

G.11.5. Turn on the controller by pressing the button.

G.11.6. The controller can be controlled 1) by the computer or 2) by the front panel using the buttons:

1) Using Front panel:

G.11.6.1. The commands to the rate table are being set on the screen using the four buttons: run/menu, increase, decrease, and enter.

G.11.6.2. From the menu select the mode of motion. The table is limited to rate rotation (deg/sec).

G.11.6.3. Find the desire speed by pressing the increase or decrease followed by the enter button results in different input rotations.

G.11.6.4. After the desire speed is selected press run to apply the rotation to the table. Start with low input rotation and make sure all cables are secured before applying higher input rate.

G.11.6.5. Press run again to stop the rotation.

2) Using Remote controller like PC:

G.11.6.6. A RS232 to USB cable is needed to communicate to the controller.

G.11.6.7. The RS232 side will be connected to the back of the rate table and USB side to the computer.

Figure G.57: Single Axis Rate table to apply input rate of rotation

G.11.6.8. After the necessary physical connection is done, open a COM terminal to establish the communication with the rate table. An example of COM terminal software is an executable file "Termite 3.4" by Softpedia.

G.11.6.9. Check if the communication is successful by monitoring the terminal screen. If there is not communication, adjust the COM port and baud rate to establish a proper handshake between the PC and the rate table. A typical settings for Idea rate table are: Baud rate:9600, Data bits:8, Stop bits:1, Parity:none, Flow control: DTR/DSR.

G.11.6.10. After proper handshake between the PC and the rate table is done. Send the command by typing inside the terminal.

G.11.6.11. The JOG command applies rate rotation to the table. A JOG20 means rotation of $20\,^{\circ}/s$, and a JOG-20 means a rotation of $-20\,^{\circ}/s$.

G.11.6.12. Type in the command in the terminal and press enter to send the command to the rate table.

G.11.7. As input rate of rotation is being applied monitor the electronics and make sure it is secured under continuous rotation.

G.11.8. Based on the experiment in mind apply the sequence of input rotations and monitor the output.

G.11.9. At the end of the experiment, stop the input rotation.

H UCI/NGC Characterization Platform - Full Gyroscope Tuning

H.1. Purpose

This document describes the steps involved to tune the control loops of a gyroscope for open-loop, closed-loop or in virtual carouseling modes using UCI/NGC DARPA platform [94], with UITS/PALADIN interface [101].

H.2. Required and Recommended equipment

Table H.16 summarizes the components required for this measurement:

COMPONENTS TYPE	MINIMUM SPEC	RECOMMENDED
A gyroscope	Sealed LCC package	both X- and Y-modes operational resonance frequency of $< 2.7\,\text{kHz}$

Table H.16: Component required for this test measurement

Table H.17 summarizes the instruments required for this measurement:

INSTRUMENT TYPE	MINIMUM SPEC	RECOMMENDED MODELS
Power supplies	Supply ± 15 Volts, 0-3Amp	BK Precision 1672 Triple Output
UCI/NGC box	with LCC socket for device	

Table H.17: Instruments required for this test measurement

H.3. Software installation and initial settings

H.3.1. Install the GUI program

A standalone program is available at `http://nitride.eng.uci.edu /Public/Northrop_Grumman_CVG/Program/MyAppInstaller_mcr.exe`

H.3.2. After successful installation of the program, run the executable file

Program_Files : Northrop Grummin : CVG_GUI : application : CVG_GUI.exe (upon successful installation of the program a shortcut of the executable file has been placed on the desktop).

H.3.3. Initial assumption

At this point, before start tuning gyro, its assumed that the gyros nominal AC drive signal magnitude and frequency are known for both X- and Y-axes. If it's not known, a sweep measurement is needed to be applied on each mode to extract the center frequencies, while the sweep is being applied it is recommended that to vary the AC input drive voltage to be at 80% of the maximum displacement before snapping occurs. All other hardware settings are being applied with no changes

needed (i.e., carrier signal magnitude, phase delay, freq, DC bias voltages, and etc).

Test procedure:

H.4. Power up electronic Power-up the electronics (an external DC power source with a high current is needed). Plug in the banana cable with matching polarity to the supply voltage socket on the board (red +, black −). Turn on the voltage limit with 12 V, the current consumption is around 630 mA, the board is safe if the supply current limit is up to 2 A. Less than 1 A current consumption from the supply indicates a healthy electronic with no shorts on the device or broken electronics.

H.5. Software interface

H.5.1. Upon running successfully of the program, a GUI will pop up (see Fig. H.58).

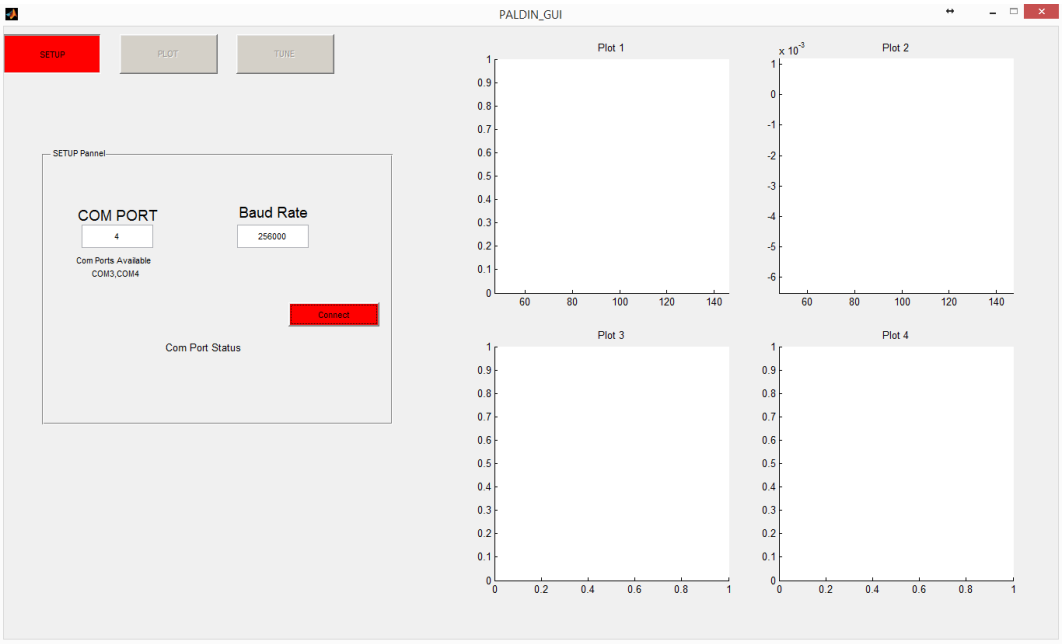

Figure H.58: CVG Software, with user interface with real-time data acquisition display

H.5.2. Select port #4, and type baud rate number 256,000 , this will automatically set the transfer data rate through PC, USB and platform. Press connect, at this point if the connect button is red it means it is not working. If it still shows red, change the port number to other COM ports (this may be different from PC to PC, Note: settings could be adjusted through the control panel). A green button color, means it is connected, and everything is well.

H.5.3. Upon successful running of the program, a command with the following message will get display. “Make 0” is activated, (Comm Port number ACTIVE).

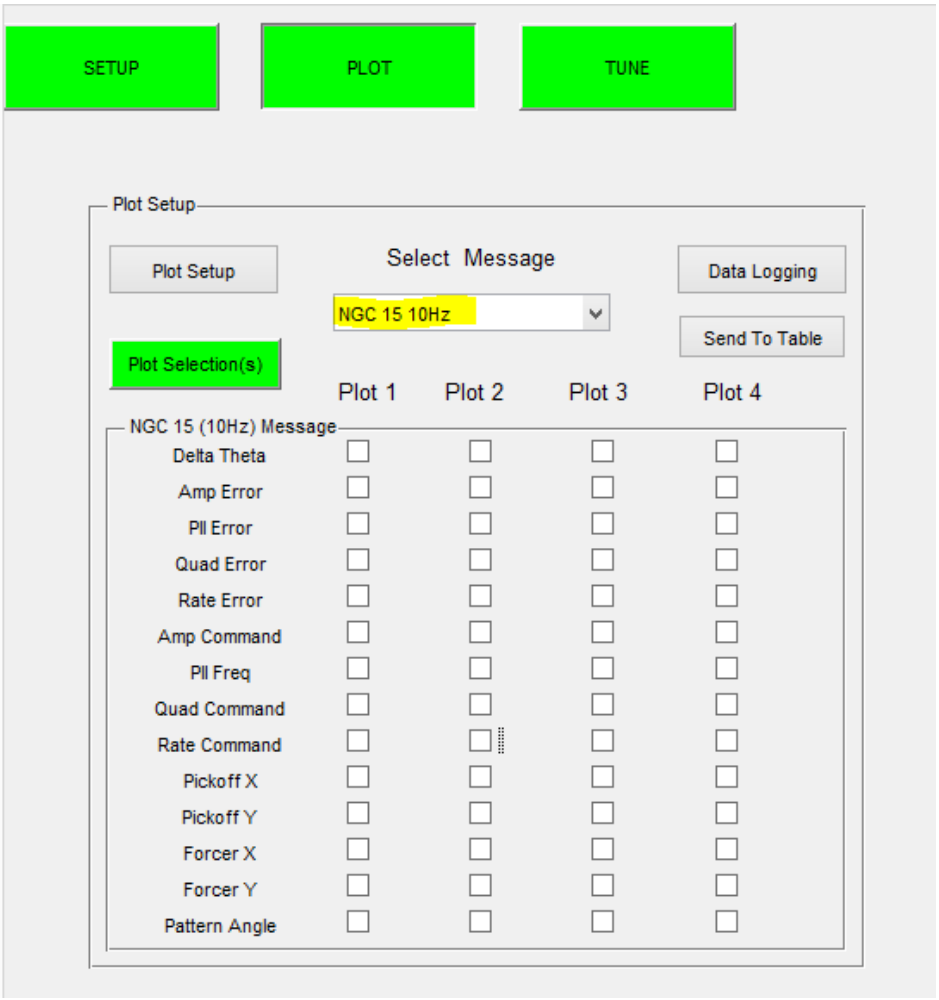

Figure H.59: Software plotting option. Selection of the gyro data rate transfer 10 Hz, control loop parameters to be shown on the (quadrant) subplots

H.5.4. From top sections press → plot → select msg → NGC 15 Hz, (for overnight data recording 1 Hz data is sufficient) (see Fig. H.59)

H.5.5. All knobs supposed to be green, if not something is not working right. A stop at this point is necessary (see Fig. H.60).

Four plots, can be display based on interested signals.
ACL, PLL, RCL and QCL are the basic closed-loop procedure for tune up (see Fig. H.61).

H.6. Make sure that no AC drive signal is present in both the AN (x) and ND (y) outputs

H.6.1. The Kp, Ki, and integrator values of the ACL, RCL, and QCL should be zeroed. Leave PLL as is with its existing gains.

H.6.1.1. If the PLLs gains are zero, then set Kp to 0.0005 and set Ki to 0.00003. This will serve as a good starting point for the PLL.

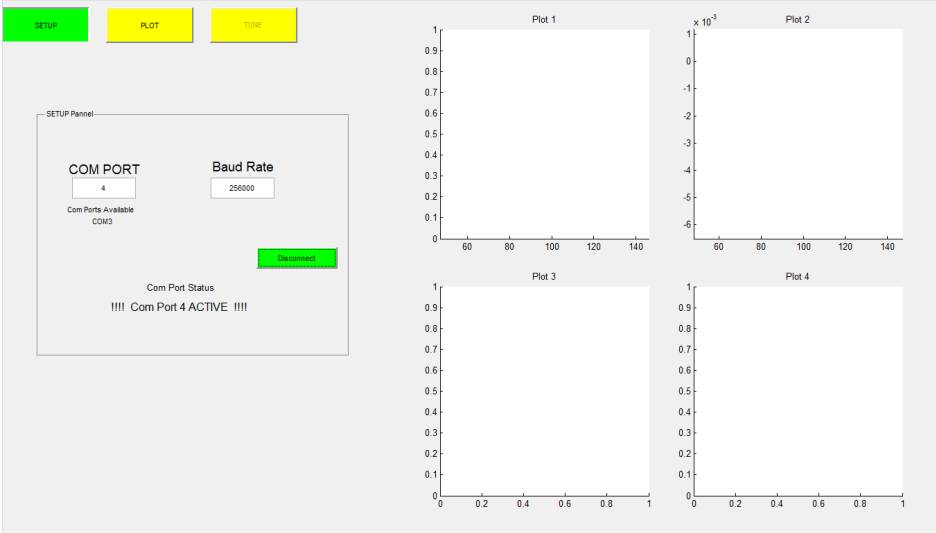

Figure H.60: GUI interface, real-time data display after successful connection to the board

H.7. Plug in the desire QMG gyroscope

H.7.1. The current configuration of the board only accepts QMG-ph1 in DIP package and QMG-ph2 in LCC package. For LCC device characterization, there is no orientation. For DIP configuration the orientation matters, please refer to the wire bonding document. (in general, pin#1 indicates the ground connection of the device)

H.8. Setup the nominal amplitude of the AC drive signal.

H.8.1. Set a nominal amplitude command in ACL by setting a fixed fsda value in the integrator.

H.8.2. The nominal fsad value depends on both the QMG and any gain applied to the signal in the electronics. With the nominal drive voltage known, calculate the nominal fsad and apply it into the amplitude loops integrator value. Since the ACLs gains are zero, the loops signal output is fixed in amplitude

H.8.2.1. The voltage scale factor on the CVG electronics CODEC chip is about 1.77 V rms per fsda when all other gains (both electrical and in software) are equal to 1.

H.8.2.2. For a typical Q=1,000 QMG, or low vacuum QMG, the nominal drive AC magnitude is usually around 800 to 900 mV 0-peak, or around 570 to 635 mV rms (under certain hardware conditions). Therefore, the fsda value in the integrator should fall around 0.322 to 0.359 fsda.
e.g., for device ID:QMG78HD, the nominal drive fsda value is 0.3558

H.8.2.3. For a much higher Q QMG, say a Q of 300,000, the nominal fsda will be much less, around 0.0008 to 0.0013 fsda.
Be careful when adjusting the amplitude command of a high Q device as it may easily overdrive the resonator.

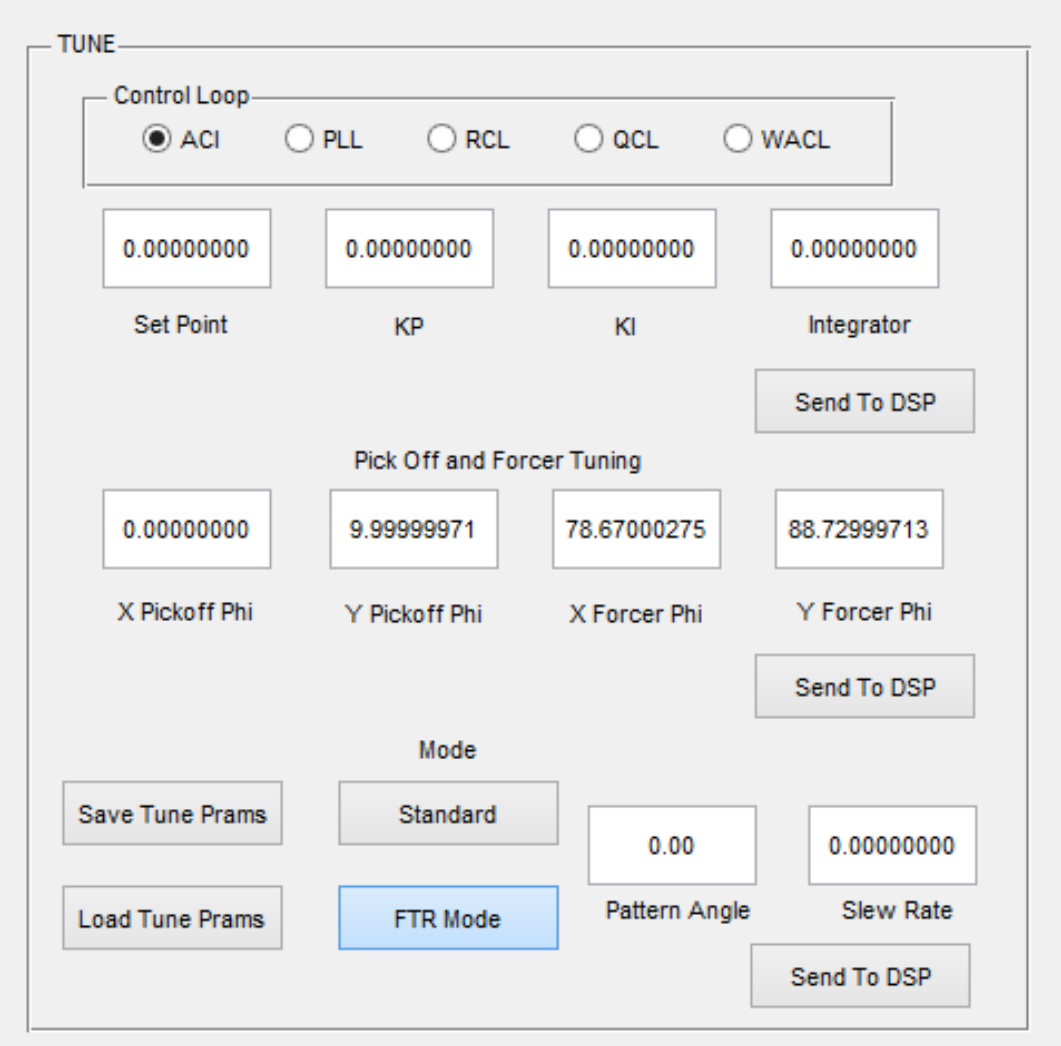

Figure H.61: PID tune-up GUI. Send/set parameters of each loop to the CODEC. Main loops are: Amplitude, Phase, Rate, Quadrature and Angle. Set drive forcer and pickoff phases.

H.9. If necessary, adjust the drive signals frequency until its at (or near) the gyros resonant frequency

H.9.1. Monitor amplitude measurement. For a high Q device, the measurement will display sinusoidal behavior when PLL frequency is not optimal. The slower the frequency of the sinusoidal amplitude measurement, the closer the PLL is to gyro resonant frequency.

H.9.2. Change the PLLs integrator value to steer frequency. The integrator value is the frequency offset from the PLLs default center frequency.
e.g., for the QMG firmware, the center frequency is 2,898 Hz.

H.9.3. Keep in mind that this loops gains are non-zero and, therefore, closed loop. Since the forcers phase hasnt been optimized yet, the loops integrator may drift away

significantly after modifying it. If the PLL integrator (i.e., frequency output) drifts away too much, then zero out the loops gains (pKp and pKi) to open the loop before applying desired integrator value. But try to keep the PLL loop closed to make tuning easier in the subsequent step:
If the PLL still drifts away after setting it at desired frequency and re-plugging in pKp and pKi gains, then try changing x-forcers phase until the PLL is able to lock in on the resonant frequency to some extent (basically trying out the next step a bit, then falling back to this step).

H.10. Adjust the X-axis forcer phase until amplitude input (AInput) reaches a maximum.

H.10.1. For a low Q gyro, the closed-loop PLL will change frequency when adjusting the X-axis forcer phase. This is normal.

H.10.2. The PLL loop should be closed when executing this step.

H.11. Adjust the PLL gains (see note H.19).

H.11.1. See note H.19 below on instructions on adjusting loop gains.

H.11.2. While monitoring PLL input (pxInput), induce a step response to test out the loop. Simply change variable pxSetPt between 0 and some small number such as 0.01.

H.11.2.1. The bandwidth of this loop is usually pretty high, so theres no need to go onto the underdamped side

H.12. Adjust the ACL loop gains as necessary, thus closing this loop (see note H.19).

H.12.1. Apply a setpoint for this loop. Make sure that setpoint matches the nominal drive measurement in order for the ACL to maintain nominal flex amplitude on the gyro after closing it.

H.12.2. See note H.19 below on instructions on adjusting loop gains.

H.12.3. While monitoring amplitude input (aInput), induce a step response to test out the loop. Simply change variable aSetPt between its nominal value and its nominal value ± 0.01.

H.13. Apply the same X-axis forcer phase value to the Y-axis forcer phase of equal value. This will serve as a good starting point for the Y-axis forcer phase.

H.14. Set the pattern angle to 45 degrees.

H.15. Scope both AN forcer and ND forcer signals from the gyros front-end op-amp input (not the gyros forcer electrode pins) and adjust the Y-axis forcer phase until both waves are in phase to each other.

H.15.1. The criteria here is to have both forcer signals arrive in-phase to the gyro electrodes. This will account for small phase shifts due to the forcer electronics

H.16. Set the Y-axis pickoff phase to +10° degree compare to X-axis pickoff phase.

H.17. Adjust the QCL gains as needed, thus closing this loop (see note H.19).

H.17.1. If gyro delta f exceeds 5 Hz, then tuning this loop may be difficult.

H.17.1.1. It may not be possible to close this loop and the RCL loop if delta f exceeds 6 Hz. If thats the case, then consider leaving both QCL and RCL loops shut off (open) to observe its Coriolis-induced signal in the loop inputs for a loq Q QMG. For a high Q QMG, a traveling wave will start to build, causing both the QCL and RCL inputs to oscillate at that delta f until it rings down.

H.17.2. Leave its setpoint at zero.

H.17.3. See note H.19 below on instructions on adjusting loop gains.

H.17.4. While monitoring quadrature input (qInput), induce a step response to test the loop. Simply change the loops setpoint between zero and something like ±0.01.

H.18. Adjust the RCL gains as needed, thus closing this loop (note H.19).

H.18.1. Again, if gyro delta f exceeds 5 Hz, then tuning this loop may be difficult.

H.18.2. Leave its setpoint at zero.

H.18.3. While monitoring rate input (rInput), induce a step response to test this loop. Simply change the loops setpoint between zero and something like ±0.01.

The QMG (or CVG device under test) should now be functioning as a gyroscope. The next task that usually follows is measuring scale factor on a rate table and noise characterization.

H.19. **Note:**
On adjusting the P and I gains and its selection

H.19.1. A good way to start is to adjust the P gain first while the I gain is zero. But first, there should be a value in the integrator such that it keeps the loops error value at or close to zero. This can be done by temporarily setting a small value for the I gain until the loop zeroes out the error term. Then zero out the I gain.

H.19.2. With the I gain set to zero, adjust the P gain until the loop is critically damped.

H.19.3. Now adjust the I gain to take care of droop while maintaining the loop critically damped. The I gain could be increased a bit to underdamped the loop (with a certain % overshoot, usually 10% overshoot for high Q gyros) if necessary/acceptable for a bit more bandwidth.

H.19.3.1. Note that, depending on the system, additional gain may be obtained with less ringing when under-damping the P controller a bit as well (rather than solely under-damping the I controller only), or having only the P controller underdamped. This depends on the system and only needs to be explored when additional bandwidth is critical.

I List of Vendors

The following is a list of vendors whose services have been used in this work:

Digi-Key Corp
Location: Thief River Falls, MN, USA
Website: http://www.digikey.com/
Point of Contact: N/A
Phone: +1-800-344-4539
Offers electronic components and supplies various development boards.

Digilent, Inc
Location: Pullman, WA, USA
Website: https://store.digilentinc.com/
Point of Contact: N/A
Phone: +1-509-334-6306
Supplier of educational evaluation kits on microcontroller processors for prototyping.

---

dSPACE, Inc
Location: Wixom, MI, USA
Website: http://www.dspace.com
Point of Contact: Vidya Duraiswamy, <vduraiswamy@dspaceinc.com>
Phone: +1-248-295-4700
Supplier of high speed electronic control units. dSPACE MLBX (Microlab DS1302 Box) was used for gyroscope whole-angle development. The system provides capability to program the DSP and FPGA blockset parts from Matlab Simulink environment.

Kurt J. Lesker
Location: Livermore, CA, USA
Website: https://www.lesker.com/
Point of Contact: N/A
Phone: +1-800-245-1656
Supplier of vacuum chamber and pumps used for in-vacuum characterization of the devices.

Rigol Technologies, Inc
Location: Beaverton, OR, USA
Website: http://www.rigolna.com/
Point of Contact: N/A
Phone: +1-877-474-4651
Benchtop oscilloscope and function generator instruments used for debugging circuits.

Si-Ware
Location: Cairo, Egypt
Website: http://www.si-ware.com/
Point of Contact: Ahmed El-Shennawy, <ahmed.elshennawy@si-ware.com>
Phone: +20-22-266-7344
Provides ASIC solution as a standalone platform for MEMS inertial sensors. This platform was used to characterize the device in this dissertation.

Stanford Research Systems
Location: Sunnyvale, CA, USA
Website: http://www.thinksrs.com/
Point of Contact: N/A
Phone: +1-408-744-9040
Provides signal conditioning units. Following instruments were used for the experimental setup. Scaling amplifier (SIM983), analog bessel & butterworth filters (SIM965), rechargeable isolated voltage source (SIM928) and analog limiter (SIM964).

Sierra Circuits, Inc
Location: Sunnyvale, CA, USA
Website: http://www.protoexpress.com/
Point of Contact: N/A
Phone: +1-408-735-7137
The company used for manufacturing of the prototype PCBs developed in this dissertation. The assembly of the PCBs were done in-house.

Tektronix, Inc
Location: Solon, OH, USA
Website: http://www.tek.com/
Point of Contact: N/A
Phone: +1-800-462-9835
Supplier of electronic instruments. Keithley 6221 low noise current source was used to debug the gyroscope front-end electronics. Keithley 2230-30-1 programmable triple channel DC power supply was used as a precision power supply to perform gyroscope tuning.

Thorlabs, Inc
Location: Newton, NJ, USA
Website: https://www.thorlabs.com/
Point of Contact: N/A
Phone: +1-973-300-3000
Supplier of TEC elements, resistive heaters, thermistors and thermocouples which where used for local heating and thermal characterization of the device in this dissertation.

PCB Unlimited, Inc
Location: Tualatin, OR, USA
Website: http://www.pcbunlimited.com/
Point of Contact: N/A
Phone: +1-800-348-9250
Supplier of stainless steel SMT stencils to be used for in-house prototype PCB assembly.

Ideal Aerosmith, Inc
Location: Grand Forks, ND, USA
Website: http://www.ideal-aerosmith.com/
Point of Contact: N/A
Phone: +1-701-757-5601
Provides precision two-axis and three-axis positioning and rate tables system for inertial sensor characterization.

InvenSense, Inc
Location: San Jose, CA, USA
Website: http://www.invensense.com/
Point of Contact: Julius Tsai, <jtsai@invensense.com>
Phone: +1-408-988-7339
Commercial CMOS+MEMS manufacturer, the process was explored through this dissertation. Supplier of consumer grade COTS IMUs. MPU9250 was used in this dissertation.

ITmems S.R.L. Spin off del Politecnico di Milano
Location: I-20131 Milano, Italy
Website: http://www.itmems.it/
Point of Contact: Nicola Aresi and Giacomo Langfelder, <langfelder@itmems.it>
Phone: +39-02-49660460
MCP MEMS characterization platform (ITM007) was used throughout the characterization cycle in this dissertation. Typical characterization were rest capacitance extraction, resonance frequency and Q-factor measurements.

---

iX-foundry GmbH
Location: Dortmund, Germany
Website: http://www.ix-factory.de/
Point of Contact: Hans Bouwes, <h.bouwes@ix-factory.de>
Phone: +49-231-47730 (590)
Service provider for MEMS product. This foundry was used to fabricate the devices presented in this dissertation.

McMaster-Carr
Location: Elmhurst, IL, USA
Website: http://www.mcmaster.com/
Point of Contact: N/A
Phone: +1-562-692-5911
Supplier of miscellaneous hardware components used for various prototype developed in this dissertation.

National Instruments Corp
Location: Austin, TX, USA
Website: http://www.ni.com/
Point of Contact: Bhavin Desai, <bhavin.desai@ni.com>
Phone: +1-310-270-7901
The CompactRIO controller system used for personal navigation in this dissertation. The platform provides the flexibility in terms of both hardware to integrate with multiple sensors and software for programming.

Westbond, Inc
Location: Anaheim, CA, USA
Website: http://www.westbond.com/
Point of Contact: N/A
Phone: +1-714-978-1551
WestBond model 7201 was used for sensor die attachment and PCB component assembly. WestBond model 747677E was used for wirebonding of the sensor to the package used in this dissertation.

WireMasters
Location: Columbia, TN, USA
Website: http://www.wiremasters.net/
Point of Contact: N/A
Phone: +1-800-635-5342
Supplier of high data rate cables used for civil and military applications. These cables were used for the development of the personal navigation presented in this dissertation.

Zurich Instruments AG
Location: Zürich, Switzerland
Website: http://www.zhinst.com/
Point of Contact: Flavio Heer, <flavio@zhinst.com>
Phone: +41-44-5150385
Supplier of advanced lock-in amplifiers used for characterization and testing of inertial MEMS sensors developed in this dissertation

---